Search for resonances produced in association with or decaying to a Z boson at large transverse momentum with the ATLAS detector at the LHC

Kunlin Han

THESE DE DOCTORAT

NNT : 2022UPASP026

Search for resonances produced in association with or decaying to a Z boson at large transverse momentum with the ATLAS detector at the LHC

Recherche de résonances produites en association avec ou se désintégrant en un boson Z à grand moment transverse avec le détecteur ATLAS au LHC

Thèse de doctorat de l'université Paris-Saclay et de University of science and technology of China

École doctorale n○ 576 : Particules, hadrons, énergie et noyau : instrumentation, imagerie, cosmos et simulation (PHENIICS)
Spécialité de doctorat : Physique des particules
Graduate School : Physique. Référent : Faculté des sciences d'Orsay

Thèse préparée dans les unités de recherche **Laboratoire de Physique des deux Infinis Irène Joliot-Curie** (Université Paris-Saclay, CNRS) et **State Key Laboratory of Particle Detection & Electronics** (USTC), sous la direction de **Zhiqing ZHANG**, Directeur de recherche, et la direction de **Haiping PENG**, Professeur

Thèse soutenue à Hefei, le 2 mars 2022, par

Kunlin HAN

Composition du jury

Lianliang MA Professeur, Shandong University	Président
Nicolas BERGER Directeur de recherche, LAPP	Rapporteur & Examinateur
Shu LI Maître de conférences (eq. HDR), T.D. Lee Institute and Shanghai Jiao-Tong University	Rapporteur & Examinateur
Adam FALKOWSKI Directeur de recherche, IJCLab	Examinateur
Gabriel FACINI Maître de conférences, University College London	Examinateur
Zhiqing ZHANG Directeur de recherche, IJCLab	Directeur de thèse
Haiping PENG Professeur, University of Science and Technology of China	Co-Directeur de thèse

université PARIS-SACLAY

ÉCOLE DOCTORALE
Particules, hadrons, énergie et noyau : instrumentation, imagerie, cosmos et simulation (PHENIICS)

Titre: Recherche de résonances produites en association avec ou se désintégrant en un boson Z à grand moment transverse avec le détecteur ATLAS au LHC
Mots clés: ATLAS, Au-delà du modèle standard, Boson Z, Résonance

Résumé: Cette thèse présente une recherche générique de résonances réalisée avec les événements du boson Z se désintégrant en ee et $\mu\mu$ au moment transverse supérieur à 100 GeV en utilisant les données correspondant à une luminosité intégrée de 139 fb^{-1} collectées avec le détecteur ATLAS dans les collisions pp à une énergie dans le centre de masse de 13 TeV au LHC. La recherche vise des résonances produites en association avec un boson Z et apparaissant ainsi comme un recul (X) du boson Z ou être un état intermédiaire (Y) se désintégrant en un boson Z et les particules du modèle standard ou une autre résonance X. La sélection de moment transverse permet de réduire le bruit de fond du modèle standard et d'améliorer la sensibilité de la recherche. Six catégories d'événements indépendantes sont définies pour être sensibles à différentes résonances se désintégrant dans différents états finals. Les observables utilisées pour la recherche sont la masse invariante d'objets visibles dans le système de recul et celle de l'état final complet. Les distributions de masse dans les six catégories d'événements ainsi que leur combinée sont examinées pour les excès au-dessus d'une estimation du bruit de fond du modèle standard basée sur les données. Large plage de masse pour valeurs de masse de 200 GeV et jusqu'à environ 6 TeV peut être étudiée en fonction des spectres de masse et des catégories. Aucun excès significatif n'est observé dans les spectres de masse et les catégories d'événements considérés. Les limites supérieures d'exclusion sur la section efficace multipliée par le rapport de branchement multiplié par l'acceptance sont obtenues à un niveau de confiance de 95% d'une manière indépendante du modèle pour les signaux de forme Gaussienne avec trois valeurs de largeur relative de 3%, 5 % et 10%.

Title: Search for resonances produced in association with or decaying to a Z boson at large transverse momentum with the ATLAS detector at the LHC
Keywords: ATLAS, Beyond the Standard Model, Z boson, Resonance

Abstract: This dissertation presents a generic search for resonances performed with Z boson events decaying to ee and $\mu\mu$ at the transverse moment greater than 100 GeV using proton-proton collisions data collected with the ATLAS detector, corresponding to an integrated luminosity of 139 fb^{-1} with a center-of-mass energy of 13 TeV. The search aims for resonances produced in association with a Z boson and thus appearing as a recoil (X) of the Z boson or be an intermediate state (Y) decaying to a Z boson and the Standard Model particles or another resonance X.The requirement of transverse moment helps suppress the Standard Model background and enhance the sensitivity of the search. Six independent event categories are defined to be sensitive to different resonances decaying in different final states. The observables used for the search are the invariant mass of visible objects in the recoil system and the full final state. The invariant mass distributions in all six event categories and their combined one are examined for local excesses above a data-driven estimate of the Standard Model background. Large mass range for mass values down to 200 GeV and up to around 6 TeV can be studied depending on the mass spectra and categories. No significant excess is observed in any mass spectrum and event category considered. Upper exclusion limits on cross-section times branching ratio times acceptance are derived at 95% confidence level in a model-independent way for Gaussian-shaped signals with three different relative width values of 3%, 5%, and 10%.

Synthèse

Introduction

Le Modèle Standard (SM) de la physique des particules est une théorie qui décrit les particules élémentaires de la matière et leurs interactions. Il a réussi à expliquer une grande variété de résultats expérimentaux. Le boson de Higgs, la dernière particule manquante prédite par le SM, a été découvert en 2012 par les collaborations ATLAS et CMS au Large Hadron Collider (LHC). Cependant, le SM n'est pas encore une théorie complète, car il ne peut pas expliquer plusieurs phénomènes tels que la gravité, la matière noire et l'asymétrie matière-antimatière de l'univers. Un grand nombre d'extensions, appelées Beyond the Standard Model (BSM), ont été proposées pour traiter ces phénomènes, prédisant de nouvelles résonances et interactions lourdes qui pourraient être découvertes par les collisions pp à haute énergie dans le centre de masse ($\sqrt{s}$) au LHC.

L'un des éléments clés du programme de physique au LHC est la recherche de nouvelles résonances prédites dans les modèles BSM. Un grand nombre de recherches ont été effectuées au LHC. La plupart des recherches ont été effectuées de manière dépendante du modèle pour un état final spécifique. Aucune nouvelle physique n'a été trouvée jusqu'à présent.

Cette thèse présente une recherche générique de manière indépendante du modèle de résonances dans la production de $pp \to ZX$, où la résonance pourrait être dans l'état final X ou être un état intermédiaire Y se désintégrant en particules SM ou une autre résonance contenue dans X et un boson Z. Les bosons Z se désintégrant en ee et $\mu\mu$ à un moment transversal (p_{T}) supérieur à 100 GeV sont utilisés pour fournir un échantillon propre avec des efficacités de déclenchement élevées basées sur un seul ou dileptons, complétés par jet pour les événements avec des candidats ee fusionnés. Pour être plus sensibles aux différentes résonances, les événements sont classés en six catégories exclusives selon différents types de l'objet ayant le plus grand p_{T} dans X. Ces objets sont un électron, un muon, un photon, un petit-R-jet avec un paramètre de rayon $R = 0.4$, un b-jet avec le même paramètre de rayon, et un grand-R-jet avec $R = 1$, respectivement. Les distributions de masses invariantes des objets visibles dans l'état final X (m_X) et de l'ensemble des objets incluant le boson Z (m_{ZX}) dans chacune des six catégories d'événements sont définies comme des observables d'intérêt et sont examinées avec l'algorithme BumpHunter (BH) pour identifier les excès locaux de résonance au-dessus d'une estimation du bruit de fond du SM basée sur les données.

L'analyse utilise l'échantillon complet de données de collisions pp à $\sqrt{s} = 13$ TeV qui ont été enregistrées par le détecteur ATLAS au LHC dans Run 2, correspondant à une luminosité intégrée de $139\,\mathrm{fb}^{-1}$. Les résultats sont interprétés de manière indépendante du modèle en termes de signaux de forme Gaussienne avec une largeur de masse relative à trois valeurs différentes de 3%, 5% et 10% pour toutes les catégories d'événements. En fonction des catégories d'événements et des observables de masse, la recherche est effectuée

sur une large plage de masse comprise entre environ 200 GeV et plus de 6 TeV.

Le grand collisionneur de hadrons et le détecteur ATLAS

Le LHC du CERN (Centre Européen de Recherches Nucléaires) est le plus grand et le plus puissant, mais aussi le plus complexe, collisionneur du monde jamais construit par l'homme, dans un tunnel circulaire de 27 km de circonférence, creusé à 100 m sous terre. Il y a quatre expériences principales au LHC - ALICE, ATLAS, CMS et LHCb. Deux d'entre elles, ATLAS et CMS, sont de grands détecteurs polyvalents, principalement destinés à la recherche du boson de Higgs et de la nouvelle physique. À l'intérieur de l'accélérateur, deux faisceaux de particules (protons ou ions lourds) de haute énergie se déplacent à une vitesse proche de celle de la lumière en directions opposées dans des tuyaux de faisceau séparés avant d'être amenés à entrer en collision. Ils sont guidés autour de l'anneau d'accélérateur par un puissant champ magnétique maintenu par les aimants dipôles supraconducteurs. Des aimants quadripolaires supplémentaires sont utilisés pour maintenir les faisceaux focalisés, avec des aimants quadrupolaires plus forts proches des points d'intersection pour maximiser les chances d'interaction des deux faisceaux. Les aimants d'ordres multipolaires supérieurs sont utilisés pour corriger les petites imperfections dans la géométrie du champ. Le programme de physique du LHC est principalement basé sur des collisions proton–proton.

Le détecteur ATLAS est un détecteur de particules à usage général utilisé pour étudier un grand nombre de processus physiques. Il comprend un détecteur de trace interne (ID) entouré d'un solénoïde supraconducteur mince, des calorimètres électromagnétique et hadronique et un spectromètre à muons (MS) incorporant trois grands aimants toroïdaux supraconducteurs à huit bobines chacun. L'ID est constitué de détecteurs de pixels et de microstrips à granularité fine et d'un décterteur constitué de nombreux tubes à dérive (TRT). Il est immergé dans un champ magnétique axial de 2 Tesla produit par le solénoïde et assure un suivi précis des particules chargées dans la gamme $|\eta| < 2{,}5$, où η est la pseudorapidité de la particule. Le TRT fournit également des mesures de rayonnement de transition pour l'identification des électrons. Le système calorimétrique couvre la plage de pseudorapidité $|\eta| < 4{,}9$. Il est composé de calorimètres d'échantillonnage avec de l'argon liquide (LAr) ou des tuiles de scintillateur comme milieu actif, et du plomb, de l'acier, du cuivre ou du tungstène comme matériau absorbant. Le MS fournit des mesures d'identification et d'impulsion de muons pour $|\eta| < 2,7$. Le détecteur ATLAS dispose d'un système de déclenchement à deux niveaux pour sélectionner les événements à analyser.

Données et échantillons de simulation Monte Carlo

L'analyse est basée sur les données de collisions pp prises lors de Run 2 à $\sqrt{s} = 13$ TeV avec le détecteur ATLAS au LHC. Le temps d'espacement des paquets était de 25 ns. Seules les données prises sous les conditions stables des collisions de faisceaux et avec le système magnétique, le détecteur de trace, le calorimètre, et les autres sous-détecteurs

pleinement opérationnels, tels que définis par le groupe de qualité des données d'ATLAS, sont prises en compte. La luminosité totale intégrée est de 139 fb^{-1}.

Les événements candidats sont d'abord sélectionnés à l'aide de triggers non pré-échelonnés composés de triggers d'un seul lepton, de dileptons et de jet, qui se traduisent par une efficacité stable et élevée supérieure à 96%. Les triggers de leptons nécessitent soit un seul lepton isolé, soit une paire de leptons ciblant les désintégrations leptoniques des bosons Z. Pour les triggers à un seul lepton, les seuils d'impulsion transverse minimale varient entre 24 GeV et 26 GeV pour les électrons et entre 20 GeV et 26 GeV pour les muons, selon la période de prise de données. Pour les triggers de dileptons, les seuils minimaux en p_{T} varient entre 12 GeV et 17 GeV pour les électrons et entre 10 GeV et 14 GeV pour les muons. De plus, d'autres triggers de leptons avec des seuils en p_{T} plus élevés sont ajoutés pour atteindre une efficacité stable sur une large gamme de p_{T}. A très haut p_{T}, les leptons ne sont plus isolés, même les triggers d'un seul lepton avec des seuils p_{T} élevés ne sont plus efficaces. Pour cette raison, les triggers sont complétés par celui de jet avec un seuil minimum en p_{T} de 360 GeV.

Bien que l'estimation du bruit de fond de cette analyse soit basée sur les données, les échantillons simulés de Monte Carlo (MC) pour les processus des bruits de fond sont aussi utilisés pour définir les sélections d'événements, étudier les effets de résolution du détecteur et valider la stratégie de recherche. Le bruit de fond du SM provient principalement de la production de Z + jet, de diboson (ZZ, ZW, $Z\gamma$) et de quark top, simulé avec différents générateurs. De petites contributions de multijet et W + jets sont obtenues en utilisant une technique basée sur les données. Certains échantillons de signaux BSM sont également utilisés pour vérifier la sensibilité de l'analyse.

Sélection et classement des événements

Les candidats bosons Z sont sélectionnés en exigeant deux leptons de charge opposée et de même saveur (e^+e^- ou $\mu^+\mu^-$). Les deux leptons doivent satisfaire aux critères de qualité minimale pour garantir qu'ils sont produits dans la diffusion dure. Dans la région extrêmement élevée de p_{T} du boson Z, une identification de ee fusionnés est développée pour récupérer l'efficacité perdue, basée sur la méthode Boosted Decision Tree (BDT). Les candidats bosons Z doivent en outre avoir des valeurs de masse invariante comprises entre 66 et 116 GeV. Le boson Z doit également passer $p_{\text{T}} > 100$ GeV, ce qui est un compromis pour conserver des statistiques suffisantes et supprimer les contributions du bruit de fond du SM.

Dans un événement sélectionné, tous les objets visibles dans le système de recul (X) du boson Z sont triés par ordre de leur p_{T}. Six catégories exclusives d'événements sont définies en fonction du type de l'objet p_{T} de tête dans le X : les catégories de petit-R-jet (non b-jet), de b-jet, de grand-R-jet, de photon, d'électron ou de muon. Deux observables sont définies comme la masse invariante du système de recul (m_X) et celle de l'état final complet de l'événement (m_{ZX}) en utilisant tous les objets visibles sélectionnés. La classification est validée à l'aide d'échantillons de signaux montrant un faible taux de mauvaise classification

par rapport aux états finals attendus. Pour éviter les erreurs de classification potentielles et pour améliorer la sensibilité de la recherche, une catégorie combinée regroupant les six catégories est également définie.

Estimation du bruit de fond et évaluation des signaux parasites

En raison du désaccord entre la simulation MC et les données dans les spectres observables ($\mathcal{O}$) pour la plupart des catégories principalement dû au processus dominant du bruit de fond Z+jets, une approche axée sur les données est développée pour directement estimer la contribution du bruit de fond à partir des spectres de données. L'estimation du bruit de fond est obtenue en effectuant un ajustement global à l'aide d'une forme fonctionnelle,

$$f_1(x) = p_0 \left(e^{-p_1 x} + p_2 e^{-(p_1+p_3)x} + \cdots \right),$$

or

$$f_2(x) = p_0 (1-x)^{p_1} x^{p_2 + p_3 \ln x + p_4 \ln^2 x) + \cdots},$$

où $x = (\mathcal{O} - \mathcal{O}_{\min})/(\mathcal{O}_{\max} - \mathcal{O}_{\min})$ dans la première équation, et $x = \mathcal{O}/\sqrt{s}$ dans la seconde, p_0 est un facteur de normalisation et p_i avec $i = 1, \cdots$ sont des paramètres libres contrôlant la forme de la distribution $\mathcal{O}$, et $\mathcal{O}_{\min}$ et $\mathcal{O}_{\max}$ sont les plages d'ajustement inférieure et supérieure d'une observable. Le nombre de paramètres libres dépend des catégories d'événements et des observables. Une valeur globale χ^2 p est calculée pour quantifier la qualité de l'ajustement, qui doit être supérieure à 0,05. Le choix de la forme fonctionnelle, du nombre de paramètres libres et des plages de masse à ajuster est basé principalement sur le test des signaux parasites.

Le test de signal parasite est utilisé pour quantifier le biais du modèle à partir de la forme fonctionnelle sélectionnée, qui est évalué en ajustant le spectre de masse basé sur MC avec une forme fonctionnelle pour modéliser la contribution attendue du bruit de fond sur une pente décroissante plus une composante de signal. Pour une recherche indépendante du modèle, cette dernière composante est choisie pour un signal de forme Gaussienne. Il inclut des effets de résolution de détecteur qui élargissent légèrement la largeur par rapport à sa valeur intrinsèque, se situant entre 3% et 10%. Le choix est déterminé par un balayage de masse utilisant diverses formes fonctionnelles et différents nombres de paramètres libres pour sélectionner celle qui fournit la qualité de l'ajustement et le rapport le moins fluctuant du signal parasite sur l'incertitude correspondante d'ajustement pour tous les points de masse entre l'intervalle de masse à ajuster.

Une fois que le choix de la plage de masse à ajuster et de la forme fonctionnelle est fait pour une distribution de masse dans une catégorie donnée, les incertitudes systématiques sont étudiées à la fois pour le bruit de fond et le signal. Il y a deux incertitudes principales prises en compte dans l'estimation du bruit de fond. Ce sont les incertitudes statistiques d'ajustement et de choix de fonction. La première est étroitement liée à la précision statistique de la distribution de masse, évaluée en comparant la distribution nominale et un ensemble de pseudo-expériences. La seconde provient du choix de la forme fonctionnelle, évaluée en comparant le résultat d'ajustement entre la forme fonctionnelle nominale et une

forme alternative, qui fournissent toutes les deux une bonne modélisation de la distribution du bruit de fond. Du côté signal, une incertitude de modélisation pour le signal de forme Gaussienne est estimée sur la base des rendements de signaux parasites, couvrant le biais possible dans la procédure d'ajustement. L'implémentation consiste à définir une enveloppe des rendements absolus du signal parasite en fonction de m_X ou m_{ZX}. Dans l'analyse statistique, les rendements totaux du signal peuvent être écrits comme :

$$N_{\text{signal}} = \mu_s \sigma_{\text{signal}} \mathcal{L}(\mathcal{A} \times \epsilon) + S_{\text{modelling}} \theta_{\text{modelling}}$$

où le premier terme reflète les rendements de signal attendus en tenant compte de la valeur de luminosité intégrée $\mathcal{L}$ et des corrections d'acceptation et d'efficacité $\mathcal{A} \times \epsilon$, et le second considère l'incertitude de modélisation avec $S_{\text{modelling}}$ étant la valeur d'enveloppe et $\theta_{\text{modelling}}$ un paramètre de nuisance. Une contrainte Gaussienne externe de moyenne 0 et de largeur 1 est appliquée sur $\theta_{\text{modelling}}$.

Stratégie de la recherche

Une fois que le bruit de fond est estimé, l'algorithme BH est utilisé pour tester la cohérence ou l'écart entre le bruit de fond et les données observées. Cet algorithme peut localiser l'excès local au-dessus du bruit de fond et quantifier le degré de divergence, sur la base de la valeur BH p.

Une stratégie de recherche proposée pour les données réelles est décrite ci-dessous :

- Pour un spectre de données donné, appliquez la même forme fonctionnelle et la même plage d'ajustement que celles obtenues à partir du spectre basé sur la simulation MC pour dériver une estimation initiale du bruit de fond et une valeur globale χ^2 p. La plage d'ajustement est ajustée en fonction des statistiques du spectre de données. L'algorithme BH est ensuite appliqué dans une plage de masse légèrement plus restreinte, appelée la "plage de masse sensible", pour obtenir une valeur BH p initiale et un intervalle qui indique l'excès le plus significatif.

- Si la valeur globale χ^2 p est supérieure à 0,05 ou si elle est inférieure au seuil mais que la valeur BH p est également inférieure à 0,01, alors nous passons à l'étape suivante. Sinon, les formes fonctionnelles alternatives ou l'augmentation de la limite de masse inférieure sont appliquées pour satisfaire les conditions.

- Un nouvel ajustement du bruit de fond est effectué en excluant l'intervalle BH initial pour obtenir une nouvelle valeur de χ^2 p. L'algorithme BH est exécuté à nouveau dans la plage de masse sensible avec le nouveau bruit de fond estimé pour obtenir une nouvelle valeur BH p et un intervalle mis à jour.

- Si la valeur globale χ^2 p et la valeur BH p sont toutes les deux supérieures à leurs seuils, l'analyse passe à la phase de définition des limites. Si la valeur globale χ^2 p est supérieure à 0,05 et que la nouvelle valeur BH p est inférieure à 0,01, un ajustement du signal plus le bruit de fond est effectué pour quantifier l'excès. Si la valeur globale

χ^2 p et celle en excluant l'intervalle BH initial sont inférieures à 0,05, cela signifie que soit le reste du spectre n'est toujours pas bien modélisé, soit il y a un autre excès significatif. Dans ces cas, nous allons soit revenir à la deuxième étape pour ajuster les formes fonctionnelles alternatives, soit répéter la troisième étape après avoir exclu le nouvel intervalle BH.

Résultats

Suite à la stratégie de recherche discutée ci-dessus, les fonctions du bruit de fond et les plages d'ajustement obtenues à partir des spectres MC sont utilisées sur les spectres de données. La plupart des fonctions sélectionnées ont une bonne description des spectres de masse des données, avec des valeurs globales χ^2 p supérieures à 0,05 et des valeurs BH p supérieures à 0,01. Pour quelques cas exceptionnels, une bonne modélisation est également obtenue en essayant les formes fonctionnelles alternatives et en ajustant les plages de masse selon la stratégie. Aucun excès significatif n'est observé dans tous les spectres de masse de toutes les catégories d'événements. L'excédent le plus important correspond à une valeur BH p d'environ 0,45 à 1,6 TeV sur le spectre m_{ZX} dans la catégorie de grand-R-jet.

Les résultats sont ensuite interprétés en extrayant les limites supérieures d'exclusion d'une manière indépendante du modèle sur des signaux de forme Gaussienne à 95% de niveau de confiance (CL) en utilisant le méthode CLs avec "binned profile likelihood ratio" comme la statistique de test. Les plages de masse sensibles aux limites sont déterminées à l'aide du calcul de la limite supérieure basé sur les spectres nominaux de masse des prédictions MC. Avec les spectres du bruit de fond nouvellement estimés, les incertitudes systématiques du bruit de fond sont mises à jour en utilisant les spectres de données réelles. Pour l'incertitude du signal de forme Gaussienne, l'incertitude relative du signal parasite est mise en œuvre car l'incertitude absolue dérivée des spectres MC ne peut pas être directement utilisée étant donné le désaccord entre les données et le MC.

Les limites observées et attendues à 95% CL sont obtenues pour des signaux de forme Gaussienne avec trois valeurs de largeur relative de 3%, 5% et 10%. Selon les observables et les catégories d'événements, les limites supérieures des sections efficaces d'un signal de forme Gaussienne avec une valeur de 3% de largeur sont d'environ 0,2 fb à une masse de 200 GeV pour m_X et 0.04 fb à $\sim$ 6 TeV pour m_{ZX}. L'impact de chacune des trois sources d'incertitude est étudié en ajoutant une à la fois sur les limites d'un signal de forme Gaussienne dans toutes les catégories. La source d'incertitude dominante est celle du signal parasite et elle aggrave la limite à basse masse de moins de 50% dans pratiquement tous les cas, à l'exception de la catégorie de petit-R-jet où elle atteint jusqu'à environ 120%.

Contents

1 - Introduction

The Standard Model (SM) of particle physics is developed to classify the elementary particles of the matter and to describe the interactions among them. It has achieved great success in explaining a wide variety of experimental results. The last missing elementary particle predicted in the SM, the Higgs boson, was also discovered in 2012 at the Large Hadron Collider (LHC). However, the SM is still not the final theory. There are a series of phenomena observed in the nature, which cannot be explained in the SM, such as the gravity, the matter-antimatter asymmetry, the difference of fermion's mass among three generations, and the Dark Matter and the Dark Energy. The SM is rather a effective approximation of the real final theory to describe the fundamental law of physics. Thus, a large number of extensions, called Beyond the Standard Model (BSM), have been proposed to solve the difficulties and complete the missing puzzle. Most of the extensions predict new heavy resonances interacting with the existing SM particles, which could be probed by the proton-proton collisions with a high center-of-mass energy at the LHC.

The LHC is the highest-energy collider experiment operating in the world. The search of new particles and new physics predicted by the BSM [1–9] is an crucial component of the LHC physics program. A large number of searches have been performed at the LHC. Most of the searches were performed in a model-dependent way for a specific final state [10–28]. No evidence of physics beyond the standard model has been observed in any of the searches performed. Unlike the discoveries of the SM particles based on a well-defined theoretical framework, some of the proposed BSM models introduce a vast number of parameters that need to be investigated and constrained from the observed data. On the experimental side, the possible phase space, such as the mass ranges and the final states, are still not fully explored by the previous searches. A model-independent search is necessary to cover as much phase space as possible.

This thesis presents a generic search in a model-independent way for resonances in the production of $pp \to ZX$ or $pp \to Y \to ZX$, where Z is the SM Z^0 boson and the resonance could be in the final state X or be an intermediate state Y decaying to SM particles or another resonance contained in X and a Z boson. One example model which predicts such resonance production is the two-Higgs-doublet model (2HDM) [29, 30]. In this model, Y would be a CP-odd state A and X the second CP-even Higgs boson H, heavier than the other SM-like CP-even Higgs boson h. The Z bosons decaying to ee and $\mu\mu$ at transverse momentum (p_{T}) greater than 100 GeV are used to provide a clean sample with high trigger efficiencies based on single or dilepton triggers, complemented with jet triggers for events with merged-ee candidates. To be more sensitive to different resonances, events are classified in six exclusive categories according to different types of the leading p_{T} object in X. The leading p_{T} objects are an electron, a muon, a photon, a small-R-jet with radius parameter $R = 0.4$, a b-jet with the same radius parameter, and a large-R-jet with $R = 1$, respectively. Invariant mass distributions of the leading p_{T} object and other objects in the final state X (m_X) and ZX (m_{ZX}) in each of the six event categories are defined

as observables of interest and are examined with the BumpHunter (BH) algorithm [31, 32] for local resonance excesses above the smoothly falling prediction of the SM taken from data-driven estimation.

The analysis uses the full data sample from $\sqrt{s} = 13$ TeV proton–proton (pp) collision at the LHC that were recorded by the ATLAS detector in Run 2 with an integrated luminosity of $139\,\text{fb}^{-1}$. The sensitivity of the search is enhanced by using the six event categories corresponding to different final states in a single analysis. Depending on the event categories and mass observables, the search is carried out over a large mass range between around 200 GeV and over 6 TeV. No significant excess of events is observed in each observable of each category. Upper limits on the production cross section times branching ratio with acceptance and efficiency were set for narrow general Gaussian-shaped resonances with three different width values of 3%, 5%, and 10% for each category.

I contributed to all studies of this analysis, documented in the main body of this dissertation, and serve as the analysis contact in a joint analysis group for this analysis. Besides, I contributed to the time resolution measurement of the RPC detector [33] and the estimation of theoretical systematics for background processes in searching for heavy resonances with the WW final state [34] documented in Appendix A and Appendix B, respectively.

The thesis is organised in the following way. Chapter 2 gives a brief introduction to the SM, BSM, and the Heavy Triplet Vector (HVT) signal model used to check the sensitivity of the analysis. Chapter 3 briefly introduces the LHC experiment and each component of the ATLAS detectors. Chapter 4 presents data and the simulated samples with corresponding efficiency studies in this analysis. Chapter 5 shows the reconstruction of physics objects, followed by a new identification method of merged-ee candidates in Chapter 6. Chapter 7 discusses the event selections and classification, including the comparison results between data and MC. Chapter 8 describes the background modelling and systematics uncertainties. Chapter 9 provides the search strategy and further validation studies. Chapter 10 presents the results for the application of search strategy to real data in full Run 2. Chapter 11 gives the conclusions and outlook. Appendix A presents the strategy and results of time resolution measurements of the RPC detectors. Appendix B shows the theoretical systematics of background and results for searching for heavy resonance with WW final state.

2 - Theory

This chapter presents an overview of the basic theory of particle physics. Section 2.1 introduces the theory of the SM. Section 2.2 shows the theory beyond the SM, which is related to the dissertation.

2.1 The Standard Model

During the second half of the 20^{th} century, physicists tried to build a theoretical framework representing our current understanding of elementary particles and their interactions, which is now called the SM of particle physics [35]. The SM classifies all known elementary particles and describes three of four known fundamental forces: the electromagnetic, weak, and strong interactions. It is a gauge quantum field theory, constructed with symmetry groups $\mathrm{SU}(3)_C \otimes \mathrm{SU}(2)_L \otimes \mathrm{U}(1)_Y$. The $\mathrm{SU}(3)_C$ group describes the strong interactions with C denoting colour charge, and $\mathrm{SU}(2)_L \otimes \mathrm{U}(1)_Y$ describes the electroweak interactions with L and Y denoting weak isopin and weak hypercharge, respectively. Over the past decades, the SM has successfully explained a wide variety of experimental results with high precision.

2.1.1 Elementary particles

In the SM, the elementary particles, with no other inner structures, are classified into fermions, gauge bosons, and the Higgs boson, as illustrated in Figure 2.1.

The fermions in the SM are elementary particles of spin-$\frac{1}{2}$ and are separated into two types, leptons, and quarks. There are 12 different fermions and the same number of corresponding antiparticles. They can be further separated into three generations, ordered by mass value. Each generation includes two quarks and two leptons. The classification between quarks and leptons is the property of colour charge.

Leptons are composed of three charged ones with an electric charge of -1, in units of elementary charge e, the electron (e^-), the muon (μ^-), and the tau (τ^-), as well as three neutral ones, the electron neutrino (ν_e), the muon neutrino (ν_μ), and the tau neutrino (ν_τ). Charged leptons can participate in electromagnetic and weak interactions, while neutrinos only allow weak interaction.

Quarks include three generations of doublets: up (u) and down (d); charm (c) and strange (s); top (t) and bottom (b). Three up-type quarks have an electric charge of $2/3$, while down-type quarks carry an electric charge of $-1/3$. Besides, quarks also carry a colour charge (red, green, and blue), allowing them to participate in the strong interaction. Gluons combine quarks via the strong interaction to form hadrons due to the phenomenon of colour confinement.

Gauge bosons in the SM are elementary particles of spin-1, including a massless photon, $W^\pm$ and Z boson, and eight massless gluons. They act as mediators to propagate the electromagnetic (photon), weak ($W^\pm$ and Z boson), and strong (gluons) interactions,

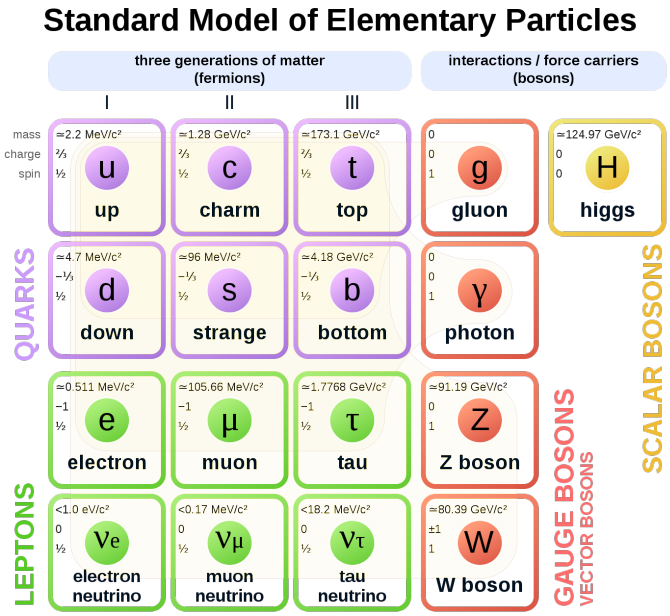

Figure 2.1: Elementary particles in the SM [36]

respectively. The $W^{\pm}$ and Z boson were discovered by the UA1 and UA2 collaborations at CERN in 1983 with mass values of about 80 GeV and 91 GeV [37, 38], respectively. The Z boson can decay to a fermion pair and its antiparticle, consisting of either leptonic or hadronic final states. Besides, there is another massive scalar boson, the Higgs boson, which is important to explain the origin of masses for massive gauge bosons ($W^{\pm}$ and Z boson) and fermions via their interactions with the Higgs field.

2.1.2 Interactions

The SM has a full gauge symmetry group of $\mathrm{SU}(3)_C \otimes \mathrm{SU}(2)_L \otimes \mathrm{U}(1)_Y$. The electromagnetic and weak interactions are unified into a single electroweak (EW) theory with $\mathrm{SU}(2)_L \otimes \mathrm{U}(1)_Y$ gauge symmetry. The strong interaction is described as the gauge group by quantum chromodynamics (QCD) [39–41] which is a gauge theory with $\mathrm{SU}(3)_C$. This section briefly introduces the mathematical formalism of the interactions in the SM.

Electromagnetic and weak interactions

Quantum electrodynamics (QED) [42–44] is an Abelian gauge theory with U(1) theory to describe the electromagnetic interaction. Subsequently, an EW theory was developed by Glashow, Weinberg, and Salam [45–48], unifying the QED and weak interaction, which is the mechanisms of the interaction between subatomic particles. The EW theory can be described by a $\mathrm{SU}(2)_L \otimes \mathrm{U}(1)_Y$ gauge group with four gauge bosons as mediators: the photon, $W^{\pm}$ and Z bosons. The generators of the group are Y (weak hypercharge) and τ^a (a=1, 2, 3) constructed with Pauli matrices for $\mathrm{U}(1)_Y$ and $\mathrm{SU}(2)_L$ group, respectively.

The weak hypercharge Y is defined as $Y = 2(Q - \tau^3)$ relating to the electric charge (Q) of particle and weak isopin (τ^3). The Lagrangian of the EW theory is written as

$$\mathcal{L}_{\rm EW} = -\frac{1}{4}W^a_{\mu\nu}W^{\mu\nu}_a - \frac{1}{4}B_{\mu\nu}B^{\mu\nu} + \sum_{\psi}\bar{\psi}\gamma^\mu(i\partial_\mu - \frac{1}{2}g'YB_\mu - \frac{1}{2}g\tau^a_L W^a_\mu)\psi, \tag{2.1}$$

where g and g' are the coupling constants for SU(2) and U(1) groups. $W^a_{\mu\nu}$ and $B_{\mu\nu}$ are the field strength tensors defined as:

$$W^a_{\mu\nu} = \partial_\mu W^a_\nu - \partial_\nu W^a_\mu + g\epsilon^{abc}W_{b\mu}W_{c\nu}, \tag{2.2}$$

$$B_{\mu\nu} = \partial_\mu B_\nu - \partial_\nu B_\mu. \tag{2.3}$$

W^a_μ and B_μ are the gauge fields, which give rise to four gauge bosons: the photon, $W^\pm$, and Z bosons, defined as

$$A_\mu = B_\mu \cos\theta_W + W^3_\mu \sin\theta_W, \tag{2.4}$$

$$W^\pm_\mu = \frac{1}{\sqrt{2}}(W^1_\mu \mp W^2_\mu), \tag{2.5}$$

$$Z_\mu = -B_\mu \sin\theta_W + W^3_\mu \cos\theta_W, \tag{2.6}$$

where the θ_W is the weak mixing angle to describe the mixing between electromagnetic and weak interactions, expressed as

$$\cos\theta_W = \frac{g}{\sqrt{g^2 + g'^2}}. \tag{2.7}$$

In the EW Lagrangian Eq. (2.1), both fermions and gauge bosons should be massless to preserve the $\mathrm{SU}(2)_L \otimes \mathrm{U}(1)_Y$ gauge symmetry, which is contrary to the experimental observations. In order to explain the origin of mass, the Englert-Brout-Higgs mechanism (EBH) [49–52] introduces the spontaneous symmetry breaking by adding an additional scalar boson. This Higgs boson interacts with all particles. The Lagrangian of the Higgs field can be written as:

$$\mathcal{L}_{\rm Higgs} = (D^\mu_L\phi)^\dagger(D_{\mu,L}\phi) - V(\phi), \tag{2.8}$$

$$V(\phi) = \mu^2\phi^\dagger\phi + \lambda(\phi^\dagger\phi)^2, \tag{2.9}$$

$$D^\mu_L = \partial_\mu + \frac{1}{2}ig'YB_\mu + \frac{1}{2}ig\tau^a_L W^a_\mu, \tag{2.10}$$

where ϕ is a four-component scalar Higgs field, λ and μ in the potential term Eq. (2.9)) are used to describe the strength of self-coupling and mass. For $\mu^2 > 0$, the ground state of the Higgs potential is at $|\phi| = 0$, corresponding to the ground state of the vacuum with U(1) symmetry. While for $\mu^2 < 0$, the ground state is at $\langle\phi\rangle = \sqrt{-\mu^2/2\lambda} = v/\sqrt{2}$ where v is the vacuum expectation value. The mass terms for $W^\pm$, Z and Higgs boson can be written as:

$$m_W = \frac{gv}{2}, \tag{2.11}$$

$$m_Z = \frac{\sqrt{g^2 + g'^2}}{2}, \tag{2.12}$$

$$m_H = \sqrt{2\lambda}v. \tag{2.13}$$

Similar to gauge bosons, the interactions between Higgs field and fermions can be added into the Lagrangian Eq. (2.8) by:

$$\mathcal{L}_{\text{Yukawa}} = -m_f\bar{\psi}\psi - \frac{m_f}{\nu}\bar{\psi}\psi H + h.c., \tag{2.14}$$

with fermion's mass $m_f = \xi_f v/\sqrt{2}$ where ξ is the coupling constant between fermions and Higgs field.

Strong interaction

The QCD is the gauge field theory describing the strong force. It is a local gauge symmetry with $\text{SU}(3)_C$, based on the conservation of colour charge (named by red, green and blue) denoted as C in the subscript. Eight massless gluons are generated in this symmetry as force carriers for the strong interaction. The corresponding Lagrangian term ($\mathcal{L}_{\text{QCD}}$) is expressed as

$$\mathcal{L}_{\text{QCD}} = \bar{\psi}_i(i\gamma^\mu(\partial_\mu\delta_{ij} - ig_s G^a_\mu T^a_{ij}) - m\delta_{ij})\psi_j - \frac{1}{4}G^a_{\mu\nu}G^{a\mu\nu}. \tag{2.15}$$

In Eq. (2.15), ψ_i is the quark field with colour index i = (r, g, b) and mass value m, γ^μ is the Dirac matrix with μ denoting the Lorentz vector index, and G^a_μ are eight gluon fields with a = (1, 2, ..., 8) coupled with a universal strong coupling constant g_s for all gluons. The term T^a_{ij} are the Gell-Mann matrices, the generators of $\text{SU}(3)_C$. $G^a_{\mu\nu}$ are the gluon field strength tensors defined as:

$$G^a_{\mu\nu} = \partial_\mu G^a_\nu - \partial_\nu G^a_\mu - g_s f^a_{bc} G^b_\mu G^c_\nu, \tag{2.16}$$

where f^{abc} is the structure constant of $\text{SU}(3)_C$ with $a\,, b\,, c$ = (1, 2, ..., 8). The interactions between quarks and gluons are described by the first part in Eq.(2.15), while the second one represents the self-interactions among the gluons.

The coupling constant g_s can be written using the running coupling constant α_s as a function of energy scale Q as $\alpha_s(Q) = g_s^2/4\pi$. It results in the fact that the coupling between quarks becomes strong at small Q (long distance) and becomes weak at large Q (short distance). With long distance, the force is sufficient to create a pair of quarks from the vacuum to form mesons or baryons, resulting in no isolated quarks being observed.

2.2 Beyond Standard Model

Although the SM successfully classifies the elementary particles and describes three known interactions, it falls short of being a complete theoretical framework for all phenomena observed in the experiments, such as the gravity and the nature of the Dark Matter. Many theories beyond the SM have been brought up, and efforts have been exploited to confirm them. For instance, supersymmetry (SUSY) theories extend the SM by adding spacetime symmetry among the bosons and fermions. Every SM fermion (boson) in the SM has a bosonic (fermionic) superpartner. With the revolution of accelerator technology,

the search for new physics is now one of the highest priority contents of the LHC physics programme.

The motivation of this dissertation is to perform a model-independent search for resonances. Without assuming a particular BSM theory, the analysis tries to cover as much phase space as possible. Gaussian-shaped signals with different width values are checked in case that there is no significant excess observed in the data. The relevant models with the same phase space can still be implemented at the cost of lower signal sensitivity than analysis searching for specific models for a given final state.

A Heavy Vector Triplet (HVT) Lagrangian [53] is introduced to parameterise the coupling of the new spin-1 heavy bosons ($V_\mu^\pm$ and V_μ^0) to the SM particles in a generic way. The simplified phenomenological Lagrangian can be written as:

$$\begin{aligned}\mathcal{L}_V = &-\frac{1}{4}D_{[\mu}V^a_{\nu]}D^{[\mu}V^{\nu]a} + \frac{m_V^2}{2}V_\mu^a V^{\mu a} \\ &+ ig_V c_H V_\mu^a H^\dagger \tau^a \overleftrightarrow{D}^\mu H + \frac{g^2}{g_V}c_F V_\mu^a J_F^{\mu a} \\ &+ \frac{g_V}{2}c_{VVV}\epsilon_{abc}V_\mu^a V_\nu^b D^{[\mu}V^{\nu]c} + g_V^2 c_{VVVHH}V_\mu^a V^{\mu a}H^\dagger H - \frac{g}{2}c_{VVVW}\epsilon_{abc}W^{\mu\nu a}V_\mu^b V_\nu^c.\end{aligned} \tag{2.17}$$

In Eq. (2.17) above, The first line includes the V kinematic and mass term with its trilinear and quadrilinear interactions from covariant derivatives

$$D_{[\mu}V^a_{\nu]} = D_\mu V_\nu^a - D_\nu V_\mu^a, \;\; D^\mu V_\nu^a = \partial_\mu V_\nu^a + g\epsilon^{abc}W_\mu^b V_\nu^c \tag{2.18}$$

where g denotes the $\mathrm{SU}(2)_L$ gauge coupling. The second line contains the direct interactions between V and Higgs current Eq. (2.19) and the SM left-handed fermionic currents Eq. (2.20), respectively:

$$iH^\dagger\tau^a\overleftrightarrow{D}^\mu H = iH^\dagger\tau^a D^\mu H - iD^\mu H^\dagger \tau^a H, \tag{2.19}$$

$$J_F^{\mu a} = \sum_f \bar{f}_L \gamma^\mu \tau^a f_L. \tag{2.20}$$

The remaining terms do not directly contribute to V decay and a single production process. Thus they are be related to the phenomenon at the LHC. The HVT bosons are coupled to the Higgs boson and the SM gauge bosons with the coupling strength $c_H g_V$ and coupled to the fermions with the coupling strength $g^2 c_F/g_V$, where the coupling strength to the Higgs boson and fermions are modified by factors, c_H and c_F, respectively, and new coupling g_V represents the coupling of the HVT to all SM particles. Similar to the production of gauge bosons in the SM, the $q\bar{q}$ annihilation (qqA) is the dominant production mechanism of the heavy gauge bosons in the s-channel.

3 - The Large Hadron Collider and the ATLAS detector

The Large Hadron Collider (LHC) is the highest-energy particle collider operating in the world, located at the European Organization for Nuclear Research (CERN). The LHC program has four collision points where seven detectors are placed around: ATLAS, CMS, ALICE, LHCb, LHCf, TOTEM, and MoEDAL with different physics targets. The ATLAS detector and the CMS detector are the general-purpose ones for precise measurements of the SM and search for new physics. A brief introduction to the LHC porgramme is presented in Section 3.1, followed by more details about the ATLAS detector in Section 3.2.

3.1 The Large Hadron Collider

The LHC is a two-ring superconducting particle accelerator and collider that provides proton-proton collisions. It was constructed in a tunnel of 27 kilometers and 50 to 175 meters depth underground, built for the Large Electron-Positron collider (LEP). As shown in Figure 3.1, the accelerators at CERN are successions of machines that increase the energy of particles step by step. The LHC is the last element of the chain. The protons are finally accelerated up to 6.5 TeV and collide at the crossing points. The protons are accelerated to 1.4 GeV after generation and further accelerated to 25 GeV in the Proton Synchrotron (PS). The Super Proton Synchrotron (SPS) is followed to increase the energy to 450 GeV. Then the protons are transferred to the main ring of the LHC and accelerated to the peak energy in 20 minutes. The final collisions are made at four crossing points of the separated LHC beam pipes, corresponding to the four main experiments: ATLAS, CMS, ALICE, and LHCb. A new fill will be injected after many protons are used. An unique run number will be assigned for each run filled by the LHC.

The designed luminosity of the LHC is $10^{34}\text{cm}^{-2}\text{s}^{-1}$ and the center-of-mass energy of proton-proton collision is 14 TeV. the first operation started in 2008. For proton-proton collision, the Run 1 period used the center-of-mass energy of 7 TeV and 8 TeV, covering 2010 and 2013 [55]. Following a two-year shutdown for hardware maintenance, the Run 2 operation period occurred between 2015 and 2018 with the increased center-of-mass energy of 13 TeV [56]. The delivered integrated luminosity versus time is shown in Figure 3.2 during the Run 1 and Run 2 periods between 2011 and 2018. The peak luminosity was reached at $2.1 \times 10^{34}\text{cm}^{-2}\text{s}^{-1}$ in 2018, with a factor of two larger than the designed one. The total delivered integrated luminosity of LHC is 153 fb^{-1} and the recorded integrated luminosity of ATLAS is 146 fb^{-1} for pp collisions in Run 2.

In addition to the hard scattering proton–proton collision of interest, the rest of the collisions are called underlying events, including the Pileup, initial state radiation (ISR), final state radiation (FSR), and other soft/collinear processes, affecting the particle reconstruction and physics analysis. The effect increases significantly with the increase of

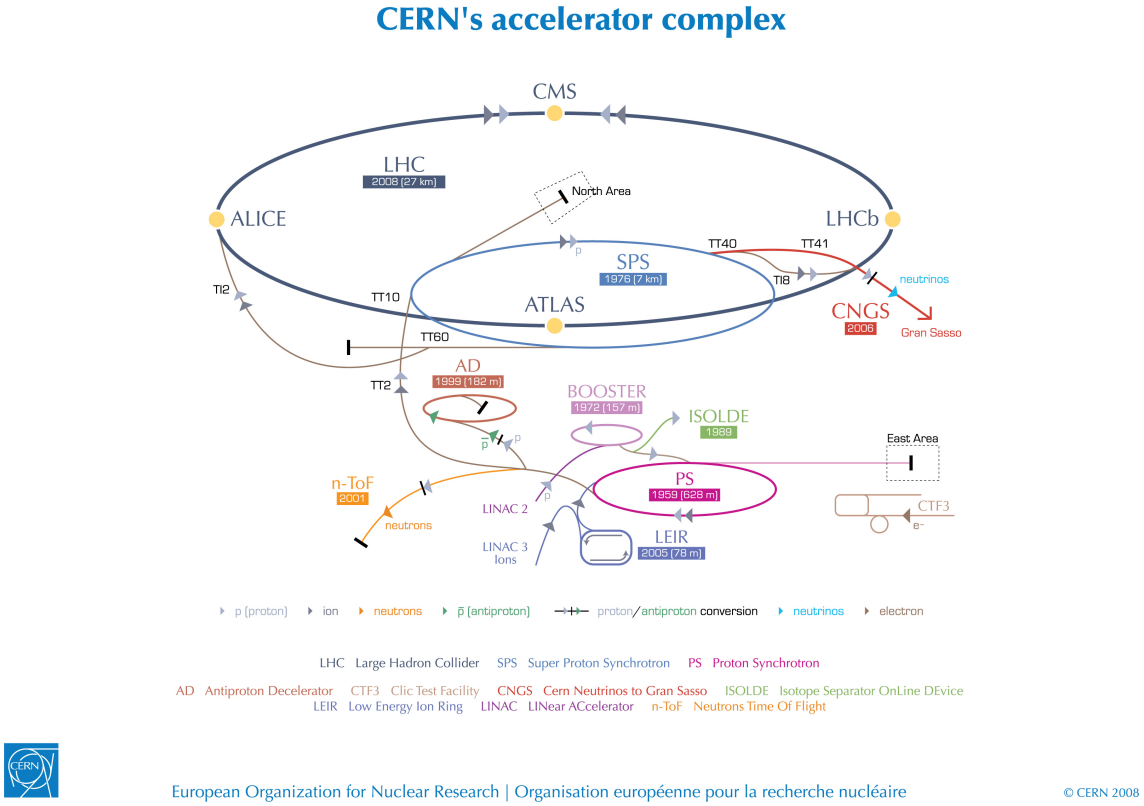

Figure 3.1: Schematic of full accelerators and detectors at CERN [54].

instantaneous luminosity. As for the Pileup, there are two types including in-time Pileup from the same bunch-crossing and out-of-time Pileup from the previous or the following collisions. The Pileup is quantified by $\langle\mu\rangle$, the mean number of interactions per bunch-crossing. Figure 3.3 shows the distributions of $\langle\mu\rangle$ of each year in Run 2 [59]. The total average number is 33.7.

3.2 The ATLAS detector

The ATLAS [60] (A Toroid LHC ApparatuS) detector is a general-purpose detector installed in the experiment cavern at Point 1 at CERN. More than 3000 physicists from 181 institutions in 38 countries work on the ATLAS experiments. Given the unprecedented high energy and luminosity from the LHC, the goals of the ATLAS detector range from more precise measurements of the parameters in the SM to the search for new physics, which was not observed by any former experiments. The search of the Standard Model Higgs boson was used as the benchmark of the performance of the ATLAS sub-detectors. The design goals of performance are listed in Table 3.1. In 2012, the ATLAS and CMS experiments independently discovered the Higgs boson.

The ATLAS detector is the largest volume particle detector ever built globally. The overall layout of the ATLAS detector is shown in Figure 3.4. It has the dimensions of a

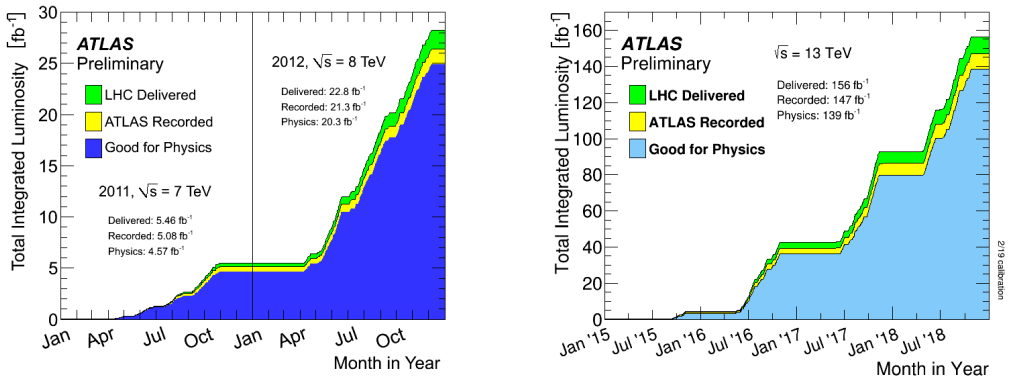

Figure 3.2: The integrated luminosity versus time for pp collisions with center-of-mass energy of 13 TeV in 2011-2012 (left) [57] and 2015-2018 (right) [58]. The green part is total integrated luminosity delivered to ATLAS. The luminosity recorded by ATLAS is shown with the yellow part. The blue part is one which was certificated be of good quality.

Table 3.1: The designed performance goals of the ATLAS detector. The units for E and p_{T} are in GeV [60].

Detector component	**Required resolution**	η **coverage**	
		Measurement	Trigger
Tracking	$\sigma_{p_{\mathrm{T}}}/p_{\mathrm{T}} = 0.05\%\ p_T \oplus 1\%$	± 2.5	
EM calorimetry	$\sigma_E/E = 10\%\sqrt{E} \oplus 0.7\%$	± 3.2	± 2.5
Hadronic calorimetry (jets)			
barrel and end-cap	$\sigma_E/E = 50\%\sqrt{E} \oplus 3\%$	± 3.2	± 3.2
forward	$\sigma_E/E = 100\%\sqrt{E} \oplus 10\%$	$3.1 < \lvert\eta\rvert < 4.9$	$3.1 < \lvert\eta\rvert < 4.9$
Muon spectrometer	$\sigma_{p_{\mathrm{T}}}/p_{\mathrm{T}} = 10\%$ at $p_T = 1$ TeV	± 2.7	± 2.4

cylinder in 44 meters long and 25 meters diameter. The total weight is about 7000 tonnes. The ATLAS detector is forward-backward symmetric concerning the interaction point. There are four main sub-systems: an inner track detector, electromagnetic and hadronic calorimeters, a muon spectrometer, and the magnet system.

The inner tracking detector, immersed in a 2 T field, provides the precise measurements of charged particles' momenta within a pseudo-rapidity (η) range of $|\eta| < 2.5$. The Electromagnetic calorimeter, surrounding the solenoid, covers the pseudorapidity range of $|\eta| < 3.2$. It is composed of a high-granularity liquid-argon (LAr) sampling calorimeter. The hadronic calorimeter consists of central barrel ($|\eta| < 1.7$) and end-cap ($1.5 < |\eta| < 3.2$) regions. The barrel comprises scintillator-tile calorimeters, and the end-cap is a LAr electromagnetic sampling calorimeter. The outermost sub-detector is the muon spectrometer which determines the overall dimension of the ATLAS detector. A trigger system is applied to record the event from the region of interest to digest the huge data from each collision.

The positions of particles at the ATLAS detectors are described using a right-handed Cartesian coordinate system. The origin locates at the collision point in the center of the

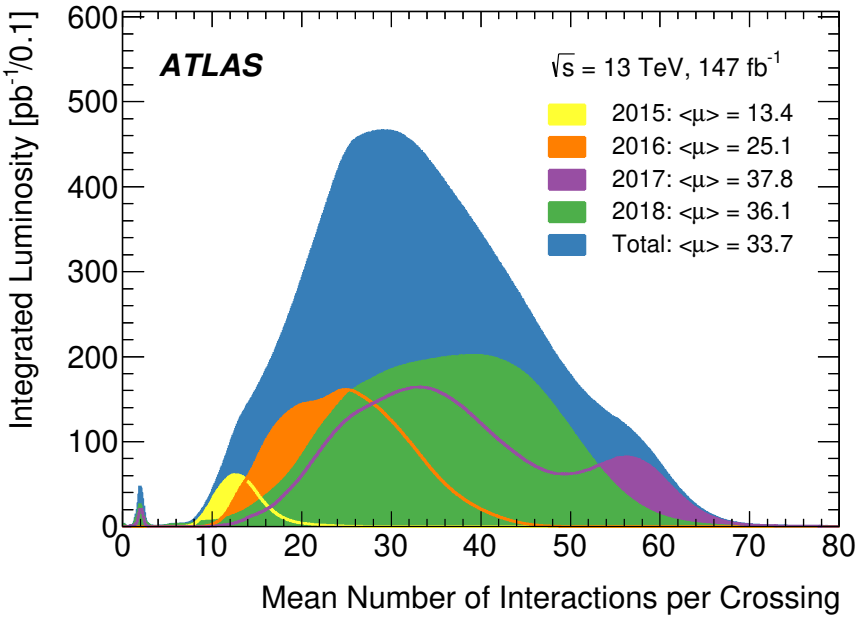

Figure 3.3: The mean number of interactions per bunch-crossing for the full Run 2 proton-proton collision datasets [59].

detectors. The x-axis points to the center of the LHC ring, and the y-axis points to the ground. The z-axis is defined along with the beam pipe. Besides, the cylinder coordinates (r-ϕ) are used to describe particle positions in the transverse plane (x-y). The azimuthal angle (ϕ) is taken from the x-axis, and the polar angle (θ) is from the positive z-axis. The pseudorapidity is defined as $\eta = -\ln\left[\tan(\frac{\theta}{2})\right]$. Angular distance between two particles is measured in units of $\Delta R = \sqrt{(\Delta\eta)^2 + (\Delta\phi)^2}$.

3.2.1 Magnet system

The magnet system [61] is designed to provide a strong magnetic field, bending the charged particles for measurements of tracks transverse momentum (p_{T}). ATLAS is equipped with a thin superconducting solenoid [62] and three superconducting toroids [63, 64]. The former surrounds the Inner Detector, while the latter are arranged outside the calorimeters. Each component of this magnetic system is listed below:

- **The solenoid** system is implemented between the Inner Detector and electromagnetic calorimeter, providing a 2 T magnetic field for the Inner Detector. The structure and material of the solenoid are optimised for the reduction the additional interactions with incoming particles.

- **The toroid** system consists of one barrel and two end-cap superconducting toroids. It provides the toroid magnetic field (0.5 and 1 T) for the Muon Spectrometer to bend the tracks of charged particles, which escape from the calorimeters.

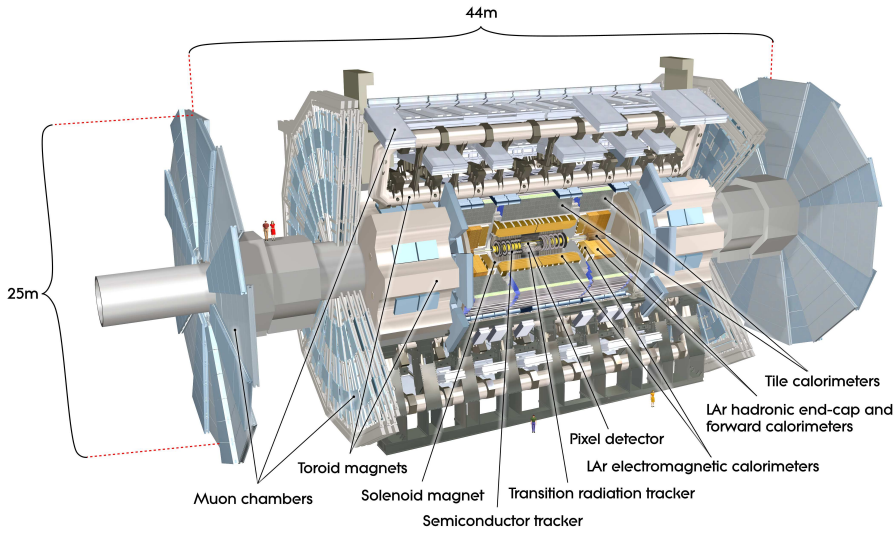

Figure 3.4: The layout of the ATLAS detector [60].

3.2.2 Inner detector

The Inner Detector [65, 66] is designed to provide high-precision measurements on momentum and vertex resolution in a considerable track density environment. A general layout of the ID and detailed structures are illustrated in Figure 3.5. The ID has a length of 6.2 meters, and a diameter of 2.1 meters, placed in a 2 T magnetic field provided by the surrounding superconducting solenoid. The ID consists of precision tracking detectors (Pixel and silicon microstrip trackers) and Transition Radiation Tracker (TRT) from the inside out. A new tracking layer, the Insertable B-Layer (IBL) [67] was added for Run 2 in the innermost of the ID.

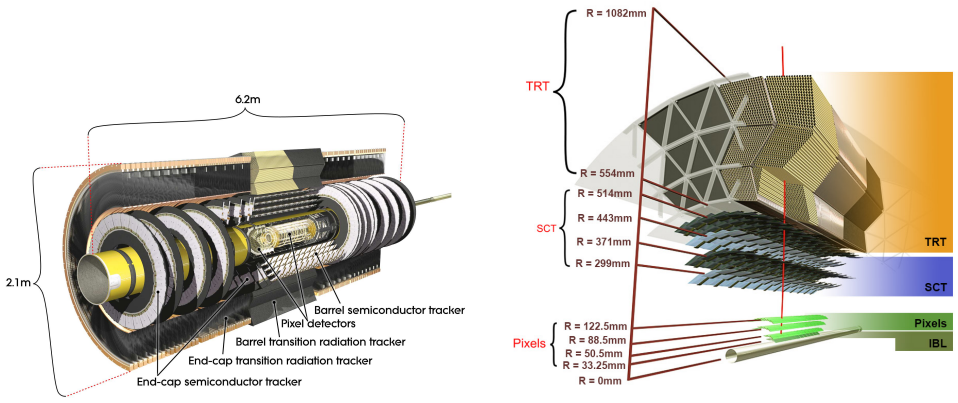

(a) (b)

Figure 3.5: (a) The cut-away view of the Inner Detector. (b) A schematic of barrel of the Inner Detector including the newly added IBL [67].

The Pixel detector [68] is designed to provide high-granularity measurements on the trajectories and vertices within $|\eta| < 2.5$. It comprises three concentric cylinders around the beam pipe in the barrel region and three disks perpendicular to the beam line in each end-cap region. There are 1774 identical pixel sensors with a minimum size in $(R-\phi) \times z$ of 50×400 µm^2. There are approximately 80.4 million readout channels in total. The intrinsic resolutions of track positions are 10 µm $(R-\phi)$ and 115 µm (z) in the barrel region and 10 µm $(R-\phi)$ and 115 µm (R) in the end-cap regions.
The Semiconductor Tracker (SCT) [69] is installed outside of the Pixel detector. It is designed to provide high-resolution pattern recognition using discrete space points (four for each track). Unlike the Pixel detector, the SCT is composed of silicon strips with a larger coverage. The silicon strips are aligned at four layers in the barrel with 2212 modules, and at nine disks in each of the end-cap regions with 1976 modules. The mean pitch value of the strips is around 80 µm. The intrinsic resolution is around 17 µm $(R-\phi) \times 580$ µm (R).
The Transition Radiation Tracker (TRT) [70] is composed of straw-tubes with a diameter of 4 mm and length of 144 (37) cm in the barrel (end-cap) region. Xenon-based gas mixture is filled in the straw-tubes, operated at a voltage of -1500 V. The TRT only provides $R-\phi$ information with an intrinsic resolution of 130 µm per straw. The lower precision of the TRT can be compensated by a large number of hit measurements and long measured track length. The TRT also provides a functional particle identification between the electrons and the charged pions withing 1 GeV $< E <$ 100 GeV.
The Insertable B-Layer (IBL) [67] is designed to cope with the high radiation in Run 2 to improve the precision and robustness of track reconstruction. This new tracking layer was implemented between the existing Pixel detector and a new, thinner beam pipe, during the long shutdown period after Run 1. Comparing to the previous track performance, the IBL helps to improve the resolution of transverse and longitudinal impact parameters (d_0 and z_0) due to the additional layer at a smaller radius.

3.2.3 Calorimetry

The Calorimeters [71, 72] are designed to absorb and measure the energy of incoming particles from the collision. Figure 3.6 illustrates a cut-way view of the ATLAS calorimeter system. In terms of functionality and performance, The calorimeter system is composed of an inner electromagnetic calorimeter and an outer hadronic calorimeter covering the pseudorapidity range of $|\eta| < 4.9$. The electromagnetic calorimeters consists of a barrel and two electromagnetic end-cap calorimeters (EMEC) with a coverage of $|\eta| < 3.2$. There is a tile calorimeter ($|\eta| < 1.0$) and two extensions ($0.8 < |\eta| < 1.7$) in the barrel for the hadronic calorimeters. Besides, two hadronic end-cap and additional forward calorimeters are installed in both side of the ATLAS detector.

Both electromagnetic and hadronic calorimeters are sampling type calorimeters, which only sample part of the energy of incident particles. A sampling calorimeter includes two alternative layers named absorber and sampler layers. The depth of calorimeters is a crucial consideration in design. It must provide suitable containment for electromagnetic and hadronic showers and avoid the punch-through of particles into the muon spectrometer.

The absorber layer is usually made of high-density material with low radiation length, initiating the particle showers. While the sampler layer has a more considerable radiation length, converting deposited energy to signals.

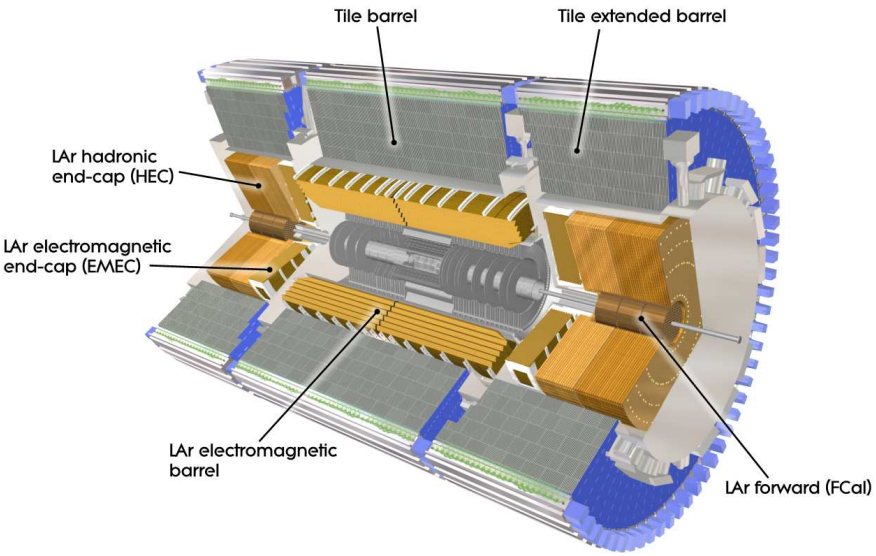

Figure 3.6: The overview of the ATLAS calorimeter system [60].

The electromagnetic calorimeter includes a barrel part ($|\eta| < 1.47$) and two end-cap ones ($1.375 < |\eta| < 3.2$), placed outside of central solenoid. The sampler layers are filled with liquid-argon (LAr) as an active medium, while absorber layers are made of lead to develop the electromagnetic showers. It has an accordion geometry to provide complete coverage in ϕ without cracks. There are three longitudinal layers with fine granularity over the region ($|\eta| < 2.5$) for precision measurements of electrons and photons. The coarser granularity in the rest can still satisfy the requirements for jet reconstruction and $E_{\mathrm{T}}^{\mathrm{miss}}$ measurements.

The hadronic calorimeter surrounds the electromagnetic calorimeter envelope composed of three components. The tile calorimeter consists of one central and two extended barrels covering $|\eta| < 1.7$. The scintillator tiles are used as the active medium, and the absorbing layer is made of steel after considering the performance and the cost. The hadronic end-cap calorimeter is LAr-copper detector covering the range $1.5 < |\eta| < 3.2$. In addition, the calorimetry is extended to higher pseudorapidity by the LAr forward calorimeter ($3.1 < |\eta| < 4.9$) to reach its designed goal.

3.2.4 Muon spectrometer

The muon spectrometer (MS) is designed to measure the tracks of charged particles, which are not absorbed in the calorimeters. It covers the pseudorapidity range of $|\eta| < 2.7$. A general cut-way layout is illustrated in Figure 3.7. The MS consists of high-precision tracking and trigger chambers for trajectory measurements and data-acquisition

trigger separately. The chambers are arranged in three cylindrical layers aligned around the beam axis in the barrel region ($|\eta| < 1.4$). There are also three layers placed in planes perpendicular to the beam pipe in the transition ($1.4 < |\eta| < 1.6$) and end-cap ($1.6 < |\eta| < 2.7$) regions.

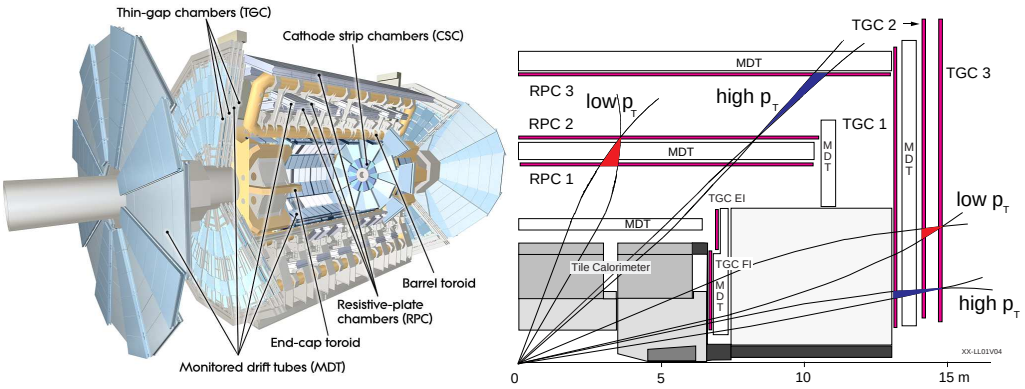

(a) (b)

Figure 3.7: (a) The cut-away view of the ATLAS muon system. (b) A schematic of muon trigger roads [33].

For the precision track chambers, most of the pseudorapidity range is covered by Monitored Drift Tubes (MDT). It is chosen after combining its high-precision measurement, mechanical deformations' predictability, and construction simplicity. The average resolution is around 80 µm per tube in each chamber. In the forward region ($2.0 < |\eta| < 2.7$), the MDT chambers are replaced by Cathode Strip Chambers (CSC) to tolerate the extremely high particle fluxes and muon track density. The resolution is 40 µm in the bending plane and around 5 mm in the orthogonal direction.

The Resistive Plate Chambers (RPC) and the Thin Gap Chambers(TGC) are used as the trigger chambers in the barrel ($|\eta| < 1.05$) and the end-cap regions, respectively. They have a total coverage of $|\eta| < 2.4$. The chambers are designed to trigger muon tracks, given the fast-response performance. They also provide excellent bunch-crossing identification and a well-defined threshold of track p_T. In addition, the trigger chambers measure the coordinate of muons orthogonal to the ones from precision-track chambers. A further analysis [33] is performed to measure the performance of RPC detectors using the collected data in 2018. The RPC detectors' intrinsic time resolution is estimated to be about one ns. Further details of the RPC chambers and their time resolution measurements are documented in Appendix A.

3.2.5 Trigger and data acquisition system

The bunch spacing time of the LHC was 50 ns in Run 1 and was increased to 25 ns in Run 2. It is impossible and meaningless to record outputs from each collision given the production cross-section of proton-proton collisions. The trigger system [73] is designed to select the events with interesting physics signatures from millions of collisions and speed

up the procedure for further analysis. The trigger system is required to be up-to-date to satisfy the challenges of the higher energy, instantaneous luminosity, and the Pileup effect with the upgrade of the LHC. Figure 3.8 illustrates the procedure of the ATLAS Trigger and Data Acquisition system in Run 2.

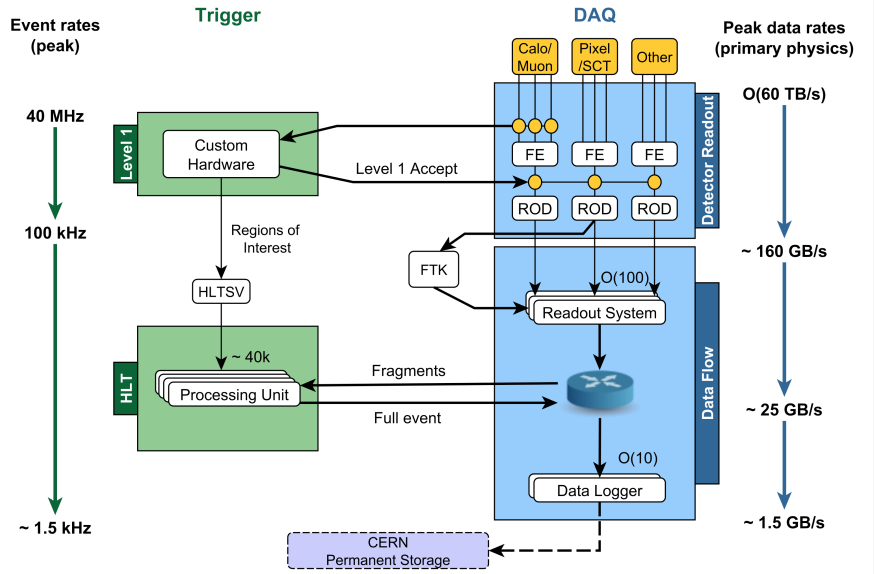

Figure 3.8: The schematic of the ATLAS Trigger and Data Acquisition system in Run 2 [74].

In the trigger system, a first-level trigger (L1) is developed based on the hardware to roughly select physical collisions, followed by a software-based high-level trigger (HLT) for further selection with a lower speed. In Run 1, the HLT was divided into the second level trigger (L2) and Event Filter (EF) farms. They are merged to share resources for better performance. The L1 trigger uses the Central Trigger Processor (CTP) to receive information from sub-detectors like calorimeters and muon spectrometers and make the decision. The trigger algorithm creates the Region-of-Interest (ROI) information for regional reconstruction. The event rate decreases to 100 kHz from 40 MHz of collision rates. Once the green light is given from the L1, the detector readout information is fed into the Read-Out System (ROS) with a data rate of around 160 GB per second. Together with the ROI information from L1, the HLT determines whether or not to keep the events. The output event rate is maintained at a level around 1.5 kHz. The accepted events will be transferred and processed by the offline algorithm for the event reconstruction and calibrations, documented in Chapter 5.

4 - Data and Monte Carlo samples

This analysis is performed using full recorded data during Run 2 of the LHC using pp collisions with a center-of-mass energy of $\sqrt{s} = 13$ TeV. The bunch spacing time was increased to 25 ns from 50 ns in Run 1. Only data taken during the stable beam collisions and with a fully operating magnet system, and tracking, and calorimeter sub-detectors, as defined by the ATLAS Data Quality group, are considered. The total integrated luminosity is 139 fb^{-1}. The triggers used and corresponding efficiency are shown in Section 4.1. Samples of simulated background and signal events are used to optimise and to validate the analysis strategy, documented in Section 4.2. The acceptance times efficiency values for the latter are given in Section 4.3.

4.1 Trigger

The candidate events are firstly selected using triggers which were not prescaled during the data-taking, as listed in Table 4.1. The lepton triggers require either a single isolated lepton or a lepton pair targeting leptonic decays of the Z bosons. For the single lepton triggers, the minimum transverse momentum (p_T) thresholds vary between 24 GeV and 26 GeV for electrons and between 20 GeV and 26 GeV for muons, depending on the data-taking period. For the dilepton triggers, the minimum p_{T} thresholds vary between 12 GeV and 17 GeV for electrons and between 10 GeV and 14 GeV for muons. In addition, another set of lepton triggers with higher p_{T} thresholds are added to reach stable efficiency over extensive p_T range. At very high p_{T}, the leptons are no longer isolated. Even the single lepton triggers with high p_T thresholds are no longer efficient. For this reason, the triggers are complemented by jet-based triggers with a minimum p_{T} threshold of 360 GeV, targeting merged-ee events documented in Chapter 6.

Table 4.1: Un-prescaled triggers used in the analysis.

Trigger type	2015	2016	2017	2018
Single electron	HLT_e24_lhmedium_L1EM20VH	HLT_e26_lhtight_nod0_ivarloose		
	HLT_e60_lhmedium_nod0			
	HLT_e120_lhloose	HLT_e140_lhloose_nod0		
Single muon	HLT_mu20_iloose_L1MU15	HLT_mu26_ivarmedium		
	HLT_mu50			
Di-electron	HLT_2e12_lhloose_L12EM10VH	HLT_2e17_lhvloose_nod0		
Di-muon	HLT_2mu10	HLT_2mu14		
	HLT_2mu18_mu8noL1	HLT_2mu22_mu8noL1		
Jets	HLT_j360	HLT_j380	HLT_j450	HLT_j420

The lepton trigger efficiency corrections provided from ATLAS Common Performance

(CP) recommendations are applied only to the MC samples to compensate for the difference between data and simulation. This efficiency is determined by Z boson candidates using the tag-and-probe method at the object level. At the event level, the trigger efficiency for candidates, passing the pre-selections in Chapter 5, are estimated by using Z+jets MC samples for each type with the following formula:

$$\epsilon_{\text{trigger}} = \frac{N_{\text{SR-like,triggered}}}{N_{\text{SR-like}}}. \tag{4.1}$$

where the $N_{\text{SR-like,triggered}}(N_{\text{SR-like}})$ is the event yields in SR-like region with (without) trigger selections applied. The overall trigger efficiency per event is about 96% at low p_{T}^{Z} and increases to above 99% for $p_{\text{T}}^{Z} > 600$ GeV for the muon channel and above 99% for all the considered p_{T}^{Z} range for the electron channel, plotted as a function of p_{T}^{Z} shown in Figures 4.1-4.2. This includes the efficiency of trigger selections and trigger matching between trigger ROI and physics objects. In the high p_{T}^{Z} region, the jet triggers help to improve the efficiency lost from lepton triggers. The gain of the jet triggers, comparing to the results with only lepton triggers, is around 2% within the full p_{T}^{Z} region.

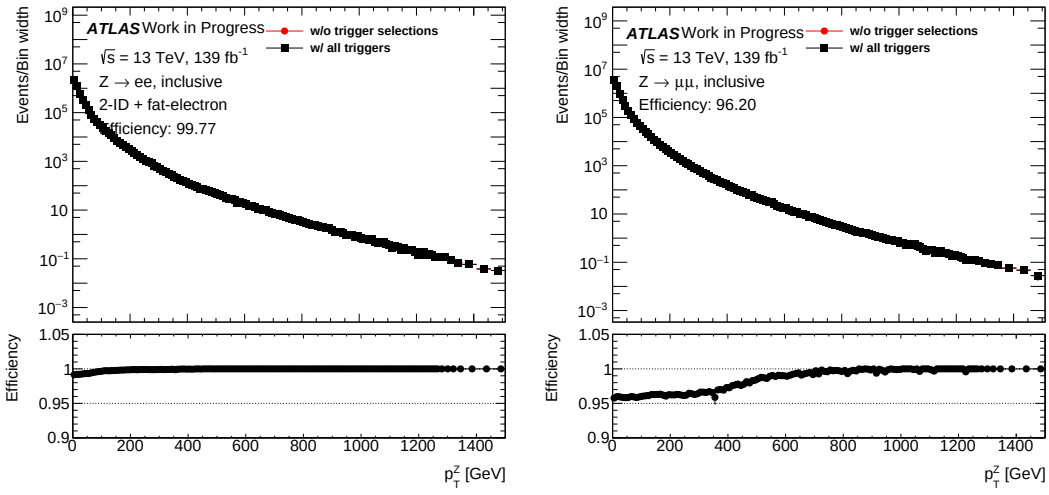

Figure 4.1: Overall trigger efficiency as a function of p_{T}^{Z} in the $Z \to ee$ (left) and $Z \to \mu\mu$ (right) decay channels.

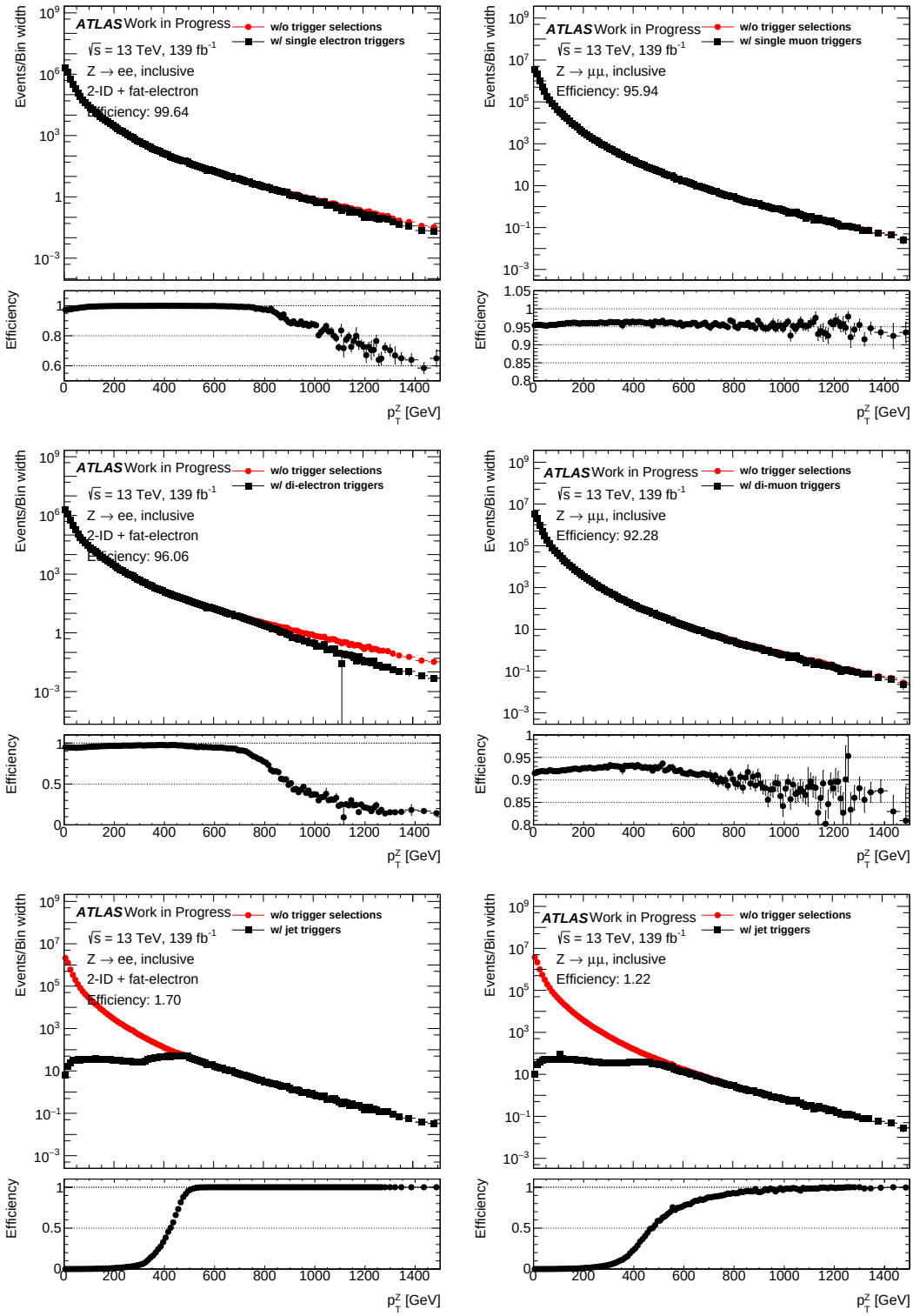

Figure 4.2: Trigger efficiency as a function of p_{T}^{Z} for the single lepton (top), dilepton (middle) and jet (bottom) triggers in the $Z \to ee$ (left) and $Z \to \mu\mu$ (right) decay channels.

4.2 MC samples

Even though this analysis is based on a data-driven approach, MC simulated samples are still used to develop the analysis strategy, selections, and validations of background functions. The SM background originates mainly from production of Z+jets, diboson (ZZ, ZW, $Z\gamma$), top-quark pair ($t\bar{t}$) and single top quarks. They are simulated with different generators described in the following. Small contributions from multijet and W+jets processes are obtained using data-driven techniques following the same procedure as in Ref. [75]. Simulated MC samples are used to optimise the analysis and define the analysis strategy.

The production of a Z boson in association with jets is modelled by SHERPA [76] v.2.2.1 with NNPDF3.0 next-to-next-leading-order (NNLO) parton distribution function (PDF) set [77]. Diagrams with up to two additional parton emissions are simulated with next-to-leading-order (NLO) precision in QCD, and with three or four additional parton emissions to leading-order (LO) accuracy [78]. Matrix elements are merged with the SHERPA parton shower using MEPS@NLO formalism [79]. An alternative sample is generated with the POHWEG-BOX v1 [80–83] at NLO in QCD comparing to the nominal ones. The generation is interfaced to PYTHIA 8.186 [84] for the modelling of the parton shower, hadronization, and underlying events, with AZNLO tune [75, 85]. The CT10 NLO PDF set [86] and the CTEQ6L1 PDF set [87] are used for the hard-scattering processes and for the parton shower, respectively.

The diboson production processes with leptonic final states are simulated using SHERPA v2.2.2. The matrix elements are calculated using the NNPDF3.0 NNLO PDF set. Diagrams with up to one additional emission are calculated with NLO precision in QCD, while diagrams with two or three parton emissions are described at LO accuracy. The various jet-multiplicity final states are merged using the MEPS@NLO formalism. The production of diboson with semi-leptonic decays is modelled using SHERPA v2.2.1 and the same PDF set.

The top-quark background includes the top-quark pair ($t\bar{t}$) and the associated production of a single top-quark with a W boson processes. The processes are generated using the POHWEG-BOX v2 [88] generator with PYTHIA 8.210. The parton shower is modelled with A14 tune [89]. The NNPDF3.0 NLO PDF set is used to calculate the matrix elements with the precision of NLO level in QCD. The top-quark mass is assumed to be 172.5 GeV to calculate the resummation damping parameter. The cross section of $t\bar{t}$ process is normalised to the predictions of TOP++2.0 program to NNL) in perturbative QCD [90].

Although this search will be a model-independent one to be as generic as possible at the end, a few signal samples are used to either check the sensitivity of the analysis or derive the constraints on its production cross-section. These samples include the heavy vector triplet (HVT) with different decaying channels: $W' \to ZW \to \ell\ell qq$ and $Z' \to ZH \to \ell\ell qq$, where Z, W and H are all SM particles. These samples were generated using MADGRAPH5_AMC@NLO [91] interfaced to PYTHIA 8.186 or 8.212 with the NNPDF23LO PDF set [92].For the HVT interpretation in the qq fusion mode, samples were generated with $g_V = 1$, referred as model A, and with the decaying topologies of $W' \to ZW \to \ell\ell qq$

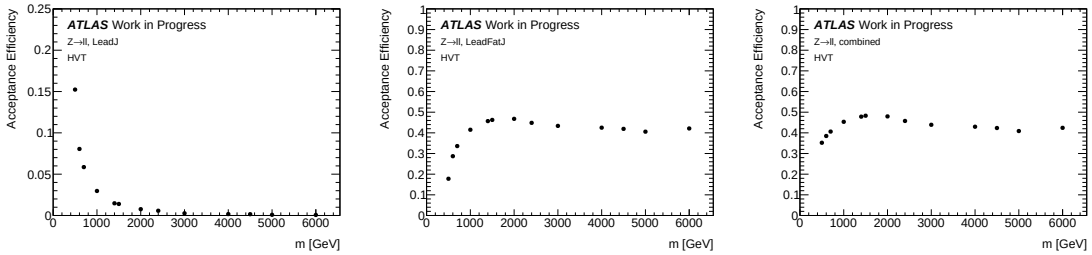

Figure 4.3: Distributions of acceptance times efficiency as a function of resonance's mass in the leading small-R-jet (left), the leading large-R-jet and the combined categories with $p_{\mathrm{T}}^{Z} > 100$ GeV.

and $Z' \to ZH \to \ell\ell qq$. The acceptance times efficiency values of these signal models are presented in Section 4.3.

All samples from MC simulation are processed through a GEANT4-based [93] simulation of the ATLAS detector. Except for the hard-scattering processes, the pileup effect of additional pp collisions in the same or neighboring bunch crossing is simulated by generating additional inelastic events. These events are generated with PYTHIA and overlaid on the hard-scattering events. The combined events from the simulation are re-weighted to data, according to the distribution of the mean number of interactions per bunch-crossing, as shown in Figure 3.3.

4.3 Signal acceptance times efficiency

The probability to reconstruct and select an event as documented in Chapter 7. The acceptance $\times$ efficiency ($\mathcal{A} \times \epsilon$), is calculated for all signal MC samples used, according to the following formula:

$$\mathcal{A} \times \epsilon = \frac{\text{Selected events}}{\text{All generatged events}} \,. \tag{4.2}$$

The obtained $\mathcal{A} \times \epsilon$ values in the combined category (definition in Section 7.2) are shown in Table 4.2. Three sets of selections are compared: no p_{T}^{Z} requirement, $p_{\mathrm{T}}^{Z} > 50$ GeV and $p_{\mathrm{T}}^{Z} > 100$ GeV. Most of them have no p_{T}^{Z} dependence, except for the signal models where m_X and m_{ZX} are close. A further check is performed on the HVT signal models with $W' \to ZW \to llqq$ final state and mass values varying from 500 GeV to 6 TeV. The corresponding acceptance times efficiency is shown in Figure 4.3 as a function of resonance's mass in three event categories: the leading small-R-jet, the leading large-R-jet, and the combined categories. The requirement of $p_{\mathrm{T}}^{Z} > 100$ GeV is applied in this study. With the increase of resonance mass, the Z boson and its recoil system become boosted, and the acceptance times efficiency has no p_{T}^{Z} dependence. The fraction of events in each category is also changed. It causes different shapes between the leading small-R-jet and the leading large-R-jet category.

Table 4.2: Acceptance times efficiency ($\mathcal{A} \times \epsilon$) values in % in the combined category for three different p_{T}^{Z} selections: no p_{T}^{Z} requirement, $p_{\mathrm{T}}^{Z} > 50$ GeV and $p_{\mathrm{T}}^{Z} > 100$ GeV in the $Z \to \ell^{+}\ell^{-}$ decaying channel.

Process	No p_{T}^{Z} cuts	$p_{\mathrm{T}}^{Z} > 50$ GeV	$p_{\mathrm{T}}^{Z} > 100$ GeV
HVT $W' \to ZW \to llqq$, 700 GeV	39.33	39.33	39.24
HVT $W' \to ZW \to llqq$, 1.2 TeV	46.29	46.29	46.29
HVT $W' \to ZW \to llqq$, 2.4 TeV	45.20	45.20	45.20
HVT $W' \to ZW \to llqq$, 600 GeV	37.44	37.36	37.09
HVT $Z' \to ZW \to llqq$, 700 GeV	38.12	38.11	38.00
HVT $Z' \to ZW \to llqq$, 1.2 TeV	44.22	44.22	44.19
HVT $Z' \to ZW \to llqq$, 1.4 TeV	48.07	48.07	48.07
HVT $Z' \to ZW \to llqq$, 2.4 TeV	43.96	43.96	43.96
HVT $Z' \to ZW \to llqq$, 2.8 TeV	45.15	45.15	45.15

5 - Physics object reconstruction

After particles pass through the detector, information is collected and analyzed by offline algorithms. The physics objects are reconstructed and classified according to the signatures of interactions with the detector, as illustrated in Figure 5.1. All charged particles leave tracks due to ionization in the ID. Muons have minimal energy deposited in the calorimeters and leave tracks in the Muon Spectrometer. Electrons and photons generate showers and deposit all energy inside the EM calorimeters. Hadrons generate showers in the hadronic calorimeters due to interaction with detector materials. Electrons and hadrons are fully reconstructed by matching the calorimeter clusters and ID tracks. The neutrinos do not interact with any detector and are estimated by the missing transverse energy.

This chapter will briefly introduce the reconstruction algorithms of track, vertex, electron, photon, muon, and jet used in this analysis. The overlap removal procedure is also presented to select signal objects from the hard scattering.

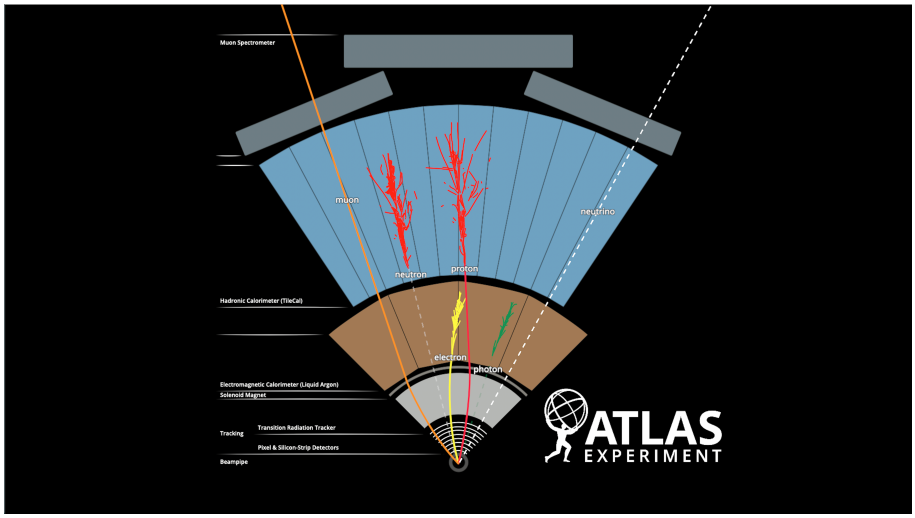

Figure 5.1: Schematic of how particles interact with the ATLAS detector [94].

5.1 Inner Detector track

Charged particle tracks are reconstructed and measured with the high-granularity tracking detector sensors in the ID, close to the Interaction Point (IP). With the increase in luminosity and energy of the LHC, the track reconstruction efficiency will be limited by the comparable separation between highly collimated charged particles and individual sensors. A multi-staged algorithm [95] is developed and employed at the start of Run 2 to prevent efficiency losses.

In the first step, clusters are assembled from hit measurements in the pixel and SCT sensors, where the deposited energy yields a charge above a threshold. From the clusters, the space points are defined by three-dimensional measurements on the point where the charged particle interacts with the ID. An iterative combinatorial track finding algorithm is performed using the track seeds formed from sets of three space points. Track seeds are fed to a combinatorial Kalman filter [96] to build track candidates considering the remaining space-points in the detector. The ambiguity solver is applied to remove the overlapped clusters and fake tracks. A trained artificial neural network (NN) is used to identify merged clusters to cope with efficiency losses in a high-density track environment.

5.2 Primary vertex

Based on the charged particle tracks measured in the ID, the primary vertices (PVs) are reconstructed where proton-proton inelastic collisions happen. The PV reconstruction is a fundamental ingredient for any physics programme at the ATLAS. A set of tracks are selected by specific vertex track selection criteria [97] shown below:

- $p_{\mathrm{T}} > 400$MeV; $|d_0| < 4$ mm; $\sigma(d_0) < 5$ mm; $\sigma(z_0) < 10$ mm;
- At least four hits in the SCT detector;
- At least nine silicon (SCT or pixel) hits;
- No pixel holes.

Where d_0 and z_0 denote the track's transverse and longitudinal impact parameters concerning the center of the luminous region, and $\sigma(d_0)$ and $\sigma(z_0)$ represent the uncertainties on the measured values of d_0 and z_0. The hole on a track is defined as the missing observed hits given the predicted trajectory. An iterative vertex fitting procedure is performed using estimated seed positions and selected tracks. The procedure is repeated with the additional tracks in the event.

In this analysis, events are required to have at least one PV with a minimum of two associated tracks, each with $p_{\mathrm{T}} > 500$ MeV. In the events which have more than one selected PVs, the one with the highest sum of squares of transverse momenta of contributing tracks, denoted as $\sum p_{\mathrm{T}}^2$, is considered. At the same time, the others are regarded as originating from the pileup.

5.3 Electron and photon

Electrons [98] are reconstructed from clusters of energy deposits in the calorimeter that match a track reconstructed in the ID. Photons [99] are composed of the converted photon, which is cluster matched to a conversion vertex, and unconverted one, which is cluster matched to neither an electron track nor a conversion vertex. This section will briefly introduce the reconstruction algorithm, identification, and isolation for electron and photon [100].

5.3.1 Reconstruction algorithm

The reconstruction algorithm of electron and photon firstly prepares clusters and tracks. The clusters are energy deposits measured in the EM and hadronic cells, denoted as topo-clusters. The topo-clusters are formed by proto-clusters that are larger than the expected noise thresholds. Electrons and photons only use the energy from cells in the EM calorimeter, except in the transition region ($1.37 < |\eta| < 1.63$). The ID tracks described in Section 5.1 sare loosely matched to fixed-size clusters after refitting to account for the bremsstrahlung. The photon conversion vertices are built from tracks with silicon hits and tracks only in the TRT. The conversion vertices are then matched to the selected topo-clusters.

The matched topo-clusters are used as input to build superclusters for electron and photons separately. In the first step, the seed cluster candidates are selected by order of E_{T} in the topo-clusters. Then the neighboring topo-clusters of seed one are regarded as satellite clusters, coming from the bremsstrahlung or cluster splitting. Final superclusters are formed by matching the satellite clusters with specific criteria to seed candidates. Figure 5.2 summarises the detailed procedure of supercluster-building algorithm [101].

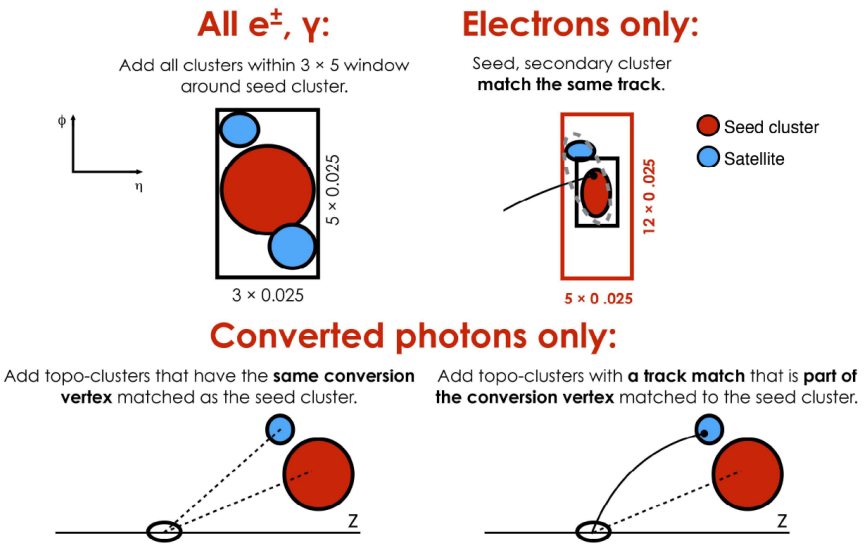

Figure 5.2: Diagram of the superclusters-building algorithm for electron and photon. Seed clusters are shown in red, satellite clusters in blue [100].

The initial energy calibration and position correction are performed on the built superclusters, followed by matching tracks and conversion vertices. The analysis-level electrons and photons are created after an ambiguity solver algorithm are applied on clusters, producing electron and photon objects. Afterward, the energies of electrons and photons are recalibrated considering the matched tracks and vertices following the procedures in Ref [101]. The shower shape and discriminating variables are calculated for electron and

photon identification.

5.3.2 Identification

The identification selections improve the quality of selected electrons and photons. In the following section, electrons, photons, and muons are defined as prompt if they are not produced in the hadronic decays. The prompt electrons are identified by likelihood discrimination based on the measured quantities from the ID, the calorimeter, and their combination. The background electrons mainly come from the heavy-flavour hadrons decays, converted photons, and energy deposits of the hadronic jets. The quantities include properties of the primary electron track, the functional PID from the transition radiation in Xenon in the TRT, the lateral and longitudinal development of the EM showers, and the spatial compatibility of the primary electron track with the reconstructed cluster. The likelihood discrimination is constructed by the logarithm of the ratio of probability functions from signal and background electrons in bins of $|\eta|$ and $|E_{\mathrm{T}}|$ separately. The discriminate thresholds are adjusted to satisfy requirements on the signal efficiency. The operating working points include "LooseLLH", "MediumLLH" and "TightLLH" with an average efficiency of 93%, 88%, and 80% correspondingly. The probability to misidentify hadrons as electrons is approximately 1% with little p_{T} dependence for the standard MediumLLH working point. In the case that the electrons originate from a high p_{T} decay, a multivariate identification method (merged-ee) is developed to recover lost efficiency. It is documented in Chapter 6. The corresponding probability to misidentify hadrons as merged-ee candidates reaches 5% at $p_{\mathrm{T}} > 500$ GeV.

Photon identification helps distinguish prompt, isolated photons from the background produced in the hadronic jets. Variables constructed for photon identification describe the development of EM shower in the EM calorimeter. It also takes into account the energy fraction leaking into the hadronic calorimeter. The working points include "Tight", "Medium", and "Loose", with fewer restrictions.

5.3.3 Isolation

In the physics analysis, the physics objects are required to be isolated from other tracks and calorimeter activities by applying p_{T}- and η-dependent isolation criteria [102]. The criteria are developed to ensure high identification efficiency and a sound rejection of objects from heavy-flavour decays or misidentification. The isolation variables are defined by the sum of the transverse energy of topo-clusters (calorimeter-based) and the sum of the transverse momentum of selected tracks (track-based) within a fixed or variable cone size around the objects.

The calorimeter-based isolation variable ($E_{\mathrm{T}}^{\mathrm{coneXX}}$, topoetconeXX) is defined by summing transverse energy of topo-clusters within a cone around the objects after corrections. The XX refers to the size of the cone by $\Delta R = \mathrm{XX}/100$. A cone size of $\Delta R = 0.2$ is used for the electron, and $\Delta R = 0.2$ and 0.4 are used for photon in the "Loose" and "Tight" working points, respectively. The track isolation variable ($p_{\mathrm{T}}^{\mathrm{varconeXX}}$, ptvarconeXX) by summing the transverse momentum of selected tracks with $p_{\mathrm{T}} > 1$ GeV and $|\eta| < 2.5$ in a variable cone size around objects. The cone size (XX) is defined by $\min(10\mathrm{GeV}/p_{\mathrm{T}}, X/100)$. The

matched tracks with electrons and photons are removed. The track is required to pass a track-to-vertex-association (TTVA) requirement to suppress the pile-up dependence.

In this analysis, electrons are required to pass MediumLLH identification and FCTight isolation for $p_{\mathrm{T}} > 25$ GeV and be within $|\eta| < 2.47$, excluding the transition region between the barrel and endcaps in the LAr calorimeter ($1.37 < |\eta| < 1.45$). The FCTight criteria are composed of both calorimeter-based and track-based isolation variables, defined as topoetcone20/$p_{\mathrm{T}} < 0.2$ and ptvarcone20_TightTTVA_pt1000/$p_{\mathrm{T}} < 0.06$. To ensure that electrons originate from the IP, requirements of $|d_0|/\sigma_{d_0} < 5$ and $|z_0 \sin\theta| < 0.5$ mm are applied on electrons. The photons used are required to pass Tight identification and FixedCutTight isolation selections for $E_{\mathrm{T}} > 25$ GeV and be within $|\eta| < 2.37$, excluding the same transition region in the LAr calorimeter as for the electrons. The primary Tight selection has an efficiency between 82% (75%) and 92% (82%) for unconverted (converted) photons depending on E_{T} and $|\eta|$.

5.4 Muon

Muons are identified by the signature of a minimum-ionising charged particle that leaves tracks in both ID and MS and has characteristic energy deposits in the calorimeter. The muon reconstruction is mainly based on the information of the ID and MS detectors. The calorimeter information will also account for corrections and tagging for specific muon candidates. This section introduces the muon reconstruction, identification, and isolation criteria.

The MS tracks begin with short straight-line track segments from hits in an individual MS station. At this level, the bending of the tracks by the magnetic field is small and the trajectory is regarded as straight-line. The preliminary track candidates are the combinations from segments in different stations using precision and trigger chambers information. A global χ^2 fit is performed on the muon track in the magnetic field. Finally, the ID and calorimeter information is combined with MS tracks to complete the global muon reconstruction. Depending on different reconstruction strategies, the following muons types are provided:

- Combined (CB) muons: identified by matching MS tracks to ID tracks followed by a combined fit based on hits. The fitting takes into account the energy loss in the calorimeter and updated the hits to improve the track quality.
- Segment-tagged (ST) muons: identified by requiring a successful matching of the extrapolated ID track and at least one MS segment.
- Calorimeter-tagged (CT) muons: identified by extrapolating ID tracks to energy deposits within the calorimeter with the signature of a minimum-ionizing particle. The track p_{T} threshold is increased to 5 GeV to suppress large backgrounds.
- Muon-spectrometer extrapolated (ME) muons: identified by MS tracks that are loosely from the IP but fail to match with any ID tracks. Such muons are used to extend the coverage out of the ID ($2.5 < |\eta| < 2.7$).

The identification and isolation requirements are applied to select muon candidates with high quality and suppress the fake or non-prompt muons produced in heavy-flavor hadrons. The identification criteria include requirements on the number hits in the ID and MS, on the properties of the track fit, and the compatibility of measurements from the ID and MS. In order to suit the needs of different physics analyses, several working points are defined, as "Loose", "Medium" and "Tight", with increasing purity and decreasing identification efficiency. An additional working point, "HighPt", is designed to improve the resolution of momentum for high p_{T} muons above 100 GeV. Similar to electron, the track-based and calorimeter-based isolation variables are defined, as mentioned in Section 5.3.3. The track-based and calorimeter-based isolations combine to reach the best performance with high resolution and low pile-up dependence.

The muon candidates used in this analysis are required to have $|\eta| < 2.7$ and pass the Medium selection for $p_{\mathrm{T}} > 25$ GeV and the "HighPt" selection for $p_{\mathrm{T}} > 300$ GeV. The efficiency for identifying a single muon is about 99%. The corresponding probability to misidentify hadrons as muons is about 0.8%. The "FCTight" isolation selection, constructed by a set of fixed cuts on $E_{\mathrm{T}}^{\mathrm{cone20}}$ (calorimeter-based) and $p_{\mathrm{T}}^{\mathrm{varconeXX}}$ (track-based) with XX = 20 and 30, is applied with efficiency of about 95%. The requirements of $|d_0|/\sigma_{d_0} < 3$ and $|z_0 \sin\theta| < 0.5$ mm are imposed on all muon candidates to ensure that muons originate from the IP.

5.5 Jet

Jets are an important physics object to describe a group of particles with tracks and deposits in the calorimeters, mainly from the hadronization of the quarks and gluons or hadronic final state of massive particles produced from the proton-proton collisions. The types of jets are used in this analysis are the small-radius (small-R) jet, the b-tagged jet, and the large-radius (large-R) jet.

Jets are reconstructed based on particle flow reconstruction [103] using the anti-k_t algorithm [104] with a radius parameter of $R = 0.4$ implemented in the FastJet package [105]. The jets are named as small-R jets in the following. The neighboring topo-clusters are grouped with requirements used as input for jet reconstruction. The kinematic variables of jet are calculated by the constituents within its cone size The pile-up dependence is suppressed after subtraction [106, 107], followed by the calibration of jet energy. More details about the estimations of jet energy scale is documented in Ref. [108].

The jets are required to have $p_{\mathrm{T}} > 30$ GeV and $|\eta| < 2.4$. The forward jets are excluded to improve the resolution of mass resonance, studied with signal samples from VBF production mode. To suppress jets that originate from pile-up, jets are required to fulfill the *Bad Loose* set of quality criteria. Furthermore, a jet-vertex tagger (JVT) [109] is applied to jets with $p_{\mathrm{T}} < 60$ GeV and $|\eta| < 2.4$ to discriminate pile-up jets.

Small-R jets containing a b-hadron are identified using a b-tagging algorithm (DL1r [110]) at the 77% b-tagging efficiency benchmark point. The simulated $t\bar{t}$ events are used to measure the identification efficiency for b-hadron jets, with a misidentification rate of less than

1% and around 20% for light jets and c-jets, respectively.

Large-R jets are reconstructed from topo-clusters [111] in the calorimeter, using the anti-k_t algorithm with a larger radius parameters of $R = 1.0$. The radius is increased to include all decaying products from massive particles, such as $W^{\pm}$ and Z bosons. A trimming procedure [112] is applied to suppress the contributions from pile-up to large-R jet's kinematic and mass variables. The sub-constituents with a smaller radius of $R = 0.2$ are removed when the fraction of p_{T} is less than 5%. The corresponding calibration is performed using simulation [108]. The jet mass is determined by considering both calorimetric topo-clusters and associated tracks [113]. The jet energy resolution for jets with a p_{T} of 1 TeV is approximately 5%. Jet candidates are required to have a p_{T} above 200 GeV and $|\eta| < 2.0$ to ensure tracking detector coverage within the jet cone.

5.6 Overlap removal

After the reconstruction of physics objects, an overlap-removal procedure is applied to avoid double counting if several independent algorithms reconstruct the same object. Successive steps of this procedure, developed by the ATLAS CP group, are summarised in Table 5.1. The steps are performed in the listed order, and only surviving objects participate in subsequent steps. The treatments between photon and jets, including small-R and large-R jets, are modified to enhance the event yields in the photon-related categories with a small misidentification, using signal samples with photon final state.

Table 5.1: Overview of the successive steps of the overlap removal [114].

Reject	**Against**	**Criteria**
electron	electron	shared track, $p_{\mathrm{T},1} < p_{\mathrm{T},2}$
muon	electron	is CT-muon and shared ID track
electron	muon	shared ID track
photon	electron	$\Delta R < 0.4$
photon	muon	$\Delta R < 0.4$
jet	electron	**Not a** b**-tagging jet** and $\Delta R < 0.2$
electron	small-R jet	$\Delta R < \min(0.4, 0.04 + 10\mathrm{GeV}/p_{\mathrm{T}}^{e})$
small-R jet	muon	**Not a** b**-tagging jet** and NumTrack < 3 and (ghost-associated or $\Delta R < 0.2$)
muon	small-R jet	$\Delta R < \min(0.4, 0.04 + 10\mathrm{GeV}/p_{\mathrm{T}}^{\mu})$
small-R jet	photon	**Not a** b**-tagging jet** and $\Delta R < 0.2$
photon	small-R jet	$\Delta R < \min(0.4, 0.04 + 10\mathrm{GeV}/p_{\mathrm{T}}^{\gamma})$
large-R jet	electron	$\Delta R < 1.0$
large-R jet	photon	$\Delta R < 1.0$
small-R jet	large-R jet	$\Delta R < 1.0$

6 - Merged-ee identifications

At high p_{T}, the Z boson is highly boosted. The two decaying leptons are close in space and may overlap, particularly for electrons. The overlap will affect the efficiency of standard isolation criteria for the electrons In several analyses, it was observed that the efficiency of the standard electron isolation requirements decreases as a function of the Z boson p_{T} starting from about 800 GeV. A tag-and-probe analysis has been performed using Z+jets samples. The efficiency of two isolation working points is shown as a function of probe electron (left) and muon (right) p_{T} in Figure 6.1. The efficiency of isolation efficiency has a sharp drop from 400 GeV for electrons, due to the overlap between them, but is stable for muons.

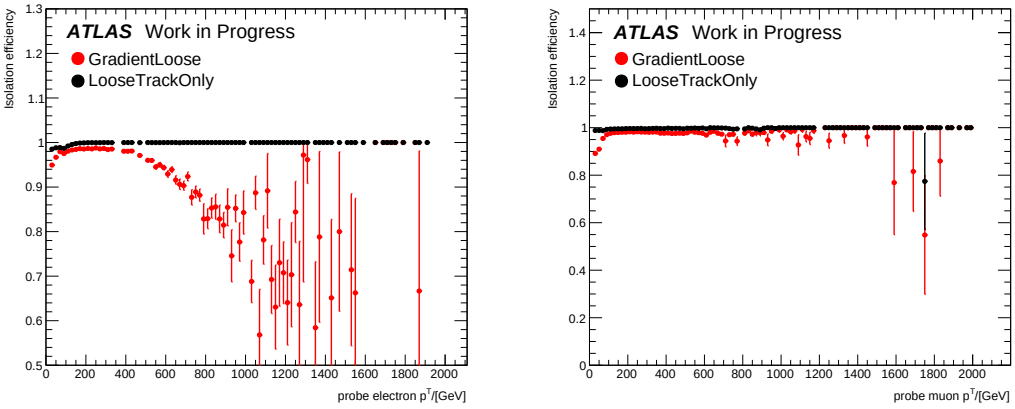

Figure 6.1: The distributions of efficiency as a function of probe electron (left) and muon (right) p_{T} at LooseTrackOnly (black) and GradientLoose (red) isolation working points.

6.1 Boosted Decision Tree analysis and selections

When the decaying electrons are close, they could not be well identified due to partial or complete overlap. These events may fail the electron triggers, and the electrons could not pass the identification and isolation criteria. To recover the efficiency at high p_{T}, the following Boosted Decision Tree (BDT) analysis is performed by using particle flow jets based on the anti-k_t algorithm with a distance parameter of $R = 0.4$. All small-R jets in the selected events are used in the BDT training. The BDT architecture and used parameter are shown in Table 6.1. The following variables are selected as inputs for the BDT analysis (when relevant, the selection is also indicated):

- $p_{\mathrm{T}}^{\mathrm{jet}}$: the transverse momentum of a jet (requiring that $p_{\mathrm{T}}^{\mathrm{jet}} > 450$ GeV),

- η^{jet}: the pseudorapidity of a jet (requiring $|\eta^{\text{jet}}| < 2.47$),
- m_{jet}: the invariant mass of a jet (requiring the expected jet mass for a $Z \to ee$ decay being around the Z-boson mass: $60 < m_{\text{jet}} < 120$ GeV),
- $f_{\text{jet}}^{\text{EM}}$: the jet energy fraction deposited in the electromagnetic (EM) calorimeter,
- $\text{Max}(E_{\text{layer}}/E_{\text{jet}})$: the maximum jet energy fraction deposited in a layer,
- $N_{\text{jet}}^{\text{track}}$: the number of tracks with $p_{\text{T}} > 500$ MeV associated to a jet (requiring $1 \leq N_{\text{jet}}^{\text{track}} \leq 7$),
- $\overline{\Delta R} \cdot p_{\text{T}}/m_{\text{jet}}$: where $\overline{\Delta R}$ is defined as $\frac{\sum(\Delta R(\text{jet,constituent}) \cdot p_{\text{T}}(\text{constituent}))}{\sum p_{\text{T}}(\text{constituent})}$,
- $n_{\text{jet}}^{\text{constituent}}$: the number of constituents of a jet,
- $n_{\text{GSF tracks}}$: the number of GSF (Gaussian Sum Filter [115]) tracks inside the jet cone ($\Delta R(\text{jet}, \text{track}) < 0.4$), which satisfies $p_{\text{T}} > 50$ GeV
- $\Sigma Q_{\text{GSF tracks}}$: the total charge of the GSF tracks satisfying the selections,
- $n_{e/\gamma \text{ clusters}}$: the number of e/γ super clusters inside the jet cone, which satisfies $p_{\text{T}} > 25$ GeV.

Events are required to fire either jet triggers or electron triggers depending on the periods as given in Table 4.1. Events with two oppositely charged same flavour leptons are vetoed since they are analysed using the standard likelihood-based electron identification. The jet energy fraction in the EM calorimeter should satisfy a p_{T}-dependent selection, and at least one but no more than eight tracks are required to be found in the jet cone. The candidate should match with at least one GSF track and satisfy $N_{\text{PFO}} - N_{\text{GSF tracks}} < 2$ to suppress γ+jets background, where N_{PFO} is the number of particle flow tracks with $p_{\text{T}} > 1$ GeV. At least one e/γ cluster is also required to be matched with the jet, with the leading e/γ cluster in the jet which has the largest p_{T}, the cluster-based mass, m_{cls} is constructed to show the 2-body decay property of the $Z \to ee$ process. The cluster-based mass is defined as $m_{\text{cls}} = \frac{\frac{1}{2}\overline{\Delta R} p_{\text{T}}^2}{\sqrt{z(1-z)}}$, where z is the energy ratio between the leading cluster and jet. The jet should satisfy $m_{\text{cls}} > 60$ GeV.

In this study, signal events are based on $Z(\to ee)$+jets MC samples requiring the merged-ee candidate matches to the true Z boson within 0.1 in ΔR, while the SM background events correspond to combined MC samples of γ+jets, $W(\to e\nu)$+jets and $W(\to e\nu)+\gamma$. The selected signal and background events are 51 490, and 4 333, respectively. The latter is further decomposed by 2974, 909, and 450 events from the background processes mentioned above. The shape of these distributions between the signal and the background is compared in Figures 6.2 and 6.3. The signal peaks around $|\eta_{\text{jet}}| = 1.5$ in Figures 6.2 are due to the missing reconstruction of electrons in the transition regions. The statistics of the background samples are, unfortunately, very limited. It can be improved by either relaxing the pre-selections or defining a specific control regions directly from data.

Table 6.1: BDT hyperparameters and search range

Parameter name	Description	Choice	Search range
BoostType	Type of boosting technique	GradientBoost	
SeparationType	Separation criterion for node splitting	GiniIndex	
Ntrees	Number of trees in the forest	600	[1, 1000]
MaxDepth	Max depth of the decision tree allowed	8	[0, 100]
MinNodeSize	Minimum fraction of training events required in a leaf node	3%	[0, 100]%
nCuts	Number of grid points in variable range used in finding optimal cut in mode splitting	80	[10, 100]
Shrinkage	Learning rate for GradientBoost algorithm	0.01	[0, 1]
BaggedSampleFraction	Relative size of bagged event sample to original size of the data sample	0.9	[0, 1]

The correlation between these variables for the signal and background events is shown in Figure 6.4.

The BDT separation between the signal and background is shown in Figure 6.5 (left). Using a series of p_{T}-dependent BDT selections varying between 0.49 at low p_{T} to -0.66 at high p_{T}, with which the efficiency of signal could be fixed at 90%, the resulting efficiency values as a function of p_{T}^{Z} are compared with that of the standard electron identification in Figure 6.5 (right). One sees clearly that the low efficiency of the standard electron identification at high p_{T} is recovered with the BDT-based merged-ee identification reaching a combined efficiency of 90%. The background rejection factor for three types of processes relevant for this analysis is shown in Figure 6.6. The performance of the BDT method is compared with the cut-based method selection using the $f_{\mathrm{jet}}^{\mathrm{EM}}$ variable at the same signal efficiency. In all cases, the background rejection is significantly better than the cut-based identification. Finally, the distributions of the eleven BDT input variables between data and MC are compared in Figure 6.7. The agreement is fairly good. There is a slight shift between data and MC on the jet mass of the Z boson. It is checked using an HVT signal sample with a mass value of 2.8 TeV that such a shift has negligible impact on the reconstructed m_{ZX} mass distributions. The BDT distribution of MC and data are compared in Figure 6.8.

Figure 6.9 shows the purity of the merged-ee identification. The purity is measured using the SM $Z(\rightarrow ee)$+jets and $Z(\rightarrow ee) + \gamma$ samples, which are used as signal, while the background consists of γ+jets, $W(\rightarrow e\nu)$+jets, $W(\rightarrow e\nu)$+γ and top processes. Figures 6.10 and 6.11 present the impact by including the merged-ee identification for both the HVT signal samples and the SM background samples in the $Z \rightarrow e^{+}e^{-}$ decay channel. The same Z mass window selection of $[66, 116]$ GeV as the standard event selection is used to measure the impact of the merged-ee identification. Compared with the event selection, which uses only the nominal electron identification to form the Z bosons, the combined one, which includes the merged-ee to identify the Z boson when the nominal electron identification fails, provides a substantial gain in statistics in the leading large-R-jet category in particular at large p_{T}^{Z}. Different from the signal results, the gains in the

m_{ZX} distribution of the SM background is much smaller. The correlation between the m_{ZX} and is complicated, and m_{ZX} is also correlated to the m_X. Finally, the gains on the SM background are quite moderate.

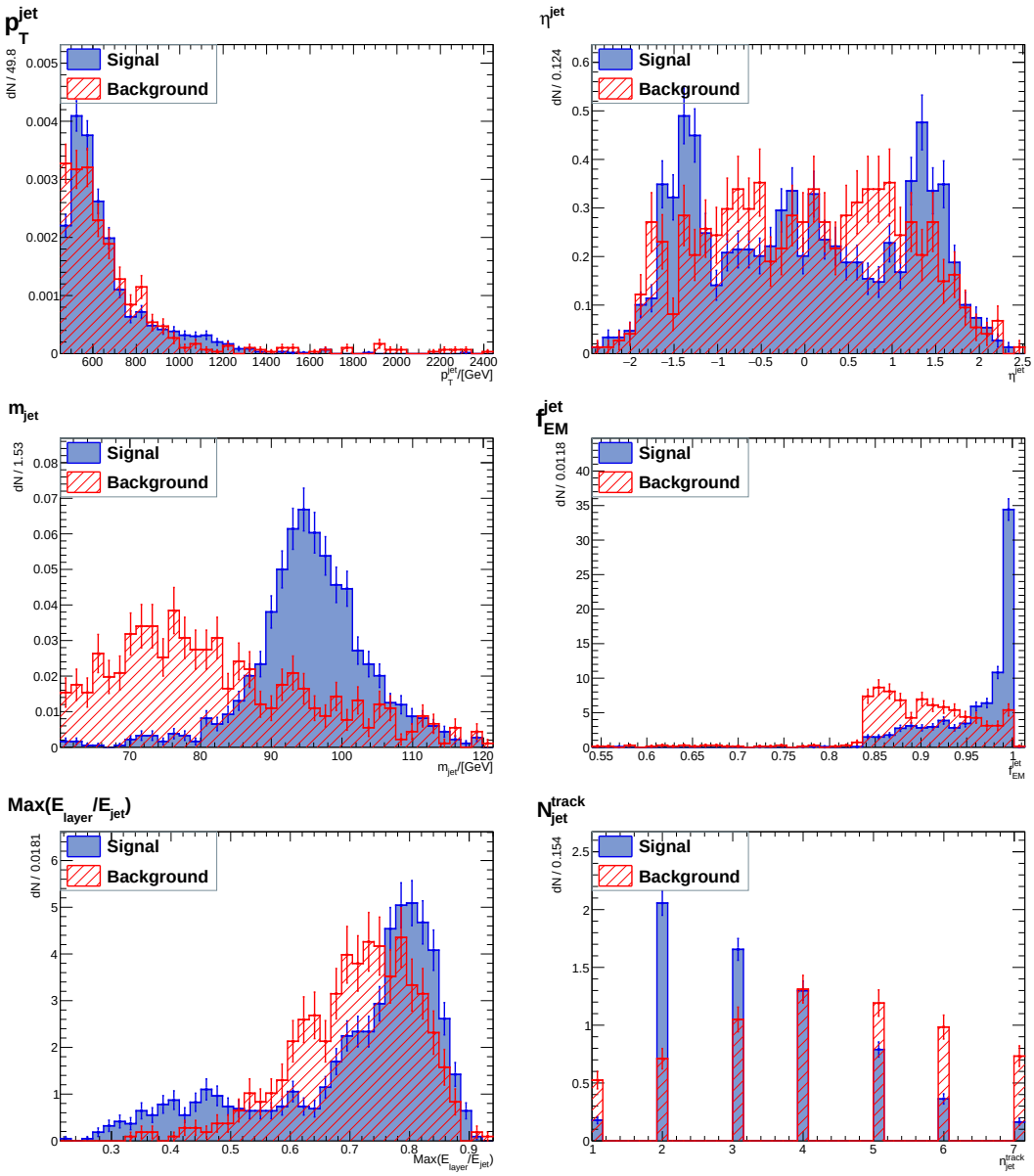

Figure 6.2: Shape comparison between boosted $Z(\rightarrow ee)$ signals (blue) and SM background (red) for six of the selected variables used in the BDT analysis of the merged-ee identification.

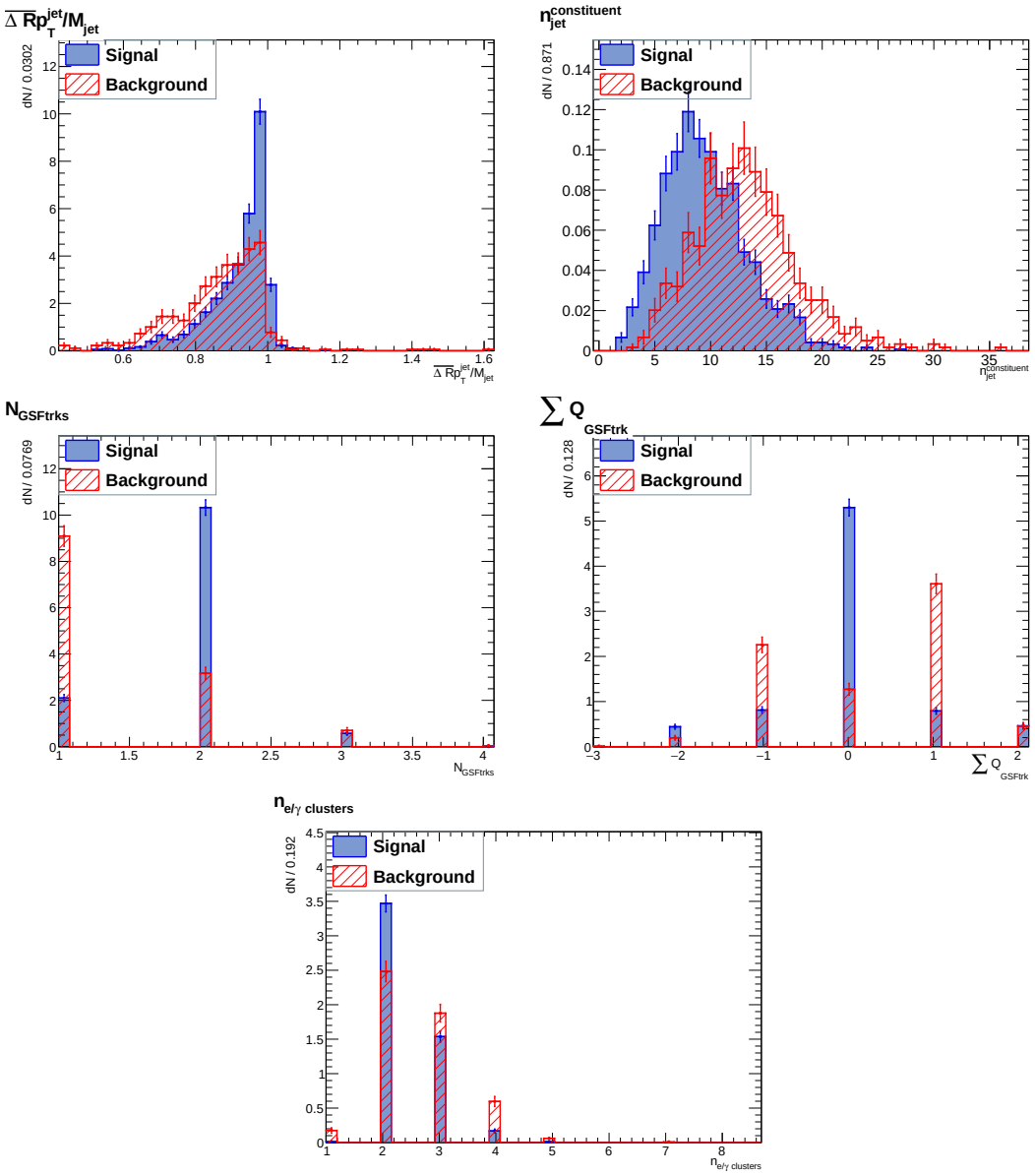

Figure 6.3: Shape comparison between boosted $Z(\rightarrow ee)$ signals (blue) and SM background (red) for five other selected variables used in the BDT analysis of the merged-ee identification.

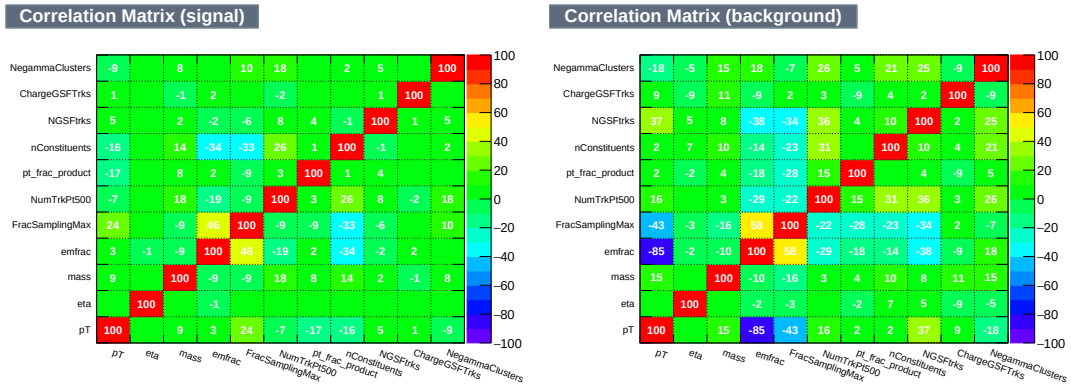

Figure 6.4: Correlation between the input variables for the signal (upper panel) and background (lower panel).

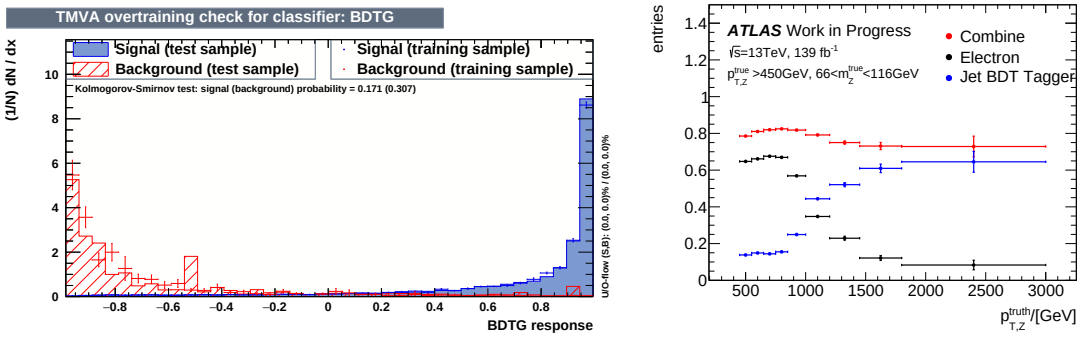

Figure 6.5: Left: the BDT separation between the signal (blue) and background (red). Right: comparison of the identification efficiencies.

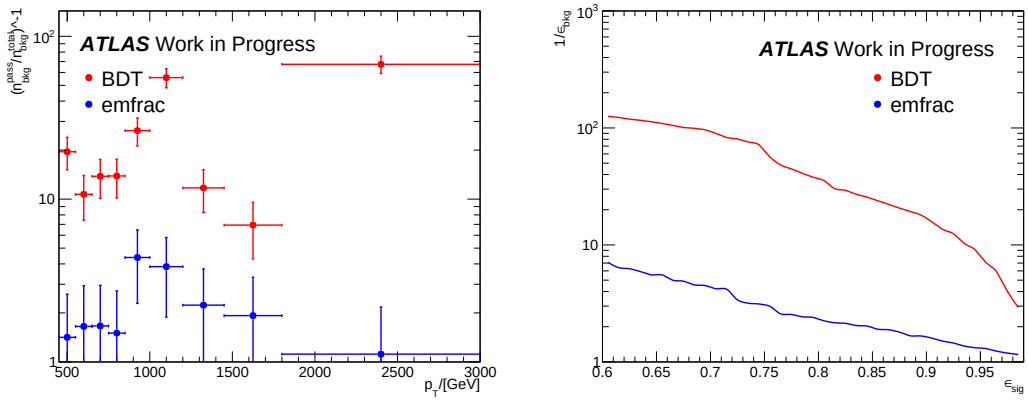

Figure 6.6: Left: background rejection on the standard model background as a function of p_{T} when signal efficiencies are fixed at 90% in each p_{T} slice. Right: background rejection factor as a function of signal efficiency. The red dots/curve show the BDT performance of this analysis whereas the blue dots/curve correspond to that of a cut-based analysis relying mainly on the jet energy fraction deposited in the EM calorimeter.

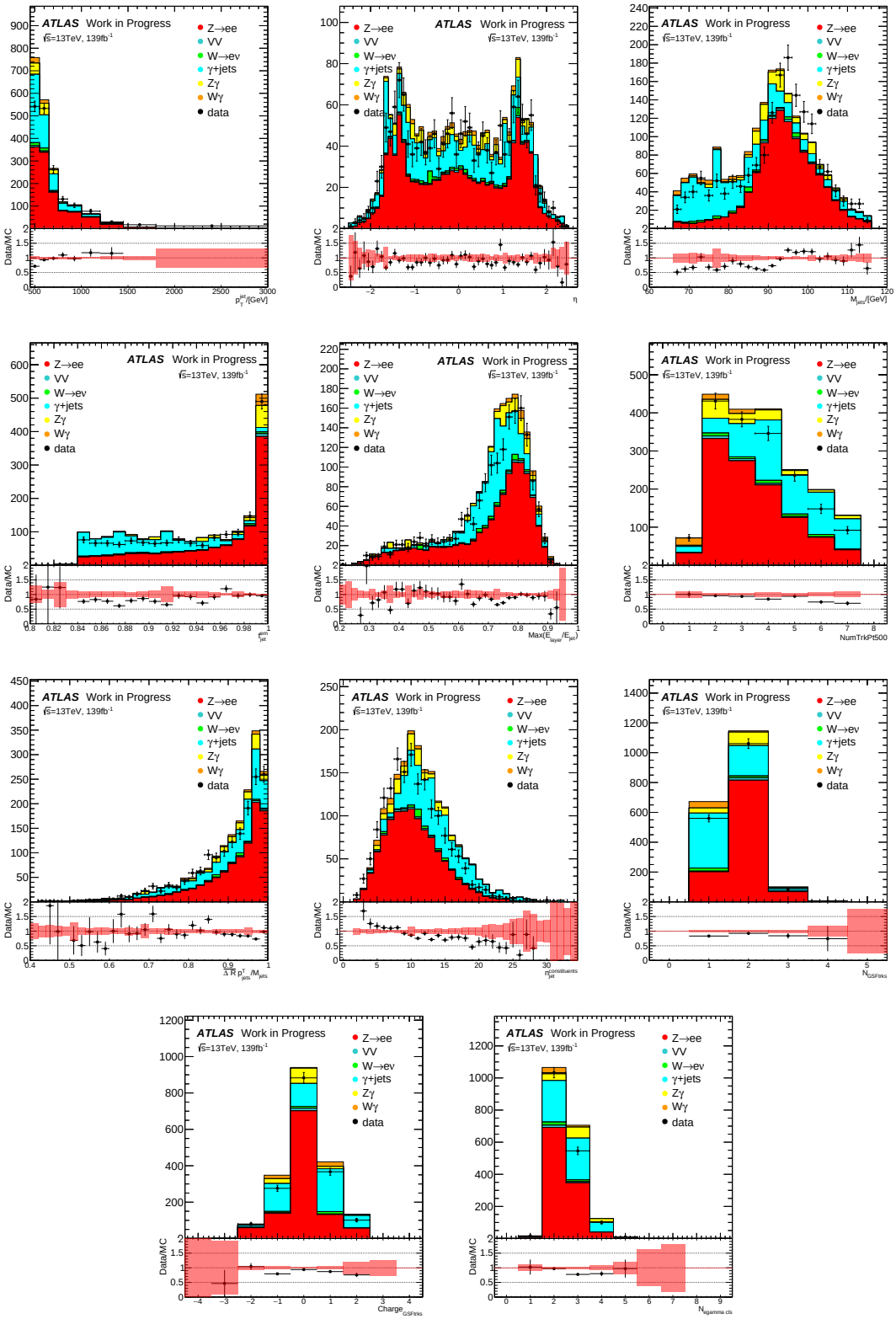

Figure 6.7: Comparison between data and MC for the input variables.

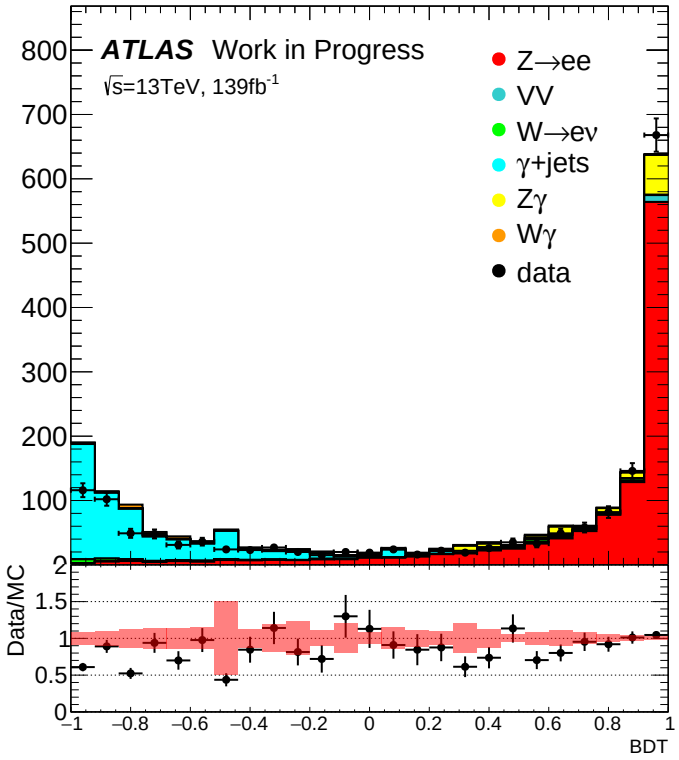

Figure 6.8: Comparison between data and MC for the BDT output

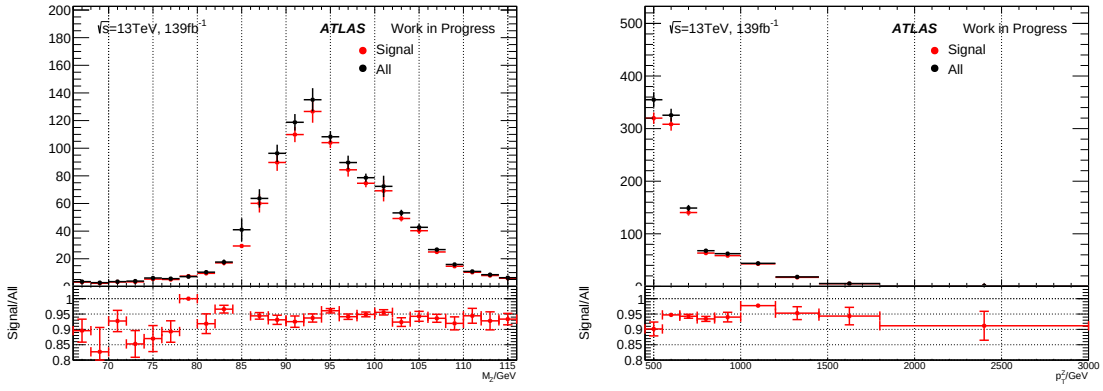

Figure 6.9: Signal purity as a function of Z boson mass (left) and the transverse momentum of the Z boson (right).

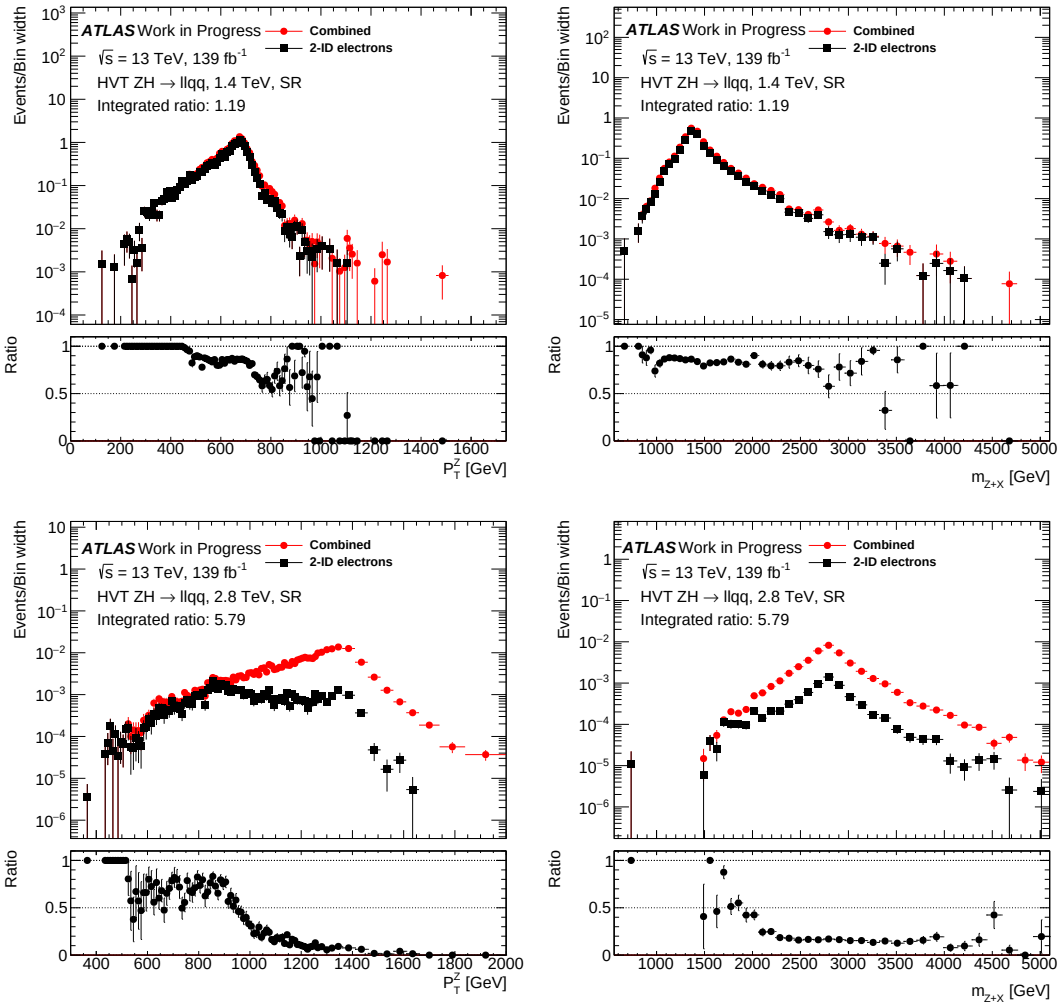

Figure 6.10: Example figures for p_{T}^{Z} (left) and m_{ZX} (right) in **LeadFatJ** in the $Z \rightarrow e^{+}e^{-}$ decay channel for HVT signal samples at two different mass values showing the gain in statistics by comparing Z bosons formed by a pair of an electron and a positron based on the standard electron identification with a combined sample in which additional Z bosons identified with merged-ee are also included.

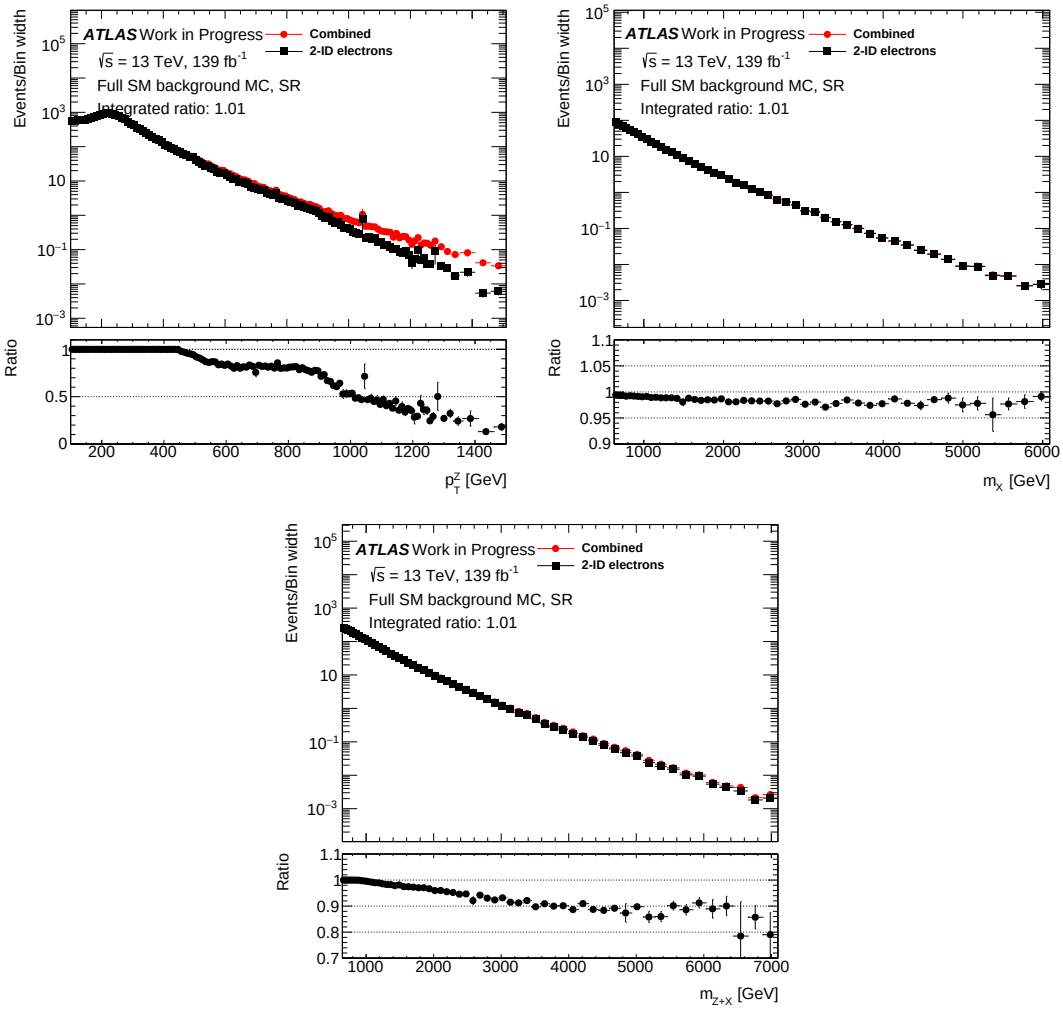

Figure 6.11: Same as Figure 6.10 but applied to the SM background samples.

7 - Event selections and classification

7.1 Event selections

Data events are firstly required to pass the data quality criteria (Good Run List) to ensure that events are collected under the excellent condition of the detector. Events must have one primary vertex associated with at least two tracks. A JetCleaning tool [116] is applied to discard events that contain jets classified as "BadLoose". The un-prescaled triggers listed in Table 4.1 are used depending on the data-taking period. Further trigger matching between trigger ROI and selected leptons is applied for lepton triggers by requiring a distance of leptons and trigger objects less than 0.1.

After passing the trigger selections, the Z-boson candidates are selected by requiring two oppositely charged and same-flavour leptons (e^+e^- or $\mu^+\mu^-$). Both leptons must satisfy the quality criteria discussed in Chapter 5. If there is more than one reconstructed Z-boson candidate, the one with mass value closest to Z-boson mass is chosen. The merged-ee identification, discussed in Chapter 6, is performed on events which fail to satisfy previous requirements to compensate the efficiency lost in high Z-boson p_{T} region. The Z-boson candidates are further required to have invariant mass values between 66 and 116 GeV around Z-boson mass. It was checked with the Z+jets events (background) and $Z' \to ZH \to llqq$ of HVT model events (signal) at three mass values of 0.7, 1.2, and 2.4 TeV as shown in Figure 7.1, that this mass window is adequate for both the ee and $\mu\mu$ channels with the Z-boson mass resolution improving as for the former and degrading for the latter.

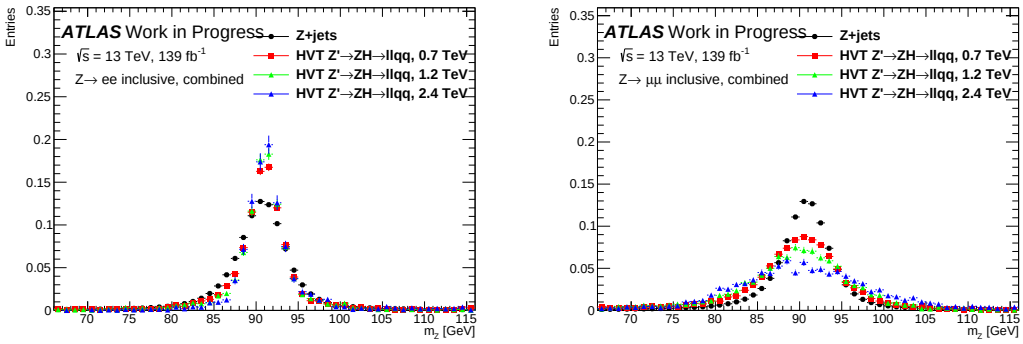

Figure 7.1: Comparison of Z-boson mass distributions of HVT signals at 0.7, 1.2 and 2.4 TeV in $Z \to e^+e^-$ (left) and $Z \to \mu^+\mu^-$ (right) decaying channel.

For this preselected sample, various kinematic variables of the Z boson are compared between data and SM predictions. Two example distributions of the invariant mass and transverse momentum are shown in Figure 7.2. The SM predictions have a reasonably good agreement with data, based on the simulated MC samples except for multijet and

W+jets processes. The contribution of the latter, though small and distributed at low p_{T}^{Z} values as it can be seen from Figure 7.2, cannot be reliably and efficiently predicted using simulated samples due to their large cross sections. They are thus estimated using data-driven techniques discussed in Section 8.1.1 following the same procedure as in Ref. [75].

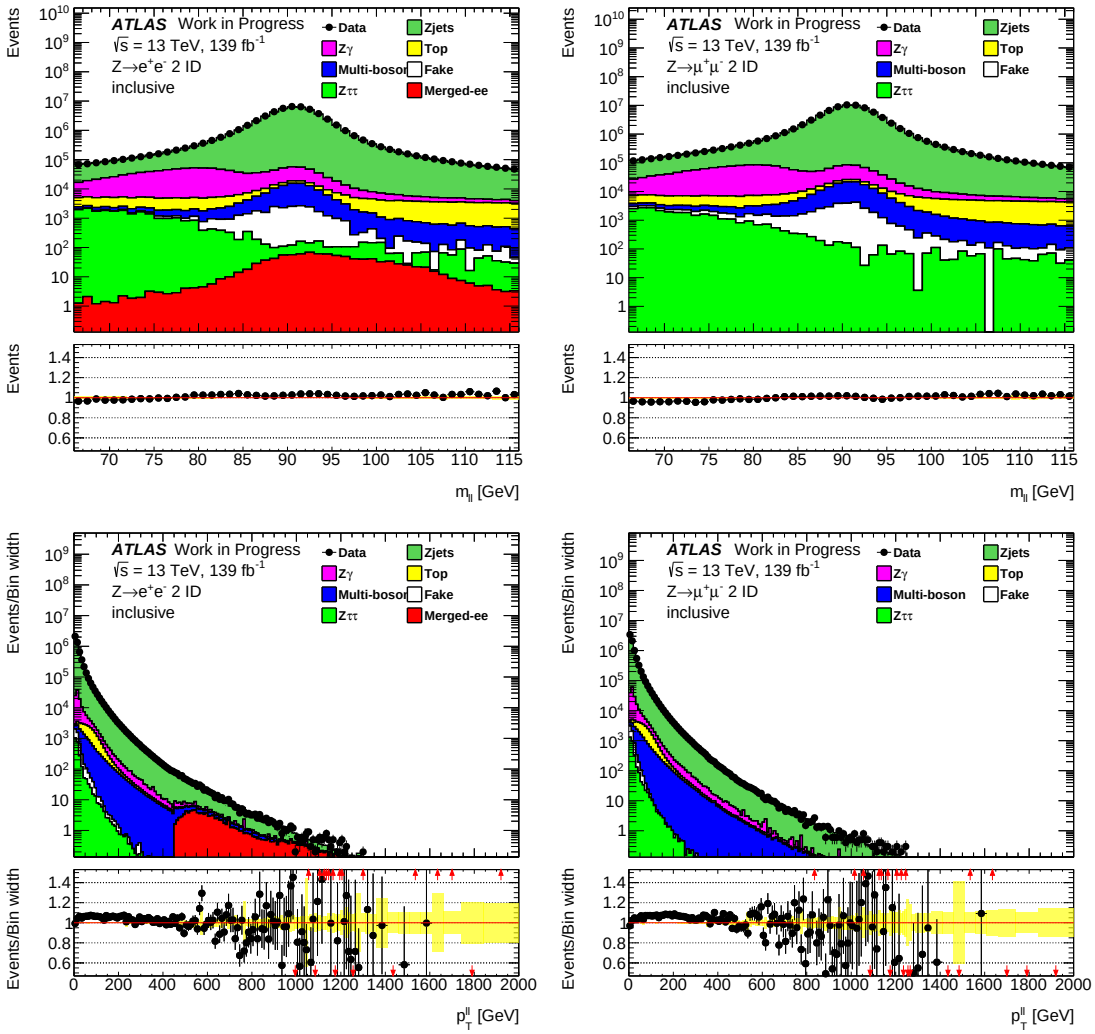

Figure 7.2: Comparison of the invariant mass (upper) and transverse momentum (bottom) distributions of the Z boson candidates between data (solid points) and MC predictions (stacked histograms) in the $Z \to e^+e^-$ (left) and $Z \to \mu^+\mu^-$ (right) decay channels at the pre-selection level. The error bands in the ratio panels represent the statistical error of the MC predictions.

To suppress the dominant SM background contributions at low p_{T}, the Z boson is selected by requiring $p_{\mathrm{T}}^{Z} > 100\,\mathrm{GeV}$. The choice of this p_{T}^{Z} is a compromise between suppressing the SM background contribution and keeping sufficient event statistics in background

estimations procedures for some of the categories. These selections define the *Signal Region (SR)*.

7.2 Event classification

In a given event in the SR, in addition to the leptons or small-R jet from Z-boson decays, all other objects are assumed to belong to the recoil system (X) of the Z boson. They are sorted in order of their transverse momentum. The leading p_{T} object in the recoil system can be a non-b small-R jet, a b-jet, a photon, a lepton (electron or muon), or a large-R jet. Six event categories are defined according to the type of these leading p_{T} objects:

- **LeadJ**: with leading small-R (non-b) jet.
- **LeadB**: with leading b-jet.
- **LeadFatJ**: with leading large-R jet.
- **LeadP**: with leading photon.
- **LeadE**: with leading electron.
- **LeadM**: with leading muon.

Each category is mutually exclusive and may be sensitive to different resonances, which are searched for using two observables defined as the invariant mass of the recoil system (m_X) and of the full final state of the event (m_{ZX}) using all the selected visible objects described in Chapter 5. Events are excluded in case that there is no other visible objects except for the selected Z boson candidate or the missing transverse momentum ($E_{\mathrm{T}}^{\mathrm{miss}}$) is the leading object, because the resonances (X or Y) cannot be fully reconstructed. The event yields of these categories for data are shown in Figure 7.3 and Table 7.1.

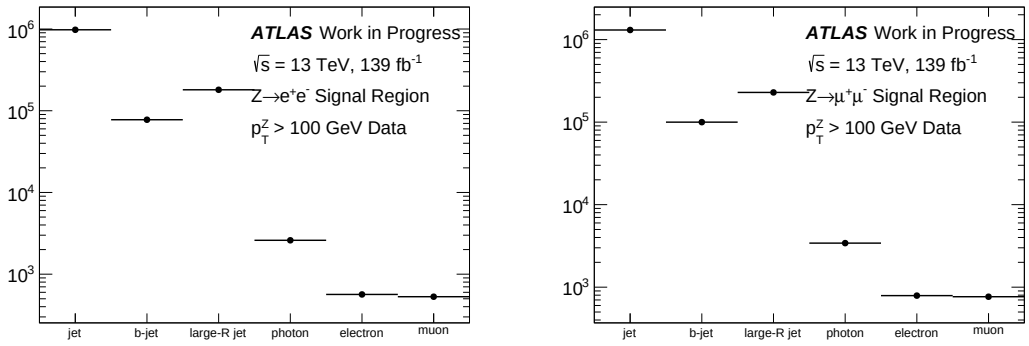

Figure 7.3: Event yields for different exclusive categories for the $Z \to e^+e^-$ (left) and $Z \to \mu^+\mu^-$ (right) channels for signal region with $p_{\mathrm{T}}^{Z} > 100$ GeV.

Table 7.1: Event yields in the signal regions of the six event categories in the $Z \to e^+e^-$ and $\mu^+\mu^-$ decay channels.

Category	LeadJ	LeadB	LeadFatJ	LeadP	LeadE	LeadM
ee (including merged-ee events)	979074	77625	181561	2601	565	530
$\mu\mu$	1307187	99927	228986	3418	790	766

In this classification definition, all selected visible objects are included for each category. The multiplicity distribution of each type of selected object in each category is present in Figure 7.4 for background samples. The majority of the visible objects are small-R jet.

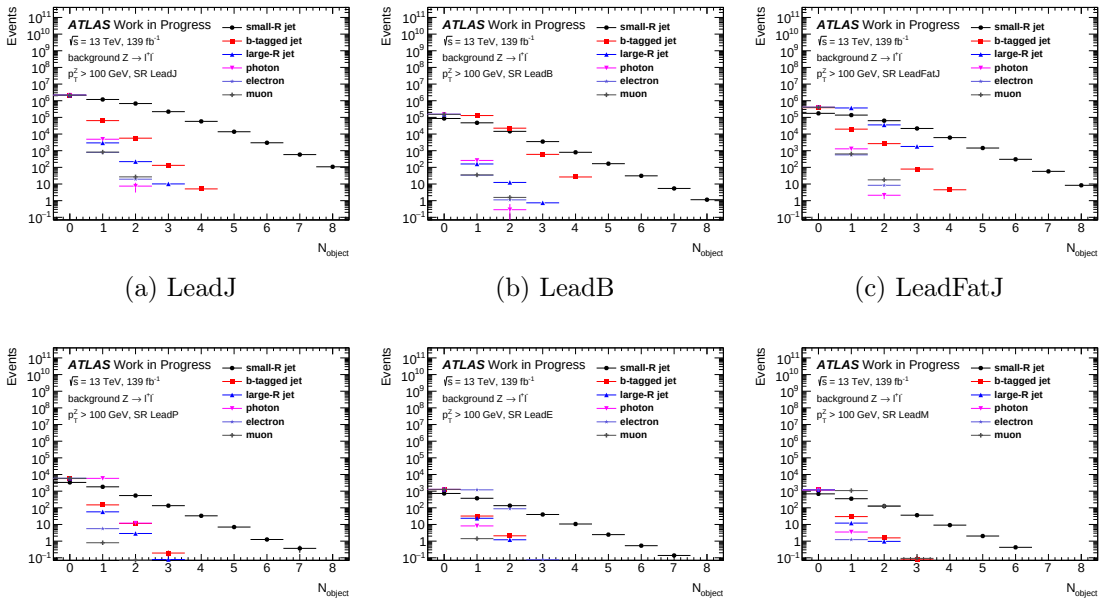

(a) LeadJ (b) LeadB (c) LeadFatJ

(d) LeadP (e) LeadE (f) LeadM

Figure 7.4: Numbers of different object types in each category in the $Z \to \ell^+\ell^-$ decaying channel.

Some of the signal events may be misclassified to the wrong category. For example, a signal process $H \to ZZ \to \ell\ell\ell\ell$ in the Narrow Width Approximation (NWA) model is expected to contribute in the leading lepton categories but may contribute to other categories due to the object reconstruction. The event yields distributions in each category are checked for two signal models with different final states, shown in Figure 7.5. The majority of events are correctly classified with a low rate of misclassification. A combined category grouping all six categories is defined to avoid potential misclassification and enhance search sensitivity in different event categories.

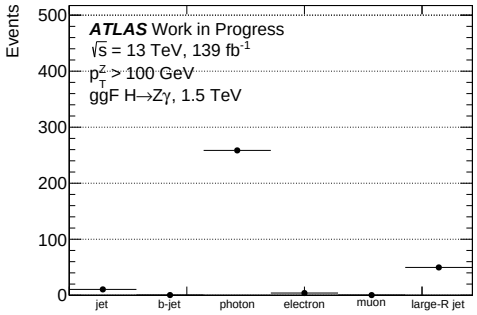

(a) Event type

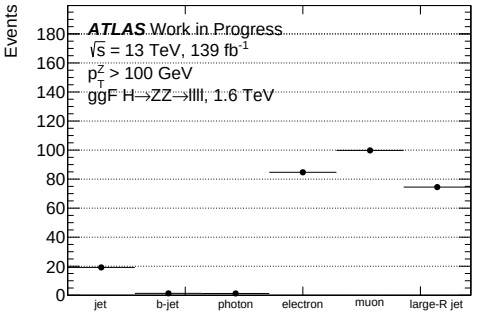

(b) Event type

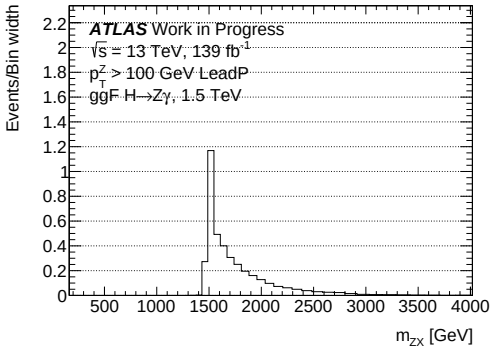

(c) m_{ZX} in LeadP category

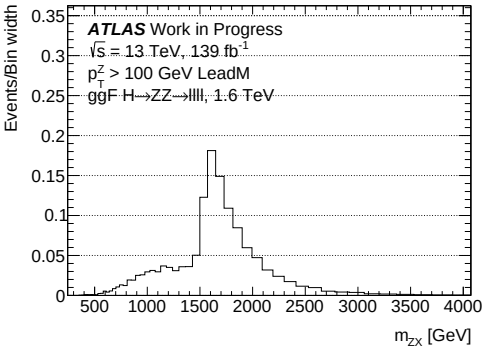

(d) m_{ZX} in LeadM category

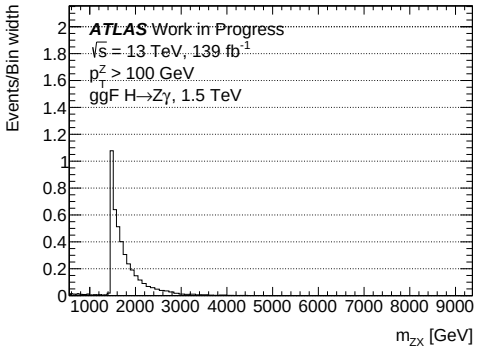

(e) m_{ZX} in combined category

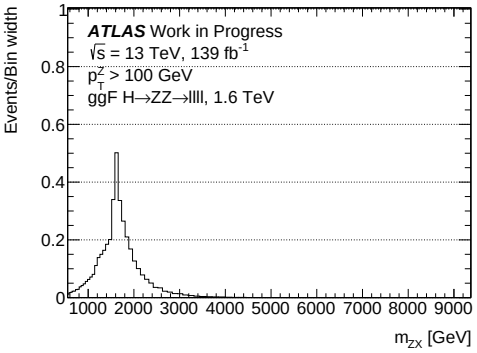

(f) m_{ZX} in combined category

Figure 7.5: Distributions of event type (top), m_{ZX} in the expected category (middle) and m_{ZX} in the combined category (bottom) for ggF $H \to Z\gamma$ with $m_H = 1.5$ TeV (left) and ggF $H \to ZZ \to \ell\ell\ell\ell$ with $m_H = 1.6$ TeV (right) signal models.

8 - Background modelling

This chapter presents the modelling of the SM background and the analysis strategy. The contributions of the SM background based on MC simulation samples are shown in Section 8.1, followed by some comparison results between data and MC in Section 8.2. A data-driven method is introduced to estimate the SM background in Section 8.3. The systematics uncertainties for background and signal are described in Section 8.4.

8.1 SM background contributions based on MC simulations

All background contributions other than the fake lepton one from multijet and W+jets processes are estimated using MC simulation samples. The MC samples are then scaled by the provided cross section, filter efficiency, and k-factor to the integrated luminosity of data collected by the ATLAS detector in full Run 2 period. The fake lepton background is estimated using a data-driven technique following the SM analysis [117], separately for the ee and $\mu\mu$ channels. During the procedure, the samples are selected by removing the p_{T}^{Z} requirement, called pre-selected samples.

8.1.1 Fake lepton background

Electron channel

The fake electron background originates from events where one or two electrons are reconstructed from misidentified QCD jets. Physics processes that dominate the QCD background are QCD multijet production and W+jets events. A method defining a discriminating variable is used to estimate the fake electron background.

The discriminating variable is chosen to the isolation variable: [1]

$$I_e^{\mathrm{min}} = \min\left(\frac{\mathrm{topoetcone20}}{27\,\mathrm{GeV}}\right) \tag{8.1}$$

where min is the minimal isolation in the pair of selected electrons. The tail of the distribution above a certain threshold is used to determine the normalization factor of the fake electron background. The entire distribution is used to determine the normalization factor of the dominant $Z \to e^+e^-$ background.

A template for the fake electron background is built by selecting events with two electrons passing loose identification selection but failing the medium one, without any isolation criteria (FCTight) applied. No opposite-sign charge requirement is imposed to maximise the statistics of the sample. Since single electron triggers have implicit isolation

[1] Our variable is slightly different from that used in [117], namely instead of normalizing to the transverse energy of the electron candidate, it is normalised to 27 GeV, corresponding to the transverse momentum threshold of the lepton selection. Detailed studies show that the background estimation using the two variables is consistent, but the latter variable's tail suffers less from those events having negative weights.

requirements, only di-electron triggers are used for the template sample, and the two electron candidates are matched to the triggering objects of used dilepton triggers. To avoid any leakage of any non-fake electron background into to the template, the contribution of the non-fake electron background estimated using MC predictions is subtracted. Before the subtraction, a shape correction (Figure 8.1) is applied to MC predictions derived from a sample similar to the pre-selected samples except that the isolation requirements on electrons are not applied. Given that the tail region in Figure 8.1 (left) has low statistics and large error, only correction factors that have less than 5% relative error are used. The value of the last bin satisfying the requirement is applied to the tail region.

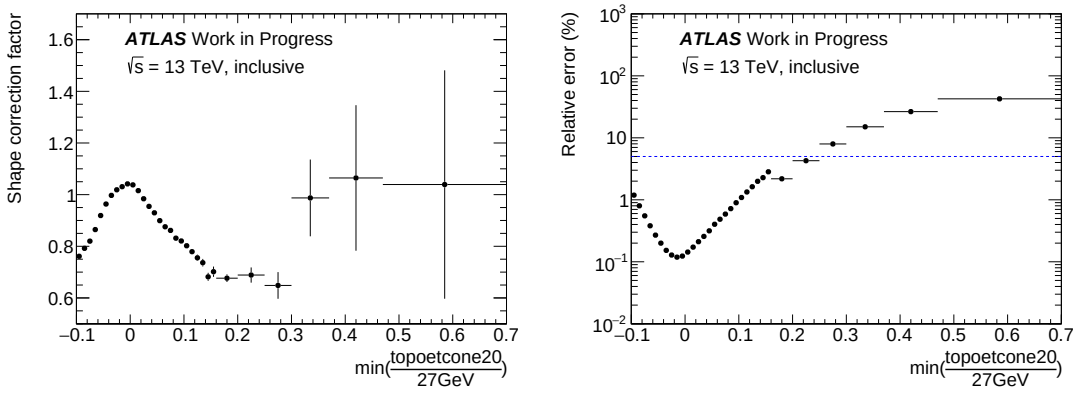

Figure 8.1: Distributions of shape correction factor (left) and corresponding relative error (right) as a function of discriminating variable. The blue dash line shows the criteria (5%) to select used correction factors.

The corresponding distributions of the control and signal regions are shown in Figures 8.2 (left) before applying the normalization factors to be determined below. For these distributions, the data, Z+jets, and other samples must pass pre-selections except that the isolation requirement is not applied.

The tail region of the $I_e^{\min}$ distribution of the control region is used to determine the normalization factor of the template sample. The region is defined by adjusting the threshold (indicated by the vertical line in the figure) by maximizing the region's statistics while requiring the contribution of the fake electron background is as important as the other background processes. An iteration procedure is performed using the entire distribution to determine simultaneously the normalization factors for the Z+jets and fake electron background with the result of 1.0081 ± 0.001 and 1.03 ± 0.25, respectively.

Since the template sample is selected without applying the isolation requirement on electrons, in addition to the above normalization factor, a further correction is needed to derive the background estimation for the pre-selected samples. The correction is the fraction of events passing the isolation requirement. The numerical value of the fraction is 0.69 ± 0.02. The corresponding distribution is shown in Figure 8.3.

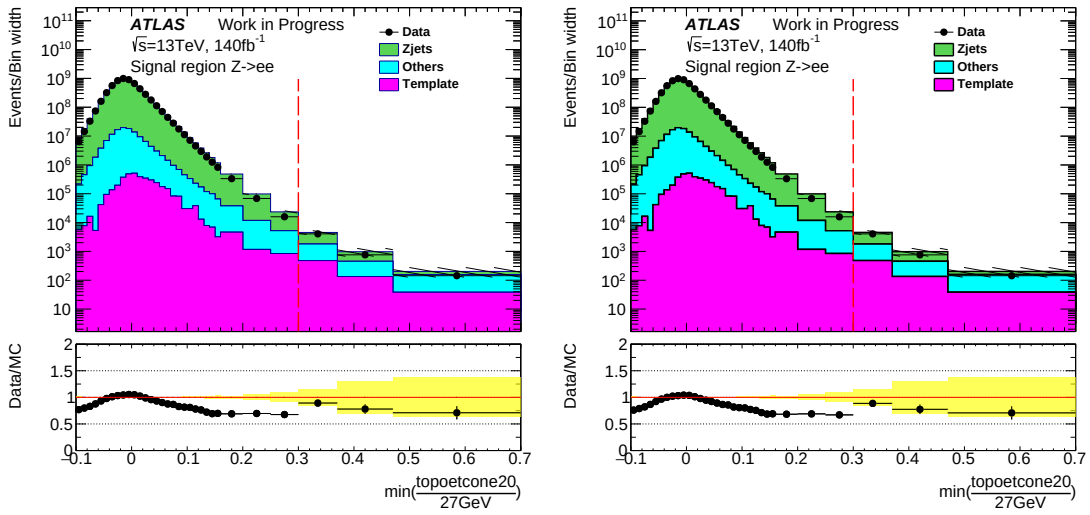

Figure 8.2: Distribution of the discriminating variable I_e^{min} before (left) and after (right) applying the normalization factors for pre-selected samples. The error bars represent the statistical error of the data whereas the error band show the statistical uncertainty of the MC predictions. The vertical line indicates the threshold above which the region is used to determine the normalization factor for the template sample. The normalization factor for the template sample using events in the tail region above the vertical line threshold in the control region is applied to the right plot.

Muon channel

Due to different fake sources of muons from electrons, an ABCD method is used to estimate the fake background contribution in the muon channel. The regions are defined by isolation and charge of two muons selected to reconstruct the Z boson candidates. The definitions of the four regions are shown in Table 8.1. For the isolation requirement, both muons are required to be either isolated or non-isolated. The method assumes that the ratio of the fake muon background in regions A and C is the same as the one in regions B and D:

$$\frac{N_{\text{A}}^{\text{fake}}}{N_{\text{C}}^{\text{fake}}} = \frac{N_{\text{B}}^{\text{fake}}}{N_{\text{D}}^{\text{fake}}} \,. \tag{8.2}$$

Table 8.1: The definition of ABCD regions in the muon channel

Region	Opposite-Sign (OS)	Same-Sign (SS)
Isolated	A	B
Non-isolated	C	D

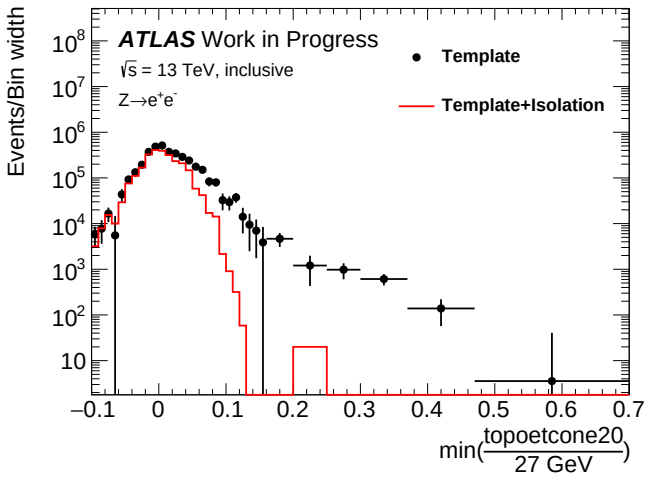

Figure 8.3: Distribution of the discriminating variable $I_e^{\min}$ showing the full template sample (black dot points) and that satisfying the isolation requirement (red lines).

The fake muon background contribution is estimated by scaling the distributions of region C with the ratio of event yields in regions B and D. This method is performed in both signal and control regions for the complete Run2 datasets and corresponding MC samples. The event yields are shown in Tables 8.2 after applying PDG rounding rules for the pre-selected events. In order to gain more statistics, in regions B and D, the Z mass window selection of [66 GeV, 116 GeV] is removed.

Table 8.2: Event yields of data and MC samples in each ABCD regions of the pre-selected samples.

Sample (SR)	Region B	Region D	Region C
Data	16513	18108	492087
Z+jets	320 ± 40	134 ± 22	279200 ± 1900
Multiboson	11562 ± 21	47.0 ± 1.2	580 ± 6
Top	980 ± 10	1371 ± 13	2269 ± 13
V+γ	4 ± 6	30 ± 10	25100 ± 400
$Z\tau\tau$	11.6 ± 3.3	11 ± 6	260 ± 50
Data-bkg (fake)	3630 ± 140	16520 ± 140	185000 ± 2000
Scale factor (N_B/N_D)		0.220 ± 0.009	
Estimated fake		40600 ± 1600	

8.1.2 Binning optimization of observables

The search for new resonances is done in the binned observables (m_X or m_{ZX}) distributions. The signal shape in the reconstruction level is a convolution of its intrinsic

width with the detector mass resolution. The binning should be optimised to ensure that the resonances could contribute over several bins with minor effects from statistics fluctuations. The binning optimization is based on the detector resolution consideration for each observable in each category. The study is performed using the MC samples of dominant background: Z+jets for the LeadJ, LeadB, and LeadFatJ categories; Z+γ in the LeadP category and diboson in the LeadE and LeadM categories.

The detector resolution of m_X and m_{ZX} are evaluated using the Root Mean Square (RMS) values by doing matching between truth and reconstruction objects for all final states, including the leptons from the Z boson decays in the case of m_{ZX}. The truth objects are selected using the exact kinematic requirements as the reconstruction ones in Chapter 5. All truth leptons are dressed by including nearby photons. The truth X variable is based on the selected truth objects that match reconstructed ones within certain radius distance thresholds. The un-matched truth objects are not considered. For example, Figure 8.4 show the correlation between reconstructed observables (m_X and m_{ZX}) and the truth ones in ee and $\mu\mu$ channel for the LeadJ category. An expected linear correlation between reconstructed and truth observables is observed for m_X and m_{ZX} in all the categories.

The detector resolution distributions are shown in Figure 8.5 for the LeadJ category. In all the categories, the resolutions in the decay channels of $Z \to e^+e^-$ and $Z \to \mu^+\mu^-$ are highly consistent. Therefore in the following, the two channels are merged. The resolution distributions are parameterised by smooth functions defined in Eq. (8.3) for m_X and defined in Eq. (8.4) for m_{ZX}, as shown in the top of Figure 8.6.

$$f(x) = e^{p_0+p_1 x} + p_2 + p_3 x, \tag{8.3}$$

$$f(x) = p_0 \mathrm{Erf}(p_1 + p_2 x) + p_3 x. \tag{8.4}$$

Once the detector resolution curves are obtained, the binning is determined by an iterative procedure starting from a low mass boundary, following the study of the dijet analysis [118]. The bin boundaries are chosen such that the bin width is equal to the detector resolution at a given mass and monotonically increases, as shown at the bottom of Figure 8.6. This bin size of the variables varies between around 10 GeV at low mass and up to 300 GeV at high mass.

To check if the optimised binning is adequate for the Gaussian-shape signals with varying widths considered in this analysis, two Gaussian-shaped signals with two extreme width values of 0% and 15% are compared with signals from a signal model at two different value values in the leading large-R-jet category. The Gaussian-shaped signals are folded with detector resolution effects, which is discussed in Section 8.3.2. The shape of the m_{ZX} distributions is compared in Figures 8.7. In all the cases, the resonance signals extend over more than one bin. The mass width of the signal models is between those of the Gaussian-shaped signals, justifying the choice of the binning and the considered width values of the Gaussian-shaped signals.

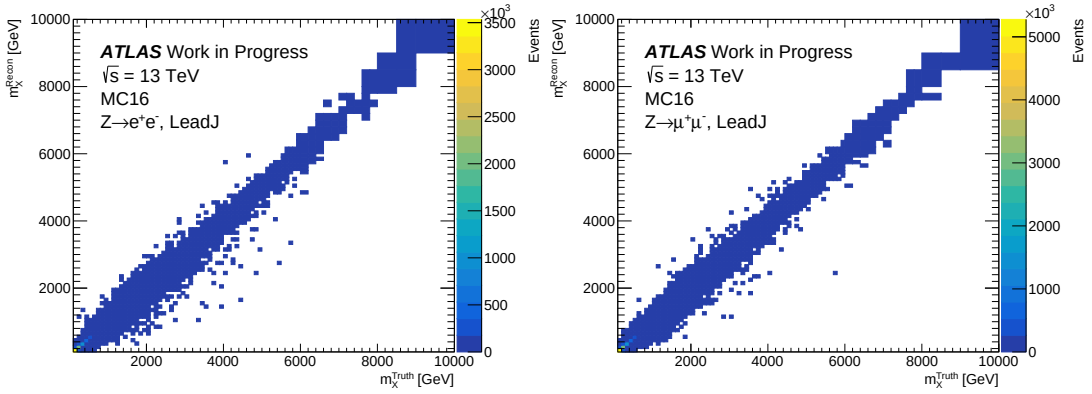

(a) m_X in $Z \to e^+e^-$ (b) m_X in $Z \to \mu^+\mu^-$

(c) m_{ZX} in $Z \to e^+e^-$ (d) m_{ZX} in $Z \to \mu^+\mu^-$

Figure 8.4: The correlation between the reconstructed mass and the corresponding truth one for m_X (top) and m_{ZX} (bottom) in the $Z \to e^+e^-$ (left) and $Z \to \mu^+\mu^-$ (right) channels.

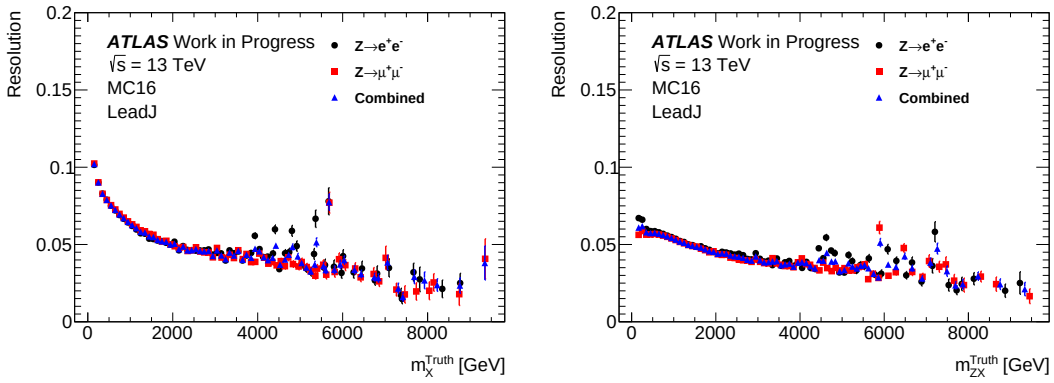

(a) m_X (b) m_{ZX}

Figure 8.5: The m_X (left) and m_{ZX} (right) mass resolution (σ_m/m)distributions in the LeadJ category, comparing the $Z \to e^+e^-$ and $Z \to \mu^+\mu^-$ channels. The error bars are statistical.

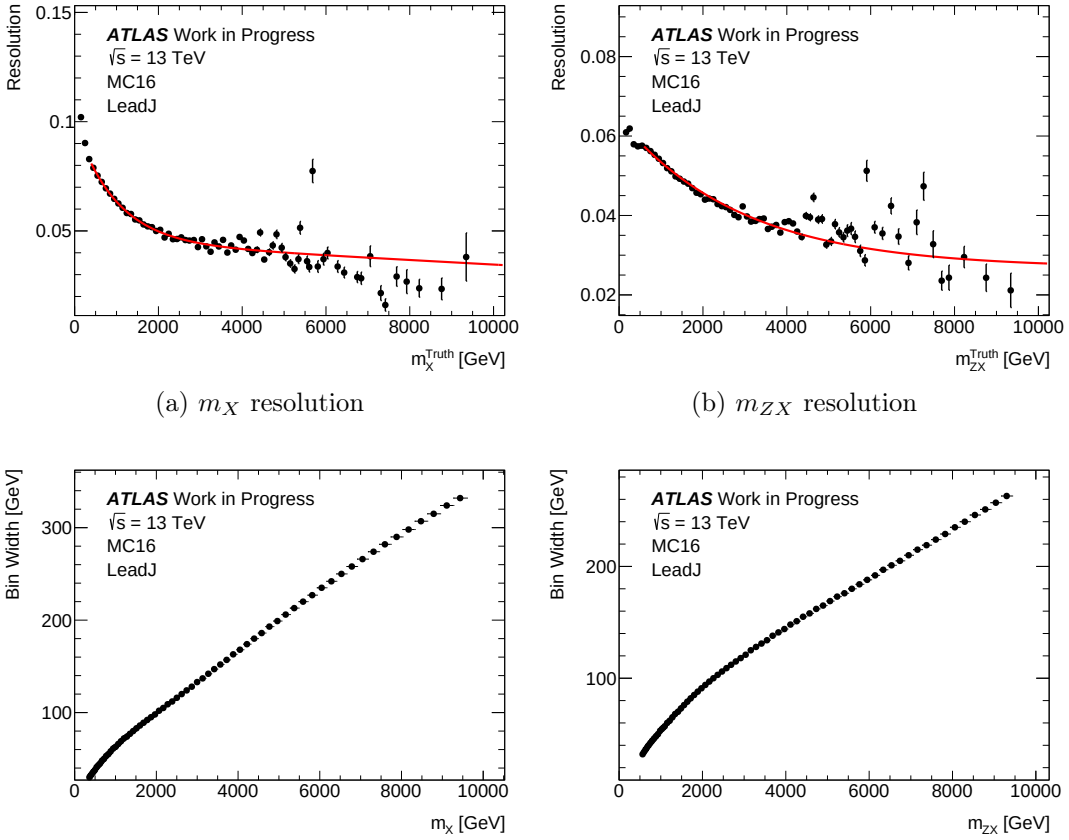

(a) m_X resolution

(b) m_{ZX} resolution

(c) m_X bin width

(d) m_{ZX} bin width

Figure 8.6: The m_X (left) and m_{ZX} (right) mass resolution (σ_m/m) superposed with the fitted function (top) and derived bin width (bottom) in the LeadJ category

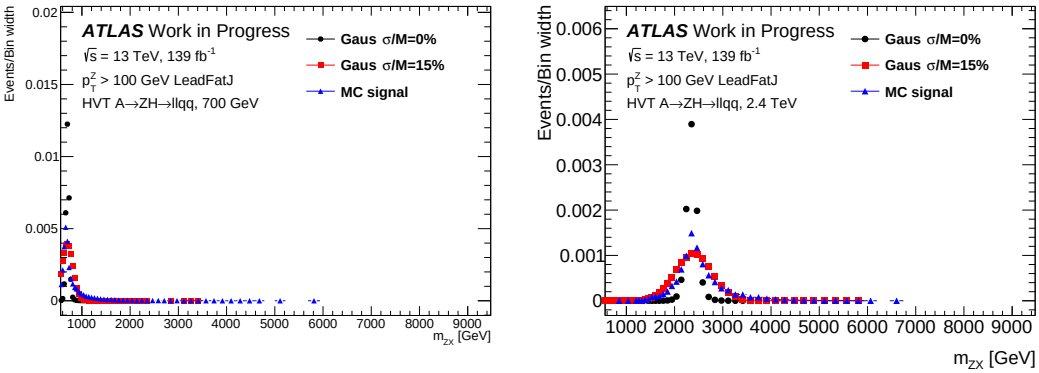

(a) $m_A = 700$ GeV, LeadFatJ (b) $m_A = 2.4$ TeV, LeadFatJ

Figure 8.7: The distributions of m_{ZX} in the LeadFatJ category for HVT signal $Z' \to ZH \to \ell\ell qq$ with two different mass points: 700 GeV, and 2.4 TeV, comparing to Gaussian-shaped signals with the same mass points and relative width values of 0% and 15%.

8.2 Comparison between data and MC

The observable distributions of the SM predictions of the two Z boson decay modes in the SR are compared in shape in Figure 8.8 for the LeadJ category. In the ee channel, a small contribution of merged-ee events is included. The inclusion of the merged-ee events increases the SM background event yields at the high mass m_X and m_{ZX} tails by less than about 2.5% and 15%, respectively, as shown in Figure 6.11. The most significant impact of the inclusion of the merged-ee events is on the increased sensitivity to potential heavy resonances with mass values beyond 1 TeV in the leading large-R jet category, as shown in Figure 6.10. For all mass spectra, the two Z boson decay modes are combined in the following search due to their similar event yields and shape. The combination also helps to gain statistics, especially for the three low statistics categories.

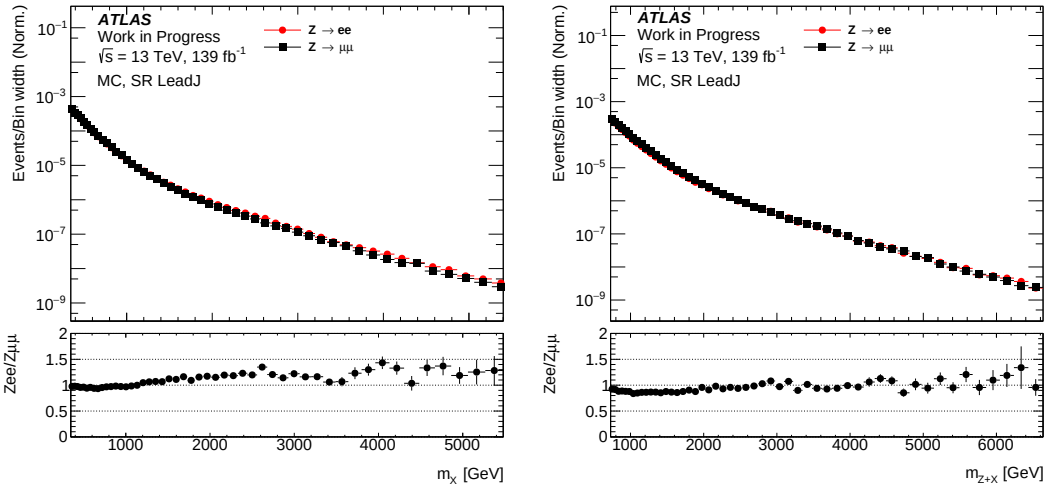

Figure 8.8: Shape comparison between $Z \to e^+e^-$ and $Z \to \mu^+\mu^-$ decay channels on m_X (left) and m_{ZX} (right) in the leading small-R-jet (LeadJ) in the SR.

Before the data are unblinded, an independent event sample with a lower p_{T}^{Z} threshold of 50 GeV with one of the leptons passing a looser lepton identification selection but failing the nominal one is defined temporarily as the *Control Region (CR)*. The definitions of the SR and CR are summarised in Table 8.3. However, the usefulness of the CR is limited as it has an order of magnitude fewer events than the SR does, given the high efficiency of the lepton identification criteria. The components of the SM background contributions are similar to the SR's with a slightly increased fraction of fake lepton backgrounds. A comparison of observable distributions in shape is made. It is observed to be comparable between the CR and the SR. The CR is not used to *control* modelling of any specific background process. It is used to perform basic checks between data and the expected SM background contributions. The comparison are made, for instance, for various kinematic distributions of the leading objects; for the correlation between the Z boson and its recoil system; and for the two observables. One example for the leading small-R-jet category is

shown here in Figures 8.9-8.10. A significant difference in shape between data and the SM predictions is observed in Figures 8.10-8.15. Likely, such a difference is also there in the SR. Therefore, it is clear that the MC based predictions cannot be directly used to provide a reliable estimation of the SM background contribution. Instead, a data-driven estimate of the SM background is performed using the data mass spectra directly, following e.g., Refs. [119, 120]. The choice of functional forms and mass ranges to be used for data is nevertheless determined first using the MC-based SM predictions in the SR.

Table 8.3: The definitions of the signal regions and control regions.

Event Selections	
Signal Region (SR)	Control Region (CR)
Trigger selections and matching	
$N_{e^+e^-} \geq 1$ or $N_{\mu^+\mu^-} \geq 1$	
Select Z candidate, closest to PDG mass	
Both leptons pass **full** signal selections	One lepton **passes** and the other **fails** Medium(LLH) selection
$66 < m_{\ell\ell} < 116$ GeV	
$p_{\mathrm{T}}^{\ell\ell} > \mathbf{100}$ GeV	$p_{\mathrm{T}}^{\ell\ell} > \mathbf{50}$ GeV

The SM predictions of the observables for the leading small-R-jet category in the SR are shown in Figure 8.16. The dominant background contribution is from the Z+jets process for this category. The contribution of the other processes, which all have similar shapes, is at least one order of magnitude smaller. These distributions provide the inputs for the background modelling study in the next section.

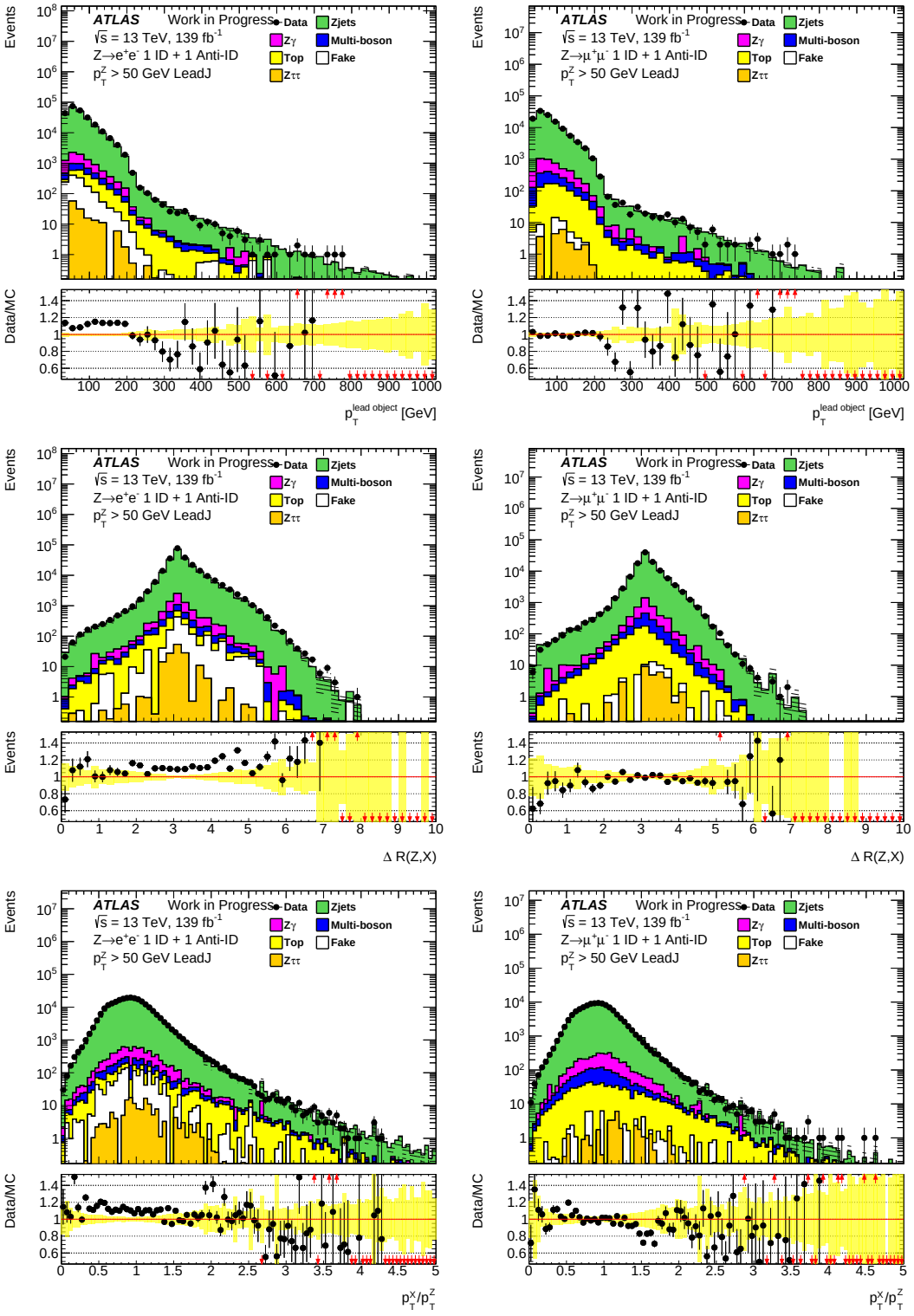

Figure 8.9: Comparison of the transverse momentum of the leading p_{T} small-R jet (upper), the difference in ΔR (middle), the balance of the transverse momenta (bottom) between the Z boson and its recoil system in the **leading small-R-jet category** between data (solid points) and MC predictions (stacked histograms) in the $Z \to e^+e^-$ (left) and $Z \to \mu^+\mu^-$ (right) decay channels in the CR.

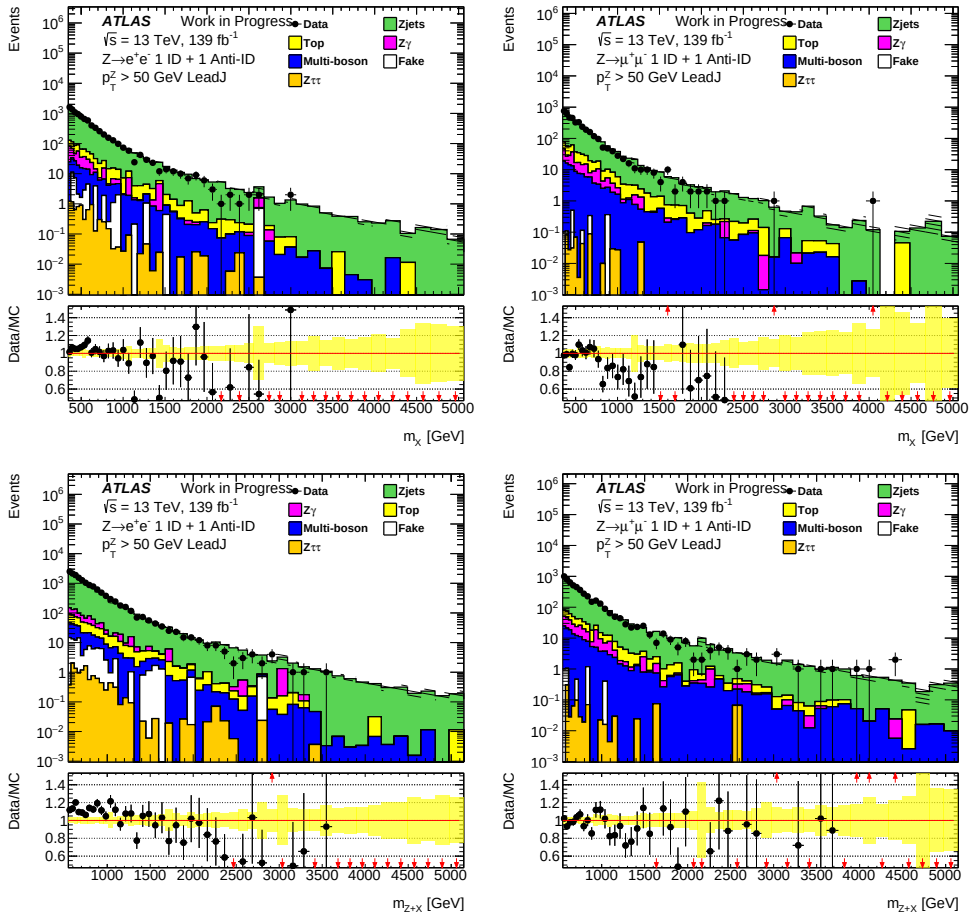

Figure 8.10: Comparison of the m_X (upper) and m_{ZX} (lower) distributions in the leading small-R-jet category between data (solid points) and SM predictions (stacked histograms) in the $Z \to e^+e^-$ (left) and $Z \to \mu^+\mu^-$ (right) decay channels in the CR.

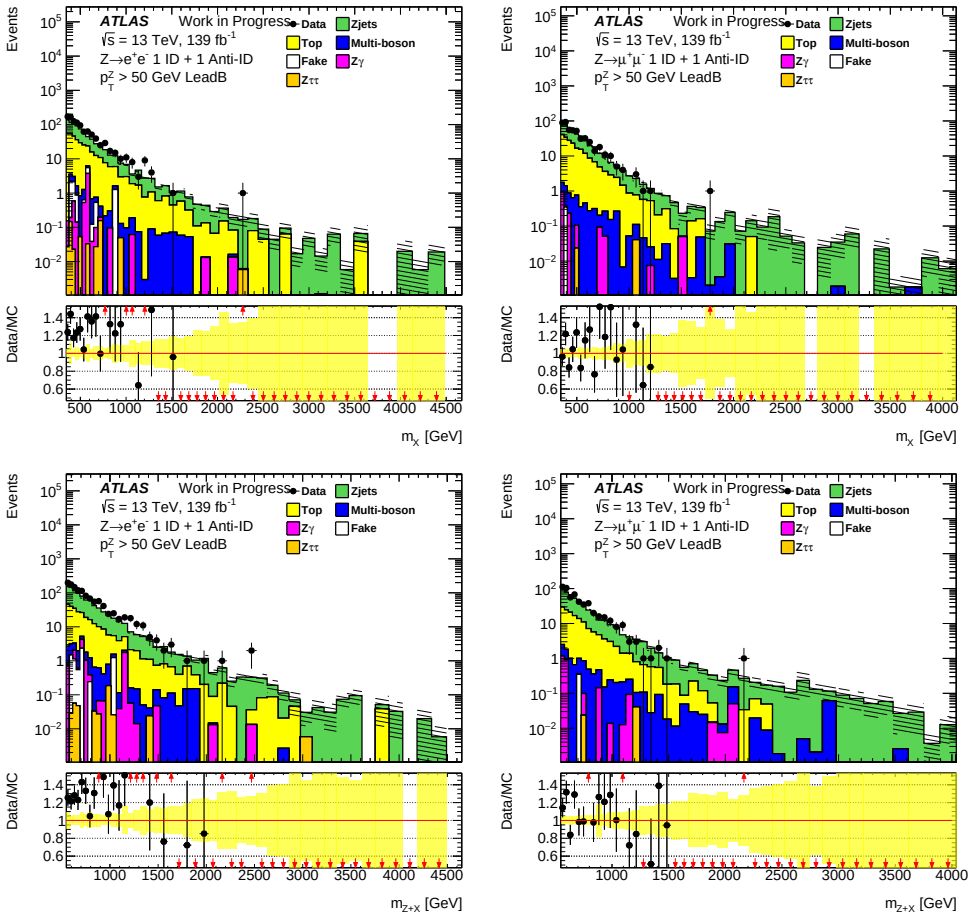

Figure 8.11: Comparison of the m_X (upper) and m_{ZX} (lower) distributions in the leading b-tagged-jet category between data (solid points) and SM predictions (stacked histograms) in the $Z \to e^+e^-$ (left) and $Z \to \mu^+\mu^-$ (right) decay channels in the CR.

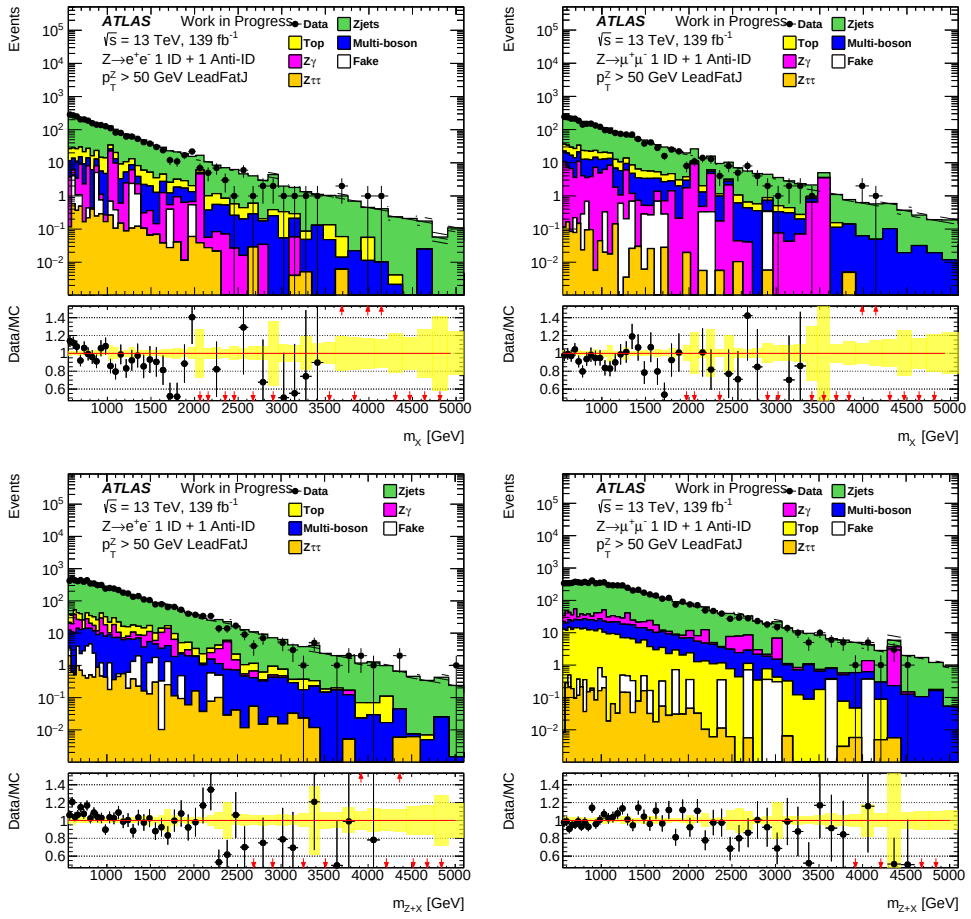

Figure 8.12: Comparison of the m_X (upper) and m_{ZX} (lower) distributions in the leading large-R-jet category between data (solid points) and SM predictions (stacked histograms) in the $Z \to e^+e^-$ (left) and $Z \to \mu^+\mu^-$ (right) decay channels in the CR.

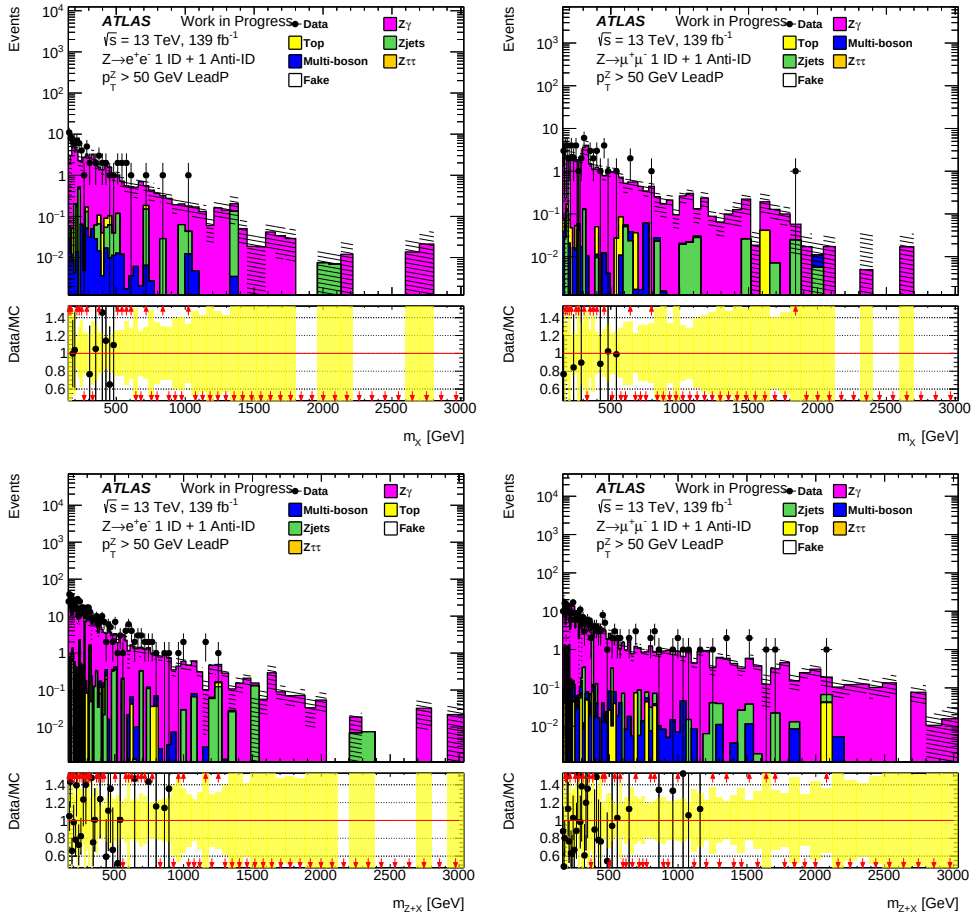

Figure 8.13: Comparison of the m_X (upper) and m_{ZX} (lower) distributions in the leading photon category between data (solid points) and SM predictions (stacked histograms) in the $Z \to e^+e^-$ (left) and $Z \to \mu^+\mu^-$ (right) decay channels in the CR.

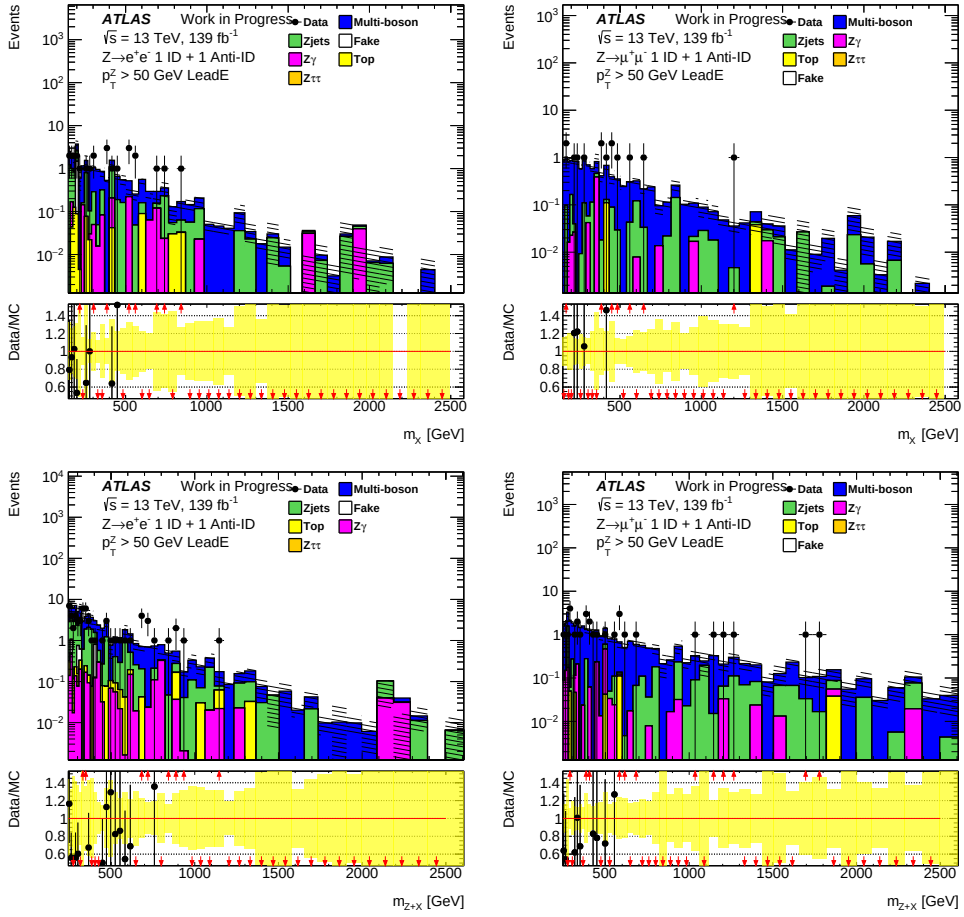

Figure 8.14: Comparison of the m_X (upper) and m_{ZX} (lower) distributions in the leading electron category between data (solid points) and SM predictions (stacked histograms) in the $Z \to e^+e^-$ (left) and $Z \to \mu^+\mu^-$ (right) decay channels in the CR.

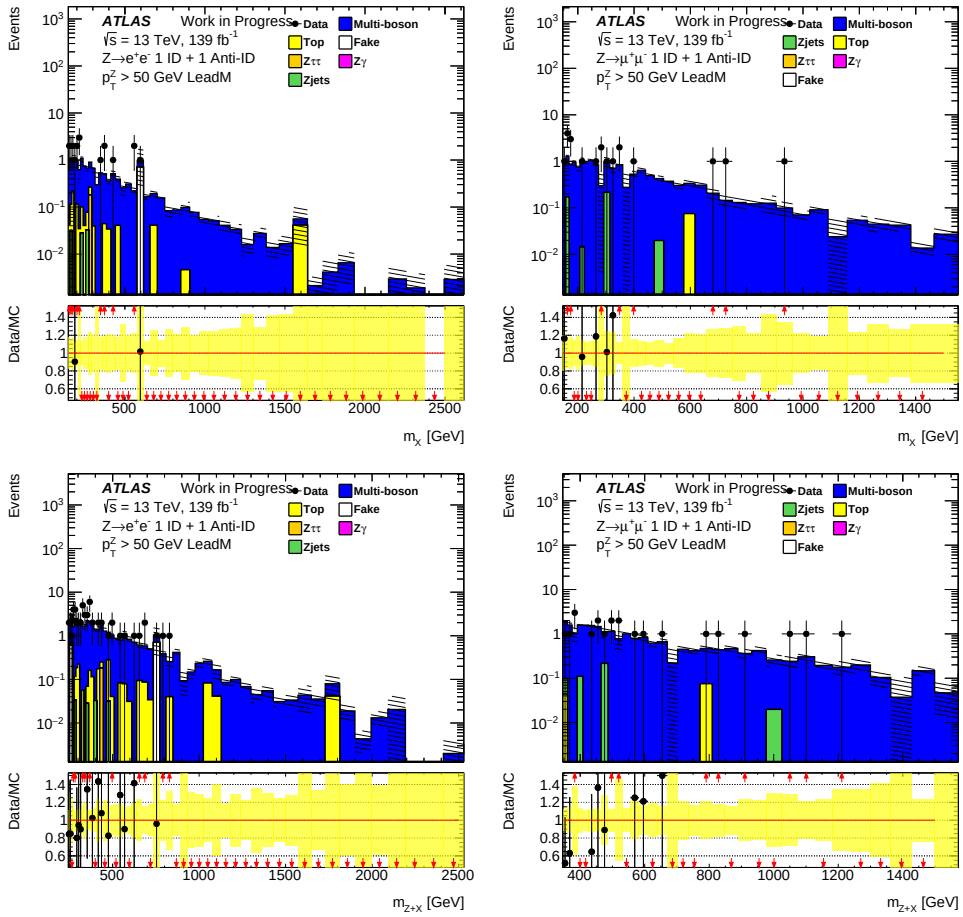

Figure 8.15: Comparison of the m_X (upper) and m_{ZX} (lower) distributions in the leading muon category between data (solid points) and SM predictions (stacked histograms) in the $Z \to e^+e^-$ (left) and $Z \to \mu^+\mu^-$ (right) decay channels in the CR.

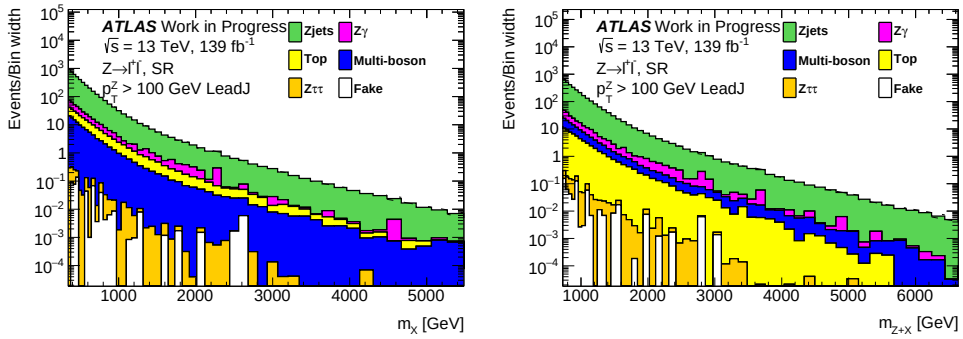

Figure 8.16: Stacked histograms of the m_X (left) and m_{ZX} (right) distributions in the leading small-R-jet category from SM predictions after smoothing in the $Z \to \ell^+\ell^-$ decay channel in the SR.

8.3 Data-driven method

In physics analyses, the signal and background components can be separated by using the different shapes of a discriminating observable. Backgrounds are often modelled by a smooth description of the distributions, directly taken from data. This data-driven method, smooth background modelling, is adequate for the case of searching for narrow signal peaks over wide ranges of the SM backgrounds. A fit is performed to the data using a model built from the probability distribution functions of the observables for each category. In order to ensure that the modelling is reliable, the selected model must accurately reproduce the distributions in practice.

8.3.1 Global function fit technique

In this analysis, the global function fit method is employed on distributions of observables ($\mathcal{O}$) to search for local excesses. This technique represents the SM background shape described as a simple function $f(\mathcal{O})$ of the observable, expressed by mathematical functions. The commonly used function forms are:

- **Exponential**:
$$f_1(x) = p_0 \left(e^{-p_1 x} + p_2 e^{-(p_1+p_3)x} + \cdots \right), \tag{8.5}$$
- **Dijet function**:
$$f_2(x) = p_0 (1-x)^{p_1} x^{p_2 + p_3 \ln x + p_4 (\ln x)^2 + \cdots}, \tag{8.6}$$

where $x = (\mathcal{O} - \mathcal{O}_{\text{min}})/(\mathcal{O}_{\text{max}} - \mathcal{O}_{\text{min}})$ in exponential functions, Eq. (8.5), and $x = \mathcal{O}/\sqrt{s}$ in dijet functions, Eq. (8.6), p_0 is a normalisation factor and p_i with $i = 1, \cdots$ are free parameters controlling the shape of the $\mathcal{O}$ distribution, and $\mathcal{O}_{\text{min}}$ and $\mathcal{O}_{\text{max}}$ are the lower and upper fit range of the observable.

Similar functional forms have been used in many previous analyses, see e.g. Refs. [120–125]. An important parameter is the observable range. A wider range can provide more information on the background shape and higher sensitivity. The large side-bands on either side of the signal peak guarantee the reliable interpolation of the background under the peak. The number of free parameters also depends on the ranges of observables in each event category. Mass spectra covering a larger mass range with higher statistics usually need more parameters than those covering a smaller mass range with lower statistics. A global χ^2 p-value is calculated to represent the agreement between observable spectra and fit results using the χ^2 value and number of degrees of freedom (NDF). The global χ^2 p-value is required to be larger than 0.05. The choice of the functional form and the number of free parameters, and the fitted mass range is based on the consideration of the spurious signal yields to be discussed in Section 8.3.3. In addition, the choice of the fitted mass range also considers that the lower limit is beyond the "turn-on" region, and the highest mass bin should have sufficient event statistics, where the yield is larger than 1.

The MC-based spectra in the SRs, as shown in Figure 8.16, are normalised to the integrated luminosity of data, and the square root of each bin content is taken into consideration as the statistical uncertainty of the mass spectra. The results of the fit to these

mass spectra in the six categories and the combined category are shown in Figures 8.17–8.19, and also in Table 8.4. In all the cases, the global χ^2 p-values are at 1, well above the required value of 0.05. It may be understood since the MC-based mass spectra are too smooth concerning the used data-like uncertainties in the fits. Indeed, when similar fits are performed using the same functional forms to the mass spectra in the control regions in data, the global χ^2 p-values do not show this feature.

Table 8.4: List of number of free parameters for different observables and event categories. Note that the fit range shown in the brackets in the first column has been rounded from their original bin edge values.

Spectrum (fit range [GeV])	Category	Function	$N_{parameters}$	χ^2 p-value
m_X [350, 5700]	LeadJ	$f_1(x)$	5	1.000
m_X [350, 3340]	LeadB	$f_1(x)$	5	1.000
m_X [630, 6085]	LeadFatJ	$f_2(x)$	3	1.000
m_X [150, 1800]	LeadP	$f_1(x)$	3	1.000
m_X [150, 1515]	LeadE	$f_1(x)$	3	1.000
m_X [150, 1230]	LeadM	$f_1(x)$	3	1.000
m_X [550, 6450]	Combined	$f_2(x)$	5	1.000
m_{ZX} [730, 6435]	LeadJ	$f_1(x)$	5	1.000
m_{ZX} [580, 4185]	LeadB	$f_1(x)$	5	1.000
m_{ZX} [650, 7095]	LeadFatJ	$f_2(x)$	3	1.000
m_{ZX} [280, 2485]	LeadP	$f_1(x)$	3	1.000
m_{ZX} [325, 2185]	LeadE	$f_1(x)$	3	1.000
m_{ZX} [290, 1900]	LeadM	$f_2(x)$	3	1.000
m_{ZX} [650, 7860]	Combined	$f_1(x)$	5	1.000

8.3.2 Folding procedure of Gaussian-shaped signals

The generic Gaussian-shaped signals used in this analysis are constructed with two floating parameters: the signal mass value (mean) and signal width (variance). A folding procedure is applied on the intrinsic Gaussian-shaped signals to take the detector resolutions into account and keep the signal consistent with the background components. The truth-level signals are folded by migration matrices, which are derived from the 2-dimensional truth-reconstruction mass plots using the dominant process in a given category as shown in Figures 8.4. The migration matrix is calculated following

$$A_{ij}^{\text{mathced}} = \frac{N_{ij}^{\text{matched}}}{\sum_k N_{ik}^{\text{matchted}}}, \tag{8.7}$$

where N_{ij}^{matched} is the matched event yield in the ith truth bin and jth reconstruction one. After the folding procedure, the signal shape is still Gaussian-like with the mass values essentially unchanged but the width values increased, especially for cases with a small

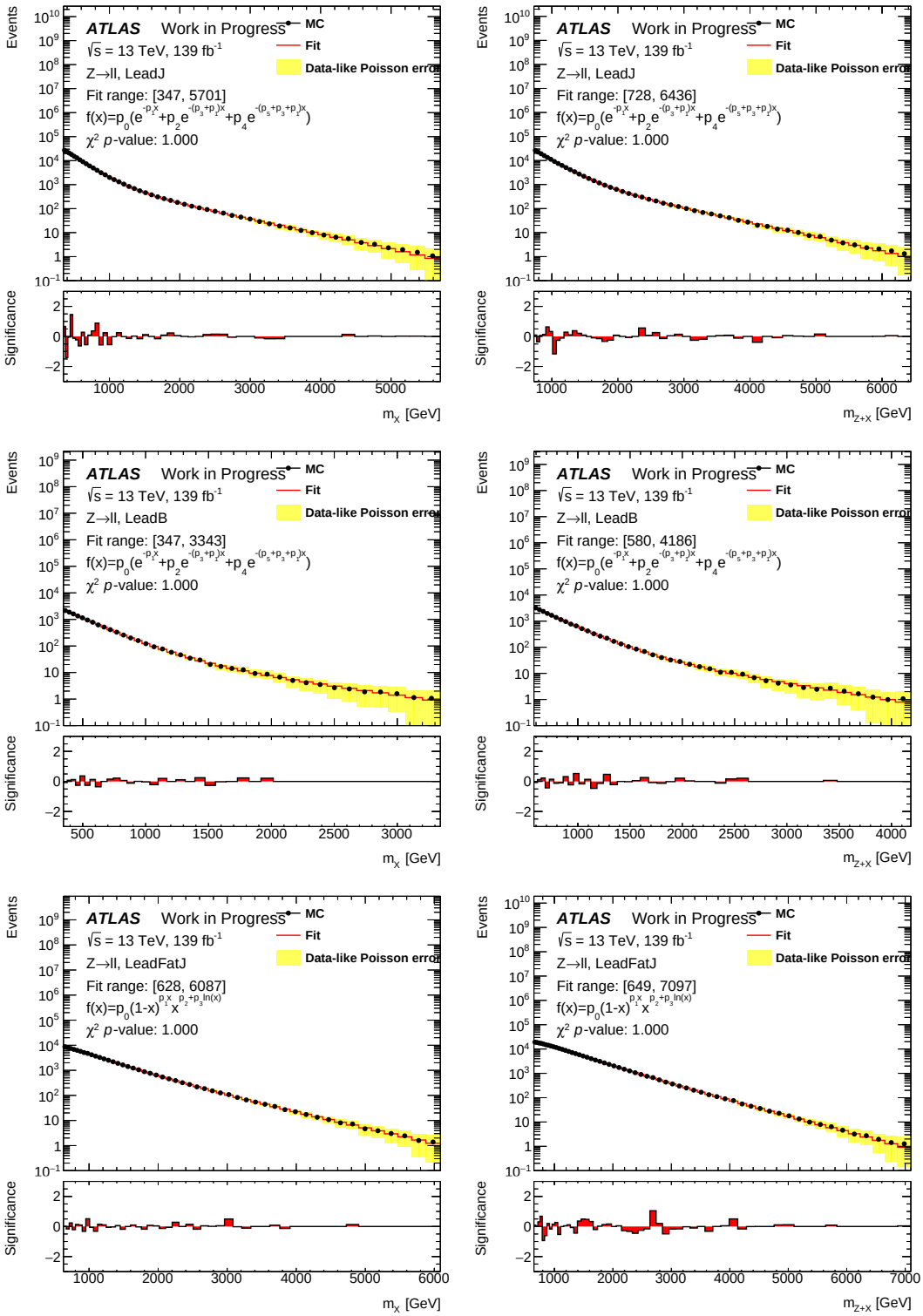

Figure 8.17: Global fitting results on m_X (left) and m_{ZX} (right) in the SRs of the leading small-R-jet (LeadJ) (top), leading b-jet (LeadB) (middle) and leading large-R-jet (LeadFatJ) (bottom) categories in the combined $Z \to \ell^+\ell^-$ decay channels.

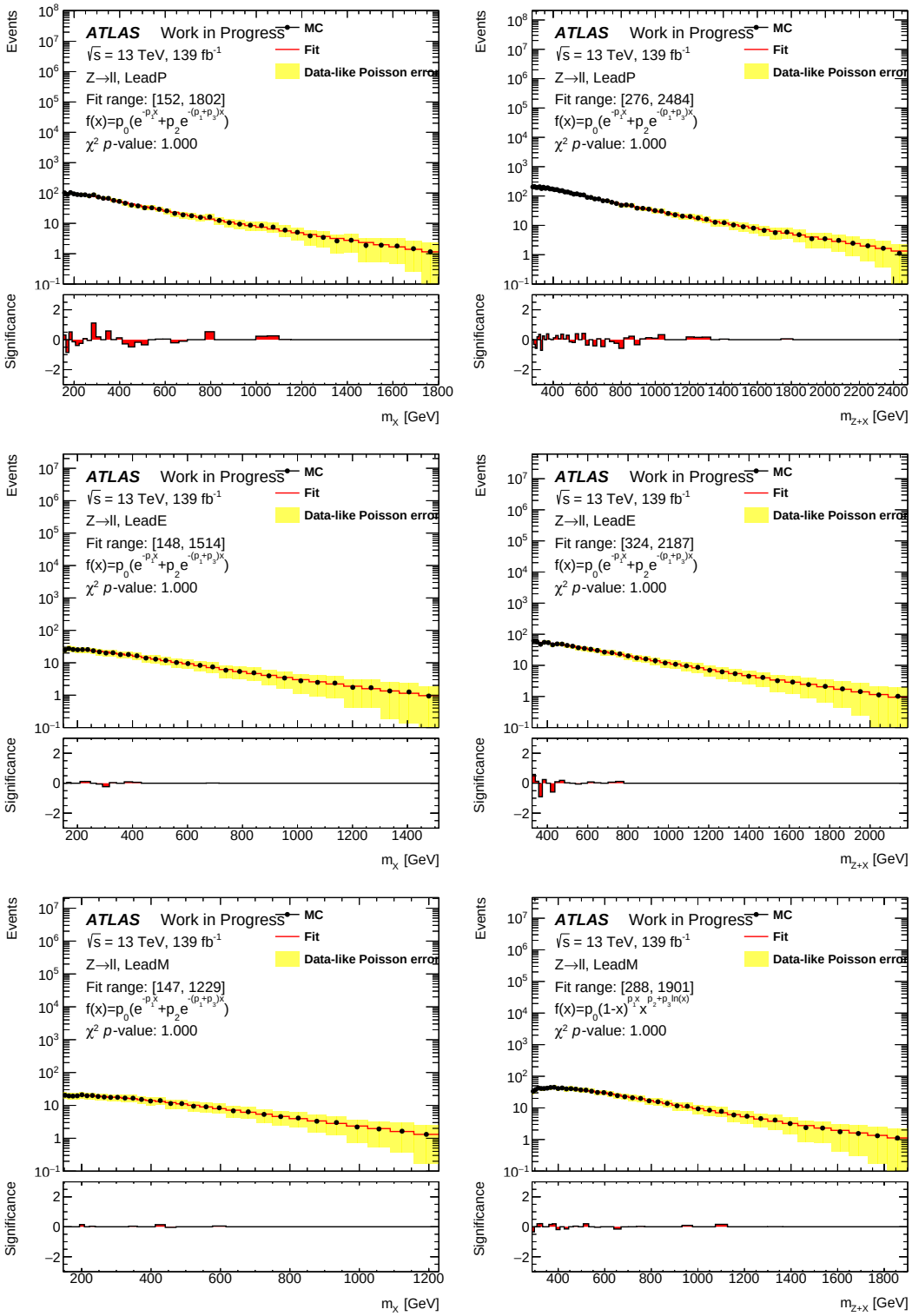

Figure 8.18: Global fitting results on m_X (left) and m_{ZX} (right) in the SRs of the leading photon (LeadP) (top), leading electron (LeadE) (middle) and leading muon (LeadM) (bottom) categories in the combined $Z \to \ell^+\ell^-$ decay channels.

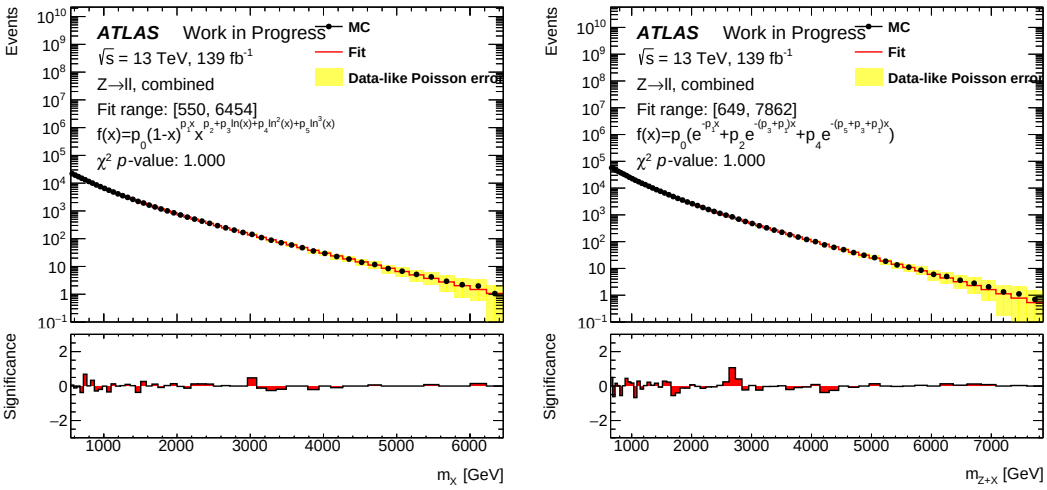

Figure 8.19: Global fitting results on m_X (left) and m_{ZX} (right) in the SR of the combined category in the combined $Z \to \ell^+\ell^-$ decay channels.

width. An example for the Gaussian-shaped signal with 10%[2] width value is shown in Figure 8.20 for m_X spectra in the leading small-R-jet category.

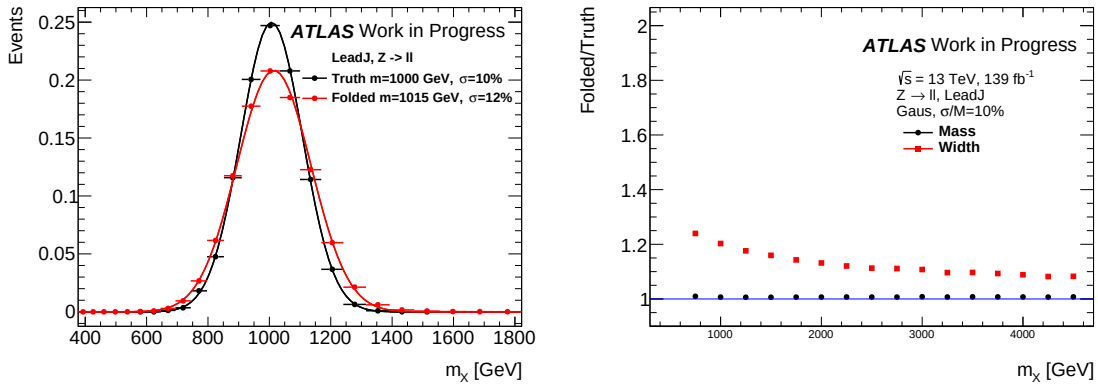

Figure 8.20: (Left) Comparison between truth and folded m_X distribution at 1 TeV with 10% width. (Right) Comparison of Gaussian parameters (mean, width) between truth and folded m_X distributions at different mass points for the leading small-R-jet category in the $Z \to \ell^+\ell^-$ decay channel.

8.3.3 Spurious signal test

The choice of functional forms and mass ranges is more challenging in terms of the model bias or spurious signal, which is evaluated by fitting the MC-based mass spectrum with a functional form modelling the expected smoothly falling SM background contribu-

[2]This number is a relative with value, calculated by the real width over signal mass.

tion plus a signal, using a Gaussian-shaped one with relative widths varying between 3% and 10% in this analysis. The detector resolution effect on the Gaussian-shaped signals is taken into account by convolution with the intrinsic width in a folding procedure, which widens the width in particular for signals with small intrinsic width values. In general, the functional form should be flexible enough to reduce the bias in signal extraction. However, excessive flexibility could lead to the background model being able to absorb part of the signal, thus reducing signal sensitivity.

The high edge of the mass range is determined by requiring at least one event in the last bin. A scanning procedure is applied to determine the combinations of low mass edge and function form. The low mass edge begins with a value that is four bins away from the peak of the SM background distribution. The function forms initially have 4 free parameters and stop at 8 and 6 for exponential functions (Eq. 8.5) and dijet functions (Eq 8.6), respectively. The final choices are determined with the smallest spurious signal yields and the least fluctuated ratio of the spurious signal yields over corresponding fitting uncertainties.

Figures 8.21–8.23 [3] show the ratio of the extracted spurious signal yields for an example Gaussian-shaped signal with a relative width of 10% over the corresponding fitted uncertainties for the m_X and m_{ZX} spectra in the SR of the six event categories as well as of the combined one, using the nominal functional forms shown in Table 8.4 in comparison with a function of the same family with more or fewer number of free parameters and with an alternative functional form.

A similar study for Gaussian-shaped signals with different width values is also performed. The corresponding results are shown in Figures 8.24–8.26. The vertical error bars are defined as $\sigma_{\text{fit}}^{\text{template}}/\sigma_{\text{fit}}$ with $\sigma_{\text{fit}}^{\text{template}}$ corresponding to the fitted uncertainty of the spurious signal when using the MC statistical uncertainty of the spectrum (namely with the SumW2Error(True) option accounting for the individual weights of the MC events) while σ_{fit} corresponding to the fitted uncertainty of the spurious signal when using the Poisson error of the spectrum, following the notations used in Ref. [126]. The size of the vertical error bar reflects thus the available statistics of the MC samples; the larger the error bar, the more limited statistics of the template samples. For most mass points, the spurious signal significance when using the nominal functional form remains smaller than 20-50% within the uncertainty. Those beyond the limits can be correlated to large fluctuations in the MC mass spectra seen in Figures 8.17–8.19.

[3] Please note that the mass range shown in the figures is narrower than the fit range because, for any Gaussian-shaped signal, it is required that its mass value is within the fit range by at least 2σ based on the folded mass and width values.

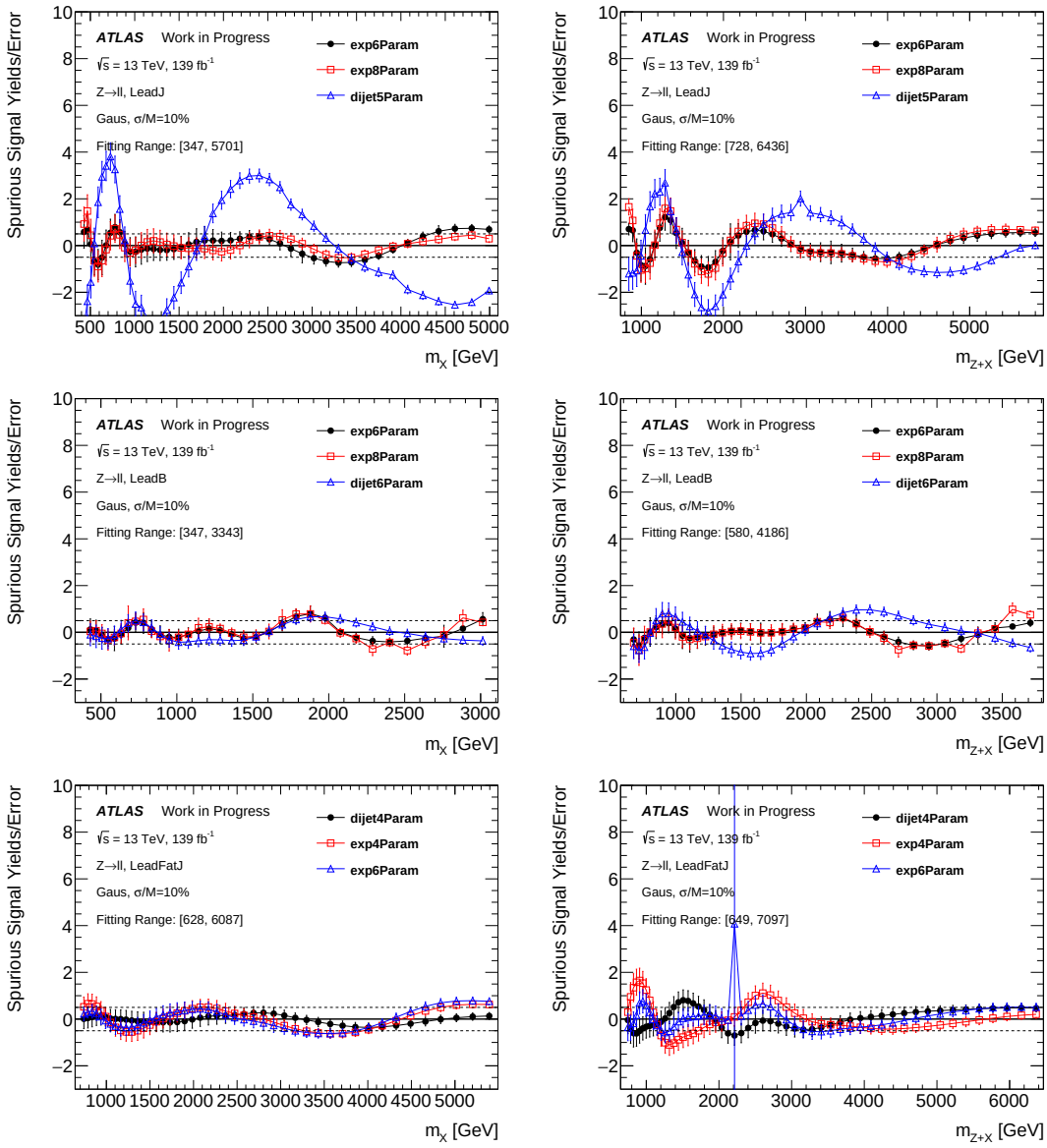

Figure 8.21: Spurious signal yield over the fitted uncertainty for a Gaussian-shaped signal with a width value of 10% as a function of m_X (left) and m_{ZX} (right) in the SRs of the leading small-R-jet (LeadJ) (top), leading b-jet (LeadB) (middle) and leading large-R-jet (LeadFatJ) categories for the combined $Z \to \ell^+\ell^-$ decay channel. See the main text for the meaning of the vertical error bars. The solid black dots represents the final selected function forms, comparing to the results of two alternative function forms shown by open red squares and open blue triangles.

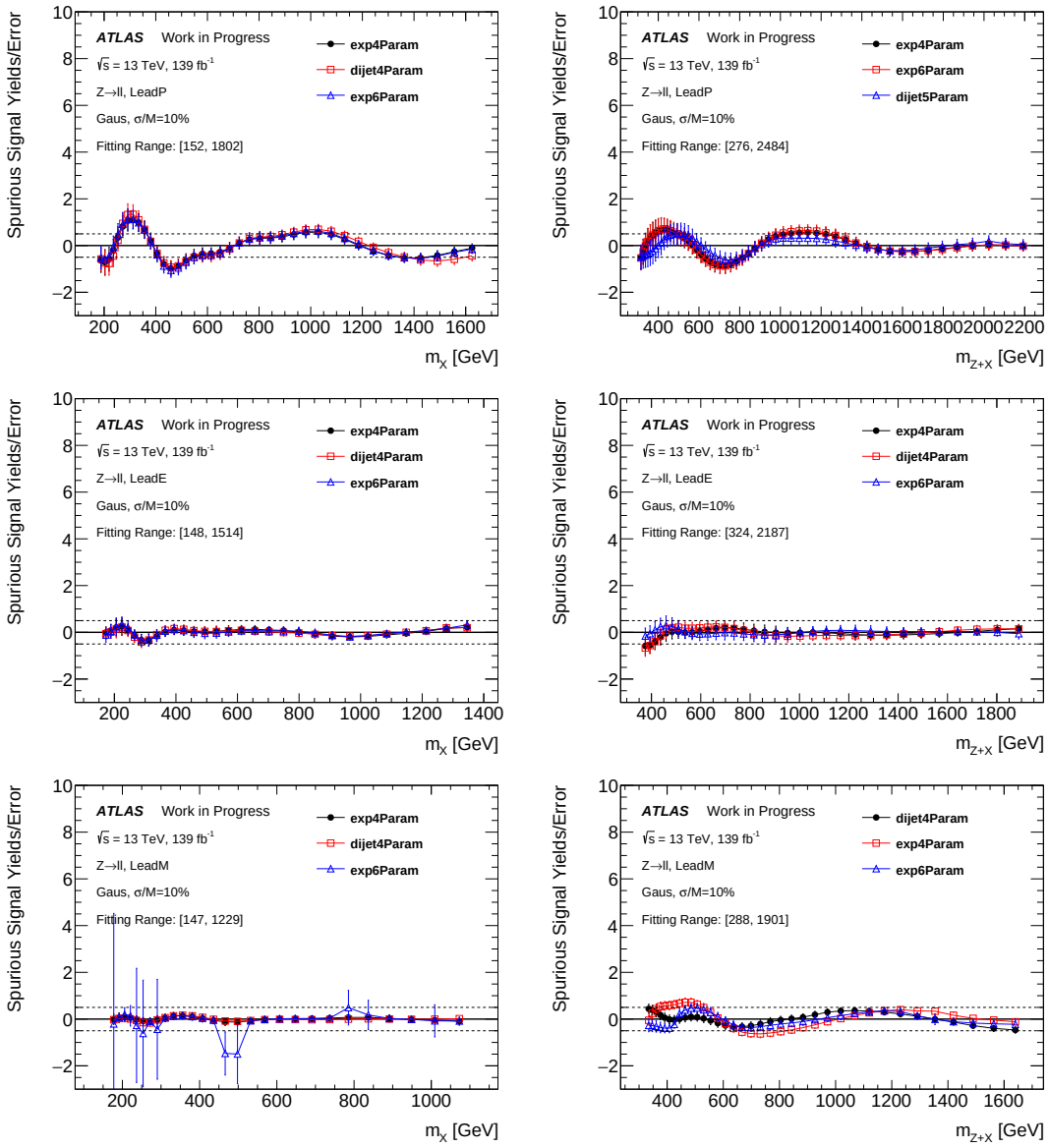

Figure 8.22: Spurious signal yield over the fitted uncertainty for a Gaussian-shaped signal with a width value of 10% as a function of m_X (left) and m_{ZX} (right) in the SRs of the leading photon (LeadP) (top), leading electron (LeadE) (middle) and leading muon (LeadM) (bottom) categories for the combined $Z \to \ell^+\ell^-$ decay channel. See the main text for the meaning of the vertical error bars.The solid black dots represents the final selected function forms, comparing to the results of two alternative function forms shown by open red squares and open blue triangles.

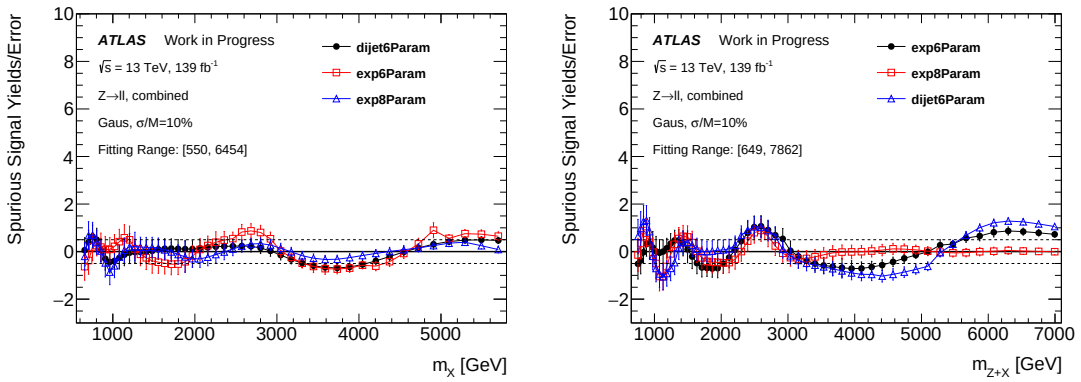

Figure 8.23: Spurious signal yield over the fitted uncertainty for a Gaussian-shaped signal with a width value of 10% as a function of m_X (left) and m_{ZX} (right) in the SR of the combined category for the combined $Z \to \ell^+\ell^-$ decay channel. See the main text for the meaning of the vertical error bars. The solid black dots represents the final selected function forms, comparing to the results of two alternative function forms shown by open red squares and open blue triangles.

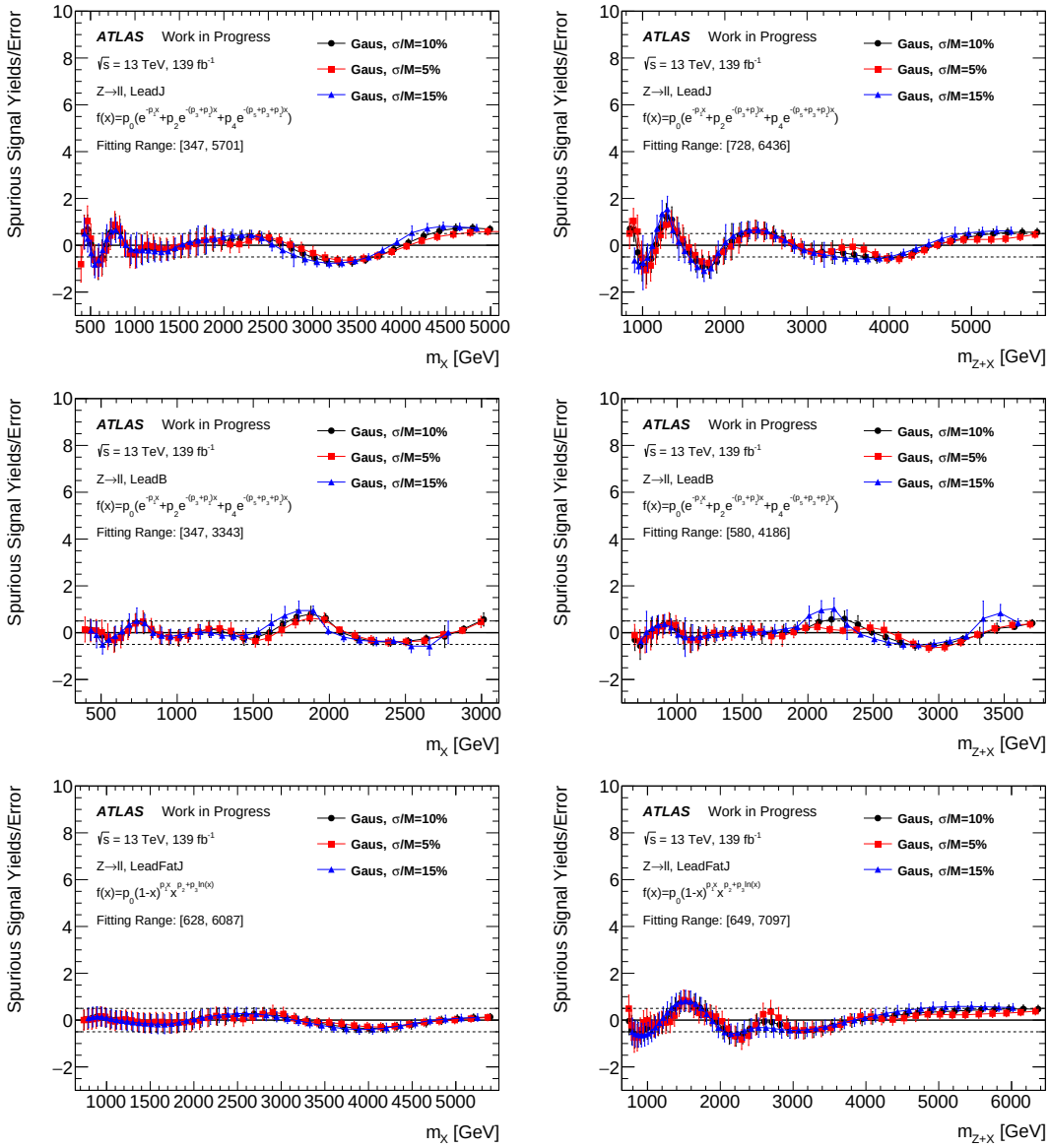

Figure 8.24: Spurious signal yield over the fitted uncertainty for Gaussian-shaped signals with width values of 5% (red squares), 10% (black dots) and 15% (blue triangles) as a function of m_X (left) and m_{ZX} (right) in the SRs of the leading small-R-jet (LeadJ) (top), leading b-jet (LeadB) (middle) and leading large-R-jet (LeadFatJ) categories for the combined $Z \to \ell^+\ell^-$ decay channel. See the main text for the meaning of the vertical error bars.

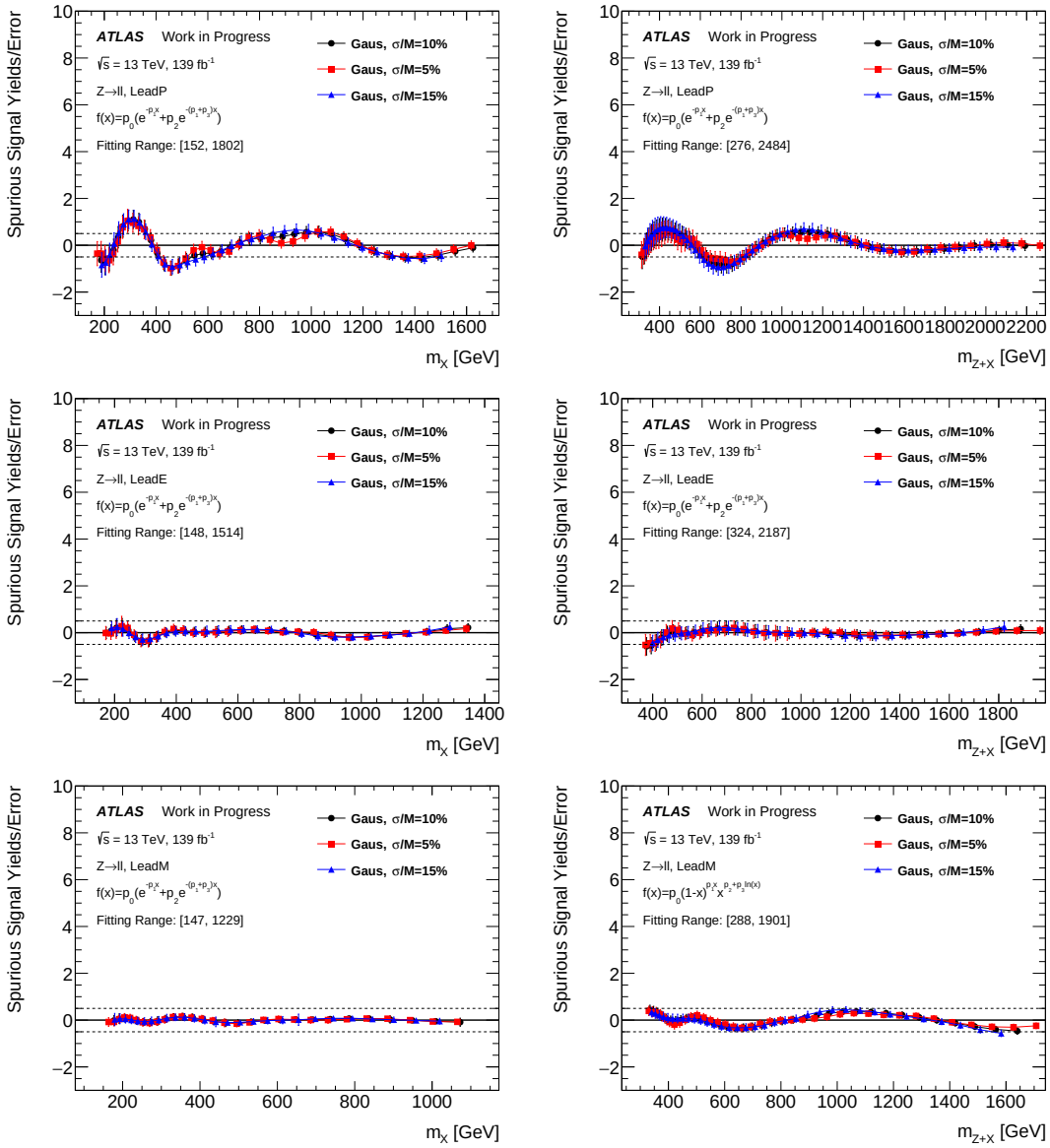

Figure 8.25: Spurious signal yield over the fitted uncertainty for Gaussian-shaped signals with width values of 5% (red squares), 10% (black dots) and 15% (blue triangles) as a function of m_X (left) and m_{ZX} (right) in the SRs of the leading photon (LeadP) (top), leading electron (LeadE) (middle) and leading muon (LeadM) (bottom) categories for the combined $Z \to \ell^+\ell^-$ decay channel. See the main text for the meaning of the vertical error bars.

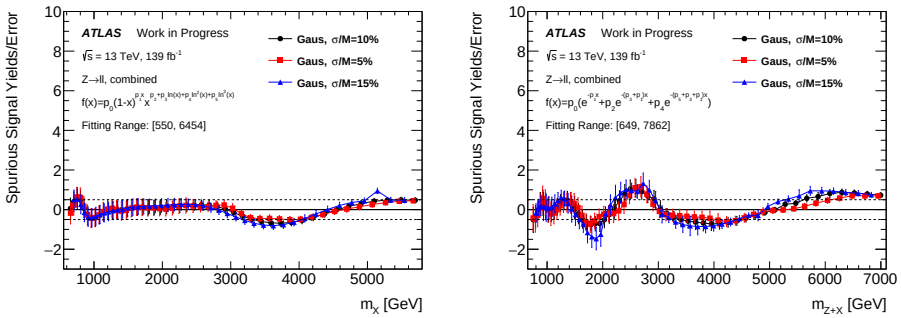

Figure 8.26: Spurious signal yield over the fitted uncertainty for Gaussian-shaped signals with width values of 5% (red squares), 10% (black dots) and 15% (blue triangles) as a function of m_X (left) and m_{ZX} (right) in the SR of the combined category for the combined $Z \to \ell^+\ell^-$ decay channel. See the main text for the meaning of the vertical error bars.

8.3.4 Global fitting results in the CRs of data

Here, the same selected functional form and fit range is also applied to the mass spectra in the control region for data. The results of the fits for the large statistics channels are shown in Figures 8.27 and 8.28 and summarised in Table 8.5. The selected nominal functional forms and fitting range can still model the mass spectra of the data in the CRs.

Table 8.5: Detailed global fit quality results for different parametrisation functions in the categories of LeadJ, LeadB, LeadFatJ and combined categories of **data** spectra in the **control region**

Spectrum (fit range [GeV])	Category	Function	$N_{parameters}$	χ^2 p-value
m_X [347, 2679]	LeadJ	$f_1(x)$	5	0.110
m_X [347, 1315]	LeadB	$f_1(x)$	5	0.147
m_X [628, 3477]	LeadFatJ	$f_2(x)$	3	0.296
m_X [550, 4263]	Combined	$f_1(x)$	5	0.224
m_{ZX} [728, 3350]	LeadJ	$f_1(x)$	5	0.684
m_{ZX} [580, 1676]	LeadB	$f_1(x)$	5	0.744
m_{ZX} [649, 4597]	LeadFatJ	$f_2(x)$	3	0.816
m_{ZX} [649, 4617]	Combined	$f_1(x)$	5	0.318

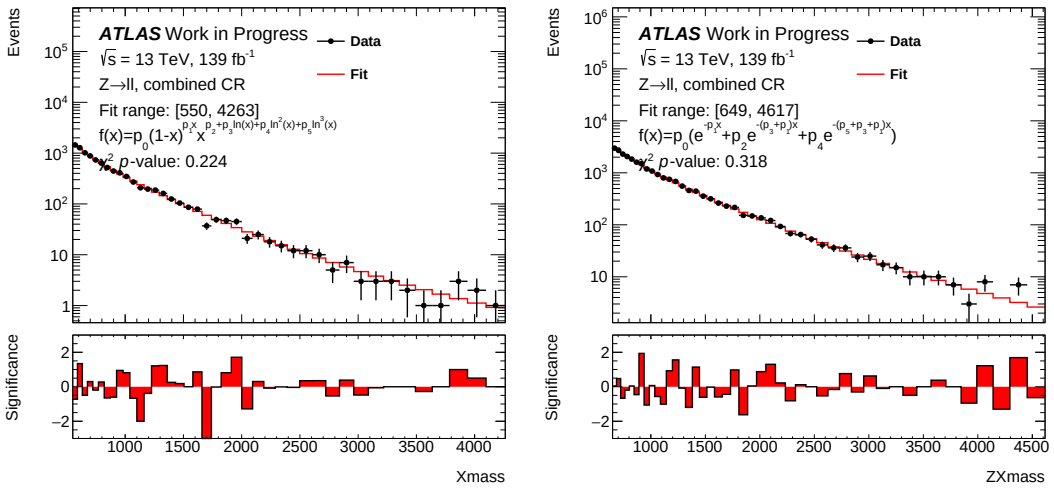

Figure 8.27: Global fitting results on m_X (left) and m_{ZX} (right) in the **CR of data** of in the combined category for the $Z \to \ell^+\ell^-$ decay channels.

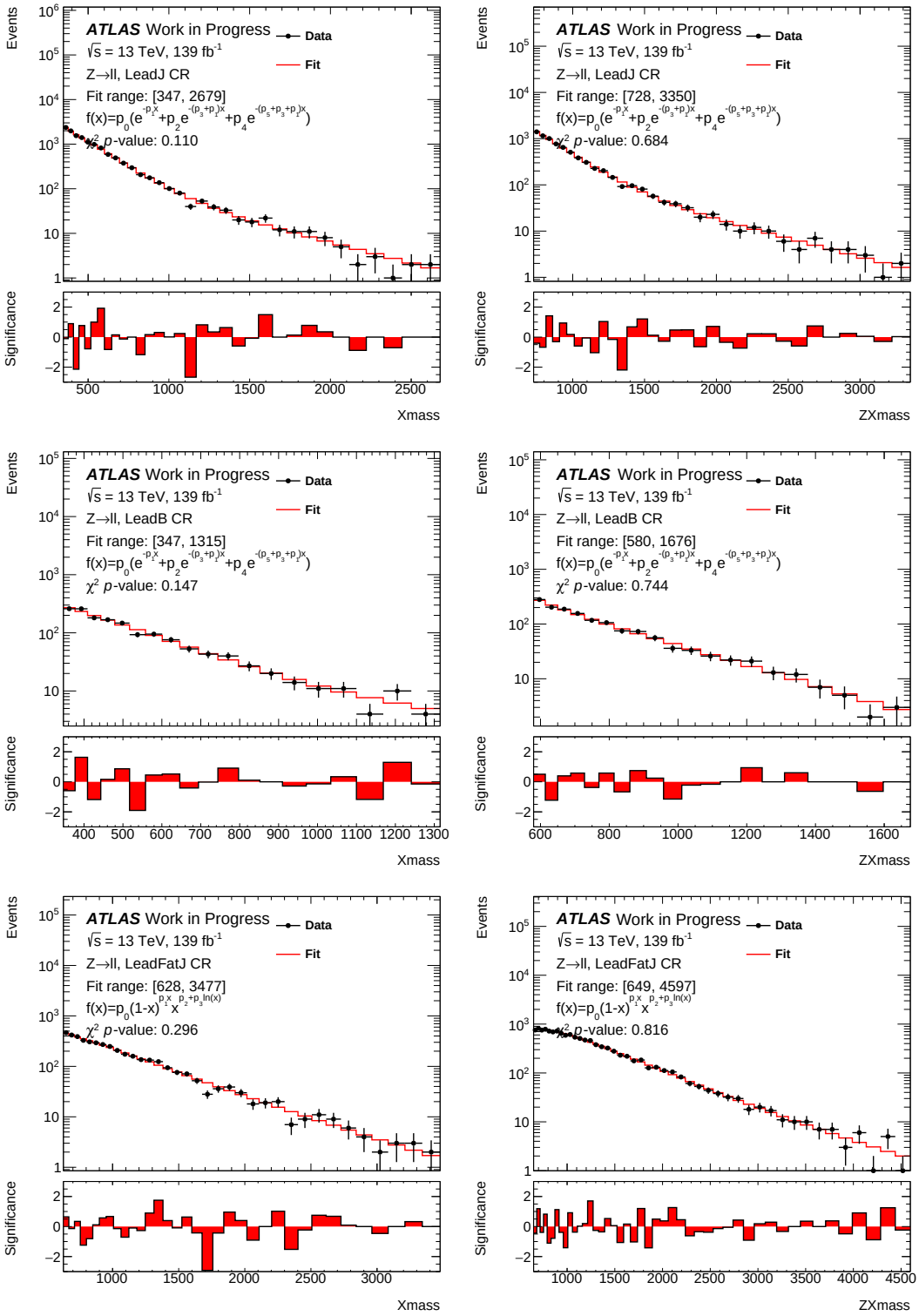

Figure 8.28: Global fitting results on m_X (left) and m_{ZX} (right) in the **CR of data** of the **LeadJ** (top), **LeadB** (middle) and **LeadFatJ** (bottom) categories for the $Z \to \ell^+\ell^-$ decay channels.

8.3.5 Further check on the spurious signal test

In addition to the spurious signal study above, a closure test has also been performed using 500 pseudo-experiments generated for each mass point by fluctuating the fitted background model of given mass spectra. The same procedures as the previous spurious signal test are repeated on each pseudo-experiment. As a function of mass, the average ratio is around 0 with a variance of 1, as shown in Figure 8.29.

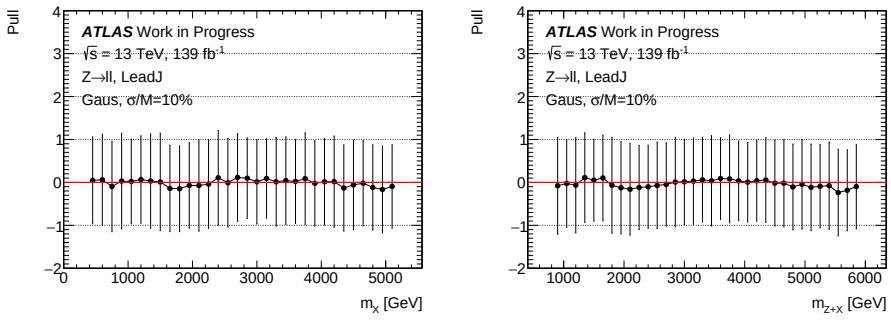

Figure 8.29: The closure test results for each mass point (based on 500 pseudo-experiments) with a relative width of 10% in m_X (left) and m_{ZX} (right) spectrum in **LeadJ** category in the SR of the $Z \to \ell^+\ell^-$ decay channel.

A signal injection test is also performed to evaluate how sensitive the method is to an injected signal. For this test, a signal is injected into the expected background distribution to assess whether or not the procedure can fit the combined distribution and measure the correct signal yield. In this test, an S+B fit is performed on the combined spectra to calculate the ratio of fitted results over the injected one. Examples are shown in Figure 8.30 for Gaussian-shaped signals with three relative width values of 5%, 10%, and 15% at a mass value of 3.6 TeV in the leading small-R-jet category. Linear dependency of the average fitted signal event yields as a function of the injected one is observed.

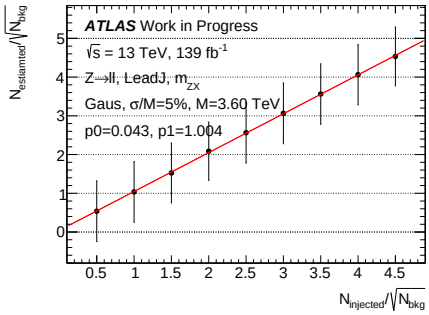

(a) $\sigma/M = 5\%$

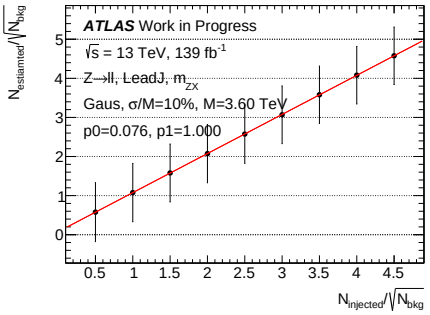

(b) $\sigma/M = 10\%$

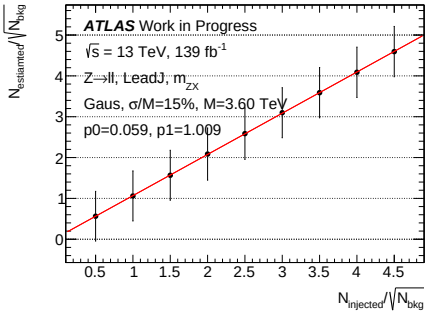

(c) $\sigma/M = 15\%$

Figure 8.30: Correlation between the average of the fitted signal event yields of 500 pseudo-experiments and the injected Gaussian-shaped signal with relative width of 5% (left), 10% (middle) and 15% (right) at 3.6 TeV as a function of injected signal event yield over the square root of the integrated background event yield within 3σ range around the signal from the SR m_{ZX} spectrum of the LeadJ category in the $Z \to \ell\ell$ channel. A linear function fit is performed with resulting slope of around 1.

8.4 Systematics uncertainties

Systematic uncertainties affecting the background estimation have two contributions. The first is associated with the statistical uncertainty raised from the fitting parameters in the fit, which depends on the statistical precision of the input distribution. It is evaluated by generating pseudo-experiments using Poisson statistics based on the fitted background model to the input distribution. Each pseudo-experiment distribution is fitted using the same starting conditions as the nominal one. The error in the fit in each bin is defined as the RMS of the function values in that bin obtained from all pseudo-experiments. The second uncertainty is related to the choice of functional forms. The difference between the nominal choice and an alternative one is used to estimate the uncertainty. The alternative functional form is either the same functional form as the nominal one but with a different number of free parameters or a different functional form. The alternative functional form is selected based on the consideration of low spurious signal yields for the nominal one. The uncertainty is then symmetrised. The results based on MC spectra in SR for LeadJ category are shown in Figures 8.31.

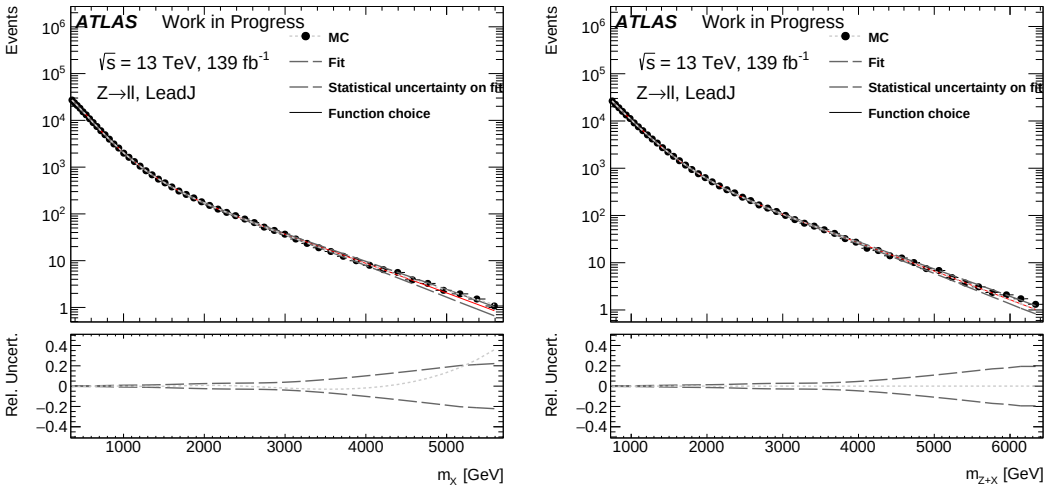

Figure 8.31: Background uncertainties from the fits shown as a function of m_X (left) and m_{ZX} (right) in the SRs of the leading small-R-jet (LeadJ) category for the combined $Z \to \ell^+\ell^-$ decay channel.

An additional modelling uncertainty for the Gaussian-shaped signal is estimated based on the spurious signal test results shown above, following the recommendations in Ref. [126]. This uncertainty is used to consider possible bias in the fits to data. The implementation is to define an envelope of absolute spurious signal yields ($|N_{\text{spurious}}|$) over m_X or m_{ZX}. The envelope is derived by a smooth parametrization passing through the local maxima values of $|N_{\text{spurious}}|$. Figures 8.32 show such an envelope result for a Gaussian-shaped signal with a relative width value of 3%, 5%, and 10% in the leading small-R-jet category. The statistical analysis assigns the modelling systematic uncertainty to signal yields with

the same shape. The total signal yield can be written as:

$$N_{\text{signal}} = \mu_s \sigma_{\text{signal}} \mathcal{L}(\mathcal{A} \times \epsilon) + S_{\text{modelling}} \theta_{\text{modelling}} \tag{8.8}$$

where the first term reflects the expected signal yields taking into account the integrated luminosity value $\mathcal{L}$ and the acceptance and efficiency corrections $\mathcal{A} \times \epsilon$, and the second one considers the modelling uncertainty with $S_{\text{modelling}}$ being the derived envelope value and $\theta_{\text{modelling}}$ a nuisance parameter. An external Gaussian constraint with mean 0 and width 1 is applied on $\theta_{\text{modelling}}$.

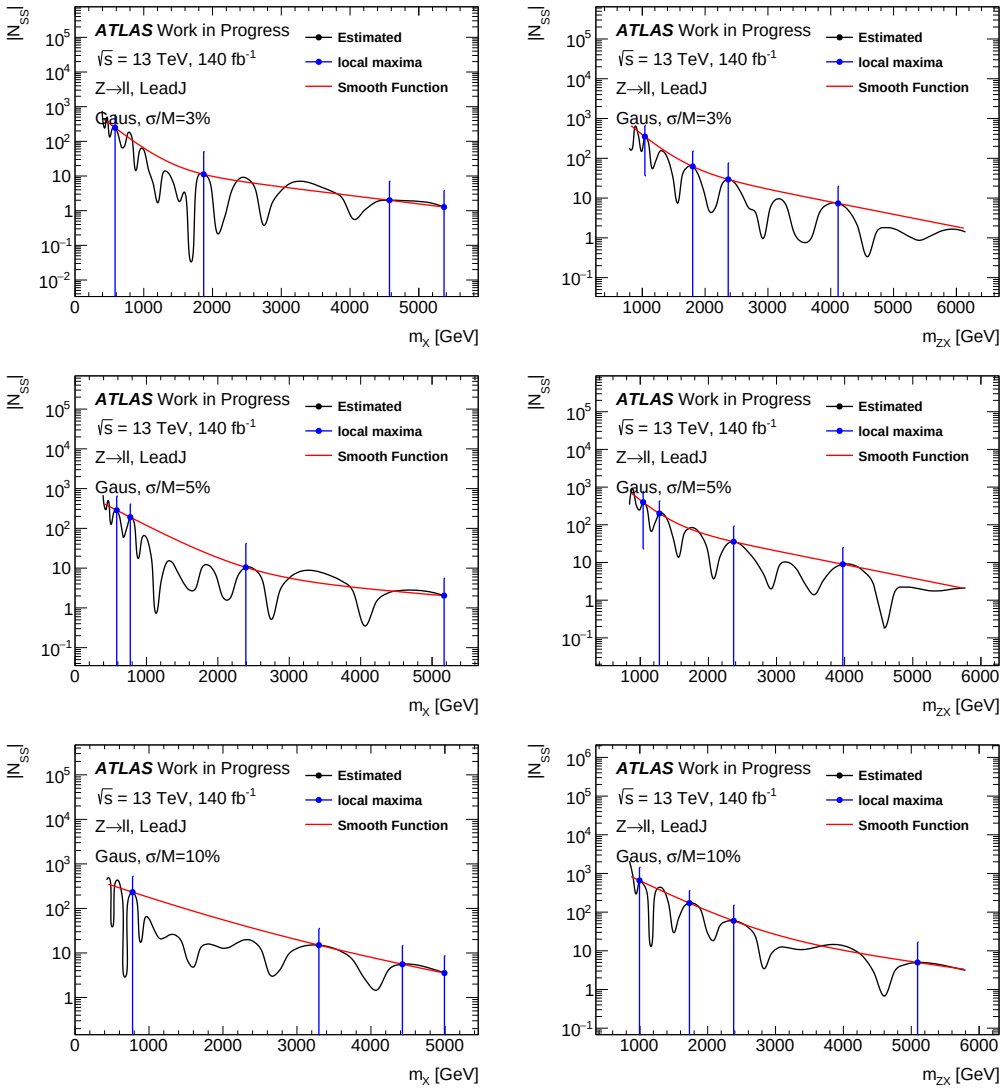

Figure 8.32: Modelling systematic uncertainty for a Gaussian-shaped signal with a relative width value of 3% (top), 5%(middle) and 10% (bottom) as a function of m_X (left) and m_{ZX} (right) in the SRs of the leading small-R-jet (LeadJ) category for the combined $Z \to \ell^+\ell^-$ decay channel. The blue dots show the local maxima used to get the smooth function and the vertical error bars correspond to the fitted uncertainties of the spurious signals.

9 - Search strategy

9.1 BumpHunter algorithm

Once the background is derived, the BumpHunter (BH) algorithm [31, 32] is employed to test the consistency or discrepancy between background and the observed data. This algorithm can locate the local excess above the background and quantifies the degree of discrepancy between the observed data and background, based on the frequentist p-value from one of three test statistics: χ^2, Log Likelihood and BumpHunter described below.

9.1.1 Frequentist p-value

In the comparison between the observed data and background, if the background comes only from the SM, this is called the background-only hypothesis or null hypothesis, denoted by H_0. If the null hypothesis is correct, the observed data, denoted D, will differ from the background-only by statistical fluctuation. The validity of H_0 can be tested by determining the probability of obtaining the data spectrum as a fluctuation of the background-only hypothesis.

The frequentist probability is commonly used in high energy physics, a statement on the frequency of a specific outcome given a large number N of repeated experiments. A frequentist hypothesis test determines the consistency between H_0 and the observed experimental outcome x by fixing in advance a value of probability α below which the hypothesis will be rejected as too discrepant. Specifically, if the observation falls in the space of possible outcomes ω such that

$$P(x \in \omega | H_0) \leq \alpha. \tag{9.1}$$

Then the null hypothesis H_0 will be rejected. Otherwise, the data is considered to be consistent with the background. A threshold of 0.05 is usually used for 95% confidence level.

Define a test statistic t as any numerical quantity that describes the compatibility between data and background, and it usually increases monotonically with decreasing compatibility. The p-value of this test statistic is determined by the probability of obtaining a value at the observed $t = t_0$ given H_0:

$$p = P(t > t_0 | H_0), \tag{9.2}$$

where small p-value means small consistency between data and background.

9.1.2 Test statistic

Three test statistics are employed in the BH algorithm to quantify the discrepancy between observed data and background: χ^2, Log Likelihood, and the BumpHunter. They are represented by a single value that characterises the degree of agreement between the observed data and background and defines p-values.

The χ^2 test statistic is defined as the sum in quadrature of the differences between observations and expectations, normalised to the variance. For a comparison where the observation and prediction are both binned histograms with contents d_i and b_i in bin i:

$$\chi^2 = \sum_i \frac{(d_i - b_i)^2}{b_i} \,. \tag{9.3}$$

The "reduced χ^2" value is defined as χ^2/NDF, which is often used to test goodness-of-fit, where NDF is the number of degrees of freedom in the fit.

The Likelihood, $\mathcal{L}$, test statistic is an effective one in comparison of two binned histograms. In comparison of a mass spectrum, each bin content follows the Poisson distribution, so the Log Likelihood is defined as the product of the Poisson probability in each bin over all bins:

$$\mathcal{L} = \prod_i \frac{b_i^{d_i} e^{-b_i}}{d_i!}. \tag{9.4}$$

The Negative Log Likelihood (NLL), $-2\ln\mathcal{L}$ is defined as:

$$-2\ln\mathcal{L} = -2\ln\prod_i \frac{b_i^{d_i} e^{-b_i}}{d_i!}. \tag{9.5}$$

Both χ^2 and log likelihood can quantify the discrepancy between the observed data and background in the individual bin. However, in comparing two binned spectra, the discrepancy in the window of neighboring bins is more meaningful. Several adjacent bins with significant excess in each bin indicate new physics. However, three bins with a significant excess, a considerable deficit, and a significant excess may produce the large χ^2 and NNL but would be of much less physical interest.

The third test statistic has therefore been defined to quantify the "bump" above the background, the "BumpHunter statistic", which is the default test statistic in the BumpHunter algorithm. For a set of adjacent bins, a value t is calculated as the Poisson probability of obtaining a result at least as significant as the one observed, define d as the sum of the data and b as the background in these neighboring bins:

$$t = \begin{cases} \sum_{n=0}^{d} \frac{b^n}{n!} e^{-b} & \text{for} \quad d < b \,, \\ \sum_{n=d}^{\infty} \frac{b^n}{n!} e^{-b} & \text{for} \quad d \geq b \,. \end{cases} \tag{9.6}$$

The above expression can be represented in terms of gamma functions:

$$t = \begin{cases} \Gamma(d+1, b) = 1 - \Gamma(d+1, b) & \text{for} \quad d < b \,, \\ \Gamma(d, b) & \text{for} \quad d \geq b \,. \end{cases} \tag{9.7}$$

This value accounts for the direction of neighboring fluctuations by looking at the overall excess or deficit in the region.

For every possible window along the mass spectrum, t is calculated. The possible windows are found by looping over all widths between the minimum and maximum bins. The BH statistic describing the overall spectrum is defined as the negative log of the smallest probability obtained for any window, defined as:

$$t_0 = -\log t_{\text{min}} \,. \tag{9.8}$$

Once the BumpHunter test statistic, Eq.(9.8), is determined, the p-value can be calculated by generating many pseudo-data derived by randomly drawing in each bin from a Poisson distribution with a parameter equal to the expected bin content from the background spectrum. The selected test statistic is then calculated for each pseudo-data. The fraction of these cases for which the test statistic is more than that in observed data can be easily computed, i.e., p-value. The full procedure to calculate the p-value obtained from a selected test statistic can be summarised as:

- Calculate the value of the test statistic t_0 which compares background-only hypothesis to observed data, t_0,
- Generate a collection of pseudo-data from background to represent a range of possible experimental outcomes in the case the background-only hypothesis is correct,
- Compare each pseudo-data with background to calculate the test statistic value for each pseudo data, t_i,
- Calculate the fraction of t_i for which $t_i > t_0$, this fraction is the p-value obtained from the test statistic t.

9.1.3 The BumpHunter algorithm

The BH algorithm compares the background with the observed data in intervals of varying widths formed by combining neighboring bins. It scans across the entire distribution with the window width varying from 2 up to half of the number of the bins. Each window in the scan computes the significance of the difference between the observed data and the background. The most significant departure from the background spectrum is defined by the bins set with the smallest probability of arising from a Poisson background fluctuation. If the measured p-value obtained from the BH statistic is less than 0.01, it may mean the existence of new physics.

As the pseudo-experiments are drawn from the background, the random fluctuations in the background-only hypothesis would create an excess anywhere in the spectrum at least as significant as the one observed, so the BH algorithm also accounts for the look-elsewhere effect.

The p-value in BH is used to quantify the discrepancy between observed data and background. The residual in each bin can also be quantified by a p-value and described in detail in [127]. A measured p-value is defined as the probability of measuring a discrepancy between data and background at least as large as the one observed in each bin. The p-value

is then translated into a z-value defined as the number of standard deviations to the right of the mean of the normal distribution:

$$p-\text{value} = \int_{z-\text{value}}^{\infty} \frac{1}{\sqrt{2\pi}} e^{-\frac{x^2}{2}} dx \,. \tag{9.9}$$

Bins with a z-value less than zero show no difference of any interest, while those with a z-value of more than two or three indicate a significant discrepancy. For clarity of interpretation, one would like the sign of the z-value drawn in residual plots to depend on whether the data falls above or below the hypothesis. Therefore, in the plots, any bins with a negative z-value are set to zero, while those with a positive z-value are drawn positive or negative depending on whether an excess or a deficit is observed.

9.1.4 Application of the BumpHunter algorithm on MC mass spectra

An application check is done by applying the BH algorithm to the SM background spectra based on MC simulation in the SRs. It is used to check whether the algorithm detects any significant fake excess. In this study, the MC spectra and the fitted ones are regarded as "observed data" and "background." Figure 9.1 presents the applied BH results in the LeadJ category. The p-value of BH statistics is found well above 0.01 and approaching 1 in most cases. The global fitting method provides good performance of background modelling for the SM MC predictions.

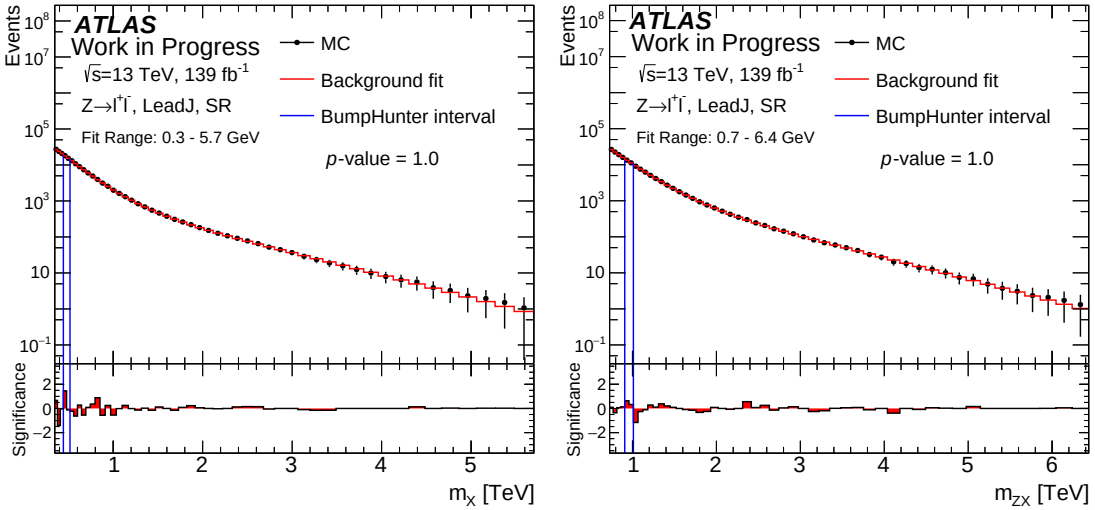

Figure 9.1: BH algorithm applied to m_X (left) and m_{ZX} (right) distributions in the **SRs** of the **LeadJ** (top) category for the $Z \to \ell^+\ell^-$ decay channel.

Besides running the BH algorithm on the SM background MC mass spectra, it is also applied to the case where the background is the fitted result from the nominal MC mass spectrum. The "observed data" is the background with signal injection. One example in the leading small-R-jet category is shown in Figure 9.2, using a Gaussian-shaped signal at 1.5 TeV with a width value of 10%. The injected signal rate varies 1 to 3 sigma using

$S/\sqrt{B}$ compared to the background around the peak. The BH algorithm can accurately locate and quantify the local excess corresponding to the injected signals.

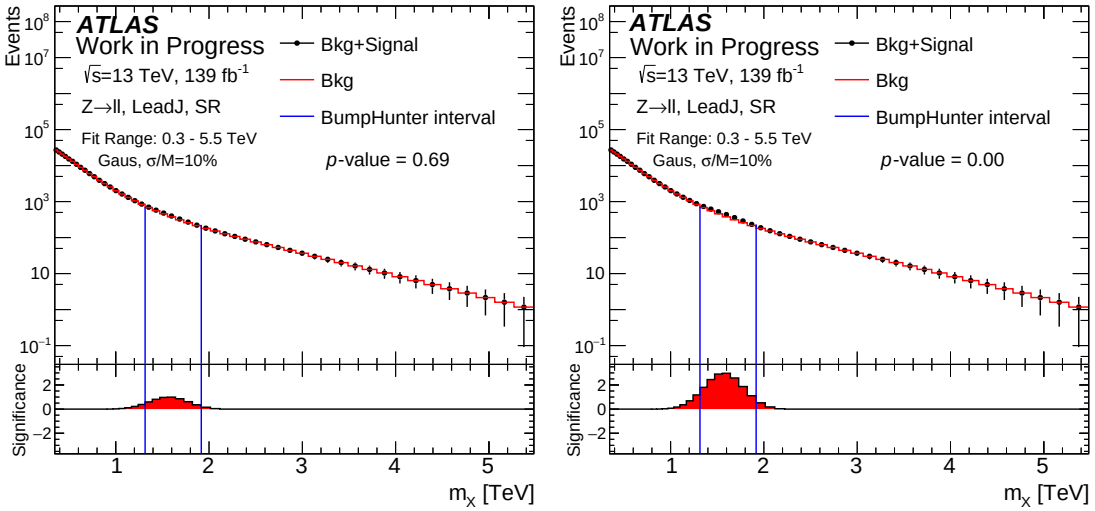

Figure 9.2: BH algorithm applied to m_X for an injected Gaussian-shaped signal at 1.5 TeV with a width value of 10% in the small-R-jet category. (left) for a signal rate of 1 σ, the BH p-value is much larger than 0.01, (right) for a signal rate of 3 σ, the BH p-value is approaching 0.

9.2 Search strategy

A search strategy (also shown in Figure 9.3) is proposed for real data:

- For a given data mass spectrum, apply the same functional form and fit range as those obtained from the MC-based spectrum to derive an initial background estimation and the corresponding global χ^2 p-value. The event statistics in real data at the high mass tail could differ from the MC expectation due to potential mismodelling in shape or normalisation affecting the upper boundary. If the data boundary is smaller than the expected one, the data boundary will be used. Otherwise, we will stick to the MC boundary but will check beyond the MC boundary the consistency between data event yields and the expectation using the extrapolated background fit. The global χ^2 p-value is used to quantify how well the whole spectrum is modelled with the chosen functional form. The BH algorithm is then applied in a slightly more restricted mass range, named as "sensitive range" to be discussed below, to get an initial BH p-value and the corresponding BH interval. The BH p-value and the interval are used to quantify and locate the most significant excess over the background estimation within the sensitive range of the spectrum.

- If the global χ^2 p-value is above a threshold value of 0.05 or if it is below the threshold, but the BH p-value is also below a threshold value of 0.01, then we proceed to the next step. The global χ^2 p-value above 0.05 means that the spectrum is well modelled. Below the threshold value, it means a mismodelling due to either non-optimal modelling choice or the existence of a signal. The threshold value of 0.01 of the BH p-value is used to indicate whether there is any significant excess or not. If the global χ^2 p-value is below 0.05, but the BH p-value is above 0.01, the nominal (nom) functional form will be tested against an alternate (alt) one with one or two more free parameters using the F-test, following the recommendation in Ref. [128]:

$$F = \frac{\left(\chi^2_{\rm nom} - \chi^2_{\rm alt}\right)/(n_{\rm alt} - n_{\rm nom})}{\chi^2_{\rm alt}/(n - n_{\rm alt})} \tag{9.10}$$

  here $\chi^2_{\rm nom}$ and $\chi^2_{\rm alt}$ are the χ^2 values for fits to the spectrum using respectively the nominal and alternate model, $n_{\rm nom}$ and $n_{\rm alt}$ are the number of free parameters in each model, and n is the number of bins used for the χ^2 computation. The value of F is large if the alternate model provides a significantly better fit to the spectrum than the nominal model. The alternate model is retained as long as $p(F) > 0.05$. If adding one or two more parameters to the nominal functional form does not help, the other functional form from Eqs. (8.5) and (8.6) will be used. If both functional forms fail, the lower mass fit boundary will be adjusted until the global χ^2 p-value is above the threshold of 0.05. Should this happen, the corresponding uncertainties and the sensitive range will be re-evaluated accordingly.

- A new background fit is performed by excluding the initial BH interval to get a side-band χ^2 p-value. The side-band χ^2 p-value differs from the global one in that

part of the spectrum is not used in the fit and the p-value calculation. The side-band p-value is usually more significant than the global one. The BH algorithm is performed again in the sensitive range using the new background estimation, including interpolating through the initial BH interval to get a new BH p-value and an updated BH interval. The new BH p-value is expected to be smaller than the initial one since the new background estimation is less affected by a potential signal in the initial BH interval. The excess within the BH interval is expected to be more significant concerning the new background estimation.

- If the global χ^2 and BH p-values are above their threshold values of 0.05 and 0.01, respectively, meaning the spectrum is well modelled, and there is no significant excess, we proceed to set exclusion limits for Gaussian-shaped signals with different width values. If the global χ^2 p-value is above 0.05, but the BH p-value is below 0.01, a signal plus background fit is performed to assess the significance of the excess. If the side-band χ^2 p-value is below 0.05, there are two possibilities: either the rest of the spectrum is still not well modelled with the nominal functional form or there is another significant excess. In the formal case, we will go back to the 2nd step to find an alternative function (including increasing the number of free parameters in the nominal functional form) or adjust the lower mass fit boundary to improve the background-only fit and repeat the procedure. In the latter case, we will exclude the second BH interval and the initial one and repeat the procedure.

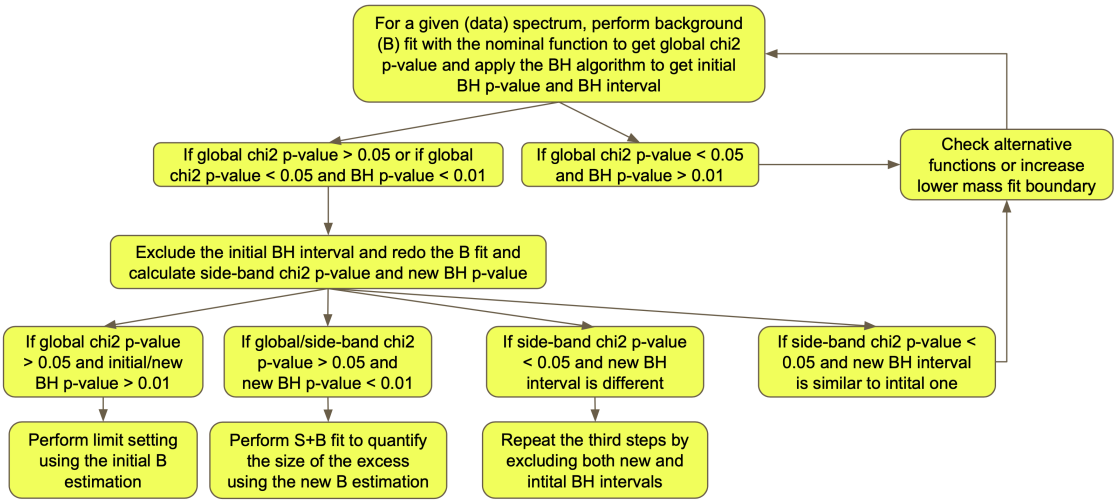

Figure 9.3: Workflow for the search strategy

The validation studies of the search strategy are based on the study using toys generated from SM background MC spectra with or without signal injection.

Under the condition that there is no signal injected in the spectra, the strategy is checked to make sure that the possibility of observing a fake excess is small. Firstly, the

nominal MC spectra are checked, and one example is shown in Figure 9.4 for the leading b-jet category. The background spectra fitted to the full mass range in the initial step and the side-bands by excluding the initial BH interval in the second step are comparable. The BH intervals from the two steps are consistent with BH p-values nearly 1.

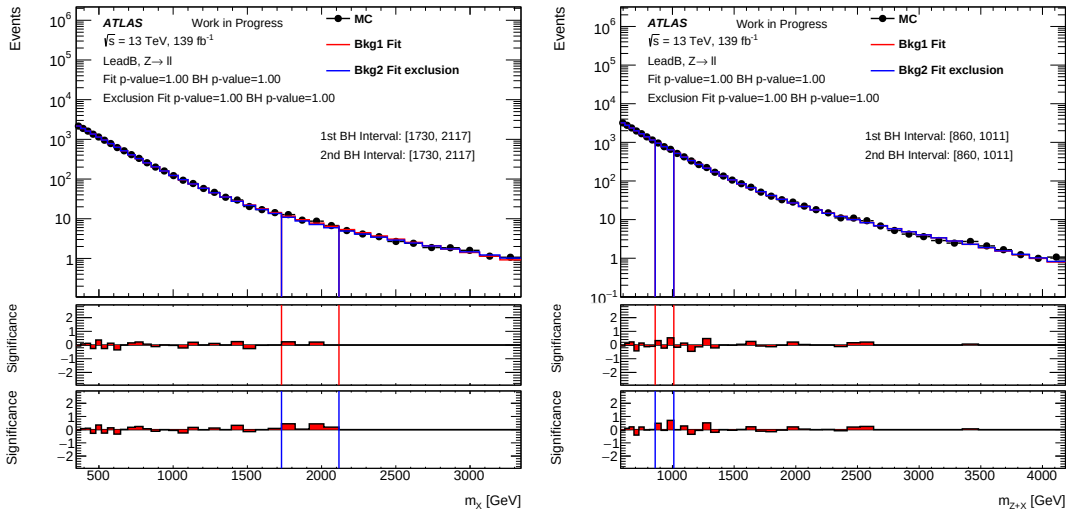

(a) LeadB m_X (b) LeadB m_{ZX}

Figure 9.4: Comparison between the fitted background spectra in two steps: one is using the full mass range and the other after excluding the initial BH interval. In each plots, the second panel shows the significance distribution from the first fit and the third one shows similar results from the 2nd fit. The red vertical lines indicates the initial BH interval and the blue vertical lines the interval in the 2nd step.

A set of 1000 pseudo-experiments is then generated from the fitted background spectra by Poisson fluctuation. The procedure is repeated for each pseudo-experiments and the BH p-values from the two steps are summarised in Figure 9.5 as an example for m_X and m_{ZX} in the leading small-R-jet category. For the full range fitting results in the first step, the fraction of pseudo-experiments with BH p-values below 0.01 is 0. The BH intervals are randomly distributed in the spectra. The fraction increases to around 10% in the 2nd step for all categories. The BH intervals from the 2nd step are still consistent with that from step one.

A signal injection scan is conducted for Gaussian-shaped signals at different mass values and relative widths to check the strategy's performance in the presence of a signal. The signal significance values of the injected signals vary between 1σ and 10σ using the following function, corresponding to the recommended one in Ref. [128]:

$$\text{significance} = \sqrt{\sum_i 2\left(N_i \ln\left[\frac{N_i(B_i+\sigma_i^2)}{B_i^2+N_i\sigma_i^2}\right] - \frac{B_i^2}{\sigma_i^2}\ln\left[1+\frac{\sigma_i^2(N_i-B_i)}{B_i(B_i+\sigma_i^2)}\right]\right)}, \tag{9.11}$$

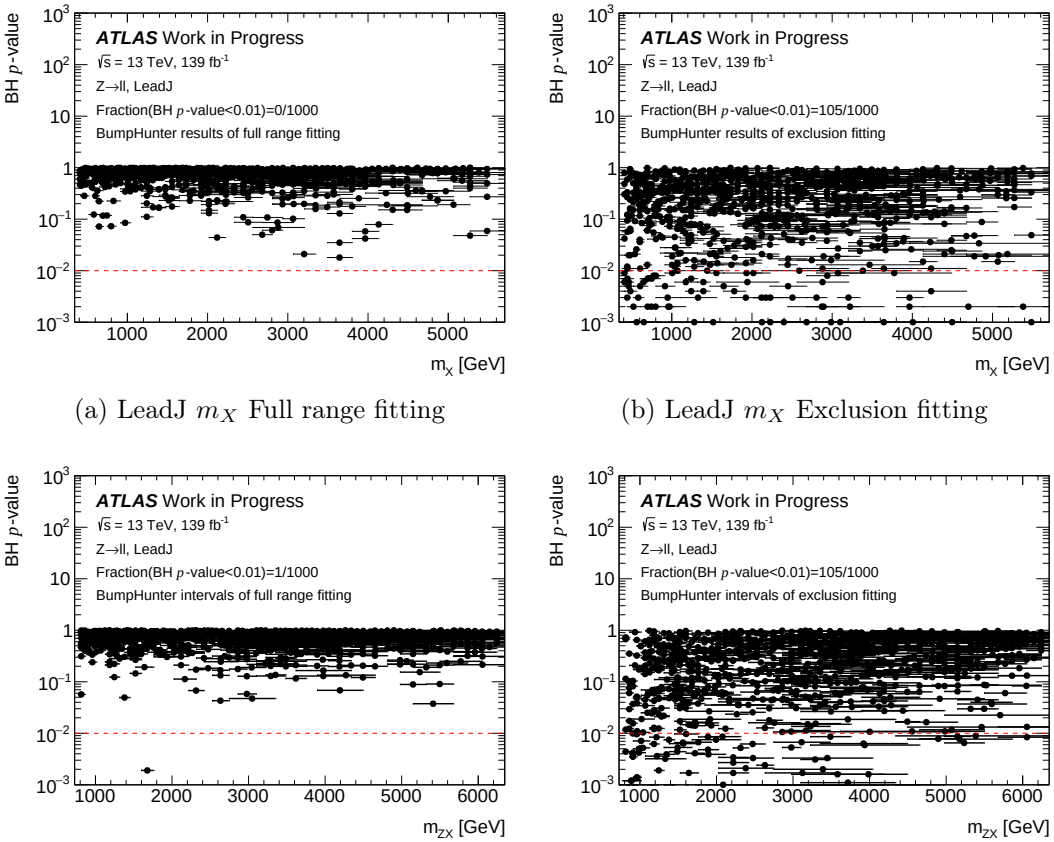

(a) LeadJ m_X Full range fitting

(b) LeadJ m_X Exclusion fitting

(c) LeadJ m_{ZX} Full range fitting

(d) LeadJ m_{ZX} Exclusion fitting

Figure 9.5: BH p-values of 1000 pseudo-experiments as a function of the BH intervals from the initial step (left) and from the 2nd step (right) using the m_X (top) and m_{ZX} (bottom) mass spectra in the leading small-R-jet category. The red horizontal dashed line represents the BH p-value threshold value of 0.01.

where S_i, B_i and N_i are the signal, background and total event yields in i^{th} mass bin, and σ_i is the corresponding uncertainty from fits in the i^{th} mass bin. This bin-by-bin formula has no dependency on the choice of the mass window size and is a much more accurate estimation than the simplified calculation of $S/\sqrt{B}$.

Figure 9.6 shows the results of one mass value (1250 GeV) and 4 width values (3%, 5%, 10% and 15%) using the m_{ZX} spectra in the leading small-R-jet category. The full curves display the initial global χ^2 and BH p-values from the first step using the full mass range and the dashed one the corresponding p-values from the 2nd step. The best signal sensitivity (the dashed red curve) is achieved for small-width signals. The sensitivity degrades as the width value increases. The analysis is not sensitive to Gaussian-shaped signals with width values of 15% or larger. The same conclusion holds for the other mass spectra and the other categories.

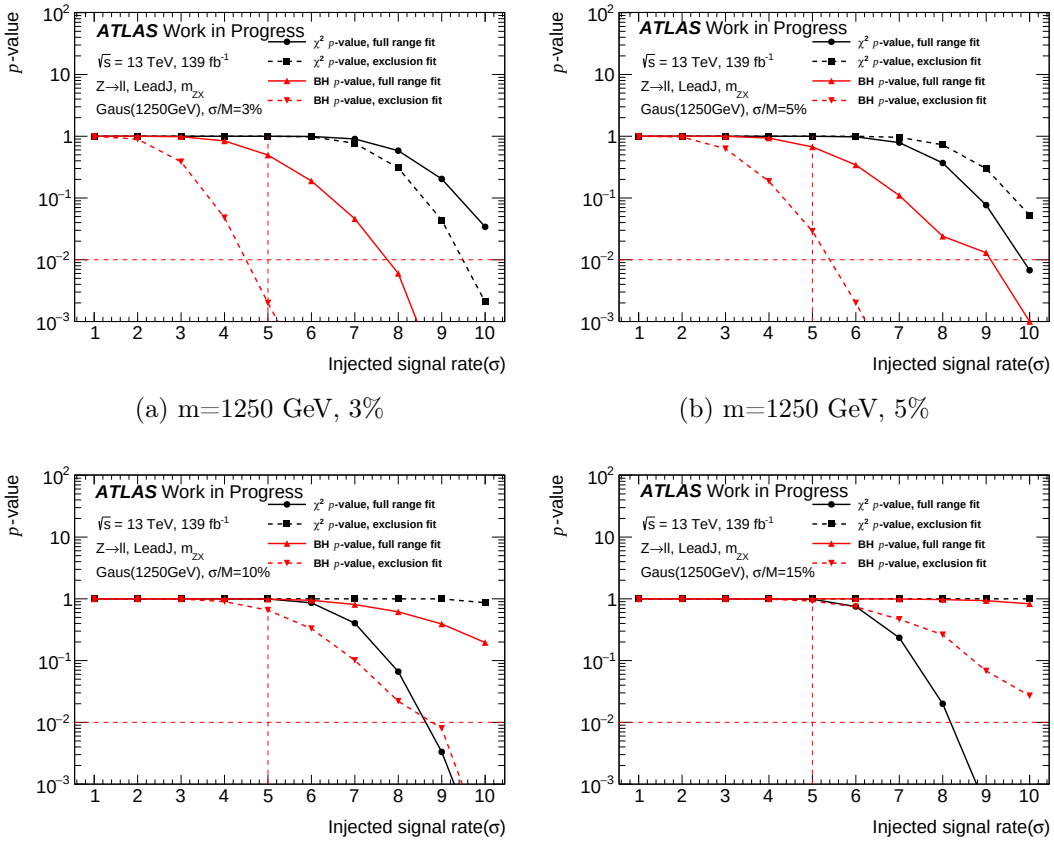

(a) m=1250 GeV, 3%

(b) m=1250 GeV, 5%

(c) m=1250 GeV, 10%

(d) m=1250 GeV, 15%

Figure 9.6: Global χ^2 and BH p-value distributions as a function of injected signal yields to the m_{ZX} spectrum in the leading small-R-jet category for Gaussian-shaped signals at 1250 GeV with four width values varying 3% to 15%. The two solid lines are from the initial step, while the two dashed lines represent results from the 2nd step.

The results are also shown in Figure 9.7 in a complementary way comparing the BH p-values from the two steps for Gaussian-shaped signals injected with a significance value of 5σ as a function of signal mass on the m_{ZX} mass spectra in the leading small-R-jet category. The signal significance is reduced due to the absorption of the background function fitting. Again, it shows that the signal sensitivity is higher for smaller width values and the mass points in the middle of the mass spectra.

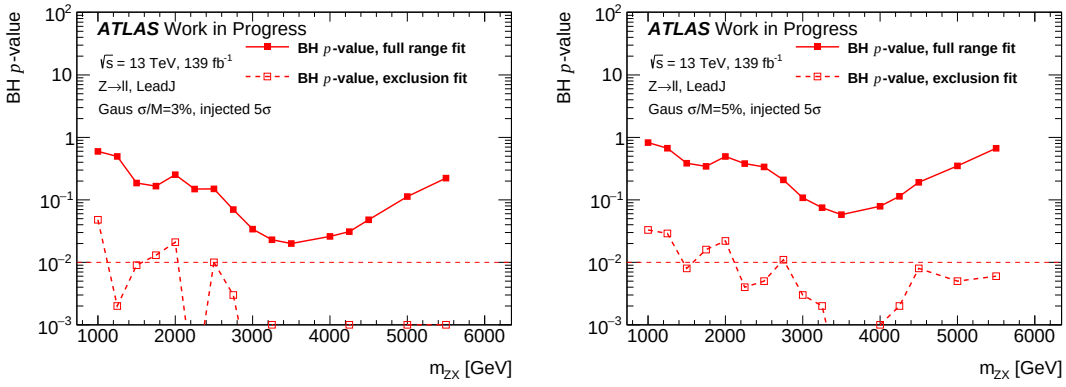

(a) 3%

(b) 5%

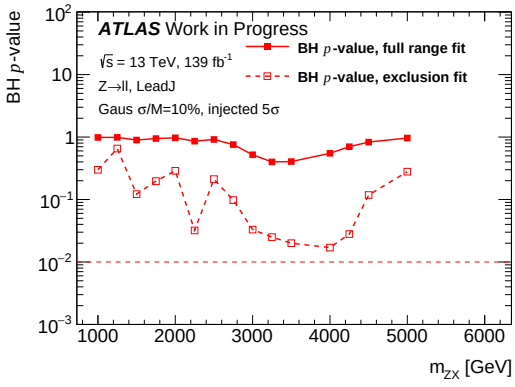

(c) 10%

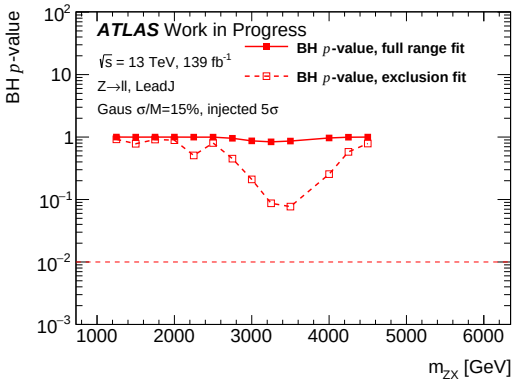

(d) 15%

Figure 9.7: BH p-value distributions as a function of signal mass for injected Gaussian-shaped signals at 5σ with width values of 3%, 5%, 10% and 15% for the m_{ZX} mass spectrum in the leading small-R-jet category.

In a further study, instead of using the nominal background spectra, a set of 100 pseudo-experiments are generated using the fitted background function with Poisson fluctuation and adding injected Gaussian-shaped signals at 5σ with three width values of 3%, 5%, and 10% on top of each pseudo-experiment. For each category, the BH p-values of the 100 pseudo-experiments are determined as a function of the BH intervals in the two steps for m_{ZX} and m_X. One example is shown in Figure 9.8. In most of the pseudo-experiments, the BH algorithm correctly identifies the injected signal's location. The fraction of pseudo-

experiments whose BH p-value is below 0.01 increases in the 2nd step with the background estimation after excluding the initial BH interval. The fractions of the numbers of correctly identified BH intervals and BH p-values below 0.01 are plotted as a function of signal mass for the three width values in Figure 9.9 for the m_{ZX} and m_X mass spectra in the leading small-R-jet category. It shows that in comparison with the original fit mass ranges given in Table 8.4 (also shown in the legend of each plot), the sensitivity for signal search is reduced in most of the categories as the signal width values increase. The effective search range is thus reduced.

Such a new signal sensitive range for each observable, category, and signal width is defined as the mass region where the fraction (correctly identified BH intervals and p-value < 0.01) is more than 50% and is shown in Table 9.1. These signal sensitive mass ranges are used for reporting BH search results. The BH algorithm does not have sufficient sensitivity to potential signals outside of these ranges. It should be pointed out that the largest sensitive range corresponding to the 3% width value is used for the BH search, and the other sensitive ranges for other width values are used when interpreting a significant excess, if any.

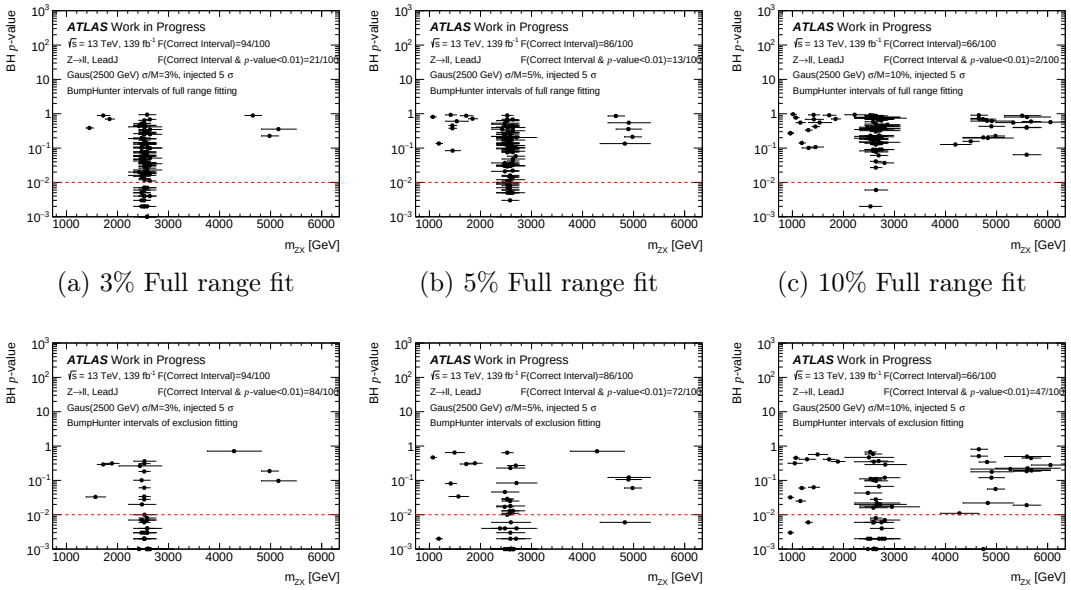

(a) 3% Full range fit (b) 5% Full range fit (c) 10% Full range fit

(d) 3% Exclusion fit (e) 5% Exclusion fit (f) 10% Exclusion fit

Figure 9.8: BH p-values for 100 pseudo-experiments as a function of BH intervals for injected Gaussian-shaped signals at 2.5 TeV at 5σ with width values of 3% (left), 5% (middle) and 10% (right) from the initial step (top) and the 2nd step (bottom) for the m_{ZX} mass spectrum in the leading small-R-jet category.

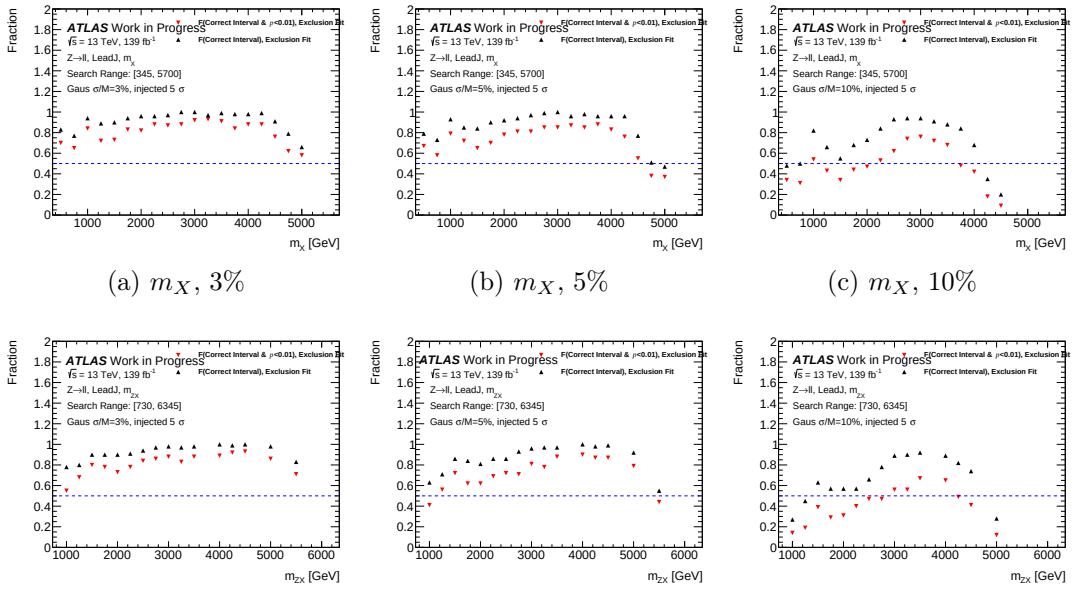

(a) m_X, 3% (b) m_X, 5% (c) m_X, 10%

(d) m_{ZX}, 3% (e) m_{ZX}, 5% (f) m_{ZX}, 10%

Figure 9.9: Fraction (correctly identified BH intervals and p-value < 0.01) of 100 pseudo-experiments as a function of signal mass for injected Gaussian-shaped signals at 5σ with width values of 3% (left), 5% (middle) and 10% (right) from two search steps for the m_X and m_{ZX} mass spectrum in the leading small-R-jet category.

Table 9.1: Fit mass range and signal sensitive mass range for different mass spectra and event categories. As in Table 8.4, the fit and sensitive ranges have been rounded.

Spectrum	Category	Width [%]	Fit range [GeV]	Sensitive range [GeV]
m_X	LeadJ	3	[350, 5700]	[350, 5480]
m_X	LeadB	3	[350, 3340]	[350, 2725]
m_X	LeadFatJ	3	[630, 6085]	[630, 5930]
m_X	LeadP	3	[150, 1800]	[150, 1575]
m_X	LeadE	3	[150, 1515]	[150, 1250]
m_X	LeadM	3	[150, 1230]	[150, 1000]
m_X	combined	3	[550, 6450]	[705, 6225]
m_X	LeadJ	5	[350, 5700]	[350, 4575]
m_X	LeadB	5	[350, 3340]	[350, 2595]
m_X	LeadFatJ	5	[630, 6085]	[700, 5870]
m_X	LeadP	5	[150, 1800]	[150, 1440]
m_X	LeadE	5	[150, 1515]	[150, 1160]
m_X	LeadM	5	[150, 1230]	[150, 965]
m_X	combined	5	[550, 6455]	[780, 6225]
m_X	LeadJ	10	[350, 5700]	[955, 3725]
m_X	LeadB	10	[350, 3340]	[795, 2335]
m_X	LeadFatJ	10	[630, 6085]	[990, 5650]
m_X	LeadP	10	[150, 1800]	[150, 1300]
m_X	LeadE	10	[150, 1515]	[150, 1050]
m_X	LeadM	10	[150, 1230]	[150, 850]
m_X	combined	10	[550, 6455]	[950, 4700]
m_{ZX}	LeadJ	3	[730, 6435]	[905, 6200]
m_{ZX}	LeadB	3	[580, 4185]	[580, 3580]
m_{ZX}	LeadFatJ	3	[650, 7095]	[650, 6870]
m_{ZX}	LeadP	3	[280, 2485]	[280, 2140]
m_{ZX}	LeadE	3	[325, 2185]	[325, 1820]
m_{ZX}	LeadM	3	[290, 1900]	[290, 1580]
m_{ZX}	combined	3	[650, 7860]	[670, 7590]
m_{ZX}	LeadJ	5	[730, 6435]	[1150, 5410]
m_{ZX}	LeadB	5	[580, 4185]	[785, 3360]
m_{ZX}	LeadFatJ	5	[650, 7095]	[745, 6870]
m_{ZX}	LeadP	5	[280, 2485]	[280, 2010]
m_{ZX}	LeadE	5	[325, 2185]	[325, 1720]
m_{ZX}	LeadM	5	[290, 1900]	[290, 1560]
m_{ZX}	combined	5	[650, 7860]	[650, 7590]
m_{ZX}	LeadJ	10	[730, 6435]	[2835, 4235]
m_{ZX}	LeadB	10	[580, 4185]	[2055, 2875]
m_{ZX}	LeadFatJ	10	[650, 7095]	[940, 6870]
m_{ZX}	LeadP	10	[280, 2485]	[275, 1775]
m_{ZX}	LeadE	10	[325, 2185]	[325, 1465]
m_{ZX}	LeadM	10	[290, 1900]	[465, 1375]
m_{ZX}	combined	10	[650, 7860]	[1670, 4830]

10 - Results

This chapter presents the results from the data in the SRs. The background estimation and BH results are reported in Section 10.1. As no significant excess is observed in the BH sensitive ranges listed in Table 9.1, Section 10.2 shows the derived exclusion upper limits on the Gaussian-shaped signal cross section times acceptance times branching ratio ($\sigma \times \mathcal{A} \times \mathrm{BR}$) at 95% Confidence Level (CL).

10.1 Results of BumpHunter search

Following the search strategy in Section 9.2, the selected background functions and fitting ranges from MC spectra are employed on the data spectra in the SRs. In some event categories, the data event yield is reduced in the high mass tail. The high edges of the fitting ranges are adjusted to the last bin with at least one event. In the other cases, the high mass boundary values keep the same as the ones from MC simulation studies. The data events above the high mass boundary have no impacts on the final BH results. The BH algorithm is applied to locate the most significant resonance excess above the newly estimated background and quantify its significance. Figures 10.1-10.7 show the initial background function fitting and BH results. After excluding initial BH intervals, the results of background function fitting and BH algorithm are consistent with initial ones. All results are summarised in Table 10.1.

Most of the selected functions have a good description of the mass spectra of the data, with global $\chi^2 p$-values larger than 0.05 and BH p-values larger than 0.01. The selected functions fail for m_{ZX} spectra in the leading large-R-jet and combined categories. Both have small global χ^2 p-values but large BH p-values. Following the workflow, the alternative functions are tried first for these exceptional cases. If the alternative ones fail to reach the criteria, the low mass boundaries are increased by one bin, and the nominal and alternative functions are retried. This procedure is repeated until satisfying the requirements, as listed in Table 10.1. No significant excess is observed in all the mass spectra and event categories. The largest excess is around 1.6 TeV of m_{ZX} spectra in the large-R-jet category with a BumpHunter p-value around 0.46.

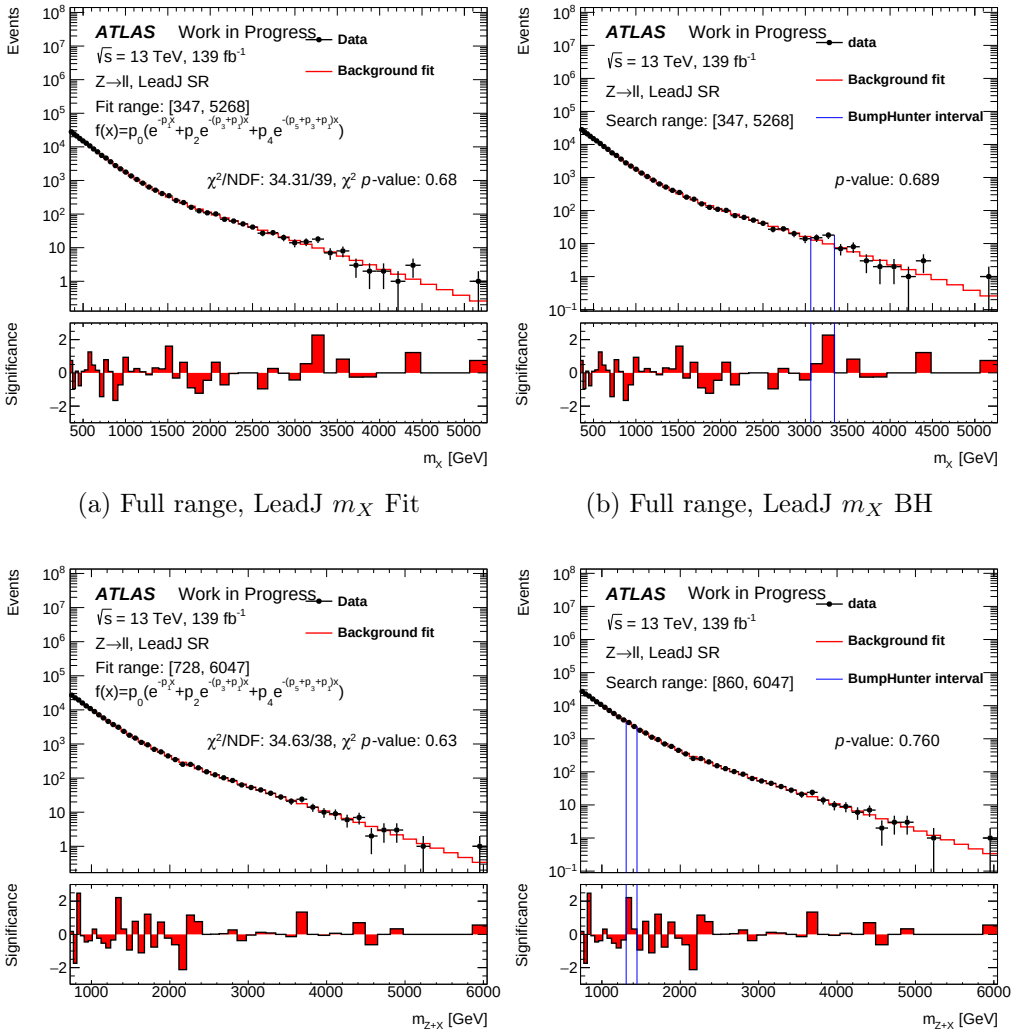

(a) Full range, LeadJ m_X Fit

(b) Full range, LeadJ m_X BH

(c) Exclusion, LeadJ m_{ZX} Fit

(d) Exclusion, LeadJ m_{ZX} BH

Figure 10.1: Results of full range background function fitting and corresponding BH in the leading small-R-jet category in the SRs of data.

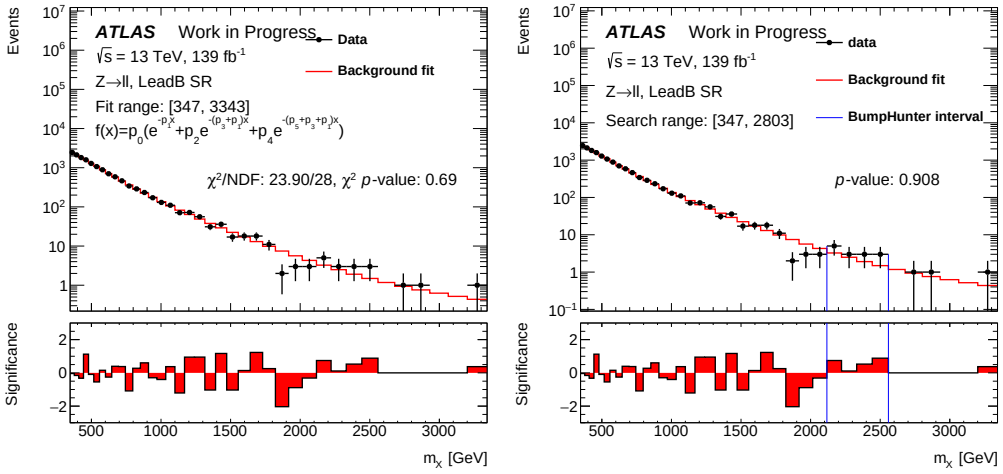

(a) Full range, LeadB m_X Fit

(b) Full range, LeadB m_X BH

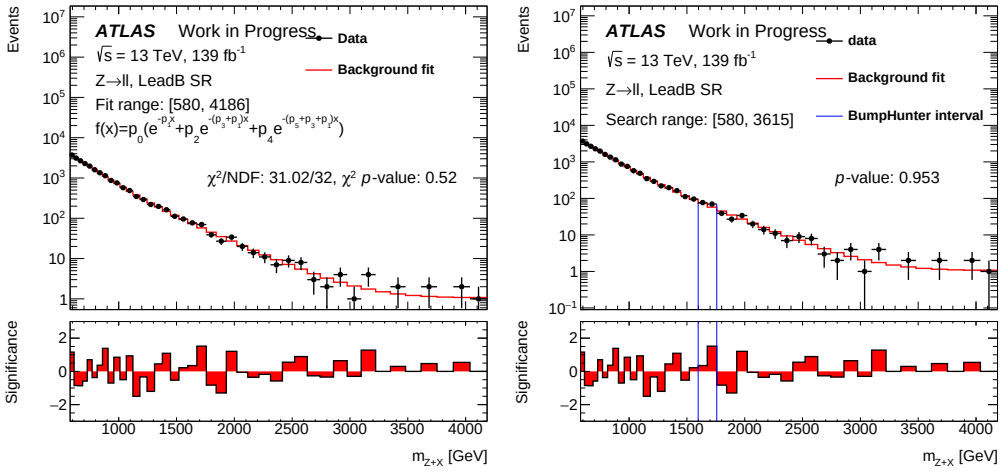

(c) Exclusion, LeadB m_{ZX} Fit

(d) Exclusion, LeadB m_{ZX} BH

Figure 10.2: Results of full range background function fitting and corresponding BH in the leading b-tagged-jet category in the SRs of data.

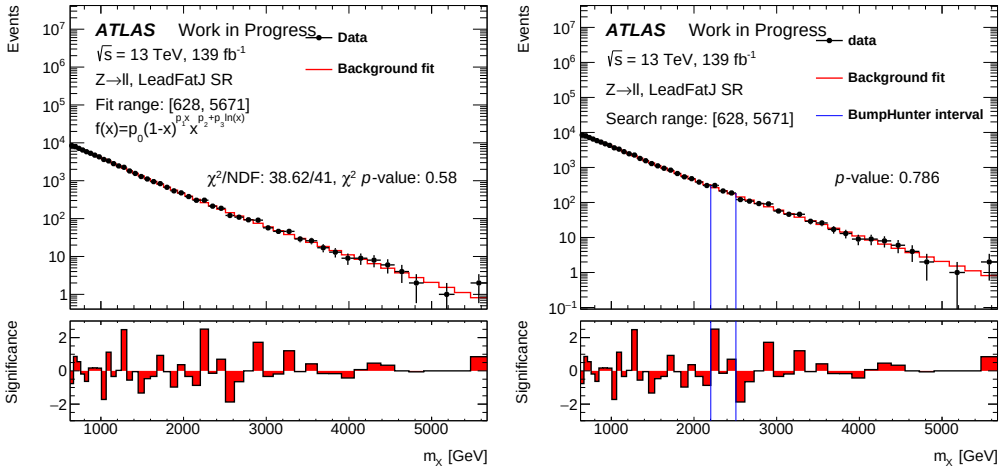

(a) Full range, LeadFatJ m_X Fit

(b) Full range, LeadFatJ m_X BH

(c) Exclusion, LeadFatJ m_{ZX} Fit

(d) Exclusion, LeadFatJ m_{ZX} BH

Figure 10.3: Results of full range background function fitting and corresponding BH in the leading large-R-jet category in the SRs of data.

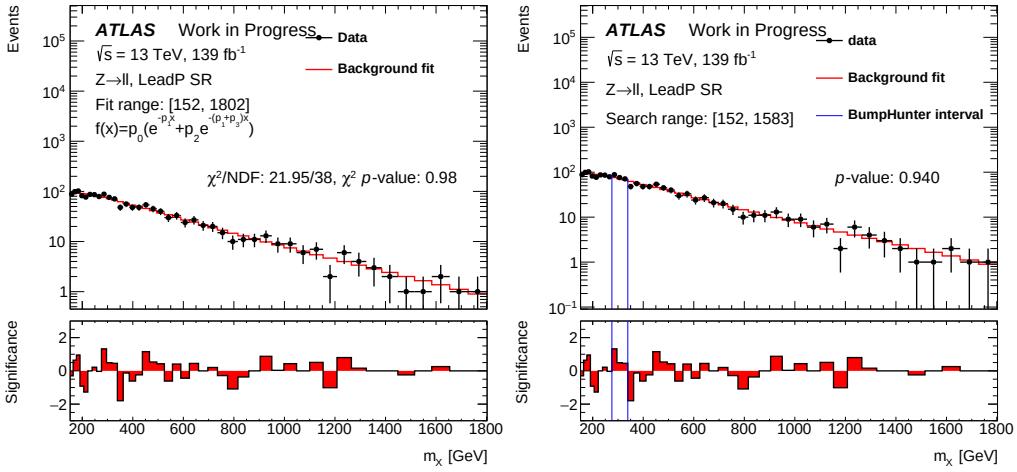

(a) Full range, LeadP m_X Fit

(b) Full range, LeadP m_X BH

(c) Exclusion, LeadP m_{ZX} Fit

(d) Exclusion, LeadP m_{ZX} BH

Figure 10.4: Results of full range background function fitting and corresponding BH in the leading photon category in the SRs of data.

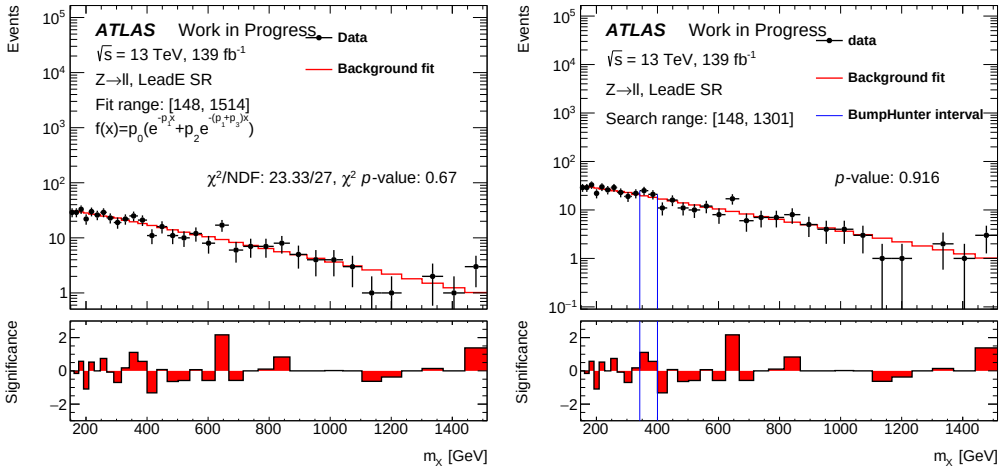

(a) Full range, LeadE m_X Fit

(b) Full range, LeadE m_X BH

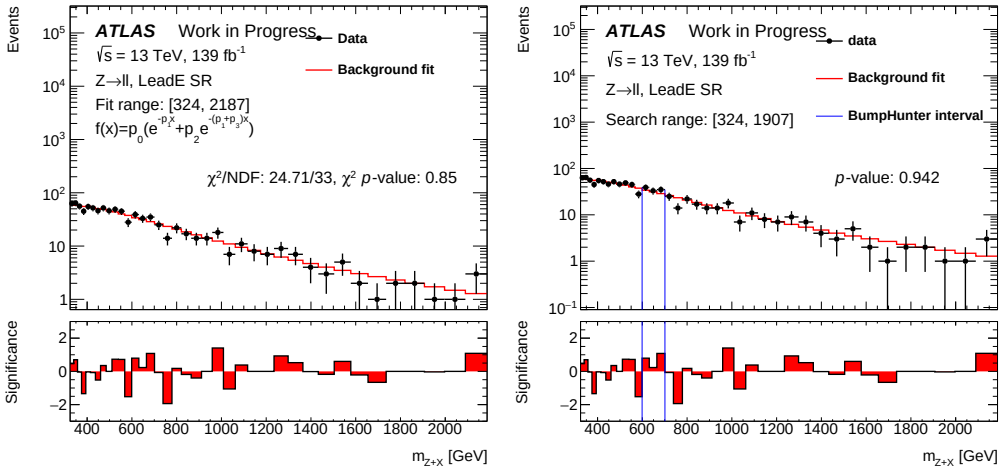

(c) Exclusion, LeadE m_{ZX} Fit

(d) Exclusion, LeadE m_{ZX} BH

Figure 10.5: Results of full range background function fitting and corresponding BH in the leading electron category in the SRs of data.

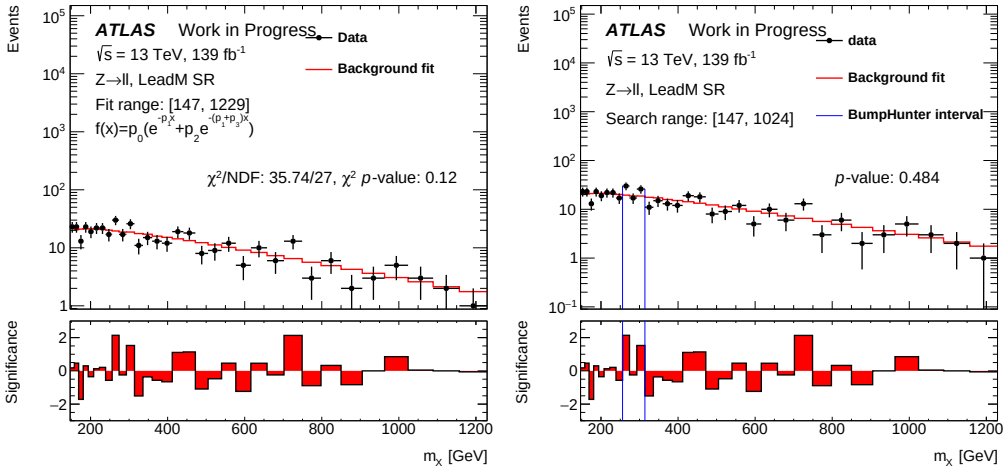

(a) Full range, LeadM m_X Fit

(b) Full range, LeadM m_X BH

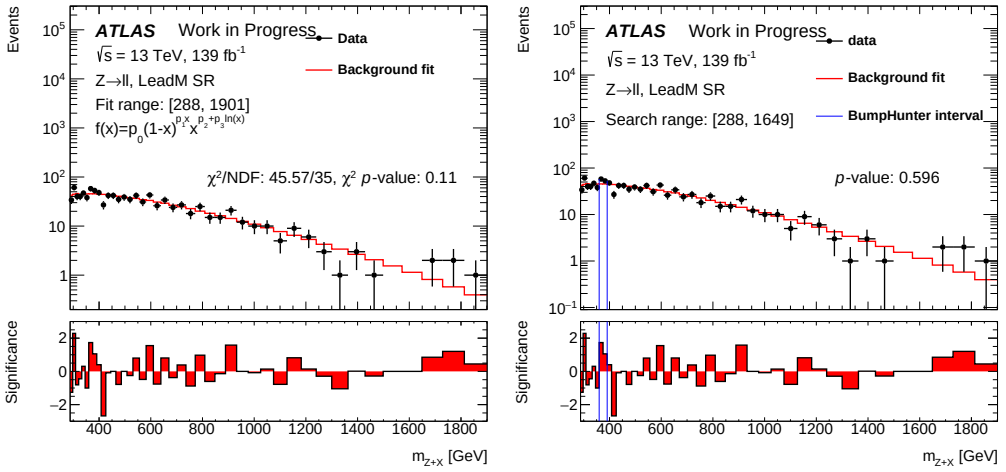

(c) Exclusion, LeadM m_{ZX} Fit

(d) Exclusion, LeadM m_{ZX} BH

Figure 10.6: Results of full range background function fitting and corresponding BH in the leading muon category in the SRs of data.

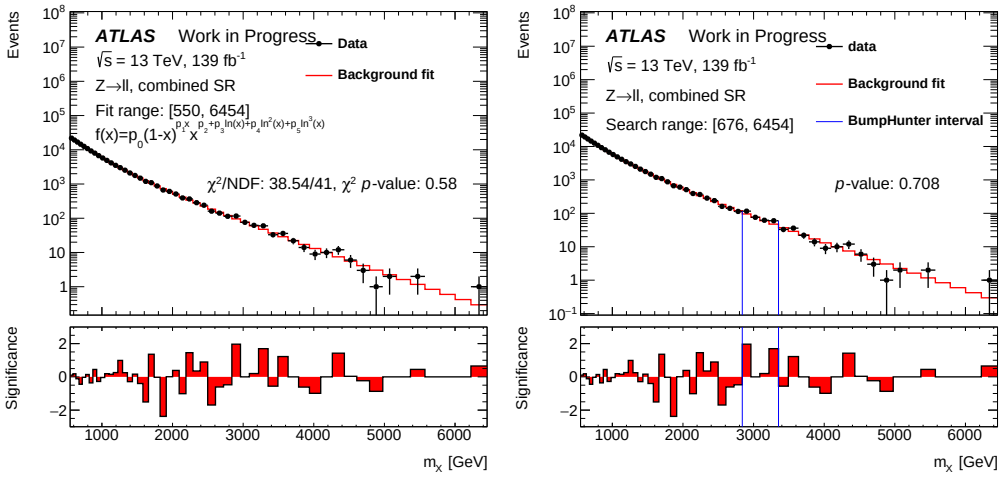

(a) Full range, Combined m_X Fit

(b) Full range, Combined m_X BH

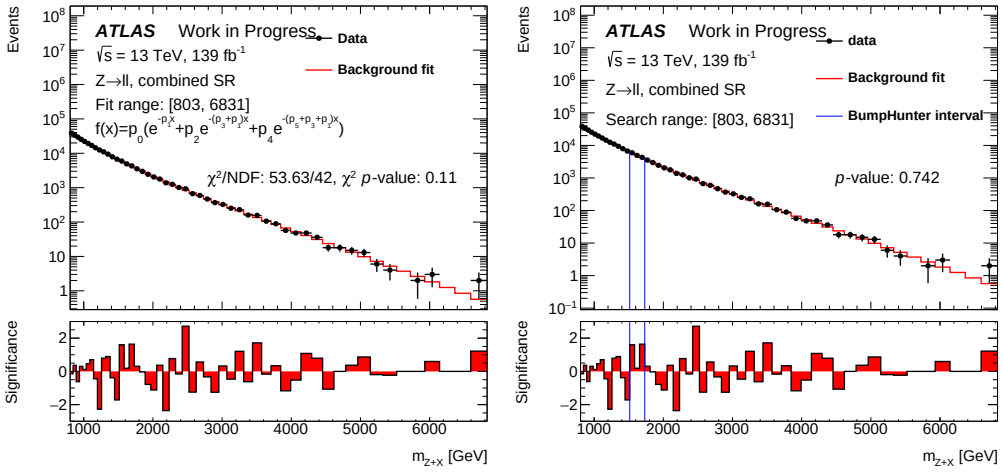

(c) Exclusion, Combined m_{ZX} Fit

(d) Exclusion, Combined m_{ZX} BH

Figure 10.7: Results of full range background function fitting and corresponding BH in the combined category in the SRs of data.

Table 10.1: Background function fit and corresponding BH results for data in all considered categories.

Category	Variable	MC Fit Ranges [GeV]	Fit function in MC	Data Fit Ranges [GeV]	Fit function in Data	Full Range χ^2 p-value	Full Range BH p-value	Exclusion χ^2 p-value	Exclusion BH p-value
LeadJ	m_X	[347, 5701],	exp6Param	[347, 5268]	exp6Param	0.68	0.69	0.82	0.30
LeadJ	m_{ZX}	[728, 6436],	exp6Param	[728, 6047]	exp6Param	0.63	0.76	0.77	0.27
LeadB	m_X	[347, 3343],	exp6Param	[347, 3343]	exp6Param	0.69	0.91	0.57	0.39
LeadB	m_{ZX}	[580, 4186],	exp6Param	[580, 4186]	exp6Param	0.52	0.95	0.55	0.72
LeadFatJ	m_X	[628, 6087],	dijet4Param	[628, 5671]	dijet4Param	0.58	0.79	0.77	0.61
LeadFatJ	m_{ZX}	[649, 7097],	dijet4Param	[831, 6652]	exp4Param	0.05	0.46	0.09	0.10
LeadP	m_X	[152, 1802],	exp4Param	[152, 1802]	exp4Param	0.98	0.94	0.98	0.69
LeadP	m_{ZX}	[276, 2484],	exp4Param	[276, 2205]	exp4Param	0.84	0.69	0.90	0.45
LeadE	m_X	[148, 1514],	exp4Param	[148, 1514]	exp4Param	0.67	0.92	0.65	0.65
LeadE	m_{ZX}	[324, 2187],	exp4Param	[324, 2187]	exp4Param	0.85	0.94	0.89	0.85
LeadM	m_X	[147, 1229],	exp4Param	[147, 1229]	exp4Param	0.12	0.48	0.32	0.08
LeadM	m_{ZX}	[288, 1901],	dijet4Param	[288, 1901]	dijet4Param	0.11	0.60	0.14	0.40
combined	m_X	[550, 6454],	dijet6Param	[550, 6454]	dijet6Param	0.58	0.71	0.69	0.30
combined	m_{ZX}	[649, 7862],	exp6Param	[803, 6831]	exp6Param	0.11	0.74	0.20	0.29

10.2 Results of upper limits for the Gaussian-shaped signals

The limit setting phase is performed if no significant deviations from the background-only hypothesis are reported in the search phase. Firstly, the workspace [129] files are generated for each background spectrum and the Gaussian-shaped signal models using the HistFitter framework [130]. The xmlWSBuilder package [131] is then used to combine all models and corresponding systematics. Finally, exclusion upper limits on the signal cross-section times acceptance times branching ratio ($\sigma \times \mathcal{A} \times \mathrm{BR}$) are extracted at 95% CL employing the CL_s method [132] with a binned profile likelihood ratio as the test statistics using CommonStatTools [133]. The limits are obtained by adjusting the normalisation of signal strength μ_s of a template representing the shape of the nominal signal model in question until a CL_s p-value of 0.05 is reached. The obtained μ_s will be directly the estimated signal yields for the Gaussian-shaped signal models. One can convert the upper limit on signal yields to an upper limit on $\sigma \times \mathcal{A} \times \mathrm{BR}$ (The efficiency ϵ is also taken into account and absorbed by $\mathcal{A}$) by dividing by the corresponding integrated luminosity.

The signal sensitive ranges for limit settings are determined using the nominal mass spectra of the MC predictions based on the knowledge of upper limit calculation. In this study, a set of pseudo-experiments are generated for both background and signal with the strength of signal set to the expected limit at 95% CL. A global S+B fit procedure is performed for each pseudo-experiment. The exclusion limit is extracted in each one. Based on the requirement of 95% CL, the fraction of smaller values concerning the nominal upper limit (referred to as limits from the nominal background distributions, not from the pseudo-experiments) should be less than 5%, which indicates the nominal limits are conservative and the modelling of signals and backgrounds make sense. Given the fluctuation of toy datasets, a downwards excess by 5% could be acceptable. If the fraction of the higher upper limit relative to the nominal one is less than 90%, the signal mass used to generate toy datasets is adjusted to a higher value to satisfy the 90% criterion.

Three Gaussian-shaped signals with different widths are tested for the m_{ZX} and m_X spectra in all seven categories. The mass values chosen in this study are starting point and ending point of signal sensitivity ranges. The results are present in Table 10.2, in which the fractions for all situations are listed. The upper limits distributions of 1000 toys of Gaussian-shaped signals with three width values are shown in Figure 10.8 for the leading small-R-jet category.

With the new estimated background spectra as shown in Figures 10.1-10.2, the systematic uncertainties of background are updated following the same procedures as MC studies documented in Section 8.4. They are composed of the statistical uncertainty of fitting and uncertainty form fitting function choice. An example is shown for the leading small-R-jet category in Figure 10.9. As shown in the Table 10.1, the fit ranges in the data spectra is reduced in some categories. The envelope estimations of the spurious signal uncertainties are repeated after excluding the signal mass points which are outside of the fit ranges. For the uncertainties of the Gaussian-shaped signal, the relative spurious signal uncertainties are unchanged and implemented, given the mismodelling between data and MC as shown

Table 10.2: Tables for new method for signal sensitivity ranges study in all categories.

Category	Variable	Width	MC Fit Ranges [GeV]	Data Fit Ranges [GeV]	Lowest mass point [GeV]	Fraction	Highest mass point [GeV]	Fraction
LeadJ	m_X	3	[347, 5701]	[347, 5268]	430	0.9859	5195	0.9679
LeadJ	m_X	5	[347, 5701]	[347, 5268]	435	0.9799	5065	0.9719
LeadJ	m_X	10	[347, 5701]	[347, 5268]	470	0.9364	4750	0.967
LeadJ	m_{ZX}	3	[728, 6436]	[728, 6047]	840	1	5895	0.971
LeadJ	m_{ZX}	5	[728, 6436]	[728, 6047]	860	0.997	5750	0.9739
LeadJ	m_{ZX}	10	[728, 6436]	[728, 6047]	915	0.9559	5360	0.955
LeadB	m_X	3	[347, 3343]	[347, 3343]	420	0.93	3050	0.9488
LeadB	m_X	5	[347, 3343]	[347, 3343]	430	0.9258	2960	0.9478
LeadB	m_X	10	[347, 3343]	[347, 3343]	750	0.919	2750	0.9408
LeadB	m_{ZX}	3	[580, 4186]	[580, 4186]	665	0.9318	3815	0.9529
LeadB	m_{ZX}	5	[580, 4186]	[580, 4186]	680	0.9007	3705	0.9308
LeadB	m_{ZX}	10	[580, 4186]	[580, 4186]	1000	0.921	3460	0.9258
LeadFatJ	m_X	3	[628, 6087]	[628, 5671]	730	0.9639	5580	0.9759
LeadFatJ	m_X	5	[628, 6087]	[628, 5671]	745	0.9027	5440	0.9809
LeadFatJ	m_X	10	[628, 6087]	[628, 5671]	1100	0.9166	5070	0.959
LeadFatJ	m_{ZX}	3	[649, 7097]	[831, 6652]	730	0.9639	6505	0.9689
LeadFatJ	m_{ZX}	5	[649, 7097]	[831, 6652]	750	0.9569	6345	0.9709
LeadFatJ	m_{ZX}	10	[649, 7097]	[831, 6652]	815	0.9529	5910	0.9659
LeadP	m_X	3	[152, 1802]	[152, 1802]	185	0.984	1620	0.9599
LeadP	m_X	5	[152, 1802]	[152, 1802]	190	0.99	1580	0.9549
LeadP	m_X	10	[152, 1802]	[152, 1802]	205	0.996	1475	0.9509
LeadP	m_{ZX}	3	[276, 2484]	[276, 2205]	300	0.9598	2255	0.9619
LeadP	m_{ZX}	5	[276, 2484]	[276, 2205]	310	0.9579	2190	0.9539
LeadP	m_{ZX}	10	[276, 2484]	[276, 2205]	350	0.9909	2035	0.9418
LeadE	m_X	3	[148, 1514]	[148, 1514]	180	0.9458	1350	0.9529
LeadE	m_X	5	[148, 1514]	[148, 1514]	180	0.9458	1315	0.9468
LeadE	m_X	10	[148, 1514]	[148, 1514]	200	0.9478	1230	0.9448
LeadE	m_{ZX}	3	[324, 2187]	[324, 2187]	360	0.9669	1960	0.9468
LeadE	m_{ZX}	5	[324, 2187]	[324, 2187]	370	0.9338	1910	0.9478
LeadE	m_{ZX}	10	[324, 2187]	[324, 2187]	410	0.9529	1785	0.9298
LeadM	m_X	3	[147, 1229]	[147, 1229]	175	0.9367	1065	0.9438
LeadM	m_X	5	[147, 1229]	[147, 1229]	180	0.9558	1045	0.9438
LeadM	m_X	10	[147, 1229]	[147, 1229]	195	0.9608	980	0.9368
LeadM	m_{ZX}	3	[288, 1901]	[288, 1901]	320	0.9569	1680	0.9488
LeadM	m_{ZX}	5	[288, 1901]	[288, 1901]	325	0.9408	1645	0.9559
LeadM	m_{ZX}	10	[288, 1901]	[288, 1901]	365	0.9398	1530	0.9599
combined	m_X	3	[550, 6454]	[550, 6454]	650	0.9228	5940	0.982
combined	m_X	5	[550, 6454]	[550, 6454]	665	0.9358	5795	0.978
combined	m_X	10	[550, 6454]	[550, 6454]	900	0.9058	5375	0.956
combined	m_{ZX}	3	[649, 7862]	[803, 6831]	740	0.9535	7230	0.983
combined	m_{ZX}	5	[649, 7862]	[803, 6831]	755	0.9427	7040	0.98
combined	m_{ZX}	10	[649, 7862]	[803, 6831]	815	0.9348	6550	0.9818

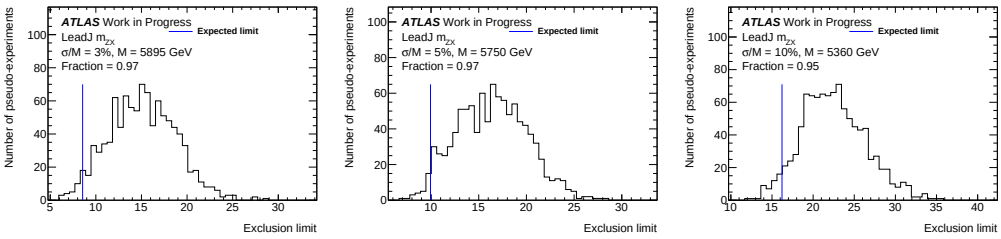

(a) 3%, $m_{ZX} = 5895$ GeV (b) 5%, $m_{ZX} = 5750$ GeV (c) 10%, $m_{ZX} = 5360$ GeV

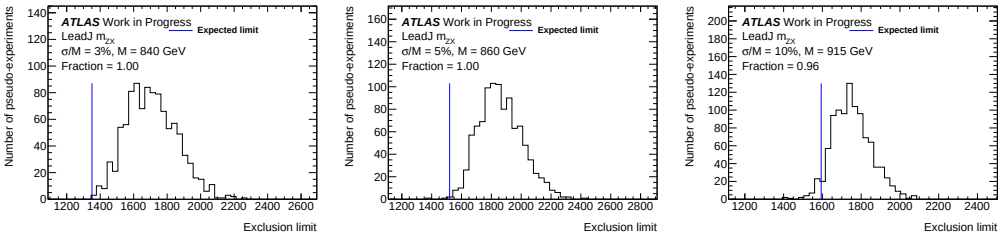

(d) 3%, $m_{ZX} = 840$ GeV (e) 5%, $m_{ZX} = 860$ GeV (f) 10%, $m_{ZX} = 915$ GeV

Figure 10.8: The upper limits distributions of 1000 toys of Gaussian-shaped signals with width of 3% (left), 5% (middle) and 10% (right) in the LeadJ category for the m_{ZX} spectrum. The blue vertical line represents the expected limits from the nominal background spectra at 95% CL.

in Figure 8.10.

The expected and observed limits at 95% CL have been derived for Gaussian-shaped signals with three relative width values of 3%, 5% and 10% and shown in Figures 10.10–10.12 for the case of 3%. The comparison of the observed limits between the three width values is shown in Figures 10.13–10.15. Depending on the observables and event categories, the upper limits on the effective cross-sections of a Gaussian-shaped signal with 3% width value are approximately 0.2 fb at a mass of 200 GeV for m_X and 0.04 fb at $\sim$ 6 TeV for m_{ZX}. Figures 10.16–10.18 show the impact of each of the three uncertainty sources discussed in Section 8 by adding one a time on the limits for a Gaussian-shaped signal with a relative width value of 3% in all the categories. The dominant uncertainty source is the fit spurious signal uncertainty. It worsens the limit at the lowest considered mass value by less than 50% in all cases except for the m_X spectrum in the leading small-R-jet category and the m_{ZX} spectrum in the leading large-R-jet category, where it reaches up to around 80%. The detector resolution effects on the limits are studied in a conservative way. It has impacts on the signal shape, resulting in changes of thes spurious signal systematics. The spurious signal systematics are re-estimated using the new signal shape, following the same procedures in Section 8.4. The ratio is calculated using limit results considering detector resolution effect over that without it, as a function of the m_X and m_{ZX} values. Figure 10.19 shows the comparison results of the m_X and m_{ZX} spectra in the leading small-R-jet category for the Gaussian-shaped signal with a width value of 3%, where the

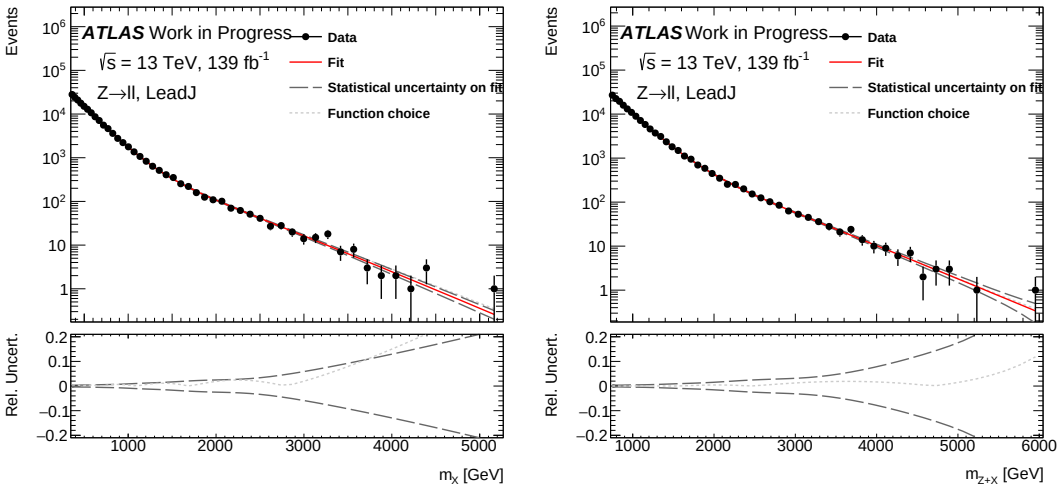

Figure 10.9: Background uncertainties shown as a function of m_X (left) and m_{ZX} (right) in the SRs of the leading small-R-jet (LeadJ) category for the combined $Z \to \ell^+\ell^-$ decay channel, based on the data spectra.

detector resolution has the largest impact. It has around 10% impact in the low mass region and is negligible in the high mass region.

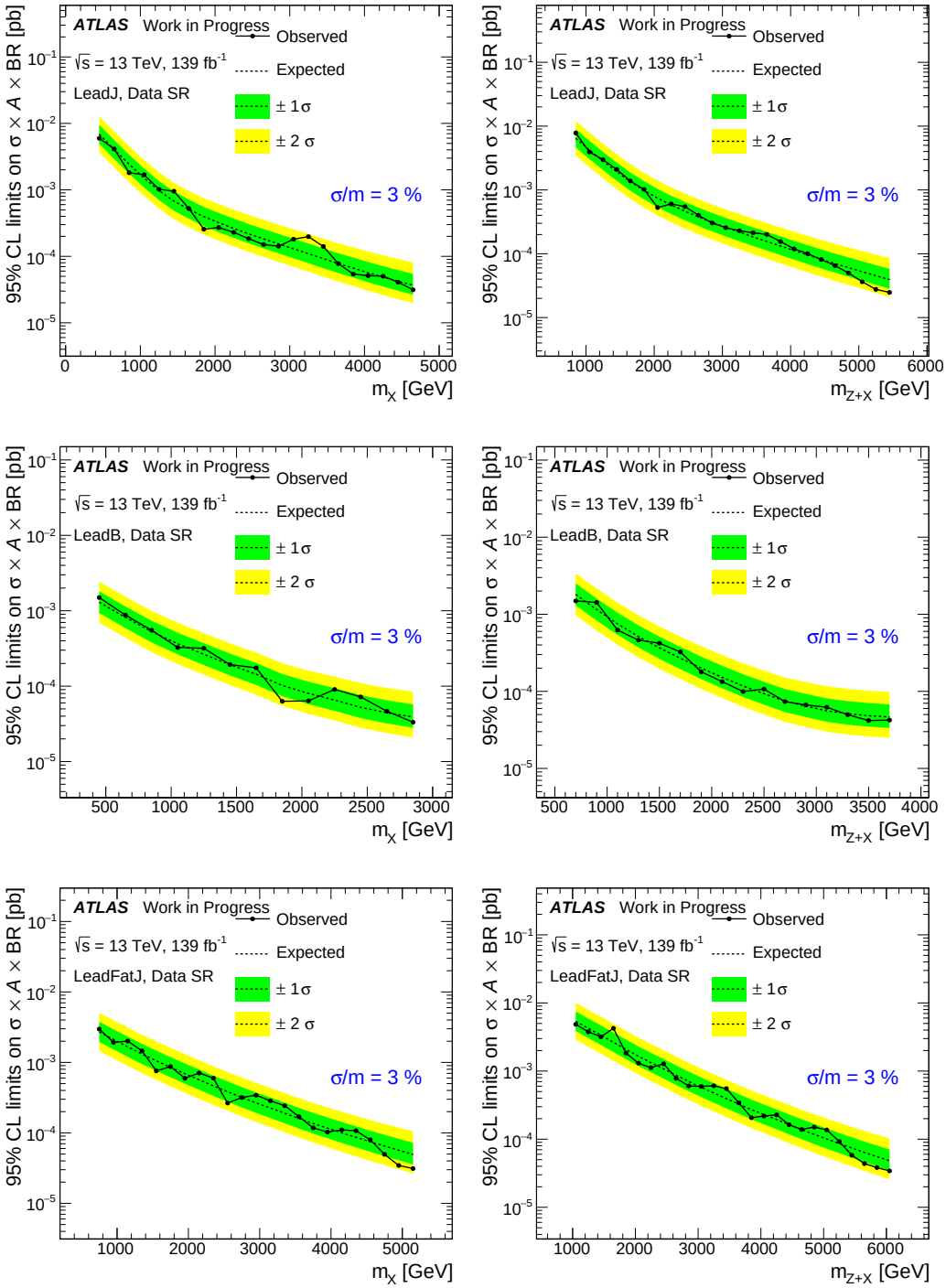

Figure 10.10: Upper limits at 95% CL on the $\sigma \times \mathcal{A} \times$ BR of a Gaussian-shaped signal with a width value of 3% as a function of m_X (left) and m_{ZX} (right) in the SRs of the leading small-R-jet (LeadJ) (top), leading b-jet (LeadB) (middle) and leading large-R-jet (LeadFatJ) (bottom) categories. The expected upper limit and corresponding $\pm 1\sigma$ and $\pm 2\sigma$ uncertainty bands are also shown.

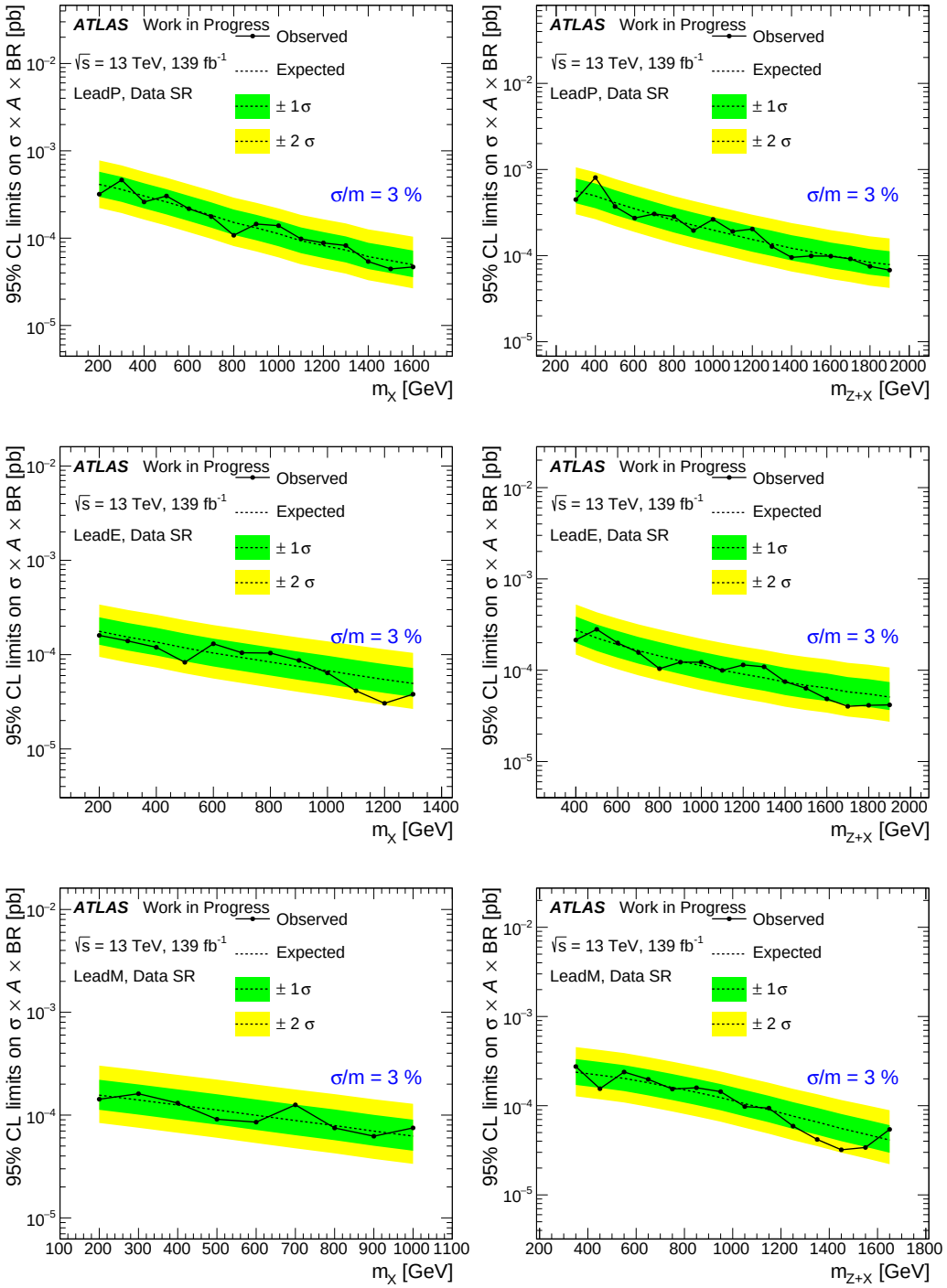

Figure 10.11: Upper limits at 95% CL on the $\sigma \times \mathcal{A} \times$ BR of a Gaussian-shaped signal with a width value of 3% as a function of m_X (left) and m_{ZX} (right) in the SRs of the leading photon (LeadP) (top), leading electron (LeadE) (middle) and leading muon (LeadM) (bottom) categories. The expected upper limit and corresponding $\pm 1\sigma$ and $\pm 2\sigma$ uncertainty bands are also shown.

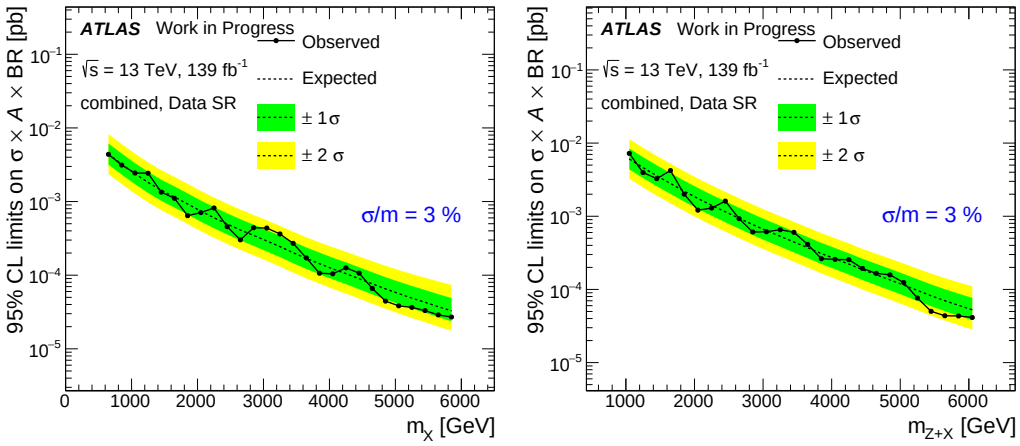

Figure 10.12: Upper limits at 95% CL on the $\sigma \times \mathcal{A} \times$ BR of a Gaussian-shaped signal with a width value of 3% as a function of m_X (left) and m_{ZX} (right) in the SR of the combined category. The expected upper limit and corresponding $\pm 1\sigma$ and $\pm 2\sigma$ uncertainty bands are also shown.

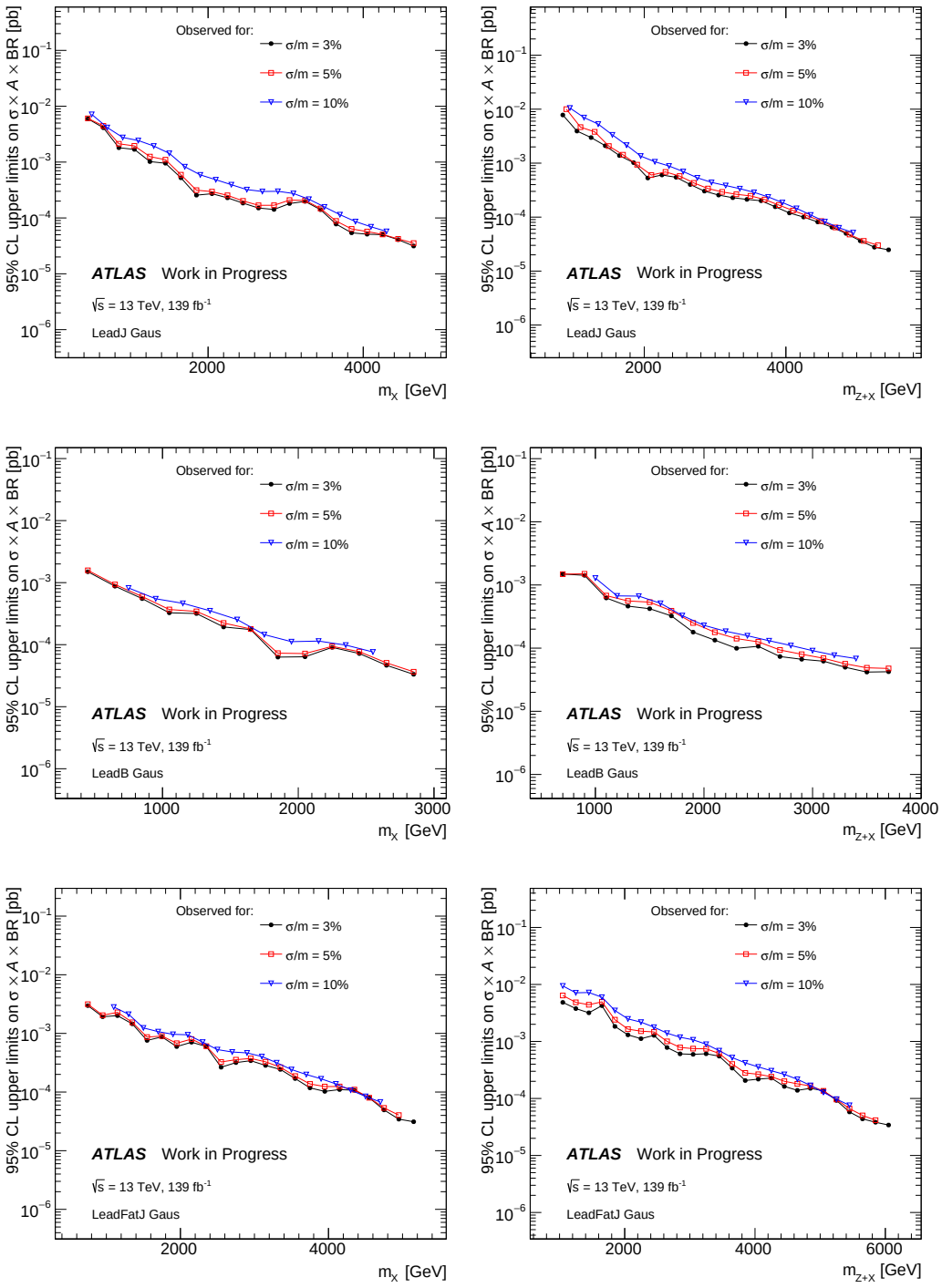

Figure 10.13: Comparison of observed 95% CL upper limits on the $\sigma \times \mathcal{A} \times$ BR of Gaussian-shaped signals with width values of 3%, 5% and 10% as a function of m_X (left) and m_{ZX} (right) in the SRs of the leading small-R-jet (LeadJ) (top), leading b-jet (LeadB) (middle) and leading large-R-jet (LeadFatJ) (bottom) categories.

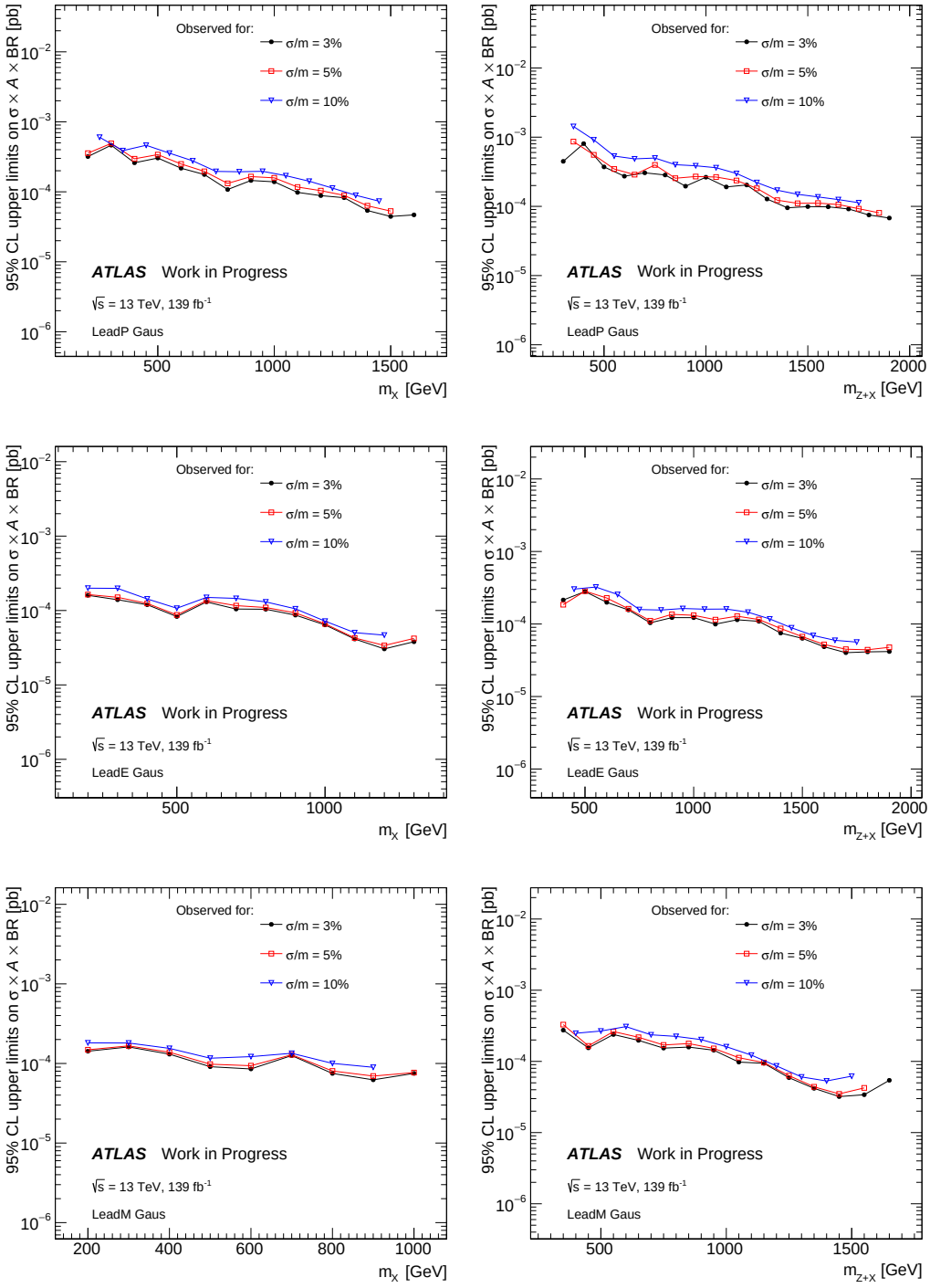

Figure 10.14: Comparison of observed 95% CL upper limits on the $\sigma \times \mathcal{A} \times \mathrm{BR}$ of Gaussian-shaped signals with width values of 3%, 5% and 10% as a function of m_X (left) and m_{ZX} (right) in the SRs of the leading photon (LeadP) (top), leading electron (LeadE) (middle) and leading muon (LeadM) (bottom) categories.

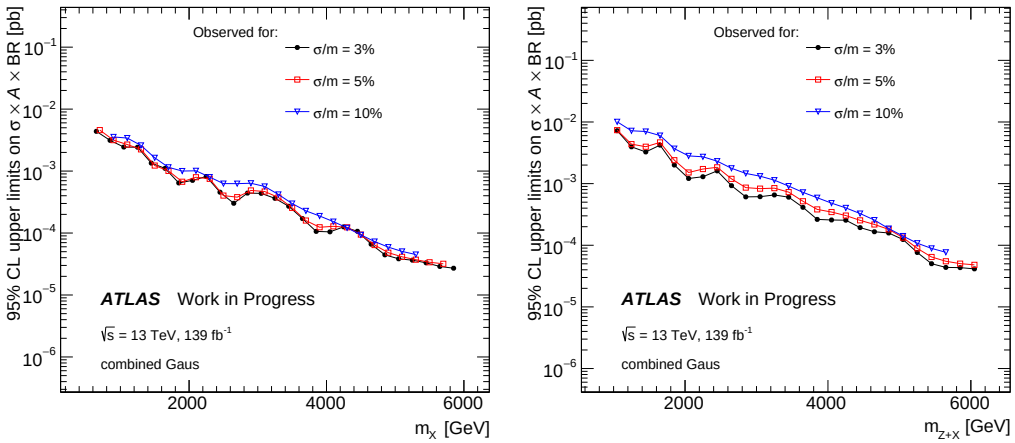

Figure 10.15: Comparison of observed 95% CL upper limits on the $\sigma \times \mathcal{A} \times \mathrm{BR}$ of Gaussian-shaped signals with width values of 3%, 5% and 10% as a function of m_X (left) and m_{ZX} (right) in the SR of the combined category.

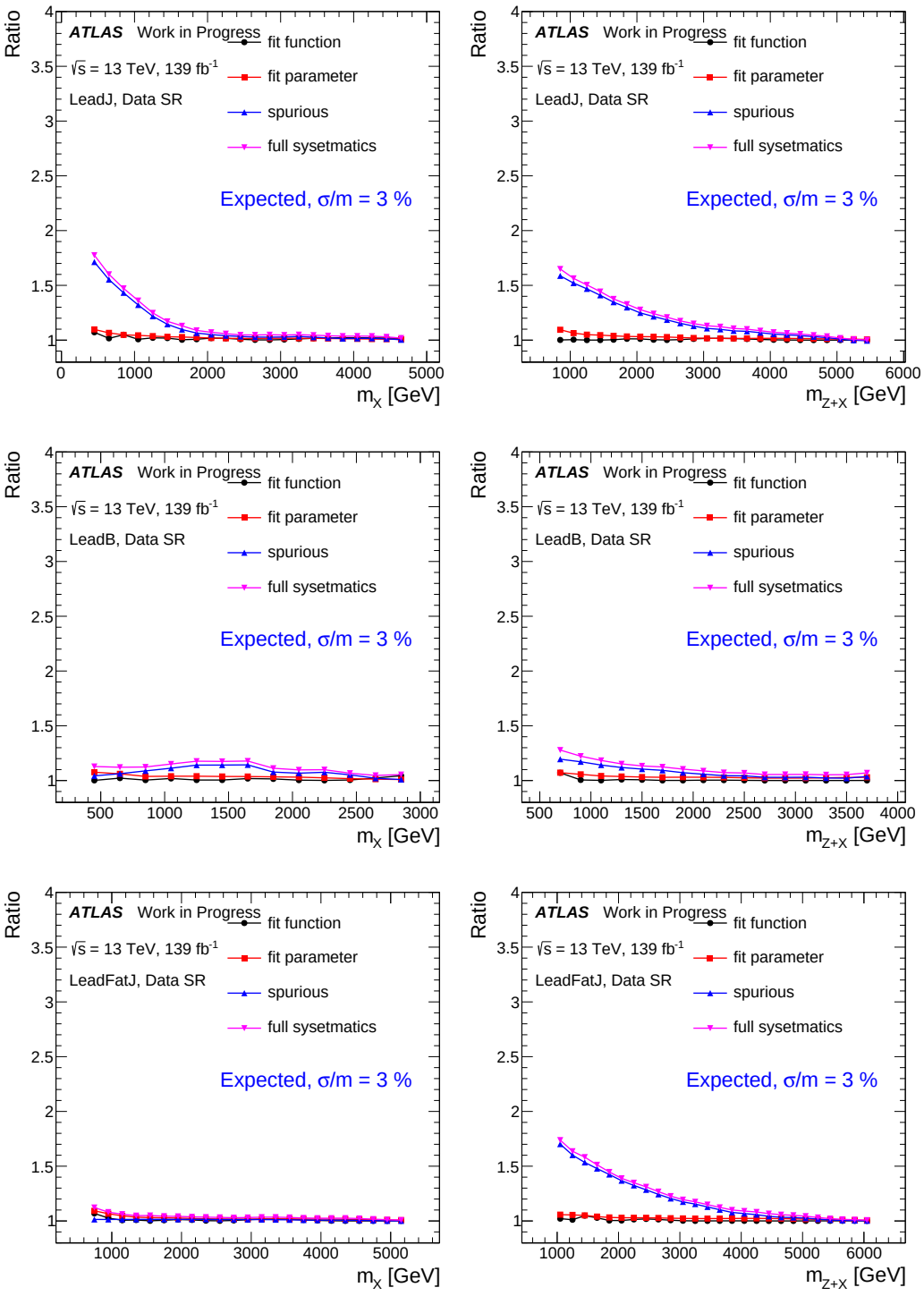

Figure 10.16: Comparison of expected 95% CL upper limits on the $\sigma \times \mathcal{A} \times$ BR of Gaussian-shaped signals with a width value of 3% for a given systematic uncertainty over that without any systematic uncertainty as a function of m_X (left) and m_{ZX} (right) in the SRs of the leading small-R-jet (LeadJ) (top), leading b-jet (LeadB) (middle) and leading large-R-jet (LeadFatJ) (bottom) categories.

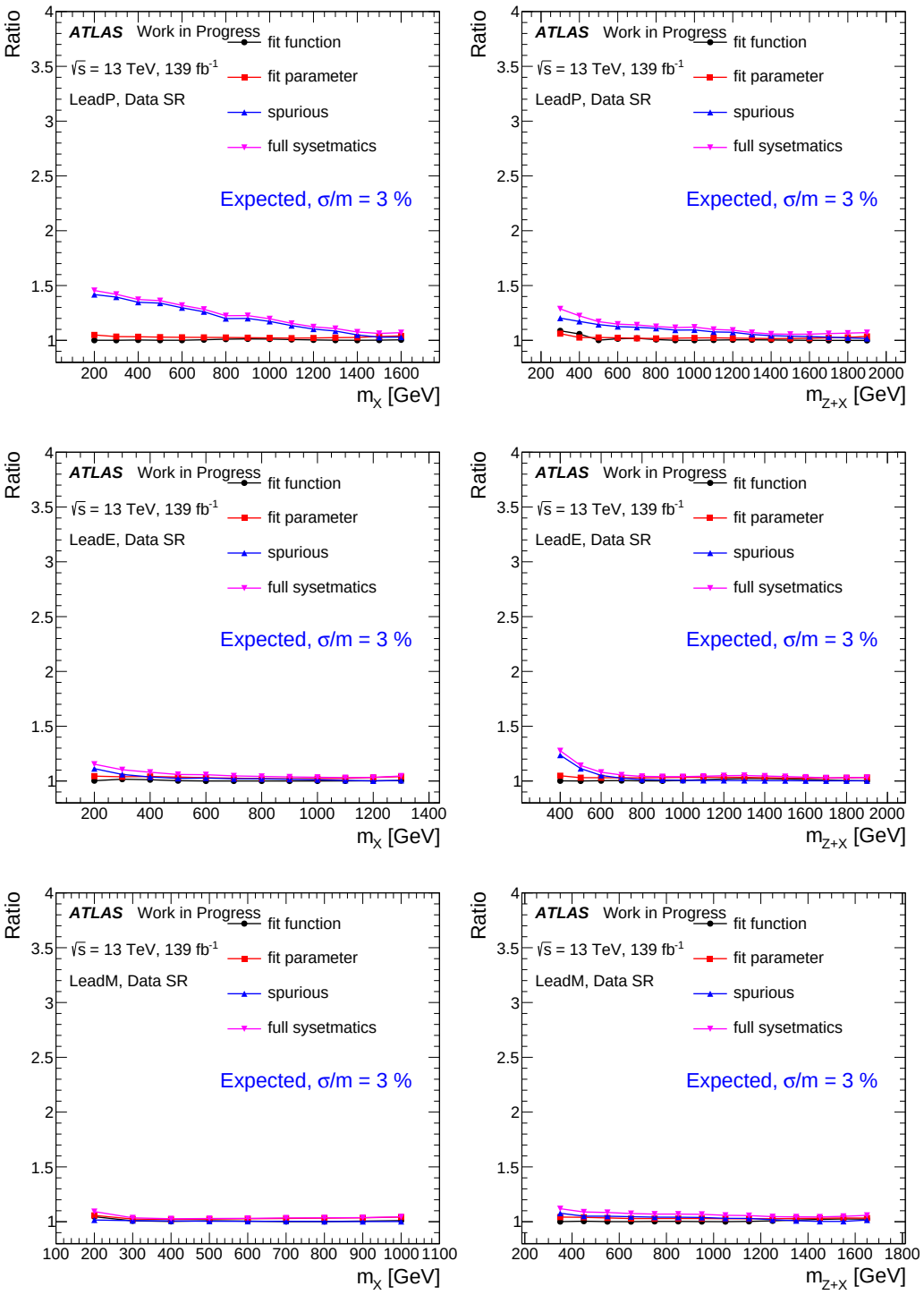

Figure 10.17: Comparison of expected 95% CL upper limits on the $\sigma \times \mathcal{A} \times$ BR of Gaussian-shaped signals with a width value of 3% for a given systematic uncertainty over that without any systematic uncertainty as a function of m_X (left) and m_{ZX} (right) in the SRs of the leading photon (LeadP) (top), leading electron (LeadE) (middle) and leading muon (LeadM) (bottom) categories.

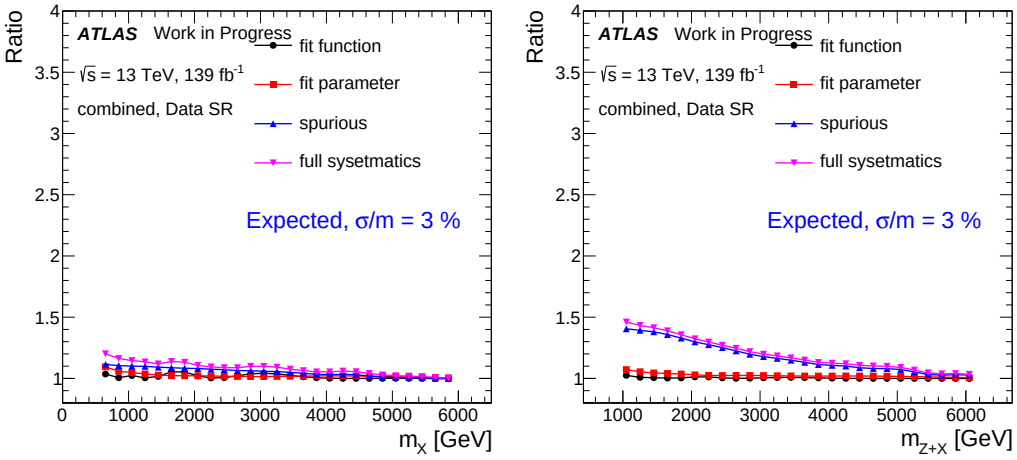

Figure 10.18: Comparison of expected 95% CL upper limits on the $\sigma \times \mathcal{A} \times$ BR of Gaussian-shaped signals with a width value of 3% for a given systematic uncertainty over that without any systematic uncertainty as a function of m_X (left) and m_{ZX} (right) in the SR of the combined category.

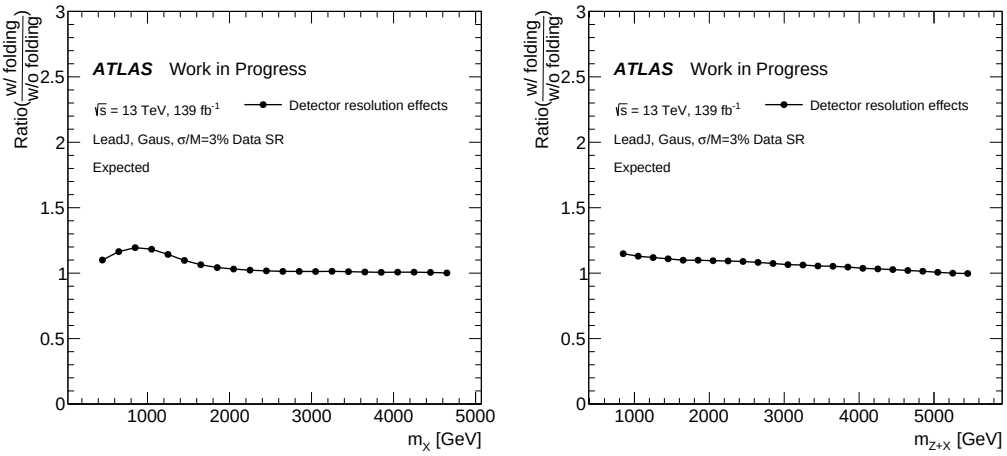

Figure 10.19: Comparison of expected 95% CL upper limits on the $\sigma \times \mathcal{A} \times$ BR of Gaussian-shaped signals with a width value of 3% for considering detector resolution effect over that without detector resolution effect as a function of m_X (left) and m_{ZX} (right) in the SR of the leading small-R-jet category.

11 - Conclusions and outlook

This dissertation reports a novel generic search for resonances produced in association with or decaying to a Z boson with subsequent decay of the latter to a ee or $\mu\mu$ pair for a transverse momentum of the Z boson greater than 100 GeV, using $139\,\text{fb}^{-1}$ of proton–proton collisions recorded at $\sqrt{s} = 13\,\text{TeV}$ with the ATLAS detector at the LHC between 2015 and 2018. Six independent event categories are defined by the leading p_{T} object in the recoil system of Z boson, which is sensitive to different final states of the potential signal. For the Standard Model background, a data-driven approach is used to estimate the invariant mass spectra of the recoil system of the Z boson and of the entire final state, including the Z boson in all six categories as well as the combined one. No significant excess is observed above the smoothly falling distributions of the Standard Model background. Constraints on a Gaussian-shaped signal with varying relative width values between 3% and 10% are derived in this thesis.

For the event classifications discussed in Chapter 7, the leading p_{T} object in X includes visible objects: non-b small-R jet, b-jet, large-R jet, photon, electron and muon. The $E_{\text{T}}^{\text{miss}}$ can be added aiming at signals which have neutrinos in the final states, like $pp \to Y \to ZZ \to ll\nu\nu$. Instead of the invariant mass, the distributions of transverse mass can be used to examine the discrepancy between the SM background predictions and data. Another point that could be improved is to require two or more objects of the same type to reconstruct X, which is likely to happen and increase signal sensitivity. With an expected larger dataset of pp collisions from the LHC Run 3 period, the event statistics and upper edge of the search range will be largely extended, especially in the low statistics event categories. Furthermore, the Z boson with full hadronic final states can be added to increase the event statistics. The branching ratio of the leptonic decays of the Z boson is relatively small compared to the hadronic decays.

A - Time resolution measurement of the RPC detector

In addition to the generic search analysis documented in the main body of this dissertation, I also participate in the performance studies of the Resistive Plate Chambers (RPCs) [33]. What I contribute is the time resolution measurements using the data from pp collisions with a center-of-mass energy of 13 TeV recorded in 2018. This appendix documents the details of time resolution measurements.

RPCs are gaseous ionization detectors used by the Level-1 muon trigger system in the barrel region of the ATLAS muon spectrometer. The RPC detectors are arranged in three concentric doublet layers and consist of approximately 3700 gas volumes, with a total surface of more than 4000 m^2. Each RPC detector chamber consists of 2 detector layers with η and ϕ readout strips. The RPC gas volumes are made of two parallel resistive (bakelite) plates separated by a 2 mm gas gap with insulating spacers as shown in Figure A.1. The readout is organised by orthogonal η and ϕ strips with 23-35 mm, with η strips measuring muon curvature. The RPC operates in the safe avalanche mode with a nominal HV of 9.6 kV. The intrinsic time resolution is around one ns, while the time to digital converter has a sampling bin of 3.125 ns.

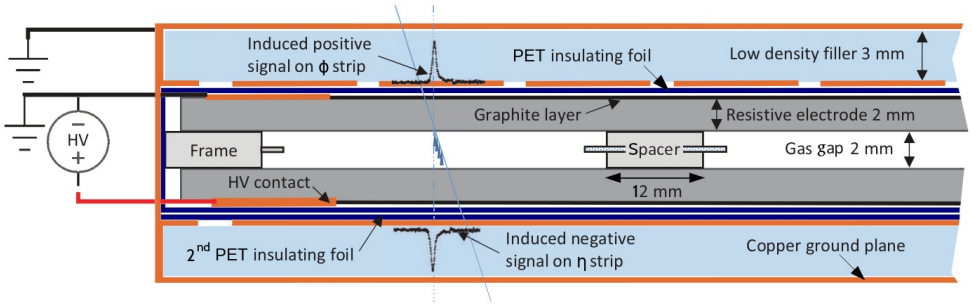

Figure A.1: Schematic of the ATLAS RPC single layer. [33]

The time resolution of the present ATLAS RPCs is measured for the entire RPC system, using the data collected in 2018 with an integrated luminosity of 60.8 fb^{-1}. The probe muons from decays of Z bosons are used to avoid potential bias from trigger timing. As shown in Figure A.2. The RPC total time resolution (σ_{total}) is estimated using the hit time differences between detector signals generated by the same muon passing through the two parallel RPC detector layers. The schematic view is shown in Figure A.3a. The time differences are computed using hits produced from a pair of η or ϕ strips closest to the track of muon. The separation distance between two layers is around 20 mm, producing little time-of-flight time. The width of the time difference distribution is extracted using a binned maximum likelihood fit of the Gaussian function. An example distribution is shown in Figure A.4a for a single pair of η strips. This procedure is performed for all possible

combinations of $\eta - \eta$ and $\phi - \phi$ pairs. Only combinations with at least 100 muon entries are used to remove inefficient strips. Additionally, the Kolmogorov–Smirnov (KS) test removed strip pairs with bad fit quality. Figure A.4b shows the distributions of Gaussian width values from the entire RPC system. The mean width value is approximately 2.1 (2.2) ns for η (ϕ) strip pairs. The small difference between η and ϕ views is due to the different cluster size composition [33].

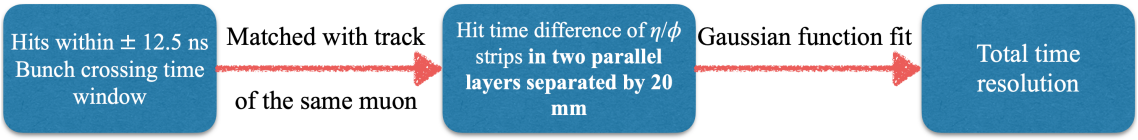

Figure A.2: Workflow of total time resolution measurement.

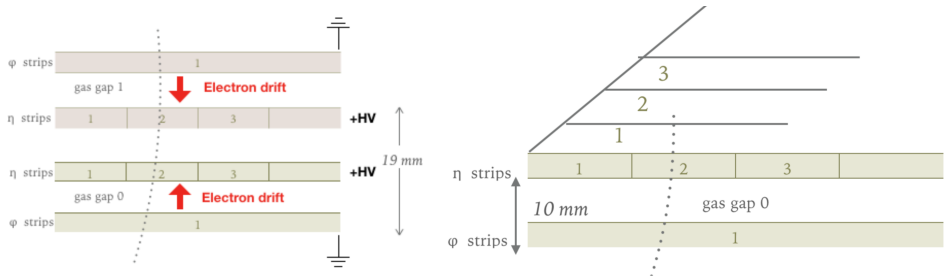

(a) (b)

Figure A.3: Sketch of RPC layers in ATLAS used to measure: (a) the total time resolution by taking the time difference using strips matched with muon track in the two layers (either two η strips or two ϕ strips), (b) the electronics time resolution by taking the time difference using a pair of η-ϕ strips in the same layer.

The RPC total time resolution can be expressed as:

$$\sigma^2_{\text{total}} = \sigma^2_{\text{intrinsic}} + \sigma^2_{\text{electronics}} \tag{A.1}$$

where $\sigma_{\text{intrinsic}}$ corresponds to the intrinsic RPC time resolution and $\sigma_{\text{electronics}}$ is the electronics component from readout system. The electronics component has several sources like the associated jitter [134]. The electronics component is estimated using the time difference between η and ϕ hits from the same muon in a single detector layer, as shown in Figure A.5. The intrinsic component is vanished due to the same avalanche induced by the passing muon. The time difference distribution is made for each pair of orthogonal η and ϕ strip pairs as shown in Figure A.3b. A binned maximum likelihood fit using the Gaussian function is performed to extract the width for each time difference distribution. Similar to the method in total time resolution, only distributions with sufficient muon entries and large KS test values are selected to remove strips with low efficiency and bad fit quality.

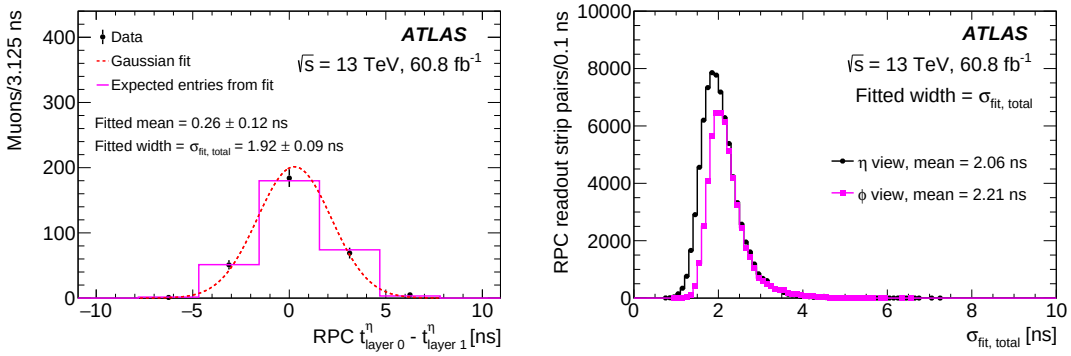

(a) (b)

Figure A.4: (a) Time-difference distribution between signals generated by the same muon in a single pair of η strips, matched with the muon track, in two parallel RPC detector layers. The bin width corresponds to the 3.125 ns sampling time. (b) Distribution of the total time differences for the all selected RPC strip pairs [33].

Figure A.5: Workflow of total time resolution measurement.

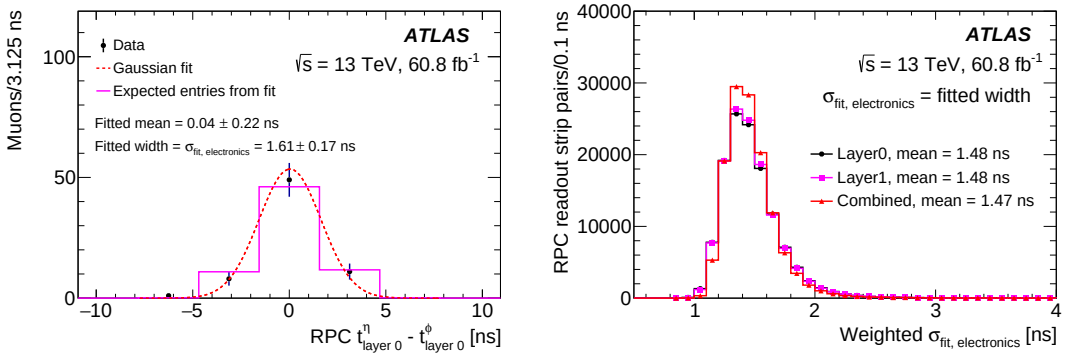

(a) (b)

Figure A.6: (a) Time-difference distribution between signals generated by the same muon in a single pair of η and ϕ strips, matched with the muon track, belonging to one detector layer. (b) Distribution of the electronic component of the time resolution [33].

An example distribution is shown in Figure A.6a for a pair of orthogonal η and ϕ strips. All possible combinations of η and ϕ strips are considered, and the statistically weighted average values are computed to present. Figure A.6b shows the Gaussian width results of time difference distributions from the entire RPC system. The intrinsic component of time resolution is extracted using the Equation A.1 and shown in Figure A.7. Then the intrinsic RPC resolution is estimated as $\sigma_{\text{intrinsic}}/\sqrt{2}$ and is approximately one ns, which is consistent with the previous measurement obtained at test-beam facilities [135].

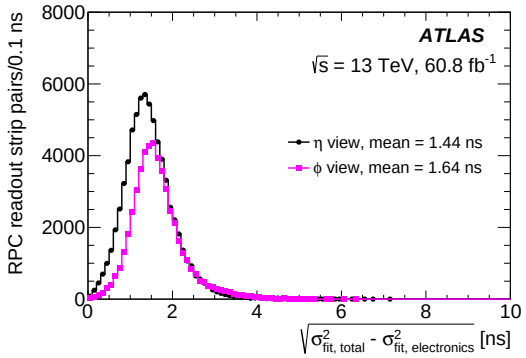

Figure A.7: Distribution of the intrinsic component of the time resolution for η and ϕ panels [33].

B - Search for heavy resonances with the WW final state

Introduction

What I contributed in the search for heavy resonances with the WW final state, which was published in Ref. [34] is the evaluation of theoretical systematic uncertainties of the main background processes. This appendix briefly introduces this analysis and focuses on my contribution.

A search for heavy resonances (R) decaying to two W bosons was performed using a dataset corresponding to an integrated luminosity of 36.1 fb^{-1} recorded by the ATLAS detector at the center-of-mass energy of 13 TeV. This analysis studied the decay mode $R \to WW \to e\nu\mu\nu$ in three event categories, two orthogonal categories with one and at least two jets optimised for the Vector Boson fusion (VBF) production with R being a heavy Higgs boson and one quasi-inclusive category optimised for the gluon-gluon fusion (ggF) production of the Higgs boson. The ATLAS and CMS collaborations have preformed several searches for a heavy Higgs boson in both leptonic and hadronic decaying final states of the VV channel [26, 136–150]. The $e\nu\mu\nu$ final state complements the previous searches with other final state, and enhances the signal sensitivity to low mass resonances.

Event selections

The WW candidates were pre-selected by requiring to have two oppositely leptons with $p_{\mathrm{T}}^{\ell,\,\mathrm{(sub)lead}} > 25$ GeV and no additional lepton with $p_{\mathrm{T}}^{\ell,\,\mathrm{other}} > 15$ GeV after applying the quality criteria. Only the different flavours channel was consider to provide the largest signal sensitivity. The invariant mass of the leading and subleading leptons ($m_{\ell\ell}$) was required to be larger than 10 GeV to reject background from low mass resonances via $\tau\tau$ decaying mode. The signal regions (SRs) were defined and optimised using the BDT method, as summarised in Table B.1, where $\Delta\eta_{\ell\ell}$ is the pseudorapidity difference between the two leptons, $\max(m_{\mathrm{T}}^{W})$ is maximum value of the transverse mass using lepton's transverse momentum (p_{T}^{ℓ}) and azimuthal angle (ϕ^{ℓ}) and azimuthal angle of missing transverse momentum ($\phi^{E_{\mathrm{T}}^{\mathrm{miss}}}$) by

$$m_{\mathrm{T}}^{W} = \sqrt{2p_{\mathrm{T}}^{\ell}E_{\mathrm{T}}^{\mathrm{miss}}\left(1-\cos(\phi^{\ell}-\phi^{E_{\mathrm{T}}^{\mathrm{miss}}})\right)}. \tag{B.1}$$

Events with at least one b-tagged jets were rejected to suppress top-quark background. Two orthogonal event categories for VBF production mode were defined by requiring only one jet ($N_{\mathrm{jet}} = 1$, $\mathrm{SR_{VBF1J}}$) and at least two jets ($N_{\mathrm{jet}} \geq 2$, $\mathrm{SR_{VBF2J}}$). The rest of the events after excluding the VBF phase space was collected by the quasi-inclusive ggF category ($\mathrm{SR_{ggF}}$). In the $\mathrm{SR_{VBF1J}}$ category, the contributions of ggF signal was minimized by two variables: the pseudorapidity of the jet (η_j) and minimum value of pseudorapidity difference between

the jet and leptons. In the SR_{VBF2J} category, the invariant mass (m_{jj}) and rapidity difference (Δy_{jj}) of the leading two jets were optimised concerning the character of the VBF signal.

Table B.1: Event selections in the ggF and VBF signal regions [34].

SR_{ggF}	SR_{VBF1J}	SR_{VBF2J}
Common selections		
$N_{b\text{-tag}} = 0$ $\lvert\Delta\eta_{\ell\ell}\rvert < 1.8$ $m_{\ell\ell} > 55$ GeV $p_{\mathrm{T}}^{\ell,\mathrm{lead}} > 45$ GeV $p_{\mathrm{T}}^{\ell,\mathrm{sublead}} > 30$ GeV veto if $p_{\mathrm{T}}^{\ell,\mathrm{other}} > 15$ GeV $\max(m_{\mathrm{T}}^{W}) > 50$ GeV		
ggF phase space	VBF1J phase space	VBF2J phase space
Inclusive in N_{jet} but excluding VBF1J and VBF2J phase space	$N_{\mathrm{jet}=1}$ and $\lvert\eta_j\rvert > 2.4$, $\min(\lvert\Delta\eta_{j\ell}\rvert) > 1.75$	$N_{\mathrm{jet}} \geq 2$ and $m_{jj} > 500$ GeV, $\lvert\Delta y_{jj}\rvert > 4$

The discriminating variable used for search was the transverse mass defined as:

$$m_{\mathrm{T}} = \sqrt{(E_{\mathrm{T}}^{\ell\ell} + E_{\mathrm{T}}^{\mathrm{miss}})^2 - |\mathbf{p}_{\mathrm{T}}^{\ell\ell} + \mathbf{E}_{\mathrm{T}}^{\mathrm{miss}}|^2}, \tag{B.2}$$

where $E_{\mathrm{T}}^{\ell\ell} = \sqrt{|\mathbf{p}_{\mathrm{T}}^{\ell\ell}|^2 + m_{\ell\ell}^2}$ and $\mathbf{p}_{\mathrm{T}}^{\ell\ell}$ is the transverse momentum vector for the leading and subleading leptons.

Background estimation

The main backgrounds in this search originated from top-quark and WW processes, with additional small contributions from W/Z+jets, multijet and other diboson processes. The top-quark and WW backgrounds were studied after normalizing to data in the control regions (CRs) with reversing or loosening some requirements in the SRs. The other backgrounds were directly taken from the MC simulations.

Top-quark events consisted of $t\bar{t}$ pair and single top in association with a W boson or another flavour quark. The top-quark CR in ggF (Top CR_{ggF}) production mode was defined as events with one b-tagged jet and passing the other cuts in the SR_{ggF}. For the VBF Top CR (Top CR_{VBF}), VBF1J and VBF2J categories were combined with the cuts on $p_{\mathrm{T}}^{\ell,\mathrm{lead}}$ and $p_{\mathrm{T}}^{\ell,\mathrm{sublead}}$ relaxed and the cuts on $\Delta\eta_{\ell\ell}$, $m_{\ell\ell}$ and $\max(m_{\mathrm{T}}^{W})$ removed. The details are summarised in Table B.2. The final purity of top-quark background is 97% and 96% in the ggF and VBF CRs, respectively.

For the WW CR in the ggF category (WW CR_{ggF}), the cut of $|\Delta\eta_{\ell\ell}|$ was reversed, and the others were unchanged. For the VBF CRs, the VBF2J category was removed due to its small contribution and a considerable contamination from the top-quark background. The

selections of the VBF1J category (WW $\mathrm{CR}_{\mathrm{VBF1J}}$) were optimised to increase the statistics. The selections are also shown in Table B.2, and the purity is 52% and 46% in the WW $\mathrm{CR}_{\mathrm{ggF}}$ and the WW $\mathrm{CR}_{\mathrm{VBF1J}}$, respectively.

Table B.2: Event selections in the ggF and VBF control regions for WW and top-quark backgrounds [34].

WW $\mathrm{CR}_{\mathrm{ggF}}$	Top $\mathrm{CR}_{\mathrm{ggF}}$	WW $\mathrm{CR}_{\mathrm{VBF1J}}$	Top $\mathrm{CR}_{\mathrm{VBF}}$
$N_{b\text{-tag}} = 0$	$N_{b\text{-tag}} = 1$	$N_{b\text{-tag}} = 0$	$N_{b\text{-tag}} \geq 1$
$\lvert\Delta\eta_{\ell\ell}\rvert > 1.8$	$\lvert\Delta\eta_{\ell\ell}\rvert < 1.8$	($\lvert\Delta\eta_{\ell\ell}\rvert > 1.8$ or	-
$m_{\ell\ell} > 55$ GeV		10 GeV $m_{\ell\ell} < 55$ GeV	$m_{\ell\ell} > 10$ GeV
$p_{\mathrm{T}}^{\ell,\,\mathrm{lead}} > 45$ GeV		$p_{\mathrm{T}}^{\ell,\,\mathrm{lead}} > 25$ GeV	
$p_{\mathrm{T}}^{\ell,\,\mathrm{sublead}} > 30$ GeV		$p_{\mathrm{T}}^{\ell,\,\mathrm{sublead}} > 25$ GeV	
veto if $p_{\mathrm{T}}^{\ell,\,\mathrm{other}} > 15$ GeV		-	
Excluding VBF1J and VBF2J phase space		VBF1J phase space	VBF1J and VBF2J phase space

Theoretical uncertainties of the main background

For the top-quark and WW backgrounds normalised in the CRs, the theoretical uncertainties were estimated for the extrapolation from the CRs to the SRs based on the prescription from the LHC Higgs Cross Section Working Group [151]. The uncertainties are missing high-order corrections, PDF variations, and additional MC modelling issues.

For the top-quark background, the dominant experimental and theoretical uncertainties are shown in Table B.3. The ME+PS represents the matrix element and parton shower modelling uncertainties estimated by comparing two sets of MC samples generated by Powheg-Box+Pythia8 and Sherpa 2.2.1. The Scale corresponds to the uncertainty of missing high-order correction. It was estimated by varying the QCD renormalisation (μ_{R}) and factorisation (μ_{F}) scales up and down by a factor of two. An additional uncertainty of 20% was applied on the contribution of the single top-quark process due to interference effects between $t\bar{t}$ and single top-quark processes [152], which corresponds to "Signal Top." The PDF uncertainties were estimated by the envelope of uncertainty within the NNPDF30NLO PDFset and by comparing the nominal values to the different PDFsets: CT14 and MMHT2014 PDFsets, following the recommendations [153]. The m_{T} dependent PDF uncertainties were considered in the three SRs, as shown in Figure B.1.

Similar relative theoretical uncertainties were estimated for the WW background, and the dominant uncertainties are summarised in Table B.4. The ME+PS uncertainty was estimated by comparing the nominal samples from Sherpa 2.2.1 and the alternative one from Powheg-Box+Pythia8. The renormalisation, factorisation and resummation (qsf) were also varied up and down by a factor of two. The CKKW (Catani-Krauss-Kuhn-Webber) [154] matching scale uncertainty was evaluated by varying between 15 GeV and

30 GeV from the nominal scale of 20 GeV. The CSS (Catani-Seymour Scheme) represents an uncertainty of the parton shower scheme. The PDF uncertainties were evaluated following the same procedure as the top-quark background and shown in Figure B.2.

Table B.3: The relative uncertainties (%) of the dominant experimental and the theoretical sources of top-quark background in the SRs and the CRs. The dominant experimental uncertainties are from Jet and b-tag and the dominant theoretical ones are from ME+PS, Scale, Single top and PDF. The last column shows the total uncertainties [34].

Source	Jet	b-tag	ME+PS	Scale	Single top	PDF	Total
$\mathrm{SR_{ggF}}$	5.2	17	1.3	3.0	4.2	2.5	19
$\mathrm{SR_{VBF1J}}$	9.6	7.8	1.0	1.6	5.9	2.6	15
$\mathrm{SR_{VBF2J}}$	9.7	14	9.5	5.0	2.1	3.4	21
Top $\mathrm{CR_{ggF}}$	2.2	4.8	0.34	0.21	2.6	3.0	6.6
WW $\mathrm{CR_{ggF}}$	5.3	18	1.1	6.3	4.0	3.2	20
Top $\mathrm{CR_{VBF}}$	8.2	3.5	10	1.5	1.3	3.7	14
WW $\mathrm{CR_{VBF1J}}$	9.9	8.3	9.4	3.9	5.3	2.7	18

Table B.4: The relative uncertainties (%) of the dominant experimental and the theoretical sources of top-quark background in the SRs and the CRs. The dominant experimental uncertainties are from Jet and Pile-up and the dominant theoretical ones are from ME+PS, μ_{R}, Resummation and PDF. The last column shows the total uncertainties [34].

Source	Jet	Pile-up	ME+PS	μ_{R}	Resummation	PDF	Total
$\mathrm{SR_{ggF}}$	1.2	1.8	2.4	1.7	3.1	2.7	5.5
$\mathrm{SR_{VBF1J}}$	17	2.8	11	7.3	5.0	2.3	23
$\mathrm{SR_{VBF2J}}$	18	3.1	38	18	1.4	2.1	47
WW $\mathrm{CR_{ggF}}$	1.1	1.8	2.6	0.95	2.9	3.6	5.9
WW $\mathrm{CR_{VBF1J}}$	16	4.5	12	11	2.3	2.8	23

Results

The statistical method to interpret the search results is described in Ref [155]. A Likelihood function $\mathcal{L}$ is defined using m_{T} distributions of the SRs and total event yields of the CRs. All systematic uncertainties, including experimental and theoretical ones, were parameterised and implemented. Figure B.3 shows the distributions of m_{T} in the three SRs. No significant excess or evidence for new heavy resonance was found. the CL_s method

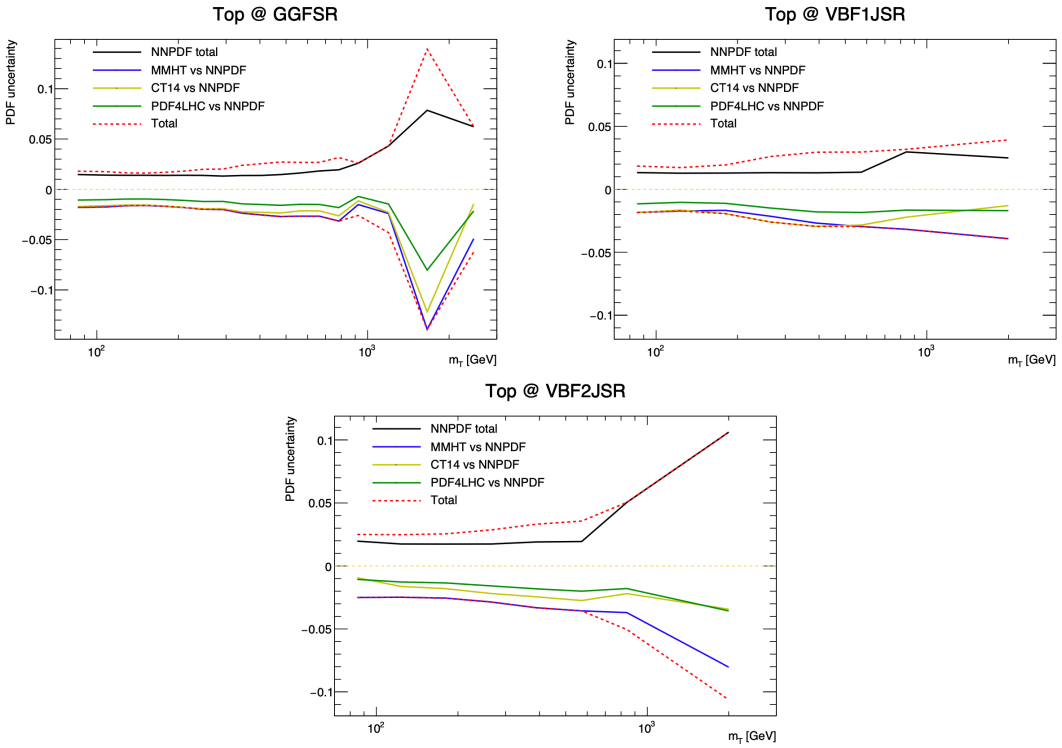

Figure B.1: PDF uncertainties as a function of m_{T} for $\mathrm{SR}_{\mathrm{ggF}}$ (top left), $\mathrm{SR}_{\mathrm{VBF1J}}$ (top right) and $\mathrm{SR}_{\mathrm{VBF2J}}$ for top-quark background.

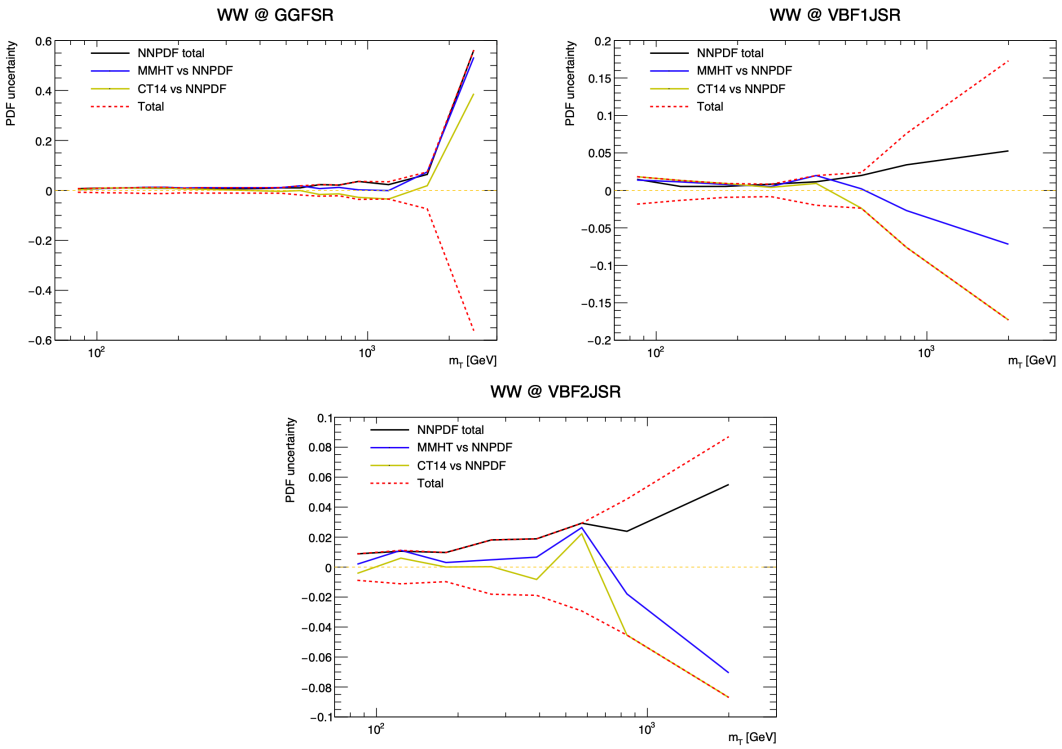

Figure B.2: PDF uncertainties as a function of m_{T} for $\mathrm{SR}_{\mathrm{ggF}}$ (top left), $\mathrm{SR}_{\mathrm{VBF1J}}$ (top right) and $\mathrm{SR}_{\mathrm{VBF2J}}$ for WW background.

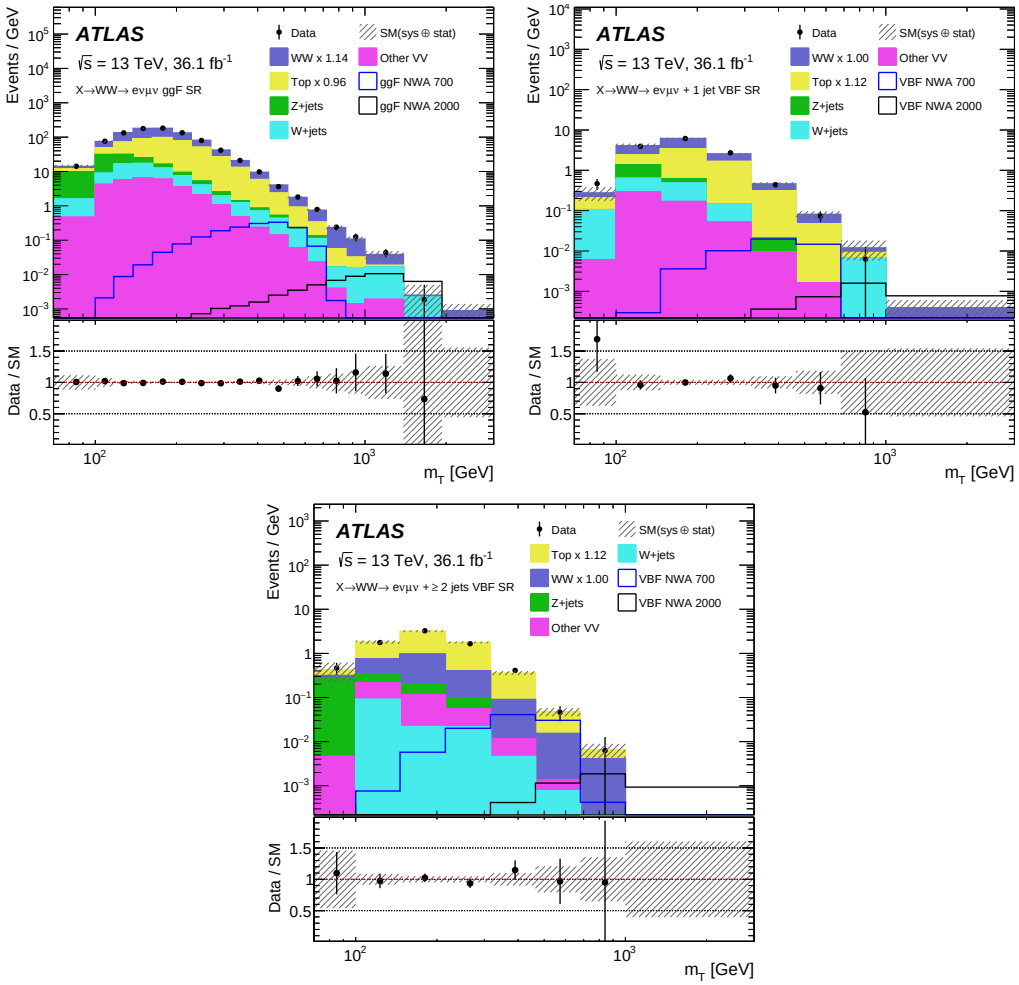

Figure B.3: The distributions of m_{T} after post-fit in the $\mathrm{SR}_{\mathrm{ggF}}$ (top left), the $\mathrm{SR}_{\mathrm{VBF1J}}$ (top right) and the $\mathrm{SR}_{\mathrm{VBF2J}}$ (bottom) categories [34].

was employed, combined with the asymptotic approximation, to compute 95% CL upper limits on signal cross section times branching ratio ($\sigma_R \times \mathrm{BR}(R \to WW)$). An example is shown in Figure B.4 for heavy Higgs boson in the narrow width approximation (NWA) scenario for ggF and VBF production, in the mass range from 200 GeV to 4 TeV.

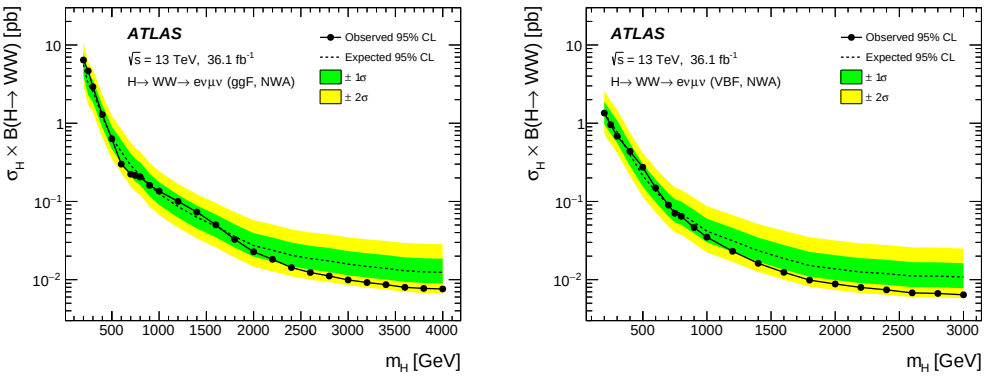

Figure B.4: 95% CL upper limits on the Higgs production cross section times branching ratio for NWA scenario in the mass ranges from 200 GeV to 4 TeV. The left plot is for ggF production and the right one is for VBF production [34].

Bibliograhph

[1] Paul Langacker, Richard W. Robinett, and Jonathan L. Rosner. "New heavy gauge bosons in pp and $p\bar{p}$ collisions". In: *Phys. Rev. D* 30 (7 Oct. 1984), pp. 1470–1487. DOI: 10.1103/PhysRevD.30.1470. URL: https://link.aps.org/doi/10.1103/PhysRevD.30.1470.

[2] Howard E. Haber and Gordon L. Kane. "The Search for Supersymmetry: Probing Physics Beyond the Standard Model". In: *Phys. Rept.* 117 (1985), pp. 75–263. DOI: 10.1016/0370-1573(85)90051-1.

[3] Guido Altarelli, B. Mele, and M. Ruiz-Altaba. "Searching for New Heavy Vector Bosons in $p\bar{p}$ Colliders". In: *Z. Phys. C* 45 (1989). [Erratum: Z.Phys.C 47, 676 (1990)], p. 109. DOI: 10.1007/BF01556677.

[4] Nima Arkani–Hamed, Savas Dimopoulos, and Gia Dvali. "The hierarchy problem and new dimensions at a millimeter". In: *Physics Letters B* 429.3-4 (June 1998), pp. 263–272. ISSN: 0370-2693. DOI: 10.1016/s0370-2693(98)00466-3. URL: http://dx.doi.org/10.1016/S0370-2693(98)00466-3.

[5] Lisa Randall and Raman Sundrum. "Large Mass Hierarchy from a Small Extra Dimension". In: *Physical Review Letters* 83.17 (Oct. 1999), pp. 3370–3373. ISSN: 1079-7114. DOI: 10.1103/physrevlett.83.3370. URL: http://dx.doi.org/10.1103/PhysRevLett.83.3370.

[6] H. Davoudiasl, J.L. Hewett, and T.G. Rizzo. "Bulk gauge fields in the Randall–Sundrum model". In: *Physics Letters B* 473.1-2 (Jan. 2000), pp. 43–49. ISSN: 0370-2693. DOI: 10.1016/s0370-2693(99)01430-6. URL: http://dx.doi.org/10.1016/S0370-2693(99)01430-6.

[7] Gian Francesco Giudice. "Naturally Speaking: The Naturalness Criterion and Physics at the LHC". In: *Perspectives on LHC Physics* (June 2008), pp. 155–178. DOI: 10.1142/9789812779762_0010. URL: http://dx.doi.org/10.1142/9789812779762_0010.

[8] Ian Low, Joseph Lykken, and Gabe Shaughnessy. "Singlet scalars as Higgs boson imposters at the Large Hadron Collider". In: *Physical Review D* 84.3 (Aug. 2011). ISSN: 1550-2368. DOI: 10.1103/physrevd.84.035027. URL: http://dx.doi.org/10.1103/PhysRevD.84.035027.

[9] R. L. Delgado et al. "Production of vector resonances at the LHC via WZ-scattering: a unitarized EChL analysis". In: *Journal of High Energy Physics* 2017.11 (Nov. 2017). ISSN: 1029-8479. DOI: 10.1007/jhep11(2017)098. URL: http://dx.doi.org/10.1007/JHEP11(2017)098.

[10] ATLAS Collaboration. *Search for a heavy Higgs boson decaying into a Z boson and another heavy Higgs boson in the $\ell\ell bb$ and $\ell\ell WW$ final states in pp collisions at $\sqrt{s}$ = 13 TeV with the ATLAS detector*. 2020. arXiv: 2011.05639 [hep-ex].

[11] ATLAS Collaboration. "Search for heavy diboson resonances in semileptonic final states in pp collisions at $\sqrt{s} = 13$ TeV with the ATLAS detector". In: (2020). arXiv: 2004.14636 [hep-ex].

[12] ATLAS Collaboration. *Search for heavy resonances decaying into a pair of Z bosons in the $\ell^+\ell^-\ell'^+\ell'^-$ and $\ell^+\ell^-\nu\bar{\nu}$ final states using 139 fb^{-1} of proton-proton collisions at $\sqrt{s}$ = 13 TeV with the ATLAS detector*. 2020. arXiv: 2009.14791 [hep-ex].

[13] ATLAS Collaboration. *Search for top squarks in events with a Higgs or Z boson using 139 fb^{-1} of pp collision data at $\sqrt{s} = 13$ TeV with the ATLAS detector*. 2020. arXiv: 2006.05880 [hep-ex].

[14] CMS Collaboration. "Search for dark matter produced in association with a leptonically decaying Z boson in proton-proton collisions at $\sqrt{s} = 13$ TeV". In: (Aug. 2020). arXiv: 2008.04735 [hep-ex].

[15] ATLAS Collaboration. "Search for the Production of a Long-Lived Neutral Particle Decaying within the ATLAS Hadronic Calorimeter in Association with a Z Boson from pp Collisions at $\sqrt{s} = 13$ TeV". In: *Phys. Rev. Lett.* 122 (2019), p. 151801. DOI: 10.1103/PhysRevLett.122.151801. arXiv: 1811.02542 [hep-ex].

[16] CMS Collaboration. "Search for a heavy pseudoscalar Higgs boson decaying into a 125 GeV Higgs boson and a Z boson in final states with two tau and two light leptons at $\sqrt{s} = 13$ TeV". In: *JHEP* 03 (2020), p. 065. DOI: 10.1007/JHEP03(2020)065. arXiv: 1910.11634 [hep-ex].

[17] CMS Collaboration. "Search for new neutral Higgs bosons through the $H \to ZA \to \ell^+\ell^- b\bar{b}$ process in pp collisions at $\sqrt{s} = 13$ TeV". In: *JHEP* 03 (2020), p. 055. DOI: 10.1007/JHEP03(2020)055. arXiv: 1911.03781 [hep-ex].

[18] CMS Collaboration. "Search for dark photons in decays of Higgs bosons produced in association with Z bosons in proton–proton collisions at $\sqrt{s} = 13$ TeV". In: *JHEP* 10 (2019), p. 139. DOI: 10.1007/JHEP10(2019)139. arXiv: 1908.02699 [hep-ex].

[19] CMS Collaboration. "Search for a heavy resonance decaying into a Z boson and a Z or W boson in $2\ell 2q$ final states at $\sqrt{s} = 13$ TeV". In: *JHEP* 09 (2018), p. 101. DOI: 10.1007/JHEP09(2018)101. arXiv: 1803.10093 [hep-ex].

[20] CMS Collaboration. "Search for $Z\gamma$ resonances using leptonic and hadronic final states in proton–proton collisions at $\sqrt{s} = 13$ TeV". In: *JHEP* 09 (2018), p. 148. DOI: 10.1007/JHEP09(2018)148. arXiv: 1712.03143 [hep-ex].

[21] CMS Collaboration. "Search for ZZ resonances in the $2\ell 2\nu$ final state in proton–proton collisions at 13 TeV". In: *JHEP* 03 (2018), p. 003. DOI: 10.1007/JHEP03(2018)003. arXiv: 1711.04370 [hep-ex].

[22] CMS Collaboration. "Search for heavy resonances decaying into a vector boson and a Higgs boson in final states with charged leptons, neutrinos and b quarks at $\sqrt{s} = 13$ TeV". In: *JHEP* 11 (2018), p. 172. DOI: 10.1007/JHEP11(2018)172. arXiv: 1807.02826 [hep-ex].

[23] ATLAS Collaboration. "Search for an invisibly decaying Higgs boson or dark matter candidates produced in association with a Z boson in pp collisions at $\sqrt{s} = 13$ TeV with the ATLAS detector". In: *Phys. Lett. B* 776 (2018), p. 318. DOI: 10.1016/j.physletb.2017.11.049. arXiv: 1708.09624 [hep-ex].

[24] ATLAS Collaboration. "Search for heavy ZZ resonances in the $\ell^+\ell^-\ell^+\ell^-$ and $\ell^+\ell^-\nu\bar{\nu}$ final states using proton–proton collisions at $\sqrt{s} = 13$ TeV with the ATLAS detector". In: *Eur. Phys. J. C* 78 (2018), p. 293. DOI: 10.1140/epjc/s10052-018-5686-3. arXiv: 1712.06386 [hep-ex].

[25] ATLAS Collaboration. "Search for a heavy Higgs boson decaying into a Z boson and another heavy Higgs boson in the $\ell\ell bb$ final state in pp collisions at $\sqrt{s} = 13$ TeV with the ATLAS detector". In: *Phys. Lett. B* 783 (2018), p. 392. DOI: 10.1016/j.physletb.2018.07.006. arXiv: 1804.01126 [hep-ex].

[26] ATLAS Collaboration. "Searches for heavy ZZ and ZW resonances in the $\ell\ell qq$ and $\nu\nu qq$ final states in pp collisions at $\sqrt{s} = 13$ TeV with the ATLAS detector". In: *JHEP* 03 (2018), p. 009. DOI: 10.1007/JHEP03(2018)009. arXiv: 1708.09638 [hep-ex].

[27] ATLAS Collaboration. "Search for resonant WZ production in the fully leptonic final state in proton–proton collisions at $\sqrt{s} = 13$ TeV with the ATLAS detector". In: *Phys. Lett. B* 787 (2018), p. 68. DOI: 10.1016/j.physletb.2018.10.021. arXiv: 1806.01532 [hep-ex].

[28] ATLAS Collaboration. "Search for heavy resonances decaying into a W or Z boson and a Higgs boson in final states with leptons and b-jets in 36 fb^{-1} of $\sqrt{s} = 13$ TeV pp collisions with the ATLAS detector". In: *JHEP* 03 (2018), p. 174. DOI: 10.1007/JHEP03(2018)174. arXiv: 1712.06518 [hep-ex]. Erratum: in: *JHEP* 11 (2018), p. 051. DOI: 10.1007/JHEP11(2018)051.

[29] T. D. Lee. "A Theory of Spontaneous T Violation". In: *Phys. Rev. D* 8 (4 Aug. 1973), pp. 1226–1239. DOI: 10.1103/PhysRevD.8.1226. URL: https://link.aps.org/doi/10.1103/PhysRevD.8.1226.

[30] G.C. Branco et al. "Theory and phenomenology of two-Higgs-doublet models". In: *Physics Reports* 516.1-2 (July 2012), pp. 1–102. ISSN: 0370-1573. DOI: 10.1016/j.physrep.2012.02.002. URL: http://dx.doi.org/10.1016/j.physrep.2012.02.002.

[31] T. Aaltonen et al. "Global Search for New Physics with 2.0 fb^{-1} at CDF". In: *Phys. Rev. D* 79 (2009), p. 011101. DOI: 10.1103/PhysRevD.79.011101. arXiv: 0809.3781 [hep-ex].

[32] Georgios Choudalakis. *On hypothesis testing, trials factor, hypertests and the BumpHunter*. 2011. arXiv: 1101.0390 [physics.data-an].

[33] Georges Aad et al. "Performance of the ATLAS RPC detector and Level-1 muon barrel trigger at $\sqrt{s} = 13$ TeV". In: *JINST* 16.07 (2021), P07029. DOI: 10.1088/1748-0221/16/07/P07029. arXiv: 2103.01029 [physics.ins-det].

[34] ATLAS Collaboration. "Search for heavy resonances decaying into WW in the $e\nu\mu\nu$ final state in pp collisions at $\sqrt{s} = 13$ TeV with the ATLAS detector". In: *Eur. Phys. J. C* 78 (2018), p. 24. DOI: 10.1140/epjc/s10052-017-5491-4. arXiv: 1710.01123 [hep-ex].

[35] WN Cottingham and DA Greenwood. *An introduction to the standard model of particle physics*. English. United Kingdom: Cambridge University Press, 1998.

[36] Wikipedia contributors. *Standard Model — Wikipedia, The Free Encyclopedia*. [Online; accessed 16-December-2021]. 2021. URL: https://en.wikipedia.org/w/index.php?title=Standard_Model&oldid=1060203113.

[37] P Hansen. "Results from the UA1 and UA2 experiments". In: (Oct. 1987), 18 p. URL: https://cds.cern.ch/record/182774.

[38] P.A. Zyla et al. "Review of Particle Physics". In: *PTEP* 2020.8 (2020), p. 083C01. DOI: 10.1093/ptep/ptaa104.

[39] H. Fritzsch, Murray Gell-Mann, and H. Leutwyler. "Advantages of the Color Octet Gluon Picture". In: *Phys. Lett. B* 47 (1973), pp. 365–368. DOI: 10.1016/0370-2693(73)90625-4.

[40] David J. Gross and Frank Wilczek. "Ultraviolet Behavior of Nonabelian Gauge Theories". In: *Phys. Rev. Lett.* 30 (1973), pp. 1343–1346. DOI: 10.1103/PhysRevLett.30.1343.

[41] H. David Politzer. "Reliable Perturbative Results for Strong Interactions?" In: *Phys. Rev. Lett.* 30 (1973), pp. 1346–1349. DOI: 10.1103/PhysRevLett.30.1346.

[42] Michael E Peskin and Daniel V Schroeder. *An introduction to quantum field theory*. Includes exercises. Boulder, CO: Westview, 1995. URL: https://cds.cern.ch/record/257493.

[43] Paul A. M. Dirac. "Quantum theory of emission and absorption of radiation". In: *Proc. Roy. Soc. Lond. A* 114 (1927), p. 243. DOI: 10.1098/rspa.1927.0039.

[44] Paul A. M. Dirac. "The quantum theory of the electron". In: *Proc. Roy. Soc. Lond. A* 117 (1928), pp. 610–624. DOI: 10.1098/rspa.1928.0023.

[45] Chen-Ning Yang and Robert L. Mills. "Conservation of Isotopic Spin and Isotopic Gauge Invariance". In: *Phys. Rev.* 96 (1954). [,150(1954)], pp. 191–195. DOI: 10.1103/PhysRev.96.191.

[46] S. L. Glashow. "Partial Symmetries of Weak Interactions". In: *Nucl. Phys.* 22 (1961), pp. 579–588. DOI: 10.1016/0029-5582(61)90469-2.

[47] Steven Weinberg. "A Model of Leptons". In: *Phys. Rev. Lett.* 19 (1967), pp. 1264–1266. DOI: 10.1103/PhysRevLett.19.1264.

[48] Abdus Salam. "Weak and Electromagnetic Interactions". In: *Conf. Proc.* C680519 (1968), pp. 367–377.

[49] Peter W. Higgs. "Broken Symmetries and the Masses of Gauge Bosons". In: *Phys. Rev. Lett.* 13 (1964). [,160(1964)], pp. 508–509. DOI: 10.1103/PhysRevLett.13.508.

[50] Peter W. Higgs. "Broken symmetries, massless particles and gauge fields". In: *Phys. Lett.* 12 (1964), pp. 132–133. DOI: 10.1016/0031-9163(64)91136-9.

[51] G. S. Guralnik, C. R. Hagen, and T. W. B. Kibble. "Global Conservation Laws and Massless Particles". In: *Phys. Rev. Lett.* 13 (1964). [,162(1964)], pp. 585–587. DOI: 10.1103/PhysRevLett.13.585.

[52] F. Englert and R. Brout. "Broken Symmetry and the Mass of Gauge Vector Mesons". In: *Phys. Rev. Lett.* 13 (1964). [,157(1964)], pp. 321–323. DOI: 10.1103/PhysRevLett.13.321.

[53] Duccio Pappadopulo et al. "Heavy vector triplets: bridging theory and data". In: *Journal of High Energy Physics* 2014.9 (Sept. 2014). ISSN: 1029-8479. DOI: 10.1007/jhep09(2014)060. URL: http://dx.doi.org/10.1007/JHEP09(2014)060.

[54] Christiane Lefèvre. "The CERN accelerator complex. Complexe des accélérateurs du CERN". Dec. 2008. URL: https://cds.cern.ch/record/1260465.

[55] R Alemany-Fernandez et al. "Operation and Configuration of the LHC in Run 1". In: (Nov. 2013). URL: https://cds.cern.ch/record/1631030.

[56] Jorg Wenninger. "Operation and Configuration of the LHC in Run 2". In: (Mar. 2019). URL: https://cds.cern.ch/record/2668326.

[57] ATLAS Collaboration. *LuminosityPublicResultsRun1*. 2020. URL: https://twiki.cern.ch/twiki/bin/view/AtlasPublic/LuminosityPublicResults.

[58] ATLAS Collaboration. *LuminosityPublicResultsRun2*. 2021. URL: https://twiki.cern.ch/twiki/bin/view/AtlasPublic/LuminosityPublicResultsRun2#Multiple_Year_Collision_Plots.

[59] G. Aad et al. "ATLAS data quality operations and performance for 2015–2018 data-taking". In: *Journal of Instrumentation* 15.04 (Apr. 2020), P04003–P04003. ISSN: 1748-0221. DOI: 10.1088/1748-0221/15/04/p04003. URL: http://dx.doi.org/10.1088/1748-0221/15/04/P04003.

[60] ATLAS Collaboration. "The ATLAS Experiment at the CERN Large Hadron Collider". In: *JINST* 3 (2008). Also published by CERN Geneva in 2010, S08003. 437 p. DOI: 10.1088/1748-0221/3/08/S08003. URL: https://cds.cern.ch/record/1129811.

[61] ATLAS Collaboration. *ATLAS Magnet System: Technical Design Report, 1*. ATLAS-TDR-6. CERN, 1997. URL: https://cds.cern.ch/record/338080.

[62] ATLAS Collaboration. *ATLAS Central Solenoid: Technical Design Report*. ATLAS-TDR-9. CERN, 1997. URL: https://cds.cern.ch/record/331067.

[63] ATLAS Collaboration. *ATLAS Barrel Toroid: Technical Design Report*. ATLAS-TDR-7. CERN, 1997. URL: https://cds.cern.ch/record/331065.

[64] ATLAS Collaboration. *ATLAS End-Cap Toroids: Technical Design Report*. ATLAS-TDR-8. CERN, 1997. URL: https://cds.cern.ch/record/331066.

[65] ATLAS Collaboration. *ATLAS Inner Detector: Technical Design Report, 1*. ATLAS-TDR-4. CERN, 1997. URL: https://cds.cern.ch/record/331063.

[66] ATLAS Collaboration. *ATLAS Inner Detector: Technical Design Report, 2*. ATLAS-TDR-5. CERN, 1997. URL: https://cds.cern.ch/record/331064.

[67] M Capeans et al. *ATLAS Insertable B-Layer Technical Design Report*. Tech. rep. Sept. 2010. URL: https://cds.cern.ch/record/1291633.

[68] ATLAS Collaboration. *Cluster Properties and Lorentz Angle Measurement in the 4-Layer Pixel Detector Using Cosmic Rays*. ATL-PHYS-PUB-2015-012. 2015. URL: https://cds.cern.ch/record/2020918.

[69] The ATLAS collaboration. "Operation and performance of the ATLAS semiconductor tracker". In: *Journal of Instrumentation* 9.08 (Aug. 2014), P08009–P08009. ISSN: 1748-0221. DOI: 10.1088/1748-0221/9/08/p08009. URL: http://dx.doi.org/10.1088/1748-0221/9/08/P08009.

[70] ATLAS Collaboration. *Particle Identification Performance of the ATLAS Transition Radiation Tracker*. ATLAS-CONF-2011-128. 2011. URL: https://cds.cern.ch/record/1383793.

[71] ATLAS Collaboration. *ATLAS Calorimeter Performance: Technical Design Report*. ATLAS-TDR-1. CERN, 1996. URL: https://cds.cern.ch/record/331059.

[72] ATLAS Collaboration. *ATLAS Liquid-Argon Calorimeter: Technical Design Report*. ATLAS-TDR-2. CERN, 1996. URL: https://cds.cern.ch/record/331061.

[73] ATLAS Collaboration. "Performance of the ATLAS trigger system in 2015". In: *Eur. Phys. J. C* 77 (2017), p. 317. DOI: 10.1140/epjc/s10052-017-4852-3. arXiv: 1611.09661 [hep-ex].

[74] Morad Aaboud et al. "Performance of the ATLAS Trigger System in 2015". In: *Eur. Phys. J. C* 77.5 (2017), p. 317. DOI: 10.1140/epjc/s10052-017-4852-3. arXiv: 1611.09661 [hep-ex].

[75] ATLAS Collaboration. "Measurement of the transverse momentum distribution of Drell–Yan lepton pairs in proton–proton collisions at $\sqrt{s} = 13\,\text{TeV}$ with the ATLAS detector". In: (2019). arXiv: 1912.02844 [hep-ex].

[76] T. Gleisberg et al. "Event generation with SHERPA 1.1". In: *JHEP* 02 (2009), p. 007. DOI: 10.1088/1126-6708/2009/02/007. arXiv: 0811.4622 [hep-ph].

[77] Richard D. Ball et al. "Parton distributions for the LHC Run II". In: *JHEP* 04 (2015), p. 040. DOI: 10.1007/JHEP04(2015)040. arXiv: 1410.8849 [hep-ph].

[78] Stefan Höche et al. "QCD matrix elements + parton showers. The NLO case". In: *JHEP* 04 (2013), p. 027. DOI: 10.1007/JHEP04(2013)027. arXiv: 1207.5030 [hep-ph].

[79] Stefan Höche et al. "QCD matrix elements + parton showers. The NLO case". In: *Journal of High Energy Physics* 2013.4 (Apr. 2013). ISSN: 1029-8479. DOI: 10.1007/jhep04(2013)027. URL: http://dx.doi.org/10.1007/JHEP04(2013)027.

[80] Paolo Nason. "A new method for combining NLO QCD with shower Monte Carlo algorithms". In: *JHEP* 11 (2004), p. 040. DOI: 10.1088/1126-6708/2004/11/040. arXiv: hep-ph/0409146.

[81] Stefano Frixione, Paolo Nason, and Carlo Oleari. "Matching NLO QCD computations with parton shower simulations: the POWHEG method". In: *JHEP* 11 (2007), p. 070. DOI: 10.1088/1126-6708/2007/11/070. arXiv: 0709.2092 [hep-ph].

[82] Simone Alioli et al. "A general framework for implementing NLO calculations in shower Monte Carlo programs: the POWHEG BOX". In: *JHEP* 06 (2010), p. 043. DOI: 10.1007/JHEP06(2010)043. arXiv: 1002.2581 [hep-ph].

[83] Simone Alioli et al. "NLO vector-boson production matched with shower in-POWHEG". In: *Journal of High Energy Physics* 2008.07 (July 2008), pp. 060–060. ISSN: 1029-8479. DOI: 10.1088/1126-6708/2008/07/060. URL: http://dx.doi.org/10.1088/1126-6708/2008/07/060.

[84] Torbjörn Sjöstrand et al. "An introduction to PYTHIA 8.2". In: *Comput. Phys. Commun.* 191 (2015), p. 159. DOI: 10.1016/j.cpc.2015.01.024. arXiv: 1410.3012 [hep-ph].

[85] ATLAS Collaboration. "Measurement of the Z/γ^* boson transverse momentum distribution in pp collisions at $\sqrt{s} = 7$ TeV with the ATLAS detector". In: *JHEP* 09 (2014), p. 145. DOI: 10.1007/JHEP09(2014)145. arXiv: 1406.3660 [hep-ex].

[86] Hung-Liang Lai et al. "New parton distributions for collider physics". In: *Physical Review D* 82.7 (Oct. 2010). ISSN: 1550-2368. DOI: 10.1103/physrevd.82.074024. URL: http://dx.doi.org/10.1103/PhysRevD.82.074024.

[87] J. Pumplin et al. "New Generation of Parton Distributions with Uncertainties from Global QCD Analysis". In: *JHEP* 07 (2002), p. 012. DOI: 10.1088/1126-6708/2002/07/012. arXiv: hep-ph/0201195.

[88] Stefano Frixione, Paolo Nason, and Giovanni Ridolfi. "A Positive-weight next-to-leading-order Monte Carlo for heavy flavour hadroproduction". In: *JHEP* 09 (2007), p. 126. DOI: 10.1088/1126-6708/2007/09/126. arXiv: 0707.3088 [hep-ph].

[89] ATLAS Collaboration. *ATLAS Pythia 8 tunes to 7 TeV data*. ATL-PHYS-PUB-2014-021. 2014. URL: https://cds.cern.ch/record/1966419.

[90] ATLAS Collaboration. "Measurements of inclusive and differential fiducial cross-sections of $t\bar{t}$ production with additional heavy-flavour jets in proton–proton collisions at $\sqrt{s} = 13$ TeV with the ATLAS detector". In: *JHEP* 04 (2019), p. 046. DOI: 10.1007/JHEP04(2019)046. arXiv: 1811.12113 [hep-ex].

[91] J. Alwall et al. "The automated computation of tree-level and next-to-leading order differential cross sections, and their matching to parton shower simulations". In: *JHEP* 07 (2014), p. 079. DOI: 10.1007/JHEP07(2014)079. arXiv: 1405.0301 [hep-ph].

[92] Stefano Carrazza, Stefano Forte, and Juan Rojo. *Parton Distributions and Event Generators*. 2013. arXiv: 1311.5887 [hep-ph].

[93] S. Agostinelli et al. "GEANT4 – a simulation toolkit". In: *Nucl. Instrum. Meth. A* 506 (2003), p. 250. DOI: 10.1016/S0168-9002(03)01368-8.

[94] Sascha Mehlhase. "ATLAS detector slice (and particle visualisations)". In: (May 2021). URL: https://cds.cern.ch/record/2770815.

[95] M. Aaboud et al. "Performance of the ATLAS track reconstruction algorithms in dense environments in LHC Run 2". In: *The European Physical Journal C* 77.10 (Oct. 2017). ISSN: 1434-6052. DOI: 10.1140/epjc/s10052-017-5225-7. URL: http://dx.doi.org/10.1140/epjc/s10052-017-5225-7.

[96] R. Frühwirth. "Application of Kalman filtering to track and vertex fitting". In: *Nuclear Instruments and Methods in Physics Research Section A: Accelerators, Spectrometers, Detectors and Associated Equipment* 262.2 (1987), p. 444. DOI: https://doi.org/10.1016/0168-9002(87)90887-4.

[97] M. Aaboud et al. "Reconstruction of primary vertices at the ATLAS experiment in Run 1 proton–proton collisions at the LHC". In: *The European Physical Journal C* 77.5 (May 2017). ISSN: 1434-6052. DOI: 10.1140/epjc/s10052-017-4887-5. URL: http://dx.doi.org/10.1140/epjc/s10052-017-4887-5.

[98] M. Aaboud et al. "Electron reconstruction and identification in the ATLAS experiment using the 2015 and 2016 LHC proton–proton collision data at $\sqrt{s} = 13\,\text{TeV}$". In: *The European Physical Journal C* 79.8 (Aug. 2019). ISSN: 1434-6052. DOI: 10.1140/epjc/s10052-019-7140-6. URL: http://dx.doi.org/10.1140/epjc/s10052-019-7140-6.

[99] M. Aaboud et al. "Measurement of the photon identification efficiencies with the ATLAS detector using LHC Run 2 data collected in 2015 and 2016". In: *The European Physical Journal C* 79.3 (Mar. 2019). ISSN: 1434-6052. DOI: 10.1140/epjc/s10052-019-6650-6. URL: http://dx.doi.org/10.1140/epjc/s10052-019-6650-6.

[100] G. Aad et al. "Electron and photon performance measurements with the ATLAS detector using the 2015–2017 LHC proton-proton collision data". In: *Journal of Instrumentation* 14.12 (Dec. 2019), P12006–P12006. ISSN: 1748-0221. DOI: 10.1088/1748-0221/14/12/p12006. URL: http://dx.doi.org/10.1088/1748-0221/14/12/P12006.

[101] M. Aaboud et al. "Electron and photon energy calibration with the ATLAS detector using 2015–2016 LHC proton-proton collision data". In: *Journal of Instrumentation* 14.03 (Mar. 2019), P03017–P03017. ISSN: 1748-0221. DOI: 10.1088/1748-0221/14/03/p03017. URL: http://dx.doi.org/10.1088/1748-0221/14/03/P03017.

[102] Yohei Yamaguchi Otilia Ducu Matt Klein. *Isolation working points*. URL: https://indico.cern.ch/event/854783/contributions/3595049/attachments/1922427/3180557/ISO_WPs_FinalList_08102019.pdf (visited on 10/08/2019).

[103] ATLAS Collaboration. "Jet reconstruction and performance using particle flow with the ATLAS Detector". In: *Eur. Phys. J. C* 77 (2017), p. 466. DOI: 10.1140/epjc/s10052-017-5031-2. arXiv: 1703.10485 [hep-ex].

[104] Matteo Cacciari, Gavin P. Salam, and Gregory Soyez. "The anti-k_t jet clustering algorithm". In: *JHEP* 04 (2008), p. 063. DOI: 10.1088/1126-6708/2008/04/063. arXiv: 0802.1189 [hep-ph].

[105] Matteo Cacciari, Gavin P. Salam, and Gregory Soyez. "FastJet User Manual". In: *Eur. Phys. J.* C72 (2012), p. 1896. DOI: 10.1140/epjc/s10052-012-1896-2. arXiv: 1111.6097 [hep-ph].

[106] Matteo Cacciari and Gavin P. Salam. "Pileup subtraction using jet areas". In: *Phys. Lett.* B659 (2008), pp. 119–126. DOI: 10.1016/j.physletb.2007.09.077. arXiv: 0707.1378 [hep-ph].

[107] Matteo Cacciari, Gavin P. Salam, and Gregory Soyez. "The Catchment Area of Jets". In: *JHEP* 04 (2008), p. 005. DOI: 10.1088/1126-6708/2008/04/005. arXiv: 0802.1188 [hep-ph].

[108] ATLAS Collaboration. "Jet energy scale measurements and their systematic uncertainties in proton–proton collisions at $\sqrt{s} = 13\,\text{TeV}$ with the ATLAS detector". In: *Phys. Rev. D* 96 (2017), p. 072002. DOI: 10.1103/PhysRevD.96.072002. arXiv: 1703.09665 [hep-ex].

[109] ATLAS Collaboration. *Tagging and suppression of pileup jets with the ATLAS detector*. ATLAS-CONF-2014-018. 2014. URL: https://cds.cern.ch/record/1700870.

[110] ATLAS Collaboration. "ATLAS b-jet identification performance and efficiency measurement with $t\bar{t}$ events in pp collisions at $\sqrt{s} = 13\,\text{TeV}$". In: *Eur. Phys. J. C* 79 (2019), p. 970. DOI: 10.1140/epjc/s10052-019-7450-8. arXiv: 1907.05120 [hep-ex].

[111] ATLAS Collaboration. "Topological cell clustering in the ATLAS calorimeters and its performance in LHC Run 1". In: *Eur. Phys. J. C* 77 (2017), p. 490. DOI: 10.1140/epjc/s10052-017-5004-5. arXiv: 1603.02934 [hep-ex].

[112] David Krohn, Jesse Thaler, and Lian-Tao Wang. "Jet Trimming". In: *JHEP* 02 (2010), p. 084. DOI: 10.1007/JHEP02(2010)084. arXiv: 0912.1342 [hep-ph].

[113] ATLAS Collaboration. *Jet mass reconstruction with the ATLAS Detector in early Run 2 data*. ATLAS-CONF-2016-035. 2016. URL: https://cds.cern.ch/record/2200211.

[114] ATLAS Collaboration. *Overlap Removal Tools*. 2017. URL: https://indico.cern.ch/event/631313/contributions/2683959/attachments/1518878/2373377/Farrell_ORTools_ftaghbb.pdf.

[115] ATLAS Collaboration. *Improved electron reconstruction in ATLAS using the Gaussian Sum Filter-based model for bremsstrahlung*. ATLAS-CONF-2012-047. 2012. URL: https://cds.cern.ch/record/1449796.

[116] ATLAS Collaboration. "ATLAS jet cleaning". In: (2016). URL: https://twiki.cern.ch/twiki/bin/viewauth/AtlasProtected/HowToCleanJets2016.

[117] Samuel Webb et al. *Measurement of the transverse momentum distribution of Drell–Yan lepton pairs in proton–proton collisions at $\sqrt{s} = 13$ TeV with the ATLAS detector*. Tech. rep. ATL-COM-PHYS-2018-305. Geneva: CERN, Mar. 2018. URL: https://cds.cern.ch/record/2310707.

[118] ATLAS Collaboration. "Search for new phenomena in dijet mass and angular distributions from *pp* collisions at $\sqrt{s} = 13\,\text{TeV}$ with the ATLAS detector". In: *Phys. Lett. B* 754 (2016), p. 302. DOI: 10.1016/j.physletb.2016.01.032. arXiv: 1512.01530 [hep-ex].

[119] ATLAS Collaboration. "Search for dijet resonances in events with an isolated charged lepton using $\sqrt{s} = 13\,\text{TeV}$ proton–proton collision data collected by the ATLAS detector". In: (2020). arXiv: 2002.11325 [hep-ex].

[120] ATLAS Collaboration. "Search for new resonances in mass distributions of jet pairs using $139\,\text{fb}^{-1}$ of *pp* collisions at $\sqrt{s} = 13\,\text{TeV}$ with the ATLAS detector". In: *JHEP* 03 (2020), p. 145. DOI: 10.1007/JHEP03(2020)145. arXiv: 1910.08447 [hep-ex].

[121] ATLAS Collaboration. "Search for Low-Mass Dijet Resonances Using Trigger-Level Jets with the ATLAS Detector in *pp* Collisions at $\sqrt{s} = 13\,\text{TeV}$". In: *Phys. Rev. Lett.* 121 (2018), p. 081801. DOI: 10.1103/PhysRevLett.121.081801. arXiv: 1804.03496 [hep-ex].

[122] ATLAS Collaboration. "Search for new phenomena in dijet events using $37\,\text{fb}^{-1}$ of *pp* collision data collected at $\sqrt{s} = 13\,\text{TeV}$ with the ATLAS detector". In: *Phys. Rev. D* 96 (2017), p. 052004. DOI: 10.1103/PhysRevD.96.052004. arXiv: 1703.09127 [hep-ex].

[123] CMS Collaboration. "Search for narrow and broad dijet resonances in proton–proton collisions at $\sqrt{s} = 13\,\text{TeV}$ and constraints on dark matter mediators and other new particles". In: *JHEP* 08 (2018), p. 130. DOI: 10.1007/JHEP08(2018)130. arXiv: 1806.00843 [hep-ex].

[124] ATLAS Collaboration. "Search for low-mass resonances decaying into two jets and produced in association with a photon using *pp* collisions at $\sqrt{s} = 13\,\text{TeV}$ with the ATLAS detector". In: *Phys. Lett. B* 795 (2019), p. 56. DOI: 10.1016/j.physletb.2019.03.067. arXiv: 1901.10917 [hep-ex].

[125] ATLAS Collaboration. "Search for light resonances decaying to boosted quark pairs and produced in association with a photon or a jet in proton–proton collisions at $\sqrt{s} = 13\,\text{TeV}$ with the ATLAS detector". In: *Phys. Lett. B* 788 (2019), p. 316. DOI: 10.1016/j.physletb.2018.09.062. arXiv: 1801.08769 [hep-ex].

[126] Nicolas Berger et al. *Recommendations for the Modeling of Smooth Backgrounds*. Tech. rep. ATL-COM-PHYS-2020-418. Geneva: CERN, May 2020. URL: https://cds.cern.ch/record/2719221.

[127] G. Choudalakis and D. Casadei. "Plotting the differences between data and expectation". In: *The European Physical Journal Plus* 127.2 (Feb. 2012), p. 25. DOI: 10.1140/epjp/i2012-12025-y. URL: https://doi.org/10.1140/epjp/i2012-12025-y.

[128] *Formulae for Estimating Significance*. Tech. rep. Geneva: CERN, Sept. 2020. URL: https://cds.cern.ch/record/2736148.

[129] Kyle Cranmer et al. *HistFactory: A tool for creating statistical models for use with RooFit and RooStats*. Tech. rep. CERN-OPEN-2012-016. New York: New York U., Jan. 2012. URL: https://cds.cern.ch/record/1456844.

[130] ATLAS Collaboration. *A software framework for statistical data analysis*. URL: https://histfitter.web.cern.ch/histfitter/.

[131] ATLAS Collaboration. *XML Analytic Workspace Bulder*. URL: https://twiki.cern.ch/twiki/bin/viewauth/AtlasProtected/XmlAnaWSBuilder.

[132] Alexander L. Read. "Presentation of search results: the CL_S technique". In: *J. Phys. G* 28 (2002), p. 2693. DOI: 10.1088/0954-3899/28/10/313.

[133] ATLAS Collaboration. *An OR of all scripts used to evluate workspace for profile likelihoods made in RooStats*. URL: https://gitlab.cern.ch/atlas-phys/exot/CommonStatTools.

[134] F. Anulli et al. "The Level-1 Trigger Muon Barrel System of the ATLAS experiment at CERN". In: *JINST* 4 (2009), P04010. DOI: 10.1088/1748-0221/4/04/P04010.

[135] G. Aielli et al. "Performance of a large-size RPC equipped with the final ATLAS front end electronics at X5-GIF irradiation facility". In: *Nucl. Instrum. Meth. A* 456 (2000), pp. 77–81. DOI: 10.1016/S0168-9002(00)00966-9.

[136] ATLAS Collaboration. "Search for a high-mass Higgs boson decaying to a W boson pair in pp collisions at $\sqrt{s} = 8$ TeV with the ATLAS detector". In: *JHEP* 01 (2016), p. 032. DOI: 10.1007/JHEP01(2016)032. arXiv: 1509.00389 [hep-ex].

[137] CMS Collaboration. "Search for a Higgs boson in the mass range from 145 to 1000 GeV decaying to a pair of W or Z bosons". In: *JHEP* 10 (2015), p. 144. DOI: 10.1007/JHEP10(2015)144. arXiv: 1504.00936 [hep-ex].

[138] ATLAS Collaboration. "Search for new phenomena in the $WW \to \ell\nu\ell'\nu'$ final state in pp collisions at $\sqrt{s} = 7$ TeV with the ATLAS detector". In: *Phys. Lett. B* 718 (2013), p. 860. DOI: 10.1016/j.physletb.2012.11.040. arXiv: 1208.2880 [hep-ex].

[139] CMS Collaboration. "Search for massive resonances in dijet systems containing jets tagged as W or Z boson decays in pp collisions at $\sqrt{s} = 8$ TeV". In: *JHEP* 08 (2014), p. 173. DOI: 10.1007/JHEP08(2014)173. arXiv: 1405.1994 [hep-ex].

[140] CMS Collaboration. "Search for massive resonances decaying into pairs of boosted bosons in semi-leptonic final states at $\sqrt{s} = 8$ TeV". In: *JHEP* 08 (2014), p. 174. DOI: 10.1007/JHEP08(2014)174. arXiv: 1405.3447 [hep-ex].

[141] ATLAS Collaboration. "Search for WZ resonances in the fully leptonic channel using pp collisions at $\sqrt{s} = 8\,\text{TeV}$ with the ATLAS detector". In: *Phys. Lett. B* 737 (2014), p. 223. DOI: 10.1016/j.physletb.2014.08.039. arXiv: 1406.4456 [hep-ex].

[142] CMS Collaboration. "Search for new resonances decaying via WZ to leptons in proton–proton collisions at $\sqrt{s} = 8\,\text{TeV}$". In: *Phys. Lett. B* 740 (2015), p. 83. DOI: 10.1016/j.physletb.2014.11.026. arXiv: 1407.3476 [hep-ex].

[143] ATLAS Collaboration. "Search for production of WW/WZ resonances decaying to a lepton, neutrino and jets in pp collisions at $\sqrt{s} = 8\,\text{TeV}$ with the ATLAS detector". In: *Eur. Phys. J. C* 75 (2015), p. 209. DOI: 10.1140/epjc/s10052-015-3425-6. arXiv: 1503.04677 [hep-ex]. Erratum: in: *Eur. Phys. J. C* 75 (2015), p. 370. DOI: 10.1140/epjc/s10052-015-3593-4.

[144] ATLAS Collaboration. "Search for high-mass diboson resonances with boson-tagged jets in proton–proton collisions at $\sqrt{s} = 8\,\text{TeV}$ with the ATLAS detector". In: *JHEP* 12 (2015), p. 055. DOI: 10.1007/JHEP12(2015)055. arXiv: 1506.00962 [hep-ex].

[145] ATLAS Collaboration. "Combination of searches for WW, WZ, and ZZ resonances in pp collisions at $\sqrt{s} = 8\,\text{TeV}$ with the ATLAS detector". In: *Phys. Lett. B* 755 (2016), p. 285. DOI: 10.1016/j.physletb.2016.02.015. arXiv: 1512.05099 [hep-ex].

[146] ATLAS Collaboration. "Searches for heavy diboson resonances in pp collisions at $\sqrt{s} = 13\,\text{TeV}$ with the ATLAS detector". In: *JHEP* 09 (2016), p. 173. DOI: 10.1007/JHEP09(2016)173. arXiv: 1606.04833 [hep-ex].

[147] CMS Collaboration. "Search for massive resonances decaying into WW, WZ or ZZ bosons in proton–proton collisions at $\sqrt{s} = 13\,\text{TeV}$". In: *JHEP* 03 (2017), p. 162. DOI: 10.1007/JHEP03(2017)162. arXiv: 1612.09159 [hep-ex].

[148] CMS Collaboration. "Combination of searches for heavy resonances decaying to WW, WZ, ZZ, WH, and ZH boson pairs in proton–proton collisions at $\sqrt{s} = 8\,\text{TeV}$ and $13\,\text{TeV}$". In: *Phys. Lett. B* 774 (2017), p. 533. DOI: 10.1016/j.physletb.2017.09.083. arXiv: 1705.09171 [hep-ex].

[149] CMS Collaboration. "Search for massive resonances decaying into WW, WZ, ZZ, qW, and qZ with dijet final states at $\sqrt{s} = 13\,\text{TeV}$". In: *Phys. Rev. D* 97 (2018), p. 072006. DOI: 10.1103/PhysRevD.97.072006. arXiv: 1708.05379 [hep-ex].

[150] ATLAS Collaboration. "Search for diboson resonances with boson-tagged jets in pp collisions at $\sqrt{s} = 13\,\text{TeV}$ with the ATLAS detector". In: *Phys. Lett. B* 777 (2018), p. 91. DOI: 10.1016/j.physletb.2017.12.011. arXiv: 1708.04445 [hep-ex].

[151] LHC Higgs Cross Section Working Group. "Handbook of LHC Higgs cross sections: 2. Differential distributions". In: (2012). arXiv: 1201.3084 [hep-ph].

[152] Stefano Frixione et al. "Single-top hadroproduction in association with a W boson". In: *JHEP* 07 (2008), p. 029. DOI: 10.1088/1126-6708/2008/07/029. arXiv: 0805.3067 [hep-ph].

[153] Hung-Liang Lai et al. "New parton distributions for collider physics". In: *Phys. Rev. D* 82 (2010), p. 074024. DOI: 10.1103/PhysRevD.82.074024. arXiv: 1007.2241 [hep-ph].

[154] Stefan Höche et al. "QCD matrix elements and truncated showers". In: *JHEP* 05 (2009), p. 053. DOI: 10.1088/1126-6708/2009/05/053. arXiv: 0903.1219 [hep-ph].

[155] ATLAS Collaboration. "Combined search for the Standard Model Higgs boson in pp collisions at $\sqrt{s} = 7\,\text{TeV}$ with the ATLAS detector". In: *Phys. Rev. D* 86 (2012), p. 032003. DOI: 10.1103/PhysRevD.86.032003. arXiv: 1207.0319 [hep-ex].

Acknowlegement

Time flies, and it's time for me to graduate. It has been a fulfilling and memorable journey since I first stepped into particle physics as an undergraduate student in 2014. I realize that it would not have been possible to finish this dissertation without my supervisors, family, and friends' enormous amount of help and support. I want to take this moment to express my heartfelt thanks to all of you.

First of all, I would like to thank my supervisor, Prof. Haiping Peng, from USTC in China, for giving me this opportunity to be a Ph.D. student under his guidance. I was fascinated by the beautiful picture of particle physics he showed to me. He always listened patiently to me about the difficulties I encountered at work and did not hesitate to help me solve problems. He taught me to understand the physics behind every step of the analysis, which allowed me to think and complete this dissertation independently.

Also, I would like to give my gratitude to my supervisor, Dr. Zhiqing Zhang, from IJCLab in French. Thanks to Zhiqing for allowing me to participate in the BSM searches in the ATLAS collaboration and study in the IJCLab. Though he was swamped in various projects, he still spared every effort to guide my work in the analysis group. He also provided me with countless help to live in French for three years as a non-French speaker. Over the past few years, I have thoroughly enjoyed every discussion with him. I benefit greatly from him and believe that this experience will influence me for a lifetime.

I would like to thank all the friends I met at USTC and Orsay who gave me help during my Ph.D. years. I will never forget the happiness and wish you a brilliant future career!

Finally, I would like to thank my family from the bottom of my heart. They have supported and encouraged me during the years I have been away from home, and this dissertation is the best gift I can give back to you.